
Louisiana Transportation Research Center

Final Report 614

Monitoring of In-Service Geosynthetic Reinforced Soil (GRS) Bridge Abutments in Louisiana

by

Murad Y. Abu-Farsakh, Ph.D., P.E.
Allam Ardah, Ph.D. Candidate
Milad Saghebfar, Ph.D.

LTRC



4101 Gourrier Avenue | Baton Rouge, Louisiana 70808
(225) 767-9131 | (225) 767-9108 fax | www.ltrc.lsu.edu

S f1. Report No. FHWA/LA.18/614		2. Government Accession No.	3. Recipient's Catalog No.
4. Title and Subtitle Monitoring of In-Service Geosynthetic Reinforced Soil (GRS) Bridge Abutments in Louisiana		5. Report Date January 2020	
		6. Performing Organization Code LTRC Project Number: 13-5GT State Project Number: 30000981	
7. Author(s) Murad Abu-Farsakh, Allam Ardah, and Milad Saghebfar		8. Performing Organization Report No.	
9. Performing Organization Name and Address Louisiana Transportation Research Center 4101 Gourrier Avenue Baton Rouge, LA 70808		10. Work Unit No.	11. Contract or Grant No. LTRC Number:13-5GT SIO Number: 30000981
12. Sponsoring Agency Name and Address Louisiana Department of Transportation and Development P.O. Box 94245 Baton Rouge, LA 70804-9245		13. Type of Report and Period Covered Final Report October 2013 to Dec 2018	
		14. Sponsoring Agency Code	
15. Supplementary Notes Conducted in Cooperation with the U.S. Department of Transportation, Federal Highway Administration			
16. Abstract <p>The FHWA has been promoting the GRS-IBS technology for bridge abutments through the Every Day Counts (EDC) initiative. To realize the potential benefits of using GRS-IBS abutments in Louisiana, the DOTD built GRS-IBS abutment for two bridges at Creek and Maree Michel in Vermilion Parish, which provided the opportunity to examine the performance and stability of GRS-IBS abutments with respect to local materials and soil conditions. An instrumentation plan was developed to monitor the short-term and long-term behavior of one of the GRS-IBS abutments. Measurements from the instrumentation provided valuable information on the performance of GRS-IBS abutments. The FHWA design of GRS-IBS abutments was verified and calibrated based on the collected data from the instrumentation measurements. Furthermore, the long-term monitoring provides the measurements needed to examine the performance, durability and long-term stability of the GRS-IBS abutments constructed over Louisiana subsurface soil, under the live traffic load and adverse weather conditions in Louisiana. The monitoring program consisted of measuring bridge deformations, settlement, strains along the reinforcement, vertical and horizontal stresses within abutment, and pore water pressure. Measurements from the instrumentations provide valuable information to evaluate the design procedure and performance of GRS-IBS bridges. The instrumentation readings showed that the magnitude and distribution of strains along reinforcements vary with depth. The locus of maximum strains in the abutment varied by surcharge load and time that did not correspond to the $(45+\phi/2)$ line, especially after the placement of steel girders. A comparison was made between the measured and theoretical value of thrust forces on the facing wall showed that the predicted loads by the bin pressure theory were close to the measured loads in the lower level of abutment. However, the bin pressure theory under predicted the thrust loads in the upper layers with reduced reinforcement spacing.</p> <p>Researchers developed 2D and 3D finite elements (FE) models using PLAXIS 2016 program to evaluate the performance of GRS abutment. The hardening soil model proposed by Schanz et al. was used to simulate the backfill materials, the linear-elastic with M-C failure criterion model was used to simulate the interface between the geosynthetic and backfill materials, and both the geosynthetic and the facing block were modeled using linear elastic model [1]. The FE models were first verified using the field test measurements. Then, a 2D FE parametric study was conducted to evaluate the effect of different variables and parameters on the performance of the GRS-IBS under service loading, in terms of lateral displacement of facing, settlement of RSF, maximum strain distribution along the reinforcement, lateral facing pressure, and location of possible failure locus. The FE results showed that that the abutment height, span length, reinforcement spacing S_v, and reinforcement stiffness have significant effect on the performance of the GRS-IBS. The effect of reinforcement spacing has higher influence than the reinforcement stiffness for the same reinforcement ratio (stiffness/ spacing) due to the composite behavior of closely reinforced soil.</p>			
17. Key Words		18. Distribution Statement Unrestricted. This document is available through the National Technical Information Service, Springfield, VA 21161.	
19. Security Classif. (of this report)	20. Security Classif. (of this page)	21. No. of Pages 209	22. Price

Field Monitoring of In-Service Geosynthetic Reinforced (GRS) Soil Bridge Abutments in Louisiana

by
Murad Y. Abu-Farsakh, Ph.D., P.E.
Allam Ardah, Ph.D. Candidate.
Milad Saghebfar, Ph.D.

Louisiana Transportation Research Center
4101 Gourrier Avenue
Baton Rouge, LA 70808

LTRC Project No. 13-5GT
State Project No. 30000981

conducted for

Louisiana Department of Transportation and Development
Louisiana Transportation Research Center

The contents of this report reflect the views of the author/principal investigator who is responsible for the facts and the accuracy of the data presented herein. The contents do not necessarily reflect the views or policies of the Louisiana Department of Transportation and Development or the Louisiana Transportation Research Center. This report does not constitute a standard, specification, or regulation.

January 2020

Project Review Committee

Each research project will have an advisory committee appointed by the LTRC Director. The Project Review Committee is responsible for assisting the LTRC Administrator or Manager in the development of acceptable research problem statements, requests for proposals, review of research proposals, oversight of approved research projects, and implementation of findings.

LTRC appreciates the dedication of the following Project Review Committee Members in guiding this research study to fruition.

LTRC Administrator

Zhongjie “Doc” Zhang, Ph.D., P.E.
Pavement and Geotechnical Research Administrator

Members

Jesse Rauser, P.E., Chair
Mark Bucci, P.E., DOTD
Jeff Lambert, P.E., DOTD
Matt Melton, P.E., DOTD
Chris Nickel, P.E., DOTD
Mike Boudreaux, P.E., LTRC
Walid Alaywan, Ph.D., P.E., LTRC
Scott Nelson, P.E., FHWA
Arturo Aguirre, P.E. FHWA
Mike Adams, P.E. FHWA
Jennifer Nicks, Ph.D., P.E., FHWA

Directorate Implementation

Sponsor Christopher P. Knotts, P.E.
DOTD Chief Engineer

ABSTRACT

The FHWA has been promoting the GRS-IBS technology for bridge abutments through the Every Day Counts (EDC) initiative. To realize the potential benefits of using GRS-IBS abutments in Louisiana, the DOTD built GRS-IBS abutment for two bridges at Creek and Maree Michel in Vermilion Parish, which provided the opportunity to examine the performance and stability of GRS-IBS abutments with respect to local materials and soil conditions. An instrumentation plan was developed to monitor the short-term and long-term behavior of one of the GRS-IBS abutments. Measurements from the instrumentation provided valuable information on the performance of GRS-IBS abutments. The FHWA design of GRS-IBS abutments was verified and calibrated based on the collected data from the instrumentation measurements. Furthermore, the long-term monitoring provides the measurements needed to examine the performance, durability and long-term stability of the GRS-IBS abutments constructed over Louisiana subsurface soil, under the live traffic load and adverse weather conditions in Louisiana. The monitoring program consisted of measuring bridge deformations, settlement, strains along the reinforcement, vertical and horizontal stresses within abutment, and pore water pressure. Measurements from the instrumentations provide valuable information to evaluate the design procedure and performance of GRS-IBS bridges. The instrumentation readings showed that the magnitude and distribution of strains along reinforcements vary with depth. The locus of maximum strains in the abutment varied by surcharge load and time that did not correspond to the $(45 + \phi/2)$ line, especially after the placement of steel girders. A comparison was made between the measured and theoretical value of thrust forces on the facing wall showed that the predicted loads by the bin pressure theory were close to the measured loads in the lower level of abutment. However, the bin pressure theory under predicted the thrust loads in the upper layers with reduced reinforcement spacing.

Researchers developed 2D and 3D finite element (FE) models using PLAXIS 2016 program to evaluate the performance of GRS abutment. The hardening soil model proposed by Schanz et al. was used to simulate the backfill materials, the linear-elastic with M-C failure criterion model was used to simulate the interface between the geosynthetic and backfill materials, and both the geosynthetic and the facing block were modeled using linear elastic model [1]. The FE models were first verified using the field test measurements. Then, a 2D FE parametric study was conducted to evaluate the effect of different variables and parameters on the performance of the GRS-IBS under service loading, in terms of lateral displacement of facing, settlement of RSF, maximum strain distribution along the reinforcement, lateral facing pressure, and location of possible failure locus. The FE results showed that that the abutment height, span length, reinforcement spacing, S_v , and reinforcement stiffness have significant effect on the performance of the GRS-IBS. The effect of reinforcement spacing has higher influence than the reinforcement

stiffness for the same reinforcement ratio (stiffness/ spacing) due to the composite behavior of closely reinforced soil.

ACKNOWLEDGEMENTS

The investigators are grateful to the Federal Highway Administration through the innovative bridge research and deployment (IBRD) and to the Louisiana Transportation Research Center (LTRC) and Louisiana Department of Transportation and Development (DOTD) for providing additional funding this project. The help and support of Zhongjie Zhang at LTRC is gratefully acknowledged. Thanks and appreciation to the crew of DOTD in Vermilion Parish and in Lafayette District for the tremendous assistance they provided. Finally, special thanks is extended to all PRC members who provided the technical assistance and the support during this study.

IMPLEMENTATION STATEMENT

The results of the short-term and long-term monitoring of the fully instrumented GRS-IBS abutment at Maree Michael Bridge demonstrated that the performance of abutment in terms of lateral deformation of face wall, settlements, strains along reinforcement, and vertical and horizontal stresses within the abutment are satisfactory, with the measured values are less than those recommended by the FHWA. Moreover, the results of the finite element parametric study showed that the GRS-IBS can be loaded to at least three times the service loading with satisfactory performance (i.e., predicted values < recommended values by FHWA). This satisfactory performance of field monitoring and finite element analysis of the GRS-IBS abutments helps DOTD design engineers to gain more confidence in using the GRS-IBS technology for future design of bridge abutments in Louisiana, which is expected to have significant economic benefits.

The use of the new GRS-IBS technology for bridge abutments has a number of advantages including reduced construction time and cost, generally fewer construction difficulties, and easier maintenance over the life cycle of the structure. These advantages have led to a significant increase in the rate of construction of GRS-IBS structures in recent years.

TABLE OF CONTENTS

ABSTRACT.....	iii
ACKNOWLEDGEMENTS.....	v
IMPLEMENTATION STATEMENT.....	vii
TABLE OF CONTENTS.....	ix
LIST OF TABLES.....	xiii
LIST OF FIGURES.....	xv
INTRODUCTION.....	1
OBJECTIVES.....	4
SCOPE.....	5
METHODOLOGY.....	7
Literature Review.....	7
Geosynthetic Reinforced Soil.....	7
GRS Numerical Modeling.....	40
Design and Analysis of GRS Structures.....	48
FHWA GRS-IBS Design Method.....	52
External Stability Analysis.....	53
Internal Stability Analysis.....	56
Maree Michel GRS-IBS Bridge.....	61
Instrumentation.....	62
PERFORMANCE MONITORING.....	69
Settlement and Deformation Measurements.....	69
Measurement of Stresses.....	74
Measurement of Pore Water Pressure.....	77
Strain Measurements along Geosynthetics.....	78
Estimation of Failure Surface.....	78
Estimation of Force against the Wall Face.....	80
FULL-SCALE STATIC LOAD TESTS.....	83
Test Setup.....	83
Results of Field Static Load Tests.....	86
Settlement and Deformation Measurements.....	86
Measurement of Soil Stresses.....	89
Estimation of Force against the Wall Face.....	93
Strain Measurements along Geosynthetics.....	95
FINITE ELEMENT ANALYSIS OF GRS-IBS AT MAREE MICHEL BRIDGE.....	99
Introduction.....	99

Two-Dimensional Finite Element (2D-FE) Analysis	100
2D-FE Numerical Model	100
Results and Discussion	103
Vertical and Lateral Deformations.....	104
Horizontal and Vertical Stresses	105
Reinforcement Strain Distribution and Axial Force	107
Strain Distribution and Vertical Pressure Distribution under RSF.....	116
Three-Dimensional Finite Element (3D-FE) Analysis	118
3D-FE Numerical Model	118
Results and Discussions	119
FINITE ELEMENT PARAMETRIC STUDY	139
FE Numerical Model.....	139
Results of FE Parametric Study	141
Effect of Abutment Height (H)	142
Effect of Span Length (L_{span})	142
Effect of Reinforcement Spacing (S_v).....	146
Effect of Reinforcement Stiffness (EA)	147
Effect of Internal Friction Angle (ϕ).....	150
Effect of Length of Reinforcement (L_r)	150
Effect of Width of Reinforced Soil Footing (B_{RSF}).....	153
Effect of Secondary Reinforcement (Bearing Bed Reinforcement)	153
Effect of Setback Distance (a_b).....	157
Effect of Foundation Type	157
Effect of Bearing Width (b)	160
Effect of Soil Compaction	164
Location of Maximum Strain Envelope.....	167
Effect of Differential Settlement on Performance of GES-IBS.....	168
Control Sections.....	168
Effect of Differential Settlement on 120-ft. Span Length.....	169
Effect of Differential Settlement under the RSF (Case 1)	169
Effect of Differential Settlement under the Reinforced-Zone including the RSF (Case 2)	169
Effect of Differential Settlement under the Retained-Soil (Case 3)	170
Effect of Differential Settlement underneath the Reinforced-Zone on Different Span Lengths (Case 2)	173
Effect of Differential Settlement on the Bump at the Bridge Slap and Approach Roadway Intersection.....	176

Effect of Differential Settlement on Lateral Facing Pressure	177
SUMMARY AND CONCLUSIONS	179
Experimental Testing Program	179
Finite Element Numerical Modeling Program.....	181
RECOMMENDATIONS	185
ACRONYMS, ABBREVIATIONS, AND SYMBOLS	187
REFERENCES	189

LIST OF TABLES

Table 1 Properties of materials for the mini pier experiments [59].....	23
Table 2 Test program for the GSGC tests [46].....	26
Table 3 Effects of CMU facing on stiffness and capacity [44]	28
Table 4 NCHRP full-scale test results [15].....	32
Table 5 Recommended allowable bearing pressure of a geosynthetic reinforced soil abutment with an integrated sill [15].....	47
Table 6 Comparison between GMSE and GRS design methods [44]	52
Table 7 Comparison between predicted and measured lateral facing defamation.....	73
Table 8 Comparison between predicted and measured lateral deformation of facing wall.....	89
Table 9 Measurement of total lateral pressure on the facing wall	93
Table 10 Measured and theoretical value of thrust force (1 b/ft)	94
Table 11 Material Properties.....	103
Table 12 Axial force in the reinforcement and the interface shear stress	113
Table 13 FE predicted axial force in the reinforcement and the interface shear stress	136
Table 14 Modified Cam-Clay Model parameter for different subgrade soils	157
Table 15 Summary of maximum strain results	163
Table 16 Summary of maximum lateral facing deformation.....	164

LIST OF FIGURES

Figure 1 Typical GRS-IBS cross section	9
Figure 2 Concept of apparent cohesion due to the presence of reinforcement [48]	12
Figure 3 Concept of apparent confining pressure due to the presence of reinforcement [50].....	13
Figure 4 Behavior of unreinforced and reinforced soil masses: (a) stress-strain and (b) volume change [47].....	14
Figure 5 Schematic diagrams of volume change behavior of compacted granular soil: (a) unreinforced soil and (b) reinforced soil [47].....	14
Figure 6 Difference between MSE and GRS technology: (a) MSE technology and (b) GRS technology [51]	16
Figure 7 Triaxial Compression Tests [52]	17
Figure 8 Schematic diagram of the long-term soil-geosynthetic performance testing apparatus [53].....	18
Figure 9 Failure modes in SGP tests [55]	19
Figure 10 Samples failed under the (a) diagonal shear failure mode and (b) wedge type shear failure mode [55]	20
Figure 11 Cylindrical GRS setup before and during testing [57]	21
Figure 12 Stress- strain curves of specimens reinforced at spacing of 12 in. and 6 in. [57]	22
Figure 13 Mini pier experiments [56].....	23
Figure 14 Stress-strain curves of mini-pier experiments [59]	24
Figure 15 Test setup of large –size triaxial test [60].....	25
Figure 16 Large-size triaxial test results [60]	25
Figure 17 GSGC test results [46].....	27
Figure 18 Loading test of the commerce city GRS wall [4].....	29
Figure 19 Havana yard pier test setup [54].....	30
Figure 20 Cross-section of Vienna railroad embankment [7].....	33
Figure 21 Cross-section of the Black Hawk Bridge abutments [7]	34
Figure 22 Feather Fall GRS abutment schematic [2].....	35
Figure 23 Cross-section of the Founder/Meadows Bridge [62].....	36
Figure 24 Mammoth Lakes West GRS abutment schematic [6]	37
Figure 25 Cross- section of Bowman Road Bridge GRS abutment [59].....	38
Figure 26 GRS foundation for Mattamuskeet Bridge [65]	40
Figure 27 Lateral earth pressure of a GRS wall [71]	41
Figure 28 Vertical stress distribution at 6-kN vertical load: (a) with and (b) without reinforcement [55].....	42
Figure 29 Horizontal stress distribution at 6-kN vertical load: (a) with and (b) without reinforcement [55]	43

Figure 30 Shear stress distribution at 6-kN vertical load: (a) with and (b) without reinforcement [55].....	44
Figure 31 Bridge approach settlement after load application [14]	45
Figure 32 Schematic of 2D plain strain finite element model [70].....	46
Figure 33 Timeline of development and advancement of reinforced soil design guidance [73]..	49
Figure 34 Conservatism of reinforcement soil design guidance [74]	50
Figure 35 Direct sliding failure [5]	53
Figure 36 Bearing capacity failure [5]	54
Figure 37 Global stability failure [5]	54
Figure 38 Lateral deformation of a GRS structure [5].....	57
Figure 39 Schematic diagram of Denver wall [12].....	58
Figure 40 Comparison between FE predicted and results of triaxial compression tests for Ottawa sand [12].....	59
Figure 41 Details of FE numerical grid	60
Figure 42 Location of GRS-IBS project site.....	61
Figure 43 Instrumentation layout.....	63
Figure 44 Arrangement of SAA for Maree Michel Bridge - GRS-IBS	65
Figure 45 Locations of earth pressure cells	66
Figure 46 Anticipated strain distributions along the geosynthetics	67
Figure 47 Settlement profile of soil foundation	69
Figure 48 Construction of the GRS abutment with time	70
Figure 49 Settlement and vertical deformation during the construction of GRS abutment.....	71
Figure 50 Lateral movements of the abutment 2 ft. behind the facing wall	73
Figure 51 Lateral movements behind GRS mass.....	74
Figure 52 Measurement of vertical pressures	76
Figure 53 Measurements of lateral pressures on the wall.....	77
Figure 54 Measurements of pore water pressures.....	77
Figure 55 Measurement of strain distribution along geosynthetics	79
Figure 56 Locations of maximum strain at various stages of construction	80
Figure 57 Measured thrust force at various stages of construction	81
Figure 58 Measured and theoretical value of thrust force	82
Figure 59 Static load test.....	83
Figure 60 Location of trucks along roadway lanes	84
Figure 61 Location of trucks along bridge.....	85
Figure 62 Axle loads of the dump truck and cone truck used in tests	85
Figure 63 Vertical deformation of GRS abutment due to the trucks load	87
Figure 64 Maximum vertical deformation due to dead load and trucks load	88

Figure 65 Profiles of lateral movements of the abutment behind the facing wall	88
Figure 66 Vertical earth pressure measurements	92
Figure 67 Strain distribution under static load test	97
Figure 68 Locations of maximum strain at various load tests	98
Figure 69 FE Mesh of the GRS-IBS and locations of the applied boundary conditions	100
Figure 70 Stress-strain curves of backfill at 115 lb/ft ³ dry density	102
Figure 71 Comparison between measured and predicted lateral deformation profiles along the wall face	106
Figure 72 Comparison between measured and predicted RSF settlement distribution	106
Figure 73 Profiles of prediction lateral deformation along the wall face at different loading conditions using FE analysis	107
Figure 74 Measured and FE predicted lateral earth pressure distribution at the GRS-IBS abutment face	108
Figure 75 FE predicted vertical stress distribution at different layers in the GRS abutment	109
Figure 76 Measured versus FE predicted strain distribution along geosynthetics for Case 1	111
Figure 77 FE Predicted strain distribution along geosynthetics for the four cases of loading ...	112
Figure 78 Maximum strain envelope for field and FE results at different loading	114
Figure 79 The distribution of relative shear stress, τ_{rel} , as determined from FE analysis for the GRS-IBS under service loading: (a) service loading Case 3, and (b) abnormal loading Case 4	115
Figure 80 (a) Strain distribution along RSF reinforcement, (b) vertical stress distribution below RSF	117
Figure 81 3D FE mesh of the GRS-IBS and locations of the applied boundary conditions	119
Figure 82 Predicted settlement of GRS-IBS due to abnormal loading (Case 3)	121
Figure 83 Predicted lateral deformation of GRS-IBS due to abnormal loading (Case 3)	122
Figure 84 Comparison of measured and FE predicted lateral deformation profiles along the wall face	122
Figure 85 3D-FE predicted lateral deformation profile along the face at different loading conditions	123
Figure 86 Comparison between measured and FE predicted of RSF settlement distribution	124
Figure 87 Strain distribution along RSF geosynthetic reinforcement	125
Figure 88 Predicted vertical stress distribution along cross-section at different layers in the GRS abutment	128
Figure 89 Predicted vertical stress distribution along longitudinal-section at different layers in the GRS abutment	129
Figure 90 Measured and FE predicted lateral pressures on wall face under different load conditions	130

Figure 91 Comparison of strain distribution along geosynthetics for Case 1 in the transverse direction	133
Figure 92 Predicted strain distribution along geosynthetics for the three cases of loading in the transverse direction	134
Figure 93 Predicted strain distribution along geosynthetics for the three cases of loading in the longitudinal direction	135
Figure 94 (a) Maximum strain envelope at different loading conditions; (b) Comparison of maximum strain envelope between field and FE results	136
Figure 95 Shear strain (Service Load)	137
Figure 96 GRS-IBS FE numerical model with geometry and boundaries conditions	140
Figure 97 Effect of abutment height on the strain distribution along geosynthetics	144
Figure 98 Effect of span length on the strain distribution along geosynthetics	145
Figure 99 Effect of a) abutment height; b) span length on the lateral facing displacement	146
Figure 100 Effect of reinforcement a) spacing; b) stiffness on the lateral facing displacement	147
Figure 101 Effect of reinforcement spacing on the strain distribution along geosynthetics	148
Figure 102 Effect of reinforcement stiffness on the strain distribution along geosynthetics	149
Figure 103 Effect of internal friction angle on the strain distribution along geosynthetics	151
Figure 104 Effect of reinforcement length on the strain distribution along geosynthetics	152
Figure 105 Effect of (a) friction angle; (b) reinforcement length on the lateral facing displacement	153
Figure 106 Effect of (a) width of RSF; (b) secondary reinforcement on the lateral facing displacement	154
Figure 107 Effect of width of reinforced soil footing (B_{RSF}) on the strain distribution along geosynthetics	155
Figure 108 Effect of secondary reinforcement on the strain distribution along geosynthetics	156
Figure 109 Effect of setback distance on the strain distribution along geosynthetics	158
Figure 110 Effect of foundation type on the strain distribution along geosynthetics	159
Figure 111 Effect of bearing width on the strain distribution along geosynthetics	161
Figure 112 Effect of (a) setback distance; (b) foundation type; (c) bearing width on the lateral facing displacement	162
Figure 113 Effect of soil compaction on the strain distribution along geosynthetics	166
Figure 114 Effect of soil compaction on the lateral facing displacement	167
Figure 115 Effect of span length, reinforcement spacing, and reinforcement stiffness on the location of maximum strain envelope	168
Figure 116 Effect of differential settlement under the RSF on the strain distribution along geosynthetics for a span length of 120 ft	170

Figure 117 Effect of differential settlement under the RSF on the lateral facing displacement for a span length of 120 ft.....	171
Figure 118 Effect of differential settlement of the reinforced-zone on the strain distribution along geosynthetics for a span length of 120 ft	171
Figure 119 Effect of differential settlement of the reinforced-zone on the lateral facing displacement for a span length of 120 ft.....	172
Figure 120 Effect of differential settlement of the retained soil on the strain distribution along geosynthetic for a span length of 120 ft.....	172
Figure 121 Effect of differential settlement of the retained soil on the lateral facing displacement for a span length of 120 ft.....	173
Figure 122 Effect of differential settlement of the reinforced-zone on the strain distribution along geosynthetics for a span length of 100 ft	174
Figure 123 Effect of differential settlement of the reinforced-zone on the lateral facing displacement for a span length of 100 ft.....	175
Figure 124 Effect of differential settlement of the reinforced-soil on the strain distribution along geosynthetics for a span length of 80 ft	175
Figure 125 Effect of differential settlement of the reinforced-soil on the lateral facing displacement for a span length of 80 ft.....	176
Figure 126 Effect of differential settlement on the bump at the intersection between the bridge slap and the approach roadway for different span lengths: a) underneath RSF, b) underneath reinforced-zone	177
Figure 127 Effect of differential settlement on lateral facing pressure for a bridge span of 120 ft. under service loading condition	178

INTRODUCTION

Reinforced earth is an ancient technique, which has happened since earliest part of human history. Early societies used straw, sticks, and branches to reinforce adobe bricks and mud dwellings [2]. Other examples of early use of soil reinforcement are dikes of earth and tree branches in China, wooden pegs used for erosion control in England, and bamboo used for revetment erosion control [3]. In the early 1960s, a French engineer Henri Vidal invented a modern method to reinforce soil. He developed reinforced earth, a system that uses steel strip as reinforcement.

Geosynthetic reinforced soil technology (GRS) was first used in the United States (US) in the 1970s by the US Forest Service (USFS). USFS used plain non-woven geotextiles to build GRS wall to support logging roads in steep mountain terrain. Shortly after the construction of GRS walls by USFS, the Colorado Department of Transportation (CDOT) began constructing GRS walls in some interstate expansion projects. Later in 1994, Colorado Transportation Institute published a design and construction manual for construction of low cost retaining walls. This manual presents guidelines for three types of GRS walls: wrapped-faced geotextile-reinforced retaining wall, timber-faced geosynthetic-reinforced wall, and modular block geosynthetic-reinforced wall [4].

GRS has a variety of applications in civil engineering such as culverts, rockfall barriers, walls, bridge piers, and bridge abutments. Over the last few years, the use of GRS technology for bridge abutments has received considerable attention. Geosynthetic Reinforced Soil Integrated Bridge System (GRS-IBS) is the coined name for a GRS wall and bridge system that was developed as part of the “Bridge of the Future” initiative by the Federal Highway Administration (FHWA) [5]. GRS-IBS is a cost effective and efficient solution for low volume, single span bridges. Furthermore, GRS-IBS can be used under a variety of foundation soil conditions. Another advantage of GRS-IBS is the elimination of the “bump” at the end of the bridge. This is due to the improved performance of these systems regarding differential settlement. However, GRS-IBS has a few shortcomings regarding applicability. These systems are not ideal for stream scour environments or conditions of soft, deep foundation soil if large settlement is a concern [6].

GRS-IBS typically consists of three main components: reinforced soil foundation (RSF), abutment, and integrated approach. The RSF is built from compacted granular aggregate wrapped with geosynthetic. The RSF is placed under the GRS abutment to provide more support and increase the bearing capacity. In addition, RSF avoids underneath water to the abutment. The GRS abutment is composed of compacted backfill and layers of geosynthetic reinforcement. Typically, spacing of geosynthetic layer decrease underneath the integrated approach. Usually, GRS abutments consists of three sides: the abutment face wall and two wing walls. In some cases, an abutment can be made by one or none of the wing walls, but it must have the facing element. The

facing element is flexible wall built from articulated units that are not rigidly attached to each other. The purpose of facing element in GRS-IBS is to protect abutment from outside weathering. Facing wall is not a structural element. The approach is also constructed with GRS to transition to the bridge.

Overall, GRS-IBS is a promising technology, which has been implemented in a series of successful case histories in the U.S. and abroad [7]. In 2010, GRS-IBS was made an Every Day Counts (EDC) initiative. The poor state of bridges in the U.S. prompted the EDC initiative. Many of the 600,000 bridges in the U.S. have structural deficiencies. Of these bridges, the vast majority are single span bridges no more than 90 ft. in length. Currently the demand for repair and future construction of bridges does not align with government budgets. Therefore, a new efficient system is required so that more bridges can be rehabilitated and constructed at low cost. GRS-IBS is a possible solution for this dilemma [5].

GRS-IBS is proficient alternative for low volume, single span bridges. It can be built in less time and over a variety of foundation soil conditions with common equipment and materials. This method is built from the inside out therefore; it reduces exposure of crew to roadside hazards and provide a safer work environment. GRS-IBS is more cost-effective than traditional bridge construction. The cost of GRS-IBS bridge is 25-30% less than cost of standard pile cap abutments on deep foundations with 2:1 slopes for off-system bridges and 50-60% lower than cost of standard department of transportation bridges. The saving is due to simplicity and flexibility of the design, speed of construction (less dependent on weather conditions), use of readily available materials and equipment, elimination of the deep foundation and other construction details associated with the approach way to the bridge, and lower maintenance costs because of elimination of the bump at the end of the bridge [5].

Numerical methods such as finite element (FE) or finite difference techniques are now extensively used for analyzing the behavior of GRS walls [8-11]. When compared with laboratory experiments and field measurements, the numerical methods have many advantages including obtaining more comprehensive results, investigating the effects of different loading conditions and study the effect of different variables and parameters, which are difficult or costly to achieve in laboratory and field tests. Numerical methods help better understanding of the performance of these soil structures and thus, they can be considered as new steps in the optimization of design methods [12, 13]. Two-dimensional numerical modeling studies have been conducted for GRS abutments under static loading [14-20]. The results of these studies showed that reinforcement spacing, relative compaction of backfill soil, reinforcement stiffness, and bridge load have significant effects on the performance of GRS abutment [20]. The preceding numerical studies have focused on 2D analysis of GRS abutments; with much less analysis has been conducted with 3D analysis.

Many numerical studies have been conducted on the behavior of a free-standing geosynthetic mechanically stabilized earth (GMSE) walls [e.g., 21-33]. A few numerical studies were conducted recently to evaluate the composite behavior of the GRS-IBS (e.g., 15, 34-41). Wu et al. conducted a finite element analysis to investigate the allowable bearing pressure on bridge sills over a GRS abutment with flexible facing [15]. They performed 72 case analyses in their study for various geometric and materials properties: sill type and width, soil strength and stiffness, reinforcement spacing, and foundation stiffness. Their results showed that the effect of reinforcement spacing on the performance of the GRS in terms of lateral deformation, sill settlement, and allowable bearing capacity is significant. They also found out that the integrated sill performs better than the isolated sills in terms of sill settlement. Wu et al. developed a finite element model to investigate the composite behavior of closely spaced reinforcement soil [42]. They conducted a FE parametric study to study the effect of the reinforcement spacing, reinforcement stiffness, and soil stiffness on the volume change behavior (soil dilation). They found out that the inclusion of geosynthetic would serve to suppress the soil dilation and lead to a stronger soil and zero volume change assumption, which has been adopted by the FHWA for estimating the lateral deformation of GRS abutment. Zheng and Fox investigated the performance of the GRS abutments under static loading conditions using the finite-difference analyses [20]. Their model was verified using the field measurement of the Founders/Meadows GRS bridge abutment. The results of their numerical simulation were in good agreement with the field measurements during the construction process and after the bridge was open to traffic loading. A corresponding FE parametric study indicates that the reinforcement spacing, the backfill compaction, and the bridge load have significant influence on the lateral facing deformations and bridge footing settlement for the GRS abutments. They also found out that the horizontal restraining forces from the bridge span have a pronounced influence on the GRS abutment deflections. Zheng and Fox conducted another parametric study to investigate the effect of reinforcement stiffness, bearing bed reinforcement, height of the bridge abutment, and bridge load on the lateral deformations and bridge seat settlement [35]. They found out that the reinforcement stiffness, bridge load, and the abutment height are the most significant factors on the performance of the GRS-IBS under static loading. It was noticed that the abutment vertical strain decreases with increasing the abutment height due to higher stress conditions and larger soil stiffness for taller abutments.

OBJECTIVES

The design methods and construction techniques for GRS abutments have evolved along with the numerous research and studies conducted on the GRS abutments. The Federal Highway Administrative (FHWA) has recently released synthesis and implementation manuals covering the background, design, construction, and performance of GRS abutments [43]. The current design for GRS Bridge is largely empirical- based and required validation for local materials and subsurface conditions and practice. This method addresses the advantages of closely-spaced geosynthetic reinforcement such as higher confinement, lower lateral deformation, suppress of dilation, and reduction in connection stress [44]. FHWA also calibrated the reliability of these models using performance test data, which have been correlated against results from laboratory and field monitoring programs [45]. However, the results of those studies are only deemed valid for the conditions specifically simulated in that research. Additionally, important design parameters such as stresses and deformations of GRS abutment need to be measured and verified against the current FHWA design method. These limitations provide a motivation to monitor the performance of the GRS abutment from construction to one year of trafficking. In addition, two sets of static load test were conducted at the end of construction and after one year of trafficking. Undoubtedly, a successful instrumentation program is necessary to achieve this goal. An extensive instrumentation program was designed to provide insight into the mechanical responses and deformation characteristics of GRS-IBS bridges.

SCOPE

In order to monitor and evaluate the performance of the in-service GRS-IBS abutment, various types of instrumentations were installed in the GRS-IBS abutment of the selected Maree Michel Bridge to record the measurements of interest. An instrumentation plan was developed to measure the load-associated and environment-associated responses and performance of the GRS-IBS abutments. The primary measurements of interest are the vertical and horizontal deformations near the front wall, settlements due to the soil foundation and the GRS-IBS backfill, the distribution of stresses in the GRS-IBS abutments and below reinforced soil foundation, and the distribution of strains along the geosynthetic reinforcements. Additionally, the possible development of pore water pressure will be monitored by piezometers while thermocouples will be installed to account for potential effects of thermal cycles on the abutment and bridge responses. Instrumentations will be carefully selected according to the needs of measurements discussed above. Five different types of instrumentations are proposed to monitor the GRS-IBS bridge abutment. Additionally, surveying was conducted at the bridge surface upon the completion of the construction and at certain intervals afterwards. To evaluate the performance of bridge under critical conditions, two sets of static load tests that were conducted on a geosynthetic reinforced integrated bridge system. In each set of tests, the bridge was surcharge loaded to stress levels well in excess of working load conditions. Sixteen loading cases, using two fully loaded trucks, were conducted on the instrumented GRS-IBS Bridge. This study is focused on using the 2-D and 3-D FE method to simulate the composite behavior of GRS-IBS system. The constitutive model for the backfill material is selected to account for the nonlinearity, soil dilation, and stress dependent behavior and is used as it is. The interface friction is simulated using M-C constitutive model. Linear elastic constitutive model was selected to simulate the geosynthetic and facing block. The results discuss the closely spaced reinforcement effect influence on the behavior of the GRS-IBS system compared to the mechanically stabilized earth (MSE) walls. In addition, the 2-D FE results is also compared with the 3-D FE. Study of reinforcement spacing, reinforcement strength, and GRS-IBS geometry is made to verify or adjust the analytical solution proposed by Pham [46].

METHODOLOGY

As discussed earlier, the main objective of this research study was to monitor the short-term and long-term behavior and performance of in-service GRS-IBS abutments in the state of Louisiana and to verify important design factors and parameters for GRS-IBS abutment, mainly stresses and deformations involved in both external and internal stability analyses. Background information on mechanism of geosynthetic reinforced soil and available design model were studied first. Based on lessons learned from previous studies, instrumentation plan for GRS-IBS Bridge was developed. An instrumentation plan was developed to measure the load-associated and environment-associated responses of the GRS-IBS abutments during the construction, under traffic load, and under static load tests. A finite element (FE) simulation for the case study at the end of construction and under dead and live load behavior was conducted. An extensive parametric study was conducted to investigate the effects of different parameters on the performance of the GRS-IBS in terms of lateral facing displacement, settlement of the RSF, maximum reinforcement strain along the reinforcement, and lateral facing pressure.

Literature Review

Geosynthetic Reinforced Soil

Reinforced earth is an ancient technique that was introduced since earliest part of human history. Early societies used straw, sticks, and branches to reinforce adobe bricks and mud dwellings [2]. Other examples of early use of soil reinforcement are dikes of earth and tree branches in China, wooden pegs used for erosion control in England, and bamboo used for revetment erosion control [3]. In the early 1960s, a French engineer invented a modern method to reinforce soil. He developed Reinforced Earth, a system in which steel strip used as reinforcement.

Geosynthetic reinforced soil technology (GRS) was first used in the United States in the 1970's by U.S. Forest Service (USFS). USFS used plain non-woven geotextiles to build GRS wall to support logging roads in steep mountain terrain. Shortly after the construction of GRS walls by USFS, Colorado Department of Transportation (CDOT) began constructing GRS walls in some of the interstate expansion projects. Later in 1994, Colorado Transportation Institute published a design and construction manual for construction of low cost retaining walls. This manual presents guidelines for three types of GRS walls: wrapped-faced geotextile-reinforced retaining wall, timber-faced geosynthetic-reinforced wall, and modular block geosynthetic-reinforced wall [4].

GRS has a variety of applications in the civil engineering such as culverts, rockfall barriers, walls, bridge piers, and bridge abutments. Over the last few years, the use of GRS technology for bridge abutments has received considerable attention. Geosynthetic Reinforced Soil Integrated Bridge

System (GRS-IBS) is the coined name for a GRS wall and bridge system that was developed as part of the “Bridge of the Future” initiative by the Federal Highway Administration (FHWA) [5]. GRS-IBS is a cost effective and efficient solution for low volume, single span bridges. Furthermore, GRS-IBS can be used under a variety of foundation soil conditions. Another advantage of GRS-IBS is the elimination of the “bump” at the end of the bridge. This is due to the improved performance of these systems about differential settlement. However, GRS-IBS has a few shortcomings regarding applicability. These systems are not ideal for stream scour environments or conditions of soft, deep foundation soil if large settlement is a concern [6].

GRS-IBS typically consists of three main components: reinforced soil foundation (RSF), abutment, and integrated approach (Figure 1). The RSF is built from compacted granular aggregate wrapped with geosynthetic. The RSF is placed under the GRS abutment to provide more support and increase the bearing capacity. In addition, RSF avoids underneath water to the abutment. The GRS abutment is composed of compacted backfill and layers of geosynthetic reinforcement. Typically, spacing of geosynthetic layer decrease underneath the integrated approach. Usually, GRS abutments consists of three sides: the abutment face wall and two wing walls. In some cases, an abutment can be made by one or none of the wing walls, but it must have the facing element. The facing element is flexible wall built from articulated units that are not rigidly attached to each other. The purpose of facing element in GRS-IBS is to protect abutment from outside weathering. Facing wall is not a structural element. The approach is also constructed with GRS to transition to the bridge.

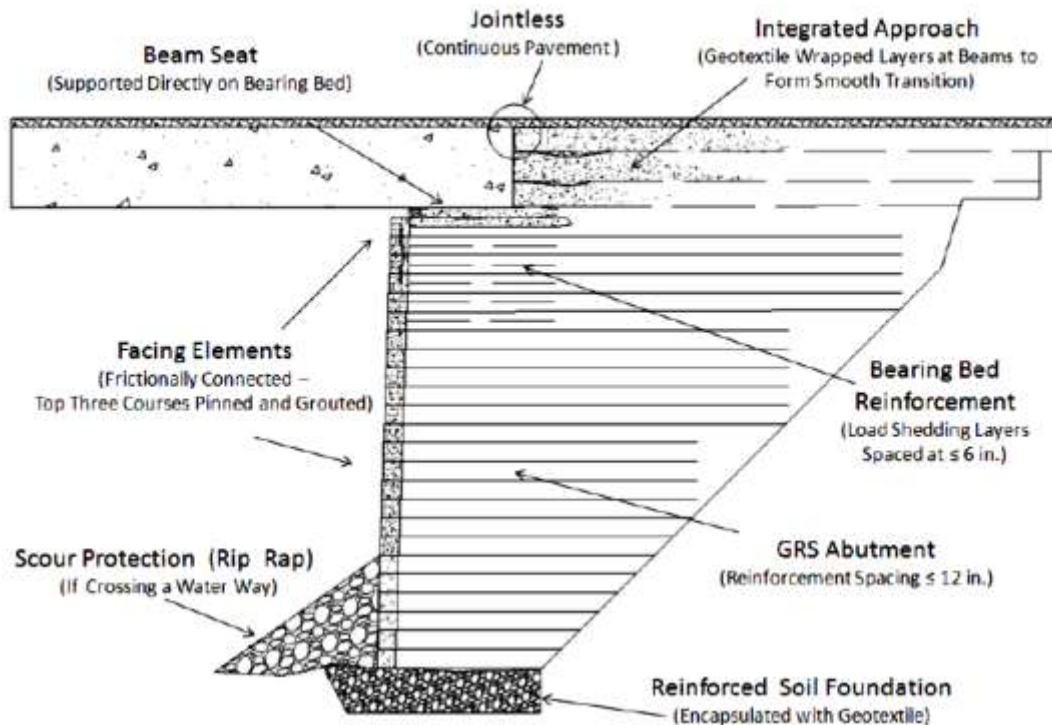


Figure 1
Typical GRS-IBS cross section

Overall, GRS-IBS is a promising technology, which has been implemented in a series of successful case histories in the U.S. and abroad [7]. In 2010, GRS-IBS was made an Every Day Counts (EDC) initiative. The poor state of bridges in the U.S. prompted the EDC initiative. Many of the 600,000 bridges in the U.S. have structural deficiencies. Of these bridges, the vast majority are single span bridges no more than 90 ft. in length. Currently the demand for repair and future construction of bridges does not align with government budgets. Therefore, a new efficient system is required so that more bridges can be rehabilitated and constructed at low cost. GRS-IBS is a possible solution for this dilemma [5].

Numerical methods such as finite element or finite difference techniques are now extensively used for analyzing the behavior of Geosynthetic Reinforced Soil (GRS) walls [8 - 11]. When compared with laboratory experiments and field measurements, the numerical methods have many advantages including obtaining more comprehensive results, investigating the effects of different loading conditions and study the effect of different variables and parameters, which are difficult or costly to achieve in laboratory and field tests. Numerical methods help better understanding of the performance of these soil structures and thus, they can be considered as new steps in the

optimization of design methods [12, 13]. Two-dimensional numerical modeling studies have been conducted for GRS abutments under static loading [14-19]. The results of these studies showed that reinforcement spacing, relative compaction of backfill soil, reinforcement stiffness, and bridge load have significant effects on the performance of GRS abutment [19, 20]. The preceding numerical studies have focused on 2D analysis of GRS abutments; with much less analysis has been conducted with 3D analysis.

Many numerical studies have been conducted on the behavior of a free-standing GMSE walls [e.g., 21-33]. A few numerical studies were conducted recently to evaluate the composite behavior of the GRS-IBS [e.g., 15, 34 - 41]. Wu et al. conducted a finite element analysis to investigate the allowable bearing pressure on bridge sills over a GRS abutment with flexible facing [15]. They performed 72 case analyses in their study for various geometric and materials properties: sill type and width, soil strength and stiffness, reinforcement spacing, and foundation stiffness. Their results showed that the effect of reinforcement spacing on the performance of the GRS in terms of lateral deformation, sill settlement, and allowable bearing capacity is significant. They also found out that the integrated still performs better than the isolated sills in terms of sill settlement. Wu et al. developed a finite element model to investigate the composite behavior of closely spaced reinforcement soil [47]. They conducted a FE parametric study to study the effect of the reinforcement spacing, reinforcement stiffness, and soil stiffness on the volume change behavior (soil dilation). They found out that the inclusion of geosynthetic would serve to suppress the soil dilation and lead to a stronger soil and zero volume change assumption, which has been adopted by the FHWA for estimating the lateral deformation of GRS abutment. Zheng and Fox investigated the performance of the GRS abutments under static loading conditions using the finite-difference analyses [20]. Their model was verified using the field measurement of the Founders/Meadows GRS bridge abutment. The results of their numerical simulation were in good agreement with the field measurements during the construction process and after the bridge was open to traffic loading. A corresponding FE parametric study indicates that the reinforcement spacing, the backfill compaction, and the bridge load have significant influence on the lateral facing deformations and bridge footing settlement for the GRS abutments. They also found out that the horizontal restraining forces from the bridge span have a pronounced influence on the GRS abutment deflections. Zheng and Fox conducted another parametric study to investigate the effect of reinforcement stiffness, bearing bed reinforcement, height of the bridge abutment, and bridge load on the lateral deformations and bridge seat settlement [35]. They found out that the reinforcement stiffness, bridge load, and the abutment height are the most significant factors on the performance of the GRS-IBS under static loading. It was noticed that the abutment vertical strain decreases with increasing the abutment height due to higher stress conditions and larger soil stiffness for taller abutments.

Benefits of GRS-IBS. GRS-IBS is a proficient alternative for low volume, single span bridges. It can be built in less time and over a variety of foundation soil conditions with common equipment and materials. This method is built from the inside out, therefore reducing exposure of crew to roadside hazards and provide a safer work environment. GRS-IBS is more cost-effective than traditional bridge construction. The cost of GRS-IBS bridge is 25-30% less than cost of standard pile cap abutments on deep foundations with 2:1 slopes for off-system bridges and 50-60% lower than cost of standard department of transportation bridges. The saving is due to following factors [5]:

- simplicity and flexibility of the design
- speed of construction (less dependent on weather conditions)
- use of readily available materials and equipment
- elimination of the deep foundation and other construction details associated with the approach way to the bridge
- Lower maintenance costs because of elimination of the bump at the end of the bridge

Mechanics of Geosynthetic Reinforced Soil. Reinforced soil is the technique where tensile elements are placed in the soil to improve stability and control deformation. To be effective, the reinforcements must intersect potential failure surfaces in the soil mass. Strains in the soil mass generate strains in the reinforcements, which in turn, tensile loads in the reinforcements. These tensile loads act to restrict soil movements and thus impart additional shear strength. This results in the composite soil/reinforcement system having greater shear strength than the soil mass alone. Several mechanisms by which geosynthetic reinforcement contributes to the increase in strength and/or stiffness of soil have been proposed. Among them, two mechanisms involve quantitative evaluation of the reinforcing effects, apparent cohesion, and apparent confining pressure [48, 49]. Recently, Wu et al. proposed a new mechanism, where the presence of closely spaced geosynthetic is believed to suppress the soil dilation [47].

Concept of Apparent Cohesion. Based on this concept, the presence of reinforced layer increases the principal stress at failure with an apparent cohesion (C_R'). As shown in the Mohr stress diagram in Figure 2, the principle stress at failure increased from σ_1 to σ_{1R} . A study by Yang shows that the ϕ value is not changed by using reinforcement as long as slippage at the soil-reinforcement interface did not occur [49].

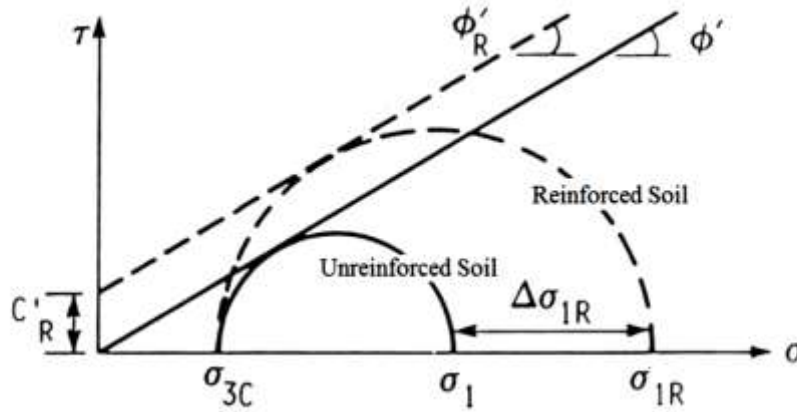


Figure 2

Concept of apparent cohesion due to the presence of reinforcement [48]

Concept of Increase of Apparent Confining Pressure. Another method to explain the mechanism of reinforced soil is the concept of increase of apparent confining pressure. In this concept, axial strength of reinforced soil increases due to increase of confining pressure. As illustrated in Figure 3, with increase of confining pressure ($\Delta\sigma_{3R}$), the axial strength of unreinforced soil (σ_1) increases to σ_{1R} . The strength of reinforced soil can be measured by triaxial test.

Schlösser and Long suggested the following equation to calculate apparent cohesion of reinforced soil (C'_R) based on the concept of apparent confining pressure [48].

$$C'_R = \frac{T_f \sqrt{K_p}}{2 S_v} \quad (1)$$

where, T_f is tensile strength of reinforcement, S_v is vertical spacing of reinforcement, and K_p is coefficient of passive earth pressure.

This equation is based on the assumption that the increase in strength of reinforcement has the same effect as a proportional decrease in vertical spacing on strength of GRS mass. However, some studies reject this assumption [50].

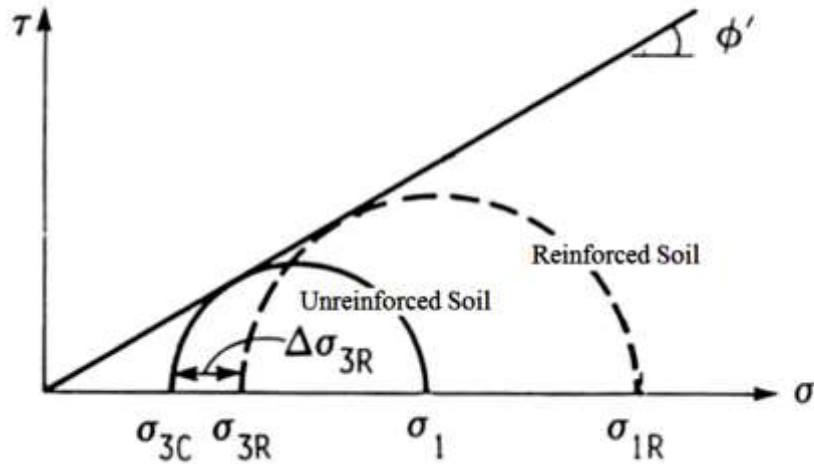


Figure 3

Concept of apparent confining pressure due to the presence of reinforcement [50]

Concept of Suppression of Soil Dilatation. Loose granular soil contracts when subjected to shear stress. Under the shear stress, soil particles fall in to the voids between the particles and cause contraction. On the other hand, the volume of dense granular soil increases when subjected to shear stress. The curve mark as test 1 in Figure 4 shows the stress-strain and volume behavior of unreinforced compacted fill material. In granular material, usually small contraction happens before volumetric strain reaches maximum compressive volumetric strain. Then, particles roll past other particles and cause dilatation, which increases volume of soil sample. Figure 5 illustrate the dilatative behavior of dense granular soil.

The presence of reinforcement can restrict dilatation of soil. Strains in the soil mass, through soil-reinforcement interface friction, generate tensile strains in the reinforcements and stretch them. Stretched geosynthetics form enclosed boundaries which tend to suppress dilatation of the soil. Wu et al. used the angle of dilatation as a quantitative measure of the degree of reinforcing effect of a GRS mass [50]. A study by Wu et al shows that soil particle sizes, reinforcement spacing, and reinforcement stiffness have significant effect on the behavior of GRS mas in terms of dilatation [47].

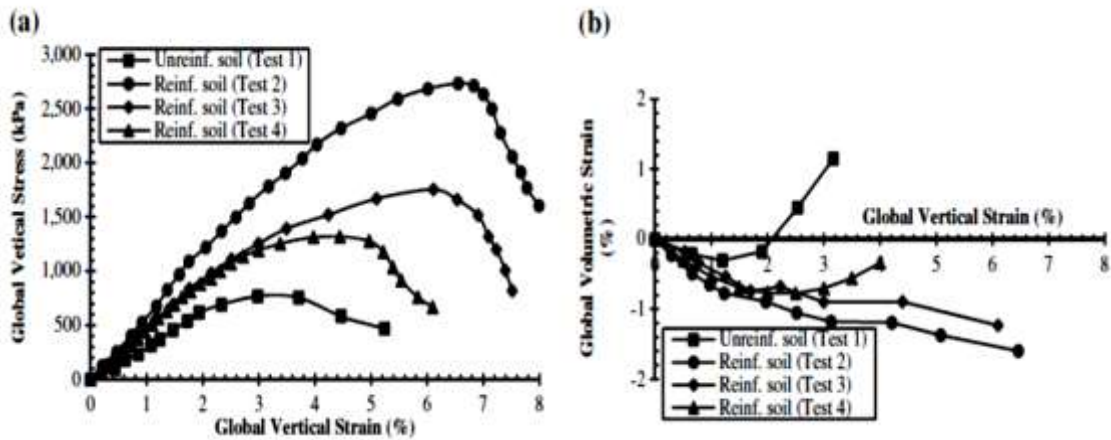


Figure 4
Behavior of unreinforced and reinforced soil masses: (a) stress-strain and (b) volume change [47]

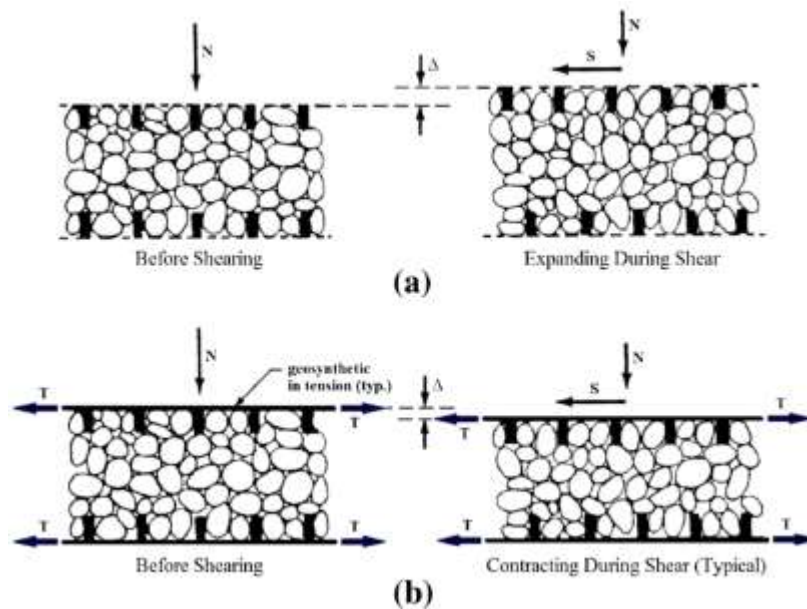


Figure 5
Schematic diagrams of volume change behavior of compacted granular soil: (a) unreinforced soil and (b) reinforced soil [47]

Difference between GRS and MSE Structures. For many years, the geosynthetic-reinforced structures were considered a simple subset of mechanically stabilized earth (MSE) structures. However, there are many fundamental engineering differences between MSE and GRS [51].

A primary difference is that the reinforcement layers are spaced differently. Vertical space between reinforcement layers in GRS is less than MSE. Layers of reinforcement are typically spaced 6-10 in. in GRS structures while MSE layers are usually spaced 24 in. The reinforcement material is also different. GRS reinforcement can be built by any geosynthetic and most commonly with a geotextile or geogrid fabric while MSE reinforcement can be any types of reinforcement like steel or geosynthetic. The connection between the reinforcement and the facing on GRS structures is frictional. The facing blocks sit directly on the reinforcing geosynthetic and are held in place purely by the friction between the reinforcement and concrete block. By contrast, with MSE structures, the face is providing external support (confinement) to the soil and must be mechanically connected to the reinforcement through devices such as shear pins, lips, or keys (FHWA website). The difference in construction results in fundamental design and performance differences between these two technologies. These performance differences, as reported by VanBuskirk and Engineering, are summarized next [51].

Soil mass and reinforced layers in MSE structures are considered as one component and designed similar to tied-back wall systems. The stabilization is designed with a given strength and spacing to resist the theoretical loading which would have been imposed by the nonstabilized soil. While GRS treats the soil and the reinforcement in a composite manner. The tightly spaced reinforcements in GRS structures imparts an elevated confining stress on soil and influence the fundamental particle-to-particle interaction of the soil.

Another fundamental difference of GRS and MSE is function of facing wall. A facing unit in MSE is provided to resist the loading imposed by the soil between the embedded tensile elements. The reinforcement is secured to the facing units to hold the facing in place. The facing units within the GRS are purely a construction aid and a façade for the wall face. As the facing only needs to resist construction-induced compaction loads. Figure 6 illustrates this fundamental difference between these two technologies. Reinforce layer in MSE is attached to two masses which have a tendency to move apart. The main function of reinforcement layer in this case is to keep them together. On the other hand, the main function of geosynthetic in GRS is to carry tensile loads.

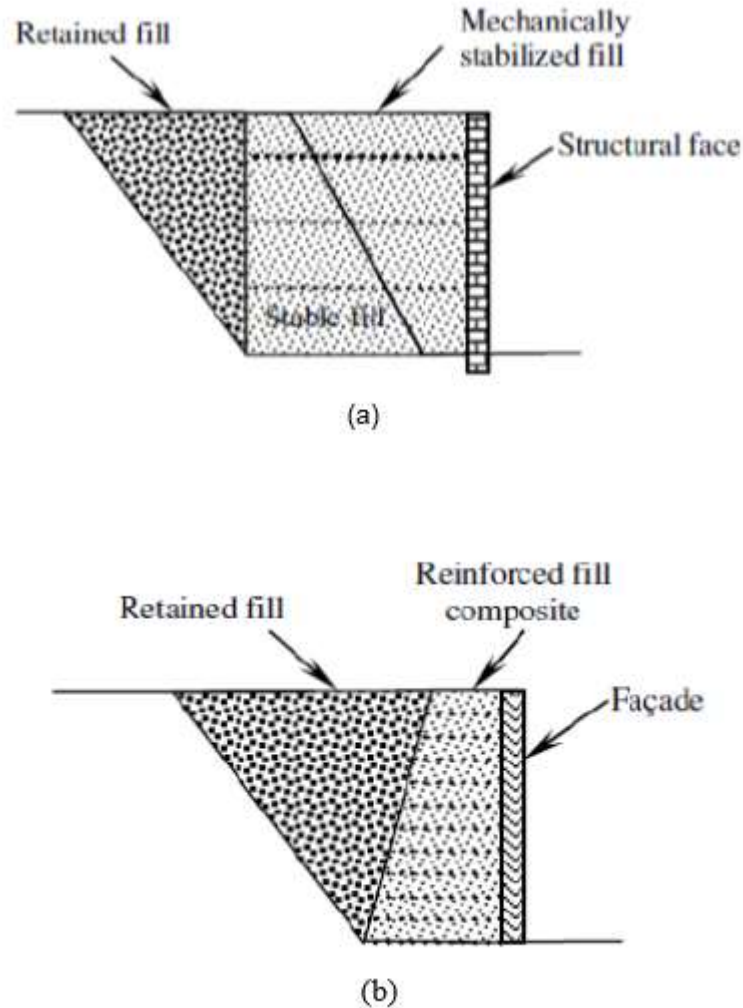


Figure 6
Difference between MSE and GRS technology: (a) MSE technology and (b) GRS technology [51]

The GRS mass usually shows higher strength due to suppression of dilation. In order to develop a shear plane in a compact or dense granular soil, the soil particles need to dilate so they can move past adjacent particles. If this does not happen, the strength of the soil mass approaches that of the aggregate. Reinforcement layer in soil mass restricts soil dilation within the surrounding soil. By decreasing the reinforcement spacing to a set distance, the zones of influence of the reinforcement on the soil mass can begin to overlap and become stiffer and stronger. Within a properly designed and constructed GRS, the fabric spacing would be sufficiently close such that the fabric resists dilation of the soil particles.

The existence of reinforcing layer increases the lateral resistance of soil mass due to compaction. By compaction, lateral stresses developed within the soil. After removal of compactor, the vertical

stress returns to normal. However, a portion of the elevated lateral stresses remains in reinforced mass as a result of reinforcement layer. These locked-in stresses increase the lateral resistance within the soil mass by providing an apparent increase in confining pressure. The level of lock-in stresses would be increased by reducing the reinforcement spacing. Therefore, this phenomenon is more significant in GRS masses with tightly spaced reinforcement than MSE walls.

GRS Laboratory Testing. This section contains a variety of laboratory test setups on GRS structures. Some are small-scale experiments, and others are large-scale lab tests on GRS samples. The focus of this section is on GRS and GRS-IBS structures.

Borns conducted a series of triaxial tests on reinforced soil specimens to compare their performance with unreinforced samples [52]. As shown in Figure 7, the sample with reinforcement at the top and bottom (number 2 in Figure 7) performed similar to unreinforced sample (number 1 in Figure 7). Reinforcement layers in specimen number 3 and 4 effectively restrained lateral deformation of soil. Borns suggested that reinforcement should be placed at the location where lateral deformation occurs to increase stiffness and strength of reinforced soil [52].

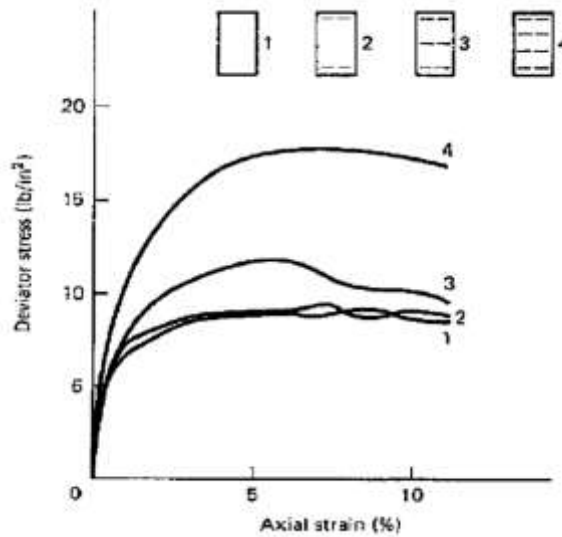


Figure 7
Triaxial Compression Tests [52]

Wu and Helwany developed a long-term soil-geosynthetic performance testing apparatus (Figure 8) [53]. In this test, the deformation of soil-geosynthetic composite is measured by applying sustained surcharge. The stress induced in the soil transfers to reinforcement and deformation of the GRS mass occurred as a result of soil-geosynthetic interaction. Ketchart and Wu used soil-geosynthetic performance testing apparatus to study the creep behavior of GRS mass. The granular and cohesive reinforced and unreinforced soil samples were loaded for a long period [54]. Results

of this study showed that reinforced granular soils did not experience creep. However, in GRS mass with granular material, load in geosynthetic decrease with time.

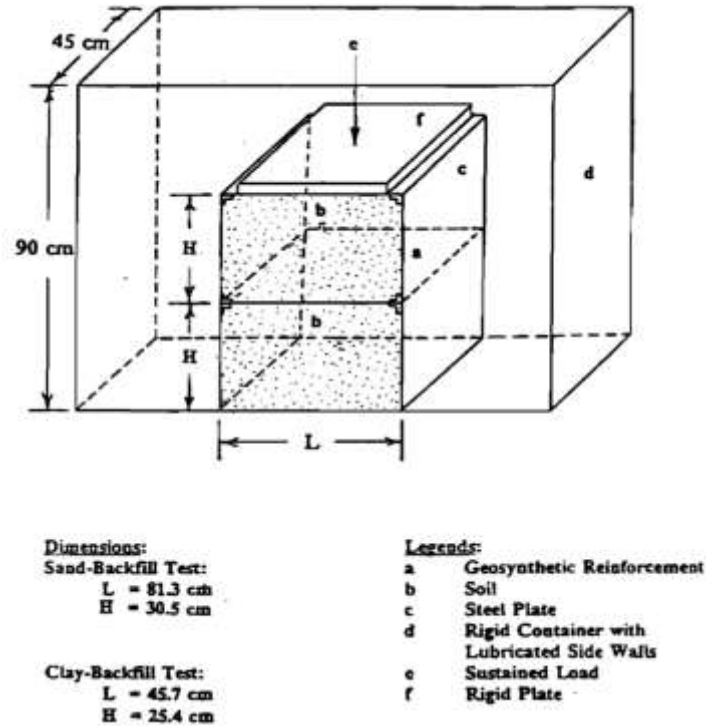


Figure 8

Schematic diagram of the long-term soil-geosynthetic performance testing apparatus [53]

A study was conducted by Ketchart and Wu to investigate on effects of various loading conditions especially preloading on the behavior of GRS masses [55]. Conventional laboratory tests such as triaxial, in-isolation load-extension, and direct shear tests performed on reinforced and unreinforced soil samples. This study shows that the reloading stiffness is depend on the confining pressure and the unloading load level and reduced with increasing preloading load level. The preloading did not affect the shear strength of the soils or the interfaces. The tensile strength of the preloaded geosynthetic specimen was only about 5% lower than that of the corresponding virgin specimen.

The Soil-Geosynthetic Performance (SGP) test was revised and used to investigate the performance of GRS masses subject to monotonic loading and unloading-reloading [55]. Vertical and horizontal deformation of test specimen as well as strain in reinforcement were measured. Two types of failure modes were observed under the monotonic loading, a diagonal shear failure and a wedge-type shear failure (Figure 9). Figure 10 shows samples failed under the diagonal shear failure and wedge type shear failure modes, respectively. The failure mode occurred in samples

with weak reinforcement and involved a single shear plane across a diagonal direction of specimen. The reinforcement rupture observed at intersection of shear plane and the middle reinforcement layer. The authors claimed that presence of reinforcement delayed a full development of diagonal shear plane, therefore increase the strength of GRS mass. The shear failure in samples with strong reinforcement was occurred in the lower part of specimen without reinforcement rupture. Strong reinforcement changes the failure mode from diagonal shear failure mode to the wedge-type shear failure mode. In initial stage of unloading-reloading test, when the deformation is small, the soil mass with and without reinforcement showed comparable performance. After mobilization of reinforcement layers, stiffness of the soil mass with reinforcement was about 30% higher than without reinforcement. Vertical and lateral deformations GRS samples reduced by 2 to 7 factor. The authors claimed that the required vertical and horizontal displacements for GRS masses to fully mobilize the reinforcing effect are 0.08 and 0.2 in., respectively.


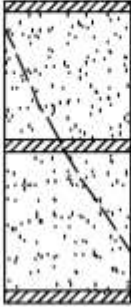
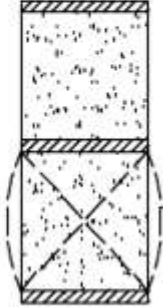
Diagonal shear failure		Wedge-type shear failure
Soil mass	GRS mass with weak reinforcement layers (e.g., Typar 3301)	GRS mass with strong reinforcement layers (e.g., Amoco 2044)
		

Figure 9
Failure modes in SGP tests [55]

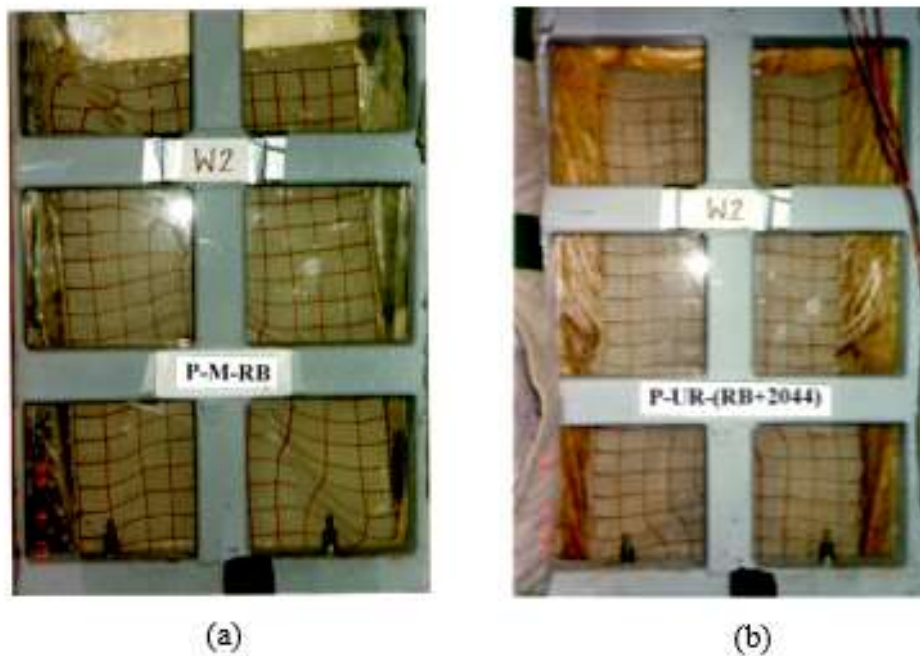


Figure 10

Samples failed under the (a) diagonal shear failure mode and (b) wedge type shear failure mode [55]

There are concerns about results of small-scale tests due to small size of samples, some factors such as gravity, soil arching, and compaction-induced stresses are not simulated properly. For this reason, a number of larger-size tests were conducted [46, 50, 56-60].

A series of large size triaxial tests were performed on large unconfined cylindrical reinforced soil samples to assess the behavior of reinforced soil and to estimate the tensile force in that reinforcement [58]. Samples were 2.5 ft. in diameter and 5 ft. in height. The backfilled soil was poorly graded sand. The soil was compacted to 95% of the modified proctor density in 6 in. lifts. Six different nonwoven polypropylene geotextiles were used in this research to find a correlation between the types of reinforcement and load carrying capacity of GRS mass. The reinforcements were placed at different spacing (6 and 12 in.). A hydraulic ram with a load cell was used to apply load. Four linear potentiometers were attached to the specimens to measure lateral displacement. Figure 11 shows test setup before and during testing. Figure 12 shows the stress-strain curves of the specimens reinforced by TG500 at spacing of 12 in. and 6 in. It can be seen that the strength of the soil-geosynthetic composite was much higher at 6 in. spacing than at 12 in. This study shows that there is meaningful correlation between the strength of reinforcement layer and performance GRS mass. Deformation of specimens decreased by using stronger reinforcement. Reinforced soil

peak strengths were observed to be between 4.8 kips/ft² and 9.64 kips/ft² at 3% to 8.5% vertical strain. Based on the location of tears in the reinforcement, it was observed that middle layers were mobilize first. Based on results of the experiment, a model was developed to estimate maximum tensile stress in reinforcement. The proposed model requires much lower reinforcement strengths to produce a desired reinforced-soil strength in comparison to other common methods. The proposed tensile strength requirement based on developed model is approximately half of that calculated using the NCMA and Demo 82 methods.



Figure 11
Cylindrical GRS setup before and during testing [57]

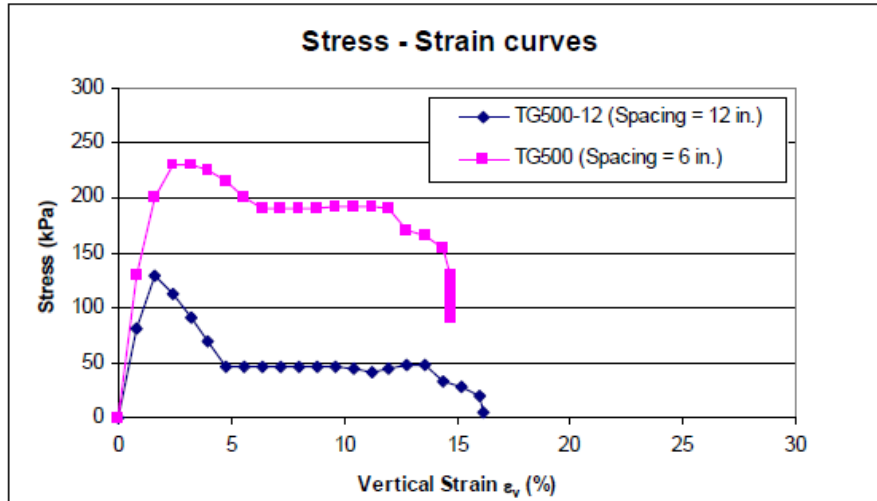


Figure 12

Stress- strain curves of specimens reinforced at spacing of 12 in. and 6 in. [57]

Adams and his associates constructed small-scale pier to study the load carrying capacity of GRS mass [56, 60]. The dimension of mini piers was 6 ft. high, 3 ft. wide and 3 ft. deep (Figure 13). The material properties of tested mini piers are shown in Table 1. The results indicated that spacing of reinforcement has more significant effect on the load carrying capacity of mini piers than strength of reinforcement layers. Figure 14 shows the vertical stress versus strain curves for unreinforced and reinforced piers. From the figure, the effect of reinforcement spacing and reinforcement strength on the behavior of the mini piers can be seen by comparing the difference between curve B (at 0.4 m spacing) and curve D (at 0.2 m spacing) and the difference between curve C (reinforcement strength = 21 kN/m) and curve D (reinforcement strength = 70 kN/m). The effect of reinforcement spacing is much more pronounced than the effect of reinforcement strength.



Figure 13
Mini pier experiments [56]

Table 1
Properties of materials for the mini pier experiments [59]

Experiment	Fill Avg. Density (kN/m ³)	Geotextile Reinforcement Schedule		
		Polypropylene type	Strength (kN/m)	Spacing (m)
MP NR	22.4	none	none	none
MP A	23.0	A2044	70.0	0.4 - 0.6
MP B	22.7	A2044	70.0	0.4
MP C	(Not Available)	A2000	21.0	0.2
MP D	22.8	A2044	70.0	0.2

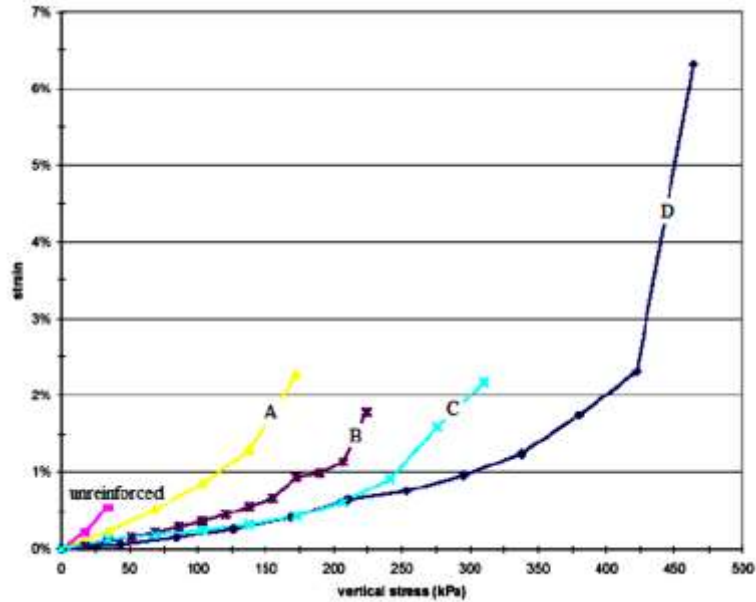
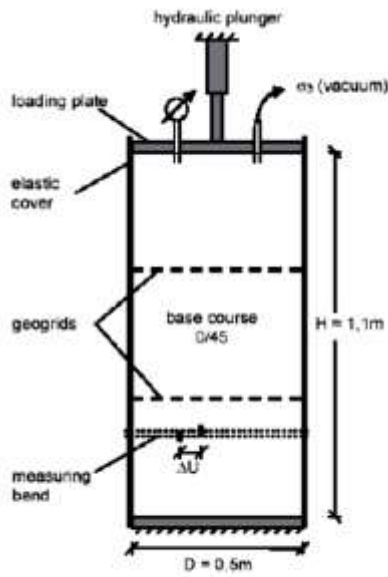


Figure 14
Stress-strain curves of mini-pier experiments [59]

Ziegler conducted a set of large-scale triaxial test on reinforced soils; see Figure 15 [60]. The dimension of mini piers was 1.1 m high and 0.5 m diameter. The stress-strain curves from this experience are illustrated in Figure 16. From this figure, the effect of number of reinforcement on strength of the specimen can be seen. The strength of the specimen increases with increasing number of reinforcement layers for strains more than about 1%. For small strain, number of reinforcement layer did not effect on strength of specimen.



(a) Schematic Diagram

(b) Large-Size Triaxial Load Cell

Figure 15
Test setup of large –size triaxial test [60]

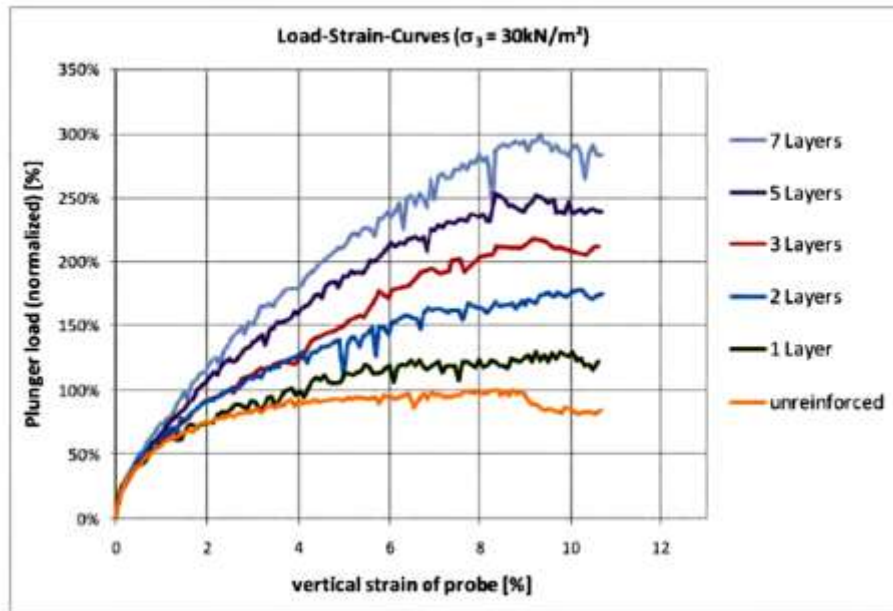


Figure 16
Large-size triaxial test results [60]

A series of Generic Soil-Geosynthetic Composite (GSGC) tests were conducted by Pham [46]. Each test specimen was 6.5 ft. tall, and 4.6 ft. depth. Hollow concrete blocks were used for facing. The vertical loads were applied on test specimens by hydraulic jack. Backfill material was well graded gravel (GW-GM according to ASTM D2487). A woven polypropylene geotextile was used for reinforcement. Vertical loads were applied until a failure was occurred in an equal increment. Table 2 shows the properties of test sections. The stress-strain curves of unreinforced and reinforced specimens are shown in Figure 17. With the presence of the reinforcement (Test 2, 3, and 4), the reinforced soil was much stronger than the unreinforced soil (Test 1). The reinforced soil masses were much more ductile than the unreinforced soil mass. Comparing the stress-strain curves of Tests 2, 3, and 4 indicated that the spacing of reinforcements has a larger impact on GRS mass performance. The strength of specimen in Test 2, with reinforcement spacing of 0.2 m, was about twice as high as the specimen in Test 4 with 0.4 m spacing. With the same reinforcement strength/spacing ratio in Tests 2 and 3, the strength of the specimen with higher reinforcement strength and spacing (Test 3) was much lower than that of the Test 2. The author claimed that reinforcement spacing plays more significant role than strength of reinforcement in a reinforced soil mass [46].

Table 2
Test program for the GSGC tests [46]

Test Designation	Geosynthetic Reinforcement	Confining Pressure	Wide-Width Strength of Reinforcement	Reinforcement Spacing, S_v
Test 1	None	34 kPa	None	No reinforcement
Test 2	Geotex 4x4	34 kPa	T = 70 kN/m	$S_v = 0.2$ m
Test 3	Double-Sheet Geotex 4x4	34 kPa	T = 140 kN/m	$S_v = 0.4$ m
Test 4	Geotex 4x4	34 kPa	T = 70 kN/m	$S_v = 0.4$ m

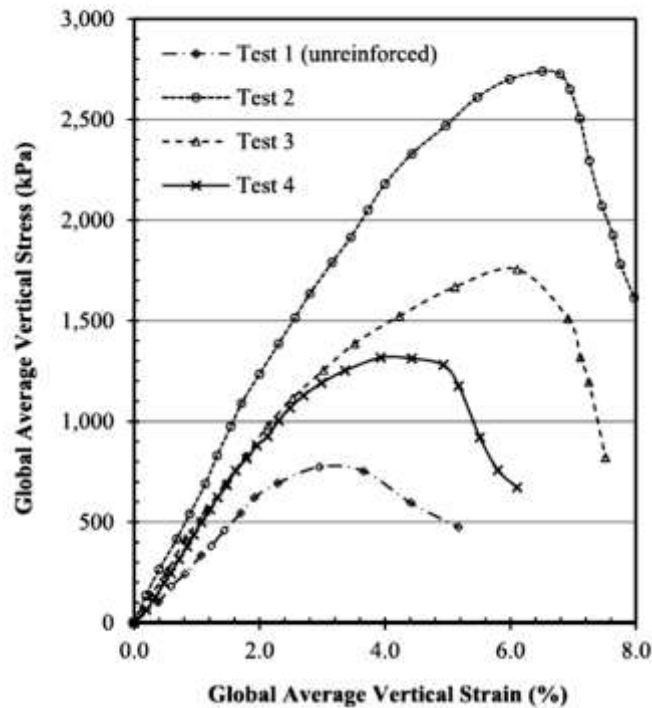


Figure 17
GSGC test results [46]

Nicks et al. conducted a series of mini-pier experiments to study the load-deformation relationship of GRS mass. In addition, this research aimed at establishing a database of GRS material properties for the purposes of design and construction of GRS-IBS bridges [44]. Mini-pier specimens were constructed from alternating layers of compacted granular fill and geosynthetic reinforcement layers connected frictionally to facing elements. The effects of several parameters including preloading, aggregate angularity, compaction level, presence of bearing bed reinforcement, and facing confinement on performance GRS composite was studied. The friction angle of backfill material impacts the ultimate strength and service limit capacity of GRS. The specimen with angular aggregate had more strength than specimen with round aggregate. Presence of bearing bed provides some additional vertical capacity at high strain level. The frictionally connected CMU facing has an impact on the performance of GRS; it provides confinement, leading to a stiffer response and an increased capacity compared to a GRS composite with no facing element. From Table 3, the facing more than doubles strength as compared to the specimen without any facing. The impact of presence of facing element is more significant for specimen with higher reinforcement spacing.

Table 3
Effects of CMU facing on stiffness and capacity [44]

Test	Facing	S_v (inch)	T_f/S_v (psf)	E_o (ksf)	$\frac{E_{o,CMU}}{E_{o,no\ CMU}}$	$q_{ult,emp}$ (psf)	$\frac{q_{ult,emp\ CMU}}{q_{ult,emp\ no\ CMU}}$
TF-2	CMU	7½	3,800	710	2.15	25,260	1.44
TF-3	None			330		17,491	
TF-6	CMU	7½	7,600	750	2.34	43,763	1.65
TF-7	None			320		26,546	
TF-9	CMU	15¼	3,800	550	2.12	22,310	2.16
TF-10	None			260		10,330	
TF-12	CMU	3-13/16	4,400	810	2.08	29,030	1.25
TF-11	None			390		23,249	
TF-14	CMU	11¼	3,800	460	2.09	23,562	1.82
TF-13	None			220		12,960	

S_v = the reinforcement spacing, T_f = the MARV value of the wide width tensile strength,
 E_o = the initial stress-strain ratio, $E_{o,CMU}$ = the initial stress-strain ratio for tests with CMU facing,
 $E_{o, no\ CMU}$ = the initial stress-strain ratio for tests without any facing, $q_{ult,emp}$ = the measured
vertical capacity, $q_{ult,emp\ CMU}$ = the measured failure pressure for tests with CMU facing, and
 $q_{ult,emp\ no\ CMU}$ = the measured failure pressure for tests without any facing.

Wu et al. conducted five large-scale generic soil geosynthetic composite (GSGC) tests to study behavior of GRS mass under well controlled conditions [50]. Extensive instrumentation was used to monitor performance of GRS samples under different reinforcement spacing, reinforcement strength and confining pressure. The results confirmed that effect of reinforcement spacing influences the GRS behavior more significantly than reinforcement strength. The experimental Results was used to develop analytical models to calculate the apparent cohesion of a GRS composite, the ultimate load-carrying capacity of a GRS mass, and the required tensile strength of reinforcement for a given reinforcement spacing. The developed equations were compared against the results of GSGC tests, large-size experiments, and finite element simulations.

GRS-IBS Full-scale Testing. This section contains a variety of GRS-IBS full-scale test setups. All test setups in this section are roughly equal to or larger than half-scale.

Commerce City Wall. In 1992, a reinforced soil retaining wall was constructed by the Colorado Department of Transportation to understand the behavior of geosynthetic reinforced soil (Figure 18). The dimension of wall was 9.5 ft. tall and 4 ft. wide [4]. The road base material was used as backfill and a uniaxial geogrid layer was used as a reinforcement. The vertical spacing between geogrids was 12 in. A weaker reinforcement instead of main reinforcement was used at

the connection between soil and facing along reinforcement layers. These reinforcements were extended 2.95 ft. into the GRS mass. The design of the anchors and connections aimed to allow lateral movement and to slide with the fill [4].

A surcharge load of 40 kips was applied to test the wall and remain for 4 months. Through linear potentiometers and measurement hook points, lateral thrust against the wall panels was monitored. Lateral deformations were extrapolated over a 100-year period. The test indicated that reinforced soil mass was stable by itself without support from the wall facing. Authors believed that Lateral deformations would not be more than 1.6 in. after 100 years [3, 4].



Figure 18
Loading test of the commerce city GRS wall [4]

Havana Yard Piers. A full-scale long-term load testing of GRS bridge abutment and pier was conducted in 1996-1997. This bridge abutment and piers conducted by the Colorado Department of Transportation and the University of Colorado at Denver. The Havana Yard project has two piers and one abutment. The test setup was constructed on RSF (Figure 19). Then a 6 in. thick concrete pad was used to support piers and abutment. The piers had 24 and 25 ft. tall. GRS mass was built from coarse grained fill material (GW-GM following ASTM D2487) and geotextile layers.

One of the piers and the abutment were loaded with concrete barriers stacked in seven layers. The dead load was applied on one of the piers for one year. The settlement of loaded pier and abutment was 1.44 and 1.07 in., respectively. The maximum lateral displacement was 0.5 in. for loaded pier and 0.17 for the abutment. Monitoring the deformation proved that creep deformation increased with time however, a significant portion of the maximum creep deformation occurred in the first two weeks of loading. About 70% to 75% of creep deformation at 70 days occurred in first 15 days. Reinforcement strains were less than 1.0% [54].

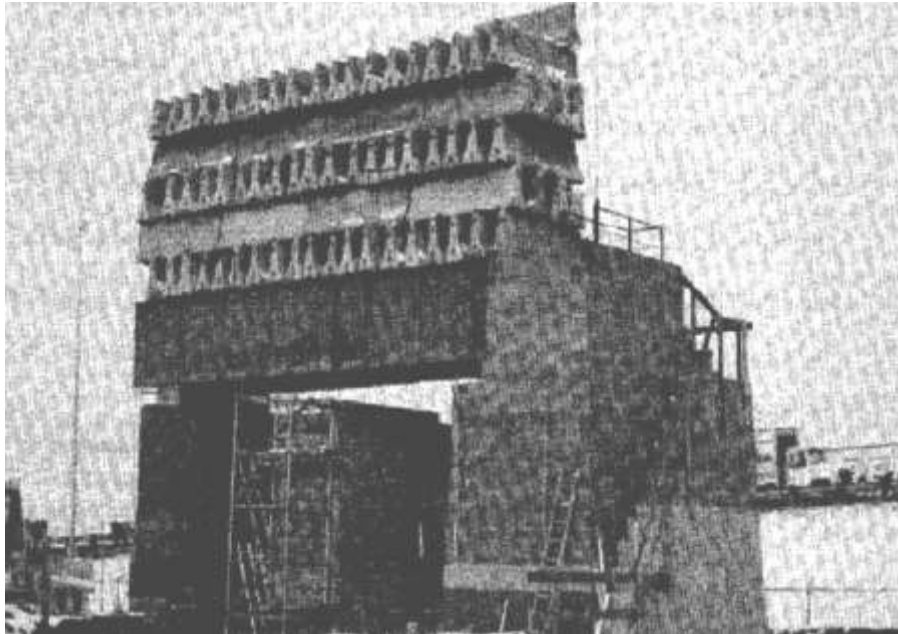


Figure 19
Havana yard pier test setup [54]

NCHRP Full-Scale Test. In 2003, two GRS bridge abutments were constructed and tested in Turner-Fairbank Highway Research Center in McLean, Virginia [15]. The abutment height was 15.25 ft. tall. The abutments were constructed on a 30 ft. long by 24 ft. wide by 3 ft. thick rigid floor. Backfill material was nonplastic silty sand (SP-SM according to Unified Soil Classification). A woven geotextile was used as reinforcement. One abutment used reinforcement with tensile strength of 4,800 lb/ft and the other with tensile strength of 1,440 lb/ft. The vertical spacing of geosynthetic reinforcement for both sections was 8 in. Concrete blocks with split-face was used as facing element [15]. A loading assembly was installed to comprise a rigid floor and apply vertical load. Loading was conducted in 1.0 ksf intervals. Each load increment was maintained for 30 minutes. In a section with stronger geotextile (Amaco test section), loading was terminated at vertical load of 17 ksf without failure. The second section (Mirafi test section) with reinforcement strength of 1,440 lb/ft experienced an excessive deformation after 8.64 ksf. Reinforcement strain,

vertical and lateral movements, and contact pressure between abutment and rigid foundation were monitored throughout testing. A summary of the abutment performance is shown in Table 4. The results show that deformations are tolerable at working loads of about 4,000 psf. The maximum movement of abutment occurred near the top of the wall.

Virginia Tech. Research was done at Virginia Tech to investigate the performance GRS abutments [61]. The main focus of this study was on effects of differential foundation settlement on GRS abutments. A 10 ft. tall and 24.5 ft. long abutment was constructed on a RSF. The backfill material was an open-graded crushed rock with a maximum particle size of 0.5 in. The chosen primary for the abutment and the RSF was a biaxial, woven polypropylene geotextile with an ultimate tensile strength of 4800 lb/ft in both directions. Facing elements were frictionally connected concrete masonry units (CMUs) with a compressive strength of 4000 psi. Concrete blocks were used to apply surcharge load. Geofam inclusions were placed underneath the left and right corner of abutment and RSF.

Table 4
NCHRP full-scale test results [15]

	Amoco Test Section	Mirafi Test Section
Reinforcement	Amoco 2044, $T_{ult} = 70$ kN/m	Mirafi 500x, $T_{ult} = 21$ kN/m
<i>Upon termination of loading:</i>		
Average Applied Pressure	814 kPa	414 kPa
Sill Settlement (front)	175 mm (6.9 in.)	189 mm (7.4 in.)
Sill Settlement (back)	152 mm (6.0 in.)	160 mm (6.3 in.)
Max. lateral movement in abutment wall	82 mm @ 4.5 m from base	115 mm @ 4.5 m from base
Max. lateral movement in wing wall	33 mm @ 3.8 m from base	86 mm @ 3.8 m from base
<i>At 200 kPa (limiting bearing capacity, per NHI manual)</i>		
Applied Pressure (average)	207 kPa	214 kPa
Sill Settlement (front)	45 mm (1.8 in.)	81 mm (3.2 in.)
Sill Settlement (back)	35 mm (1.4 in.)	64 mm (2.5 in.)
Max. lateral movement in abutment wall	24 mm @ 4.5 m from base	36 mm @ 4.5 m from base
Max. lateral movement in wing wall	18 mm @ 3.8 m from base	30 mm @ 3.8 m from base
<i>Observed Behavior:</i>		
<ul style="list-style-type: none"> • The sills in both tests tilted toward the abutment wall face (i.e. the front of the sill settled more than the back; Left and right sides of the sill settled evenly). • The abutment wall leaned forward with the maximum movement occurring near the top of the wall. The top three courses of facing blocks were pushed outward at higher loads. • The wing wall also leaned forward with the maximum movement occurring at approximately 1/6H from the top of the wall. • In both tests, tension cracks occurred parallel to the wall face and were located at end of the reinforcement. Tension cracks initiated around 150–200 kPa average applied pressure. • Most strain gauges were damaged by moisture due to the long delay of actual loading experiments; maximum strain at 200 kPa was about 2.0% • The measured contact pressure on the rigid foundation was larger in front and decreased linearly toward the back. The computation procedure in the NHI Manual yielded about the average value of the contact pressures at a given applied load. 		

To create a differential foundation settlement condition, Geofoam inclusions were exposed to solvent. Solvent dissolved the Geofoam and created a differential settlement. The results of the experiment were that a GRS abutment could be constructed rapidly and handle the effects of extreme differential foundation settlement in a robust manner. A GRS abutment subject to normal levels of field differential settlement is anticipated to perform very well. However, it is recommended that fill protection from scour conditions be employed due to the fact that after even small amounts of settlement the fill material will be subject to water action from gaps in the block facing [61].

In-Service GRS Abutments. There have been many different types of structures built using GRS technology over the last few decades; however, the primary focus of this section will be on GRS technology for the application of abutment walls. The case histories discussed in this section are for in-service loading conditions experiences.

Vienna Railroad Embankment. A GRS bridge was constructed in Vienna, Austria in 1996 to support a railroad track. A non-woven geotextile with tensile strength of 23 KN/m with elongation at break of 45% was used to reinforce backfill materials. The reinforcement spacing was 0.3 m. To achieve adequate friction between the adjacent geotextile layers, a thin layer of sandy gravel was placed on each lift prior to the installation of the next layer. As the structure had to fulfill only a temporary function, a wrapped-around wall face was used and the surface protection was omitted. The cross section of Vienna embankment is shown in Figure 20.

The settlement of bridge was measured every week at six points along the embankment. The results show that bridge performances well under the traffic load and deformation was negligible [7].

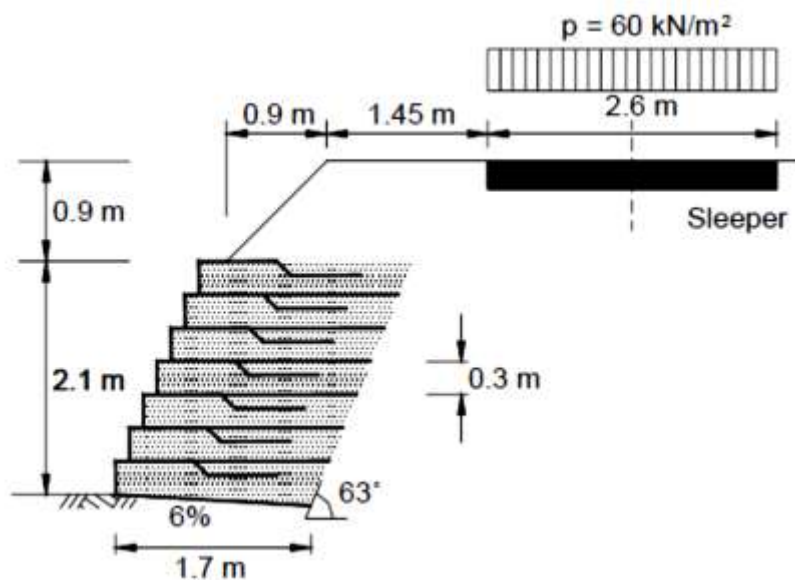


Figure 20
Cross-section of Vienna railroad embankment [7]

Black Hawk Bridge. In 1997, two rock-faced GRS were constructed in Black Hawk, Colorado, to support a 118 ft. span steel arched bridge. Each GRS abutment comprised a two-tier GRS mass with two square footings on the lower tier and a strip footing on the upper tier (Figure 21). Layers of woven geotextile at a vertical spacing of 12 in. was used to reinforce abutment soil. To reduce post-construction settlement, GRS abutments were preloaded up to 1.6 and 2 times of the design load for square footings and strip footing, respectively. Results showed that pre-loading was very effective to reduce vertical settlements. By pre-loading the footings, the vertical

settlements at the design load were reduced by a factor of 1.5 to 6.0. The lateral movement of the GRS abutments, and creep strains in the geotextile reinforcement were also reduced significantly due to the preloading. The maximum strain in the geotextiles was very low (less than 0.2%) [7].

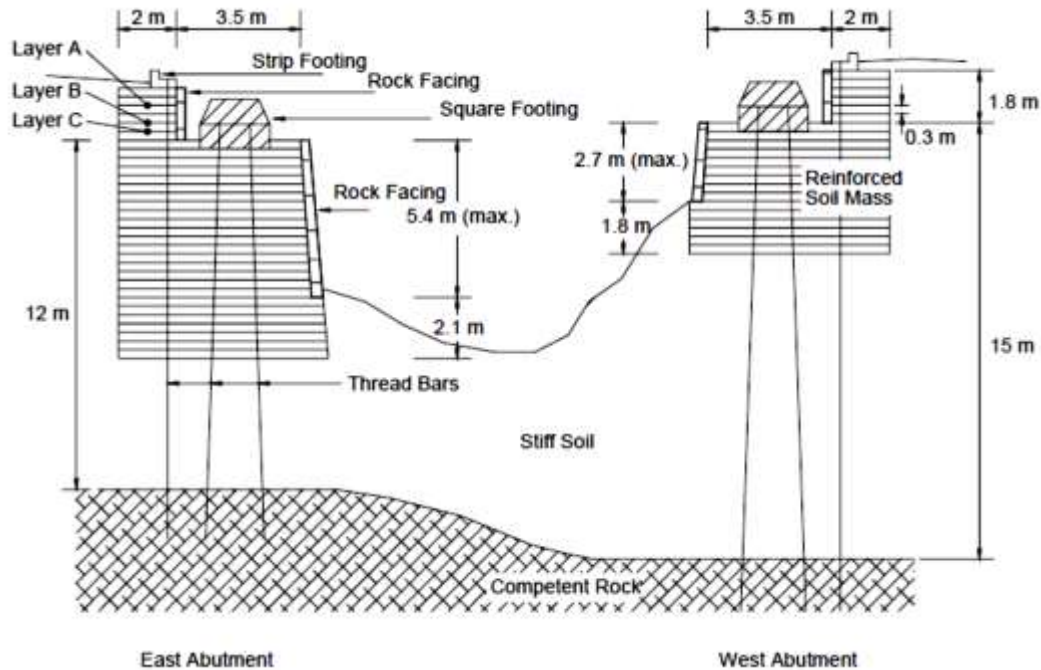


Figure 21
Cross-section of the Black Hawk Bridge abutments [7]

Feather Falls Trail Bridge. In 1999, Feather Falls Trail Bridge with a GRS abutment was constructed for a recreational hiking trail in Plumas National Forest, California (Figure 22). The bridge site was remote and there was no road access. Therefore, all equipment and materials was transported by helicopter. In this project, lightweight materials and easily construction methods were used. The abutment heights were 5 and 8 ft. high, using 6×6 in. treated timbers for facing material. Thus, the reinforcement geotextile was placed in 6 in. lifts, with an average length of 6.5 ft. Reinforcement spacing was approximately 6 in. The chosen reinforcement was a woven geotextile. Two reinforcement strengths were utilized: a 52 kN/m strength and a 70 kN/m strength. Top lifts wrapped the reinforcement over the timber face, lower lifts nailed reinforcement between timbers. The entire construction of the bridge was done by two crew in two weeks. Construction was straightforward and done through hand labor [2].

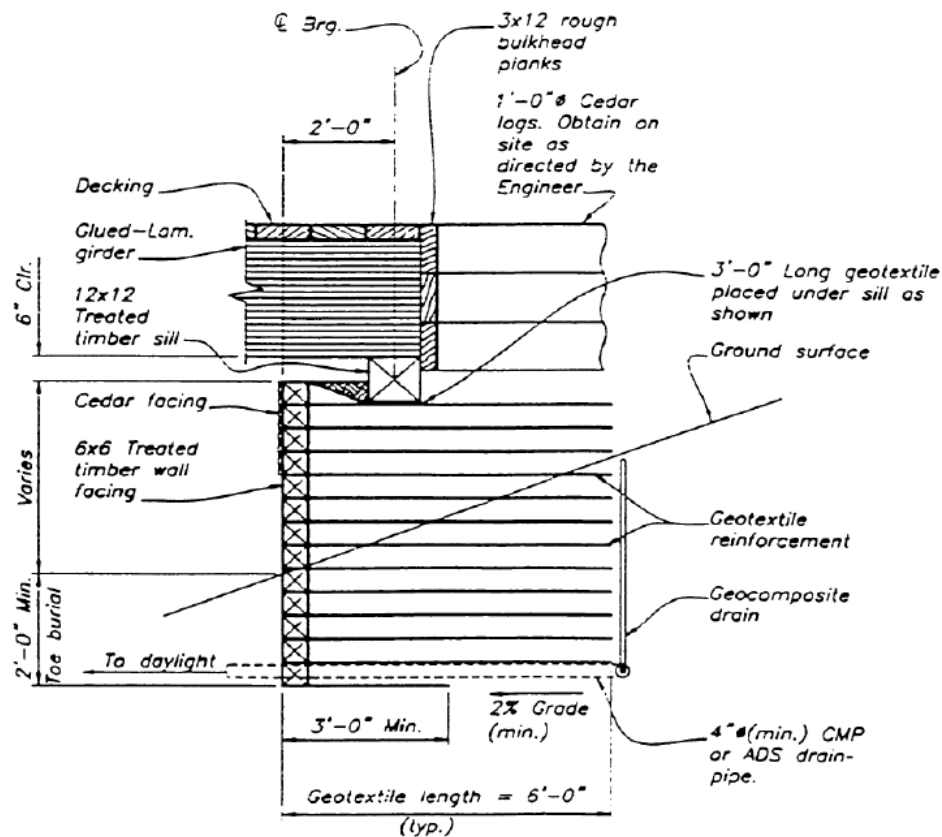


Figure 22
Feather Fall GRS abutment schematic [2]

Founder/Meadows Bridge. Founder/Meadows Bridge was constructed in 1999 near downtown Denver, Colorado as a part of Colorado State Highway 86. In this project, both the bridge and the approaching roadway structures are supported by a system of geosynthetic-reinforced segmental retaining walls. GRS structure was built based on Colorado Department of Transportation (CDOT) and American Association of State Highway and Transportation Officials (AASHTO) guideline. The main purpose of GRS abutment was to support the high concentrated loads from the bridge foundation structure and the comparatively smaller loads from the approaching highway structure without inducing significant differential settlements [62]. The bridge spans 113 ft. and is 113 ft. wide. The bridge is supported by a shallow strip footing placed on the GRS abutment with a height of 14.8 ft. the cross-section of Founder/Meadows Bridge is illustrated in Figure 23. The backfill soil used in this project classifies as SW-SM per ASTM D2487 with 35% gravel, 54.4% sand, and 10.6% fine-grained soil. Two types of geogrid were used: UX 6 below the foundation and UX 3 behind the abutment wall. The geogrid stiffness at 0

to 2% strain range measured from the wide width tensile tests results, were approximately 2000 kN/m for UX 6 and 1000 kN/m for UX 3.

Comprehensive material testing, instrumentation, and monitoring programs were incorporated into the construction operations. The front face of the GRS abutment and the abutment walls for three cross sections were monitored during construction and for 35 months while under in-service loads. The results from material testing indicates that assuming zero cohesion in the design procedure and removing the gravel portion from the test specimens lead to significant underestimation of the actual shear strength of the backfill. The observations from instrumentation indicates that the overall performance of this structure under service load before bridge opening to traffic has been satisfactory. Vertical stress in same elevation varies in different locations and it was not uniform as often assumed in design. Vertical stress is lowest value close to the facing wall, and the highest stress measured along the centerline of bridge abutment. No risk of overturning on GRS abutments was observed based on the vertical stress distribution [62].

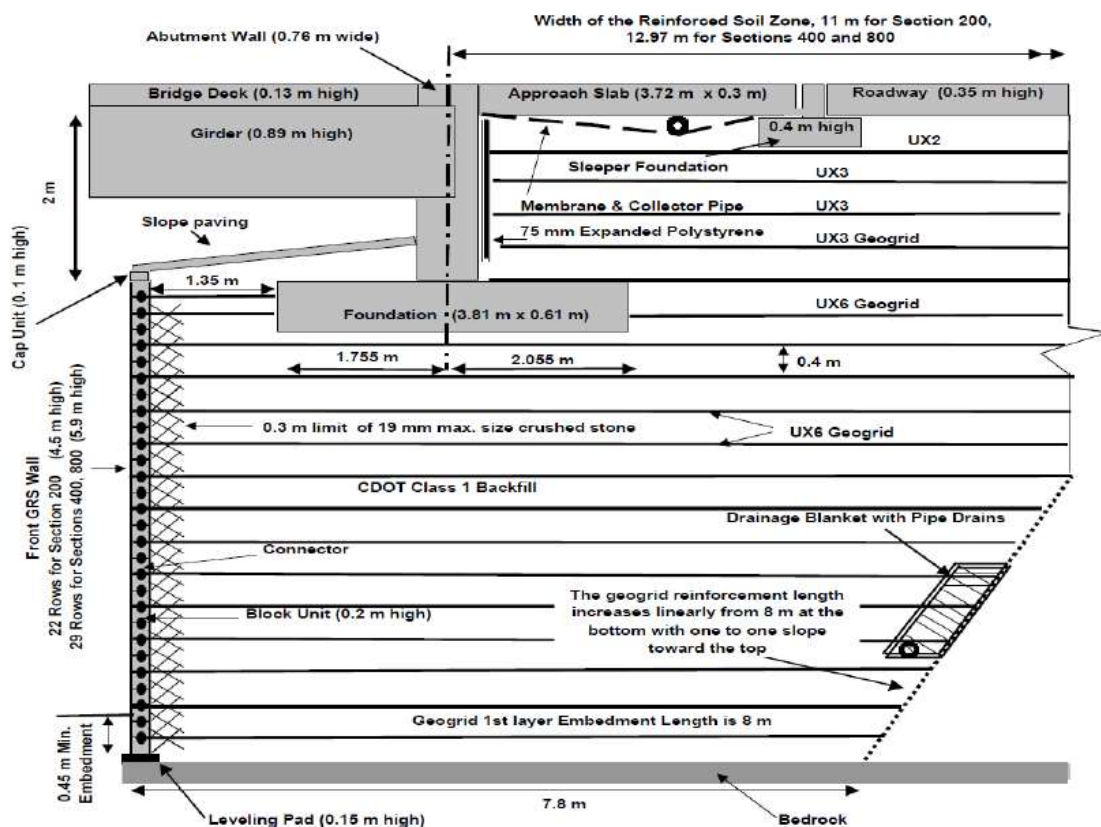


Figure 23
Cross-section of the Founder/Meadows Bridge [62]

Mammoth Lakes GRS Bridge Abutments. GRS abutment method was used to reconstruct two bridges near the mountain community of Mammoth Lakes, California, in the fall of 2000. In

this project, spread footing was built to support GRS abutments. Snow and seismic loads were main consideration to design both bridges. These bridges were designed followed by 1996 AASHTO Standard Specifications for Highway Bridges with annual revisions through 1999. A schematic of one of the west abutment is shown in Figure 24. Of the design snow load, 75% was used in computing design pseudostatic seismic forces for each bridge. GRS abutment was built by high quality, well-compacted fill materials, and closely spaced lifts. Polypropylene geotextile with tensile strength of 35 kN/m was used as reinforcement. The vertical space between geotextile layers was 6 in. [6].

These two bridges were constructed in two weeks with significantly lower cost compared to traditional methods. Survey was completed up to 6 days after bridge-deck placement. The maximum measured settlements of all abutments were 0.25 in. [6].

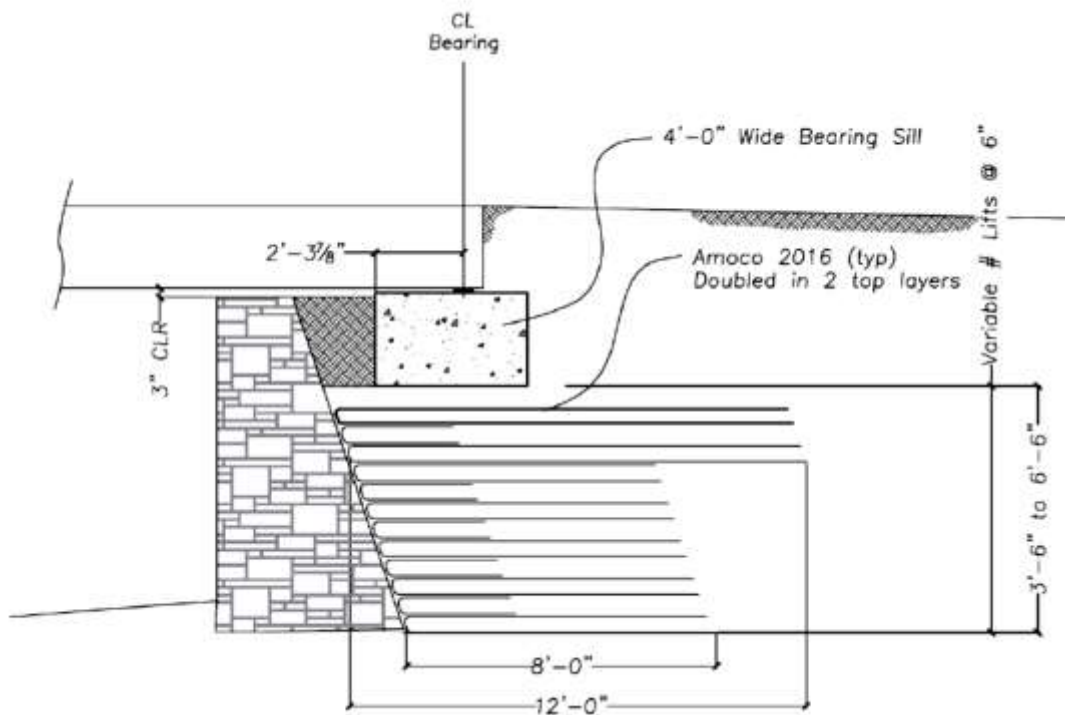


Figure 24
Mammoth Lakes West GRS abutment schematic [6]

Bowman Road Bridge. In fall of 2005, one of the first GRS bridges in the state of Ohio was built in Defiance County [59]. The project was part of the Federal Highway Administration’s (FHWA) “Bridge of the Future Program” to develop technologies to build more efficient, durable 70- to 90-ft. single-span bridges. Bowman road is an 82-ft. long bridge. GRS abutments supported the prestressed concrete box beams (Figure 25). In this project reinforced soil foundation (RSF)

was used instead of traditional concrete footings. The RSF was built by two layers of 1.5-ft. depth from well-graded compacted gravel. Entire RSF wrapped in a geotextile. GRS mass was built by 3/8 in. crushed limestone aggregate and two types of woven polypropylene geotextiles. Wide with test ultimate strengths of geotextiles were 480 lb/ft and 2100 lb/ft. The stronger geotextile was used as a primary reinforcement with spacing of 8 in. and secondary geotextiles were placed between primary reinforcement on top layers of GRS mass [59].

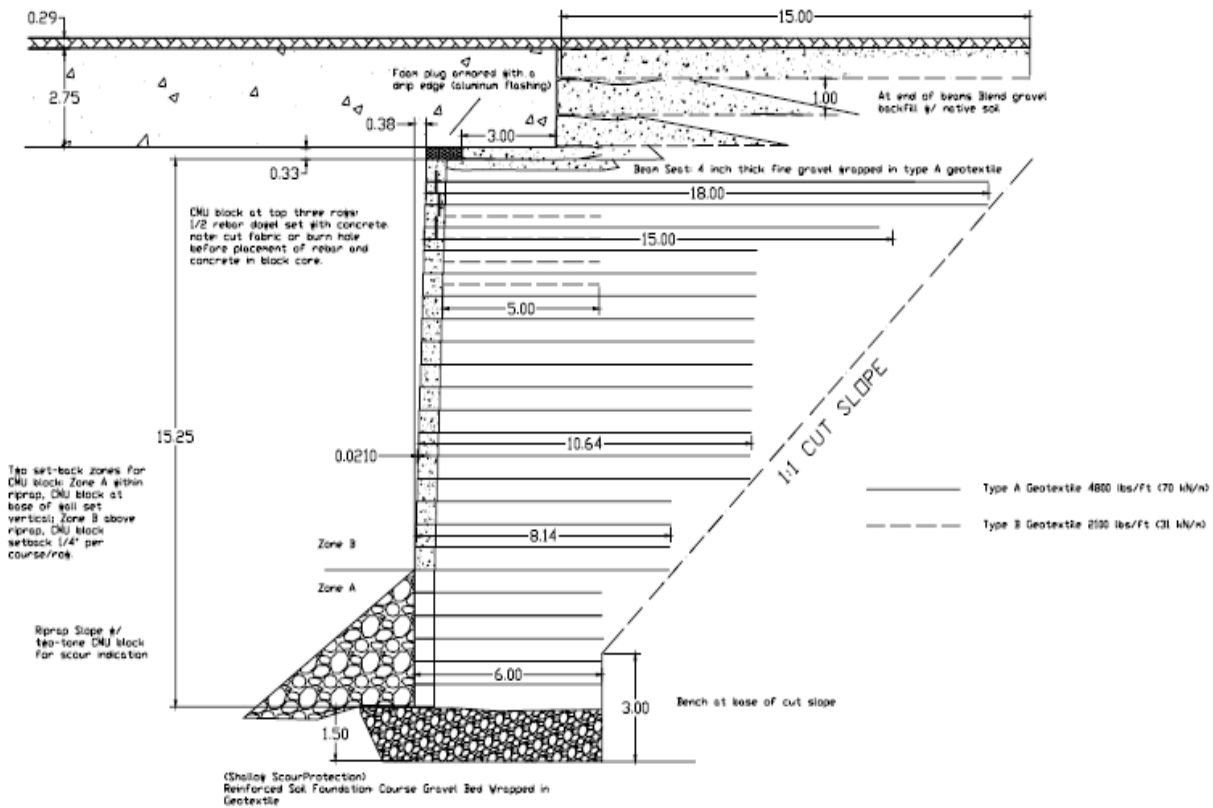


Figure 25
Cross- section of Bowman Road Bridge GRS abutment [59]

This bridge was instrumented by FHWA to monitor critical behavior over 2-3 years after construction. Several Pressure cells were installed to measure pressure below the beams and at the base of the GRS abutments. Strain gauges were installed in the beams, to correlate thermal expansion and contraction cycles to the pressure at the beam ends. Bridge settlement and movement of GRS abutments was monitored by survey. After the monitoring period, no pavement cracking has been observed. Using a GRS abutment resulted in time and cost savings. Therefore, in 2006, Defiance County, Ohio, planned to build seven more bridges supported on GRS abutments [59].

Steve Road Bridge over Tiffin River. In the fall 2009, Defiance County, Ohio, built a GRS-IBS structure to replace existing Steve Road Bridge. A 140-ft. steel girder was supported by GRS mass abutment. The abutment was constructed by AASHTO No. 89 crushed stone. A woven geotextile with a tensile strength of 4800 lb/ft with spacing of 8 in. was used as reinforcement layer [63]. The girder was heavily instrumented by strain gages and pressure cells. The abutment also instrumented with pressure cells. Survey method was used to measure movement of girder footing and abutment wall [64]. Construction time for this project was very fast. The abutments were constructed in 6 days using four to six crews.

Results from long term monitoring indicates that vertical deflections were in satisfactory range (0.4 to 1.8 in.) and there are no visible cracks at the bridge-approach interface [63]. Change in ambient temperature causes a temperature-induced load which effects on deformation of girders and abutment. Thermally induced load increased the lateral pressure behind the steel girders and vertical pressures in the abutment [64].

Mattamuskeet National Wildlife Refuge GRS Abutments. Two bridges were reconstructed in Mattamuskeet National wildlife refuge in North Carolina [65]. Severe erosion and rotting in the existing bridges was the main concern to replace them. The first existing bridge was a 23 ft. long single span bridge with aluminum deck over east Canal. The second bridge one was a two span bridge with a timber deck that spanned 28 ft. The foundation soil is soft, silty fat clay.

Two alternatives were considered for foundation of replacement bridges: concrete-pile-supported abutments and a GRS abutment system. Evaluation of the two alternatives based on their cost effectiveness and constructability showed that GRS abutment alternative is more advantageous. The GRS abutment alternative provided significant cost savings. In addition, it can reduce stress on subgrade soil and settlement by spreading the load over wider area [65].

In this project, a cellular confinement system (CCS) filled with gravel was used for the GRS abutment facing to retain the reinforced soil and to protect the abutment against erosion. Geogrid with tensile strength of 2,000 lb/ft with maximum reinforcement spacing of 16 in. was used for GRS abutment. To improve the soft clay subgrade, gravel- filled CCS was placed under the foundation. In addition, GRS system was preloaded to reduce long-term settlement. A temporary surcharge fill of compacted soil was used for 131 days preloading period. GRS abutment foundation details are shown in Figure 26.

Based on the analysis, 90% of calculated settlement after 100 days would occur during the preloading period. A monitoring program was put in place to evaluate the effects of preloading as well as long-term performance of GRS abutments. Survey measurements showed that maximum settlement during the preloading period was 2.5 in. and did not increased after 40 days [65].

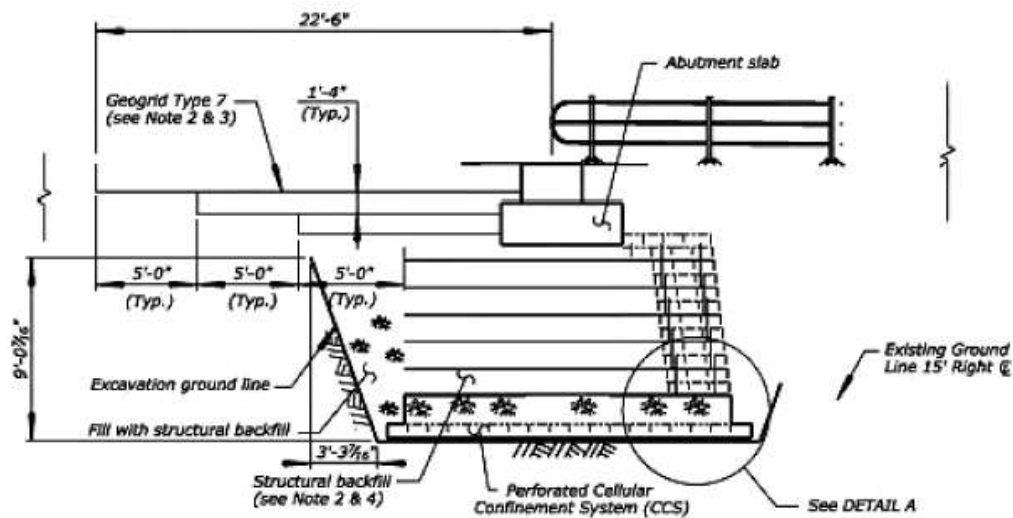


Figure 26
GRS foundation for Mattamuskeet Bridge [65]

GRS Numerical Modeling

The behavior of soil-geosynthetic composites have also been investigated through numerical analysis [26, 66 - 70]. Compared with laboratory experiments and field instrumentation, numerical methods have the following two major advantages: (1) obtaining more comprehensive results than laboratory and field tests; (2) investigating the effects of influence factors, which are difficult and/or costly to achieve in laboratory and field tests.

Chou and Wu used the FE program DACSAR to analyze the lateral pressure of a GRS wall [71]. They simulated lateral earth pressure of GRS wall along three planes: the wall face, the back of the reinforced-zone, and the plane along which the maximum tension load occurred in the reinforcement. Results of this study are shown in Figure 27. As seen in Figure 27, the load at the wall face was very low in comparison to the other planes and nearly constant with depth except near the base of the wall where the foundation partially restrains the facing movement [4]. The results of this study indicated that lateral earth pressure on the facing wall does not follow the Rankine or Coulomb earth pressure theories, which indicate an increase in lateral earth pressure with depth. Wu claimed that in well-designed GRS wall there is no need for structural wall [4].

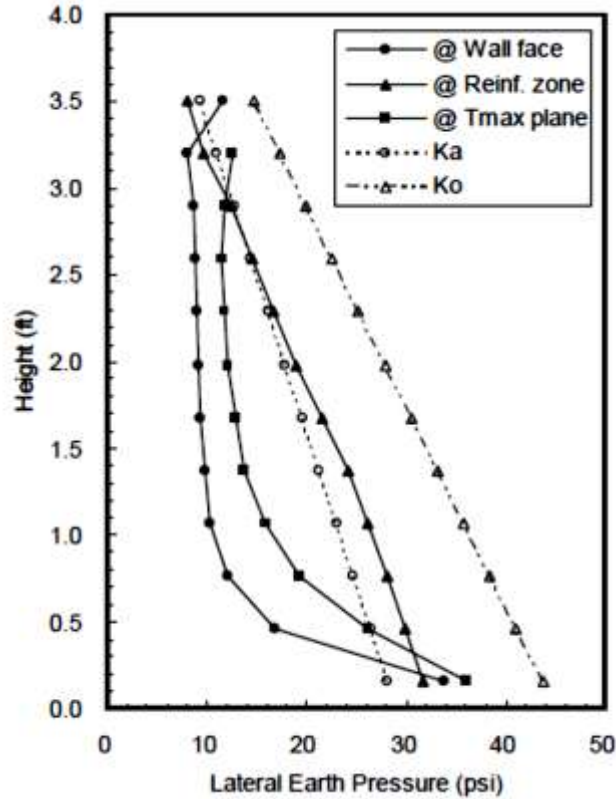


Figure 27
Lateral earth pressure of a GRS wall [71]

Ketchart and Wu developed an FE model using SSCOMPPC program to compare the stress distribution in soil mass with and without reinforcement [55]. The wide-width strength of reinforcement layer was 70 kN/m and the reinforcement spacing was 0.3 m. Figures 28, 29, and 30 present the vertical, horizontal, and shear stress distributions, respectively, at a vertical load of 6 kN. As seen in these figures, the vertical stress distribution for reinforced and unreinforced samples is almost same. However, horizontal and shear stress distribution of reinforced sample is different from unreinforced specimen. The horizontal stresses were almost uniform in unreinforced specimen. The largest horizontal stress occurred near the reinforcement and reduced with the increasing distance from the reinforcement. The shear stress in unreinforced specimen was negligible. In reinforced specimen, some shear stresses occurred near the reinforcement layer. Increase in the horizontal and shear stresses near the reinforcement result in an increase of minor principal stress. Stiffness and shear strength of the soil were subsequently increased by increasing minor principal stress. The largest increase of minor principal stress occurred near the reinforcement and reduced with the increasing distance from the reinforcement.

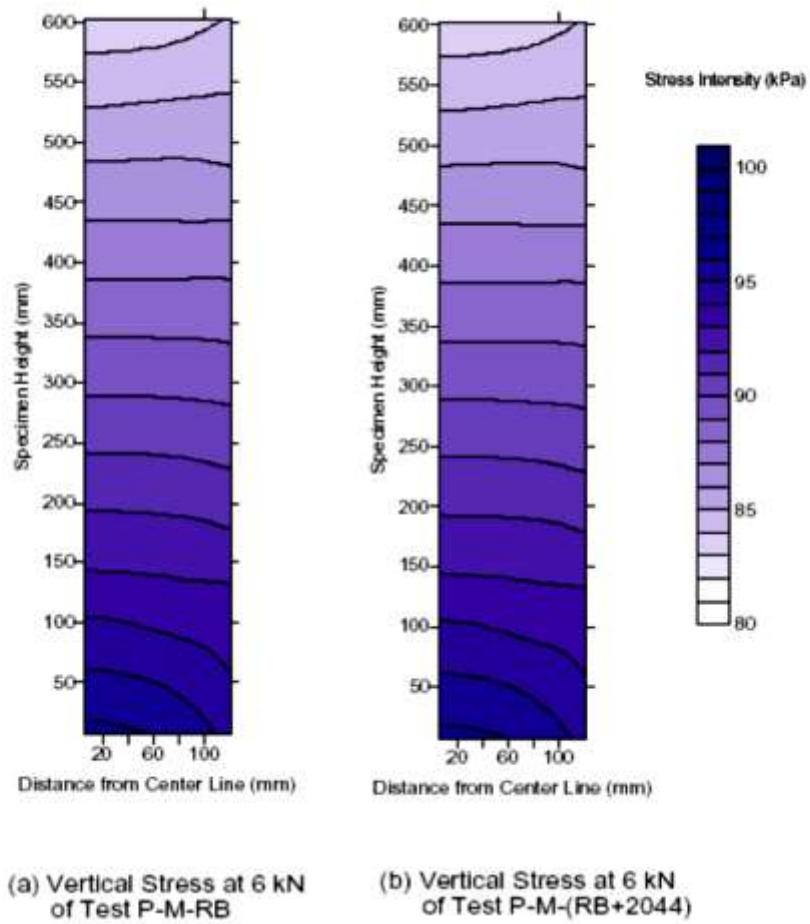
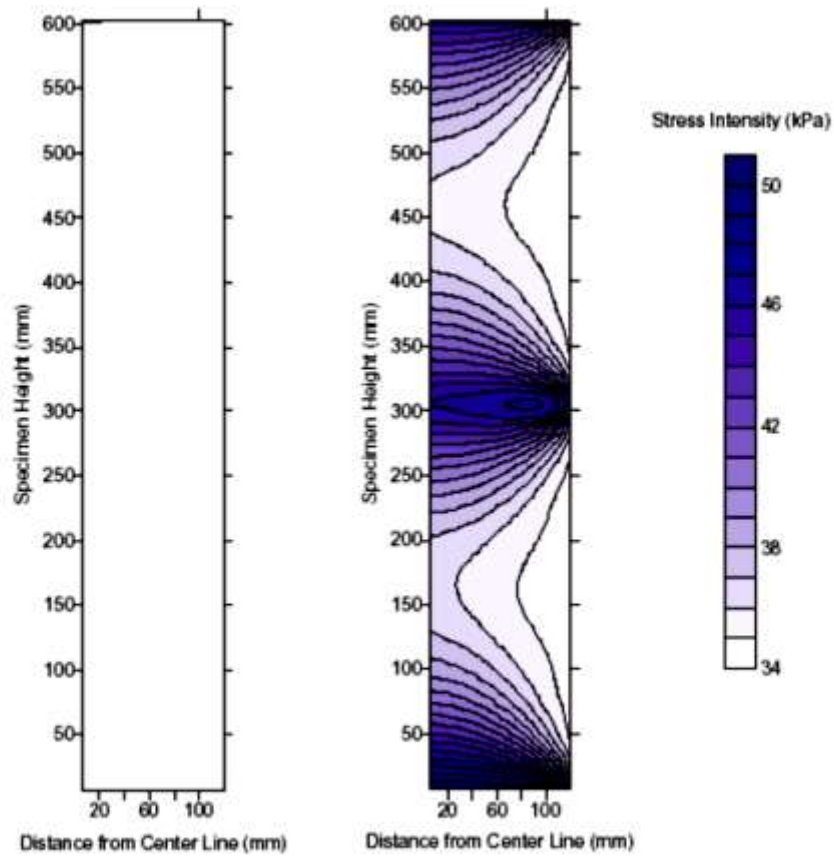


Figure 28

Vertical stress distribution at 6-kN vertical load: (a) with and (b) without reinforcement [55]



(a) Horizontal Stress at 6 kN of Test P-M-RB

(b) Horizontal Stress at 6 kN of Test P-M-(RB+2044)

Figure 29

Horizontal stress distribution at 6-kN vertical load: (a) with and (b) without reinforcement

[55]

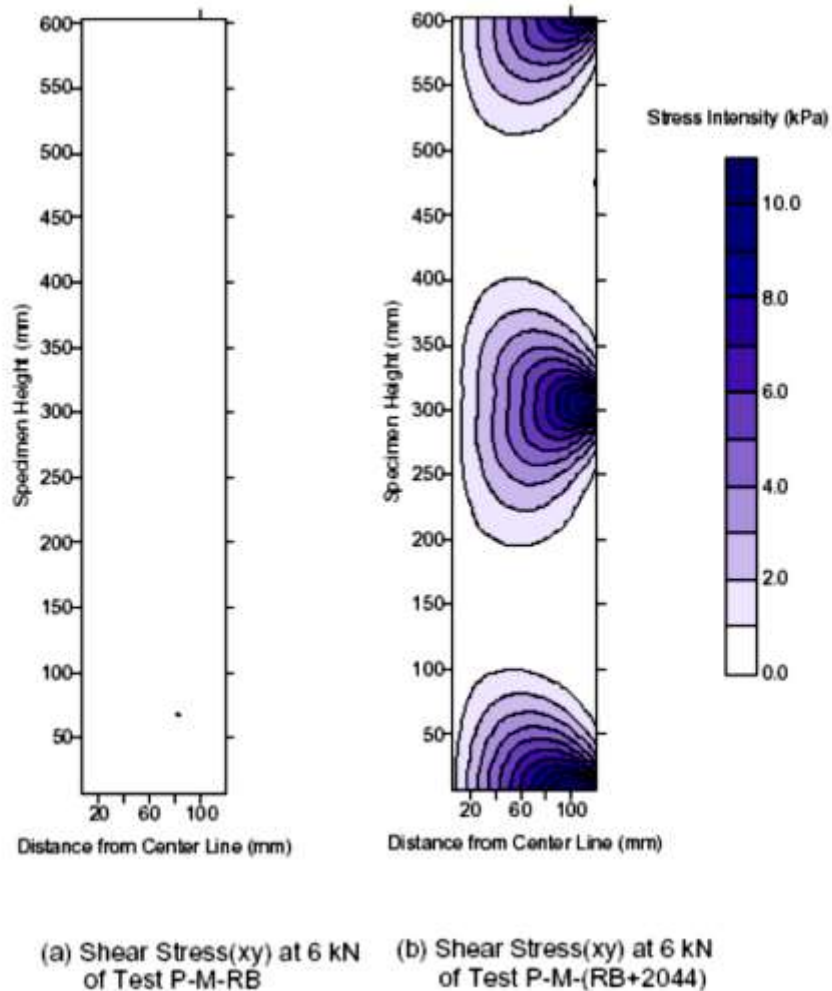


Figure 30

Shear stress distribution at 6-kN vertical load: (a) with and (b) without reinforcement [55]

Helwany et al. used DACSAR program to study the effects of foundation soil, ranging from loose sand to stiff clay, on the performance of a GRS abutment [14]. Authors used field measurements value from Founder/Meadows Bridge to verify their numerical model. Results showed that using dense sand as foundation soil results in lower abutment settlement compared to loose and medium-dense sand. Figure 31 shows the effects of the foundation soil on the behavior of the GRS wall and abutment. Figure 31 illustrates a gradual change in settlement between the bridge deck and roadway.

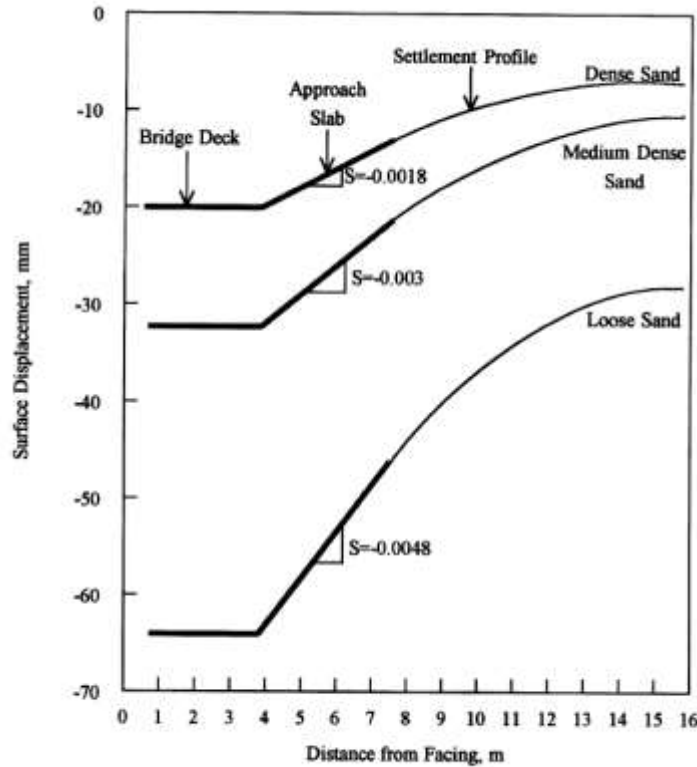


Figure 31
Bridge approach settlement after load application [14]

Vulova and Leshchinsky conducted a series of analyses using a two-dimensional finite difference program FLAC Version 3.40 (1998) [69]. From the analysis, it was concluded that reinforcement spacing was a major factor controlling the behavior of GRS walls. The analysis of GRS walls with reinforcement spacing varied from 0.2 m to 1.0 m showed that the critical wall height (defined as a general characteristic of wall stability) always increased when reinforcement spacing decreased. Reinforcement spacing also controls the mode of failure of GRS walls. In these analyses, compaction induced stresses in soil were not included.

Skinner and Rowe developed a 2D plain strain numerical model of a GRS bridge abutment over clay foundation using the AFENA program [70]. A combined viscoelastic model of an elliptical cap yield surface and a Drucker-Prager failure criterion with Perzyna's over-stress model and fully coupled consolidation was used for clay foundation. Backfill material was simulated by an elastoplastic stress-strain model with Mohr-Coulomb failure criteria. Failure at interface was modeled using a Mohr-Coulomb failure model. A schematic of model is shown in Figure 32. Skinner and Rowe claimed that stiffness and length of bottom reinforcement layers do not have a significant effect on external stability of wall. However, global stability of wall may increase by lengthening bottom reinforcement [70].

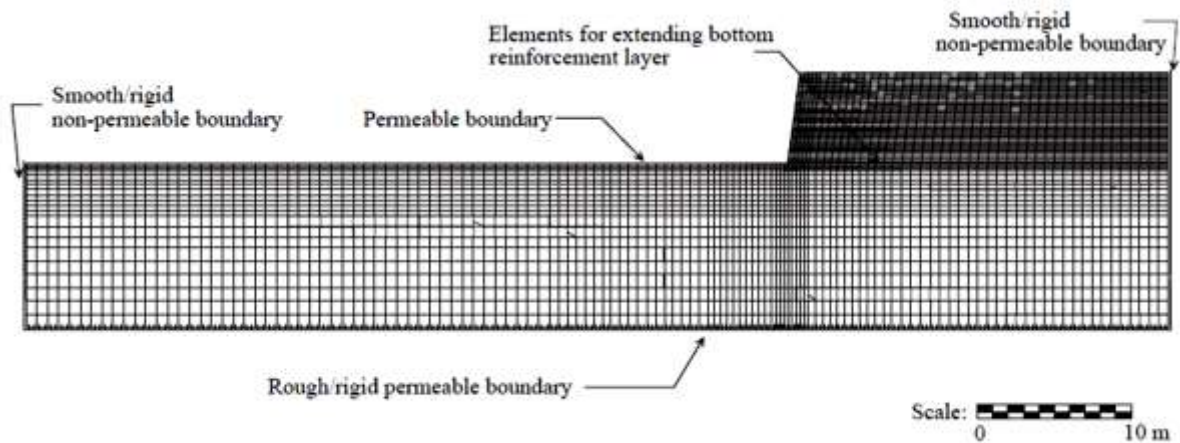


Figure 32
Schematic of 2D plain strain finite element model [70]

Wu et al. developed a finite element model to investigate the allowable bearing capacity of GRS abutments with flexible facing [15, 16]. This study was conducted by a finite element code DYNA3D/LS-DYNA. The sill, modular facing blocks, approach slab, and geosynthetic reinforcement were simulated by an elastic material model. A geologic cap model was used to capture the dilation and time dependency of the backfill material. The model evaluated by comparing the analytical results with measured data from five instrumented full-scale experiences: the spread footing experiments by Briaud and Gibbens; the spread footing experiments on reinforced sands by Adams and Collin; the FHWA Turner-Fairbank GRS bridge pier; the Garden experiment of GRS abutments in France; and the NCHRP full-scale GRS abutment loading experiments. There was significant agreement between the model and measured data. A series of analyses was performed to examine the load carrying capacity of GRS abutment for various geometric conditions and material properties. Authors recommended a bearing capacity based on limiting displacement and shear strain criterion. Table 5 shows the recommended allowable bearing pressure for GRS Bridge with 1.5 m width integrated sill. This analysis and accompanying design procedure were included in the “NCHRP GRS Method” design guidance [15].

Table 5**Recommended allowable bearing pressure of a geosynthetic reinforced soil abutment with an integrated sill [15]**

Reinforcement spacing	Design friction angle of fill ^a						
	$\phi=34^\circ$	$\phi=35^\circ$	$\phi=36^\circ$	$\phi=37^\circ$	$\phi=38^\circ$	$\phi=39^\circ$	$\phi=40^\circ$
0.2 m (8 in.)	180 kPa (26 psi)	190 kPa (27.5 psi)	200 kPa (29 psi)	220 kPa (32 psi)	235 kPa (34 psi)	255 kPa (37 psi)	280 kPa (40.5 psi)
0.4 m (16 in.)	125 kPa (18 psi)	140 kPa (20 psi)	155 kPa (22.5 psi)	175 kPa (25 psi)	195 kPa (28 psi)	215 kPa (31 psi)	240 kPa (34.5 psi)

Helwany et al. developed two finite element models, a plane strain and a three-dimensional model, using DYNA3D [72]. The plane strain model had much less degree of freedom, which makes this model run much faster than three-dimensional model. Calculated lateral displacements of the facing, at the end of construction and at an applied sill pressure of 29 psi, from plane strain model was similar to those obtained using the three-dimension model. Therefore, authors used the plane strain model to conduct a parametric study on properties of GRS abutment. Helwany et al. used the same cap soil model as Wu et al. did [16, 72]. The behavior of geosynthetic reinforcement was simulated by elastoplastic model with failure. In this model, the geosynthetic reinforcement loses its tensile capability immediately after failure. The penalty type element was used to model interface between the modular blocks and reinforcement, and between the blocks and backfill soil. The interface elements allow sliding with friction and separation. Results of parametric analysis showed that stiffness and spacing of reinforcement layer have a significant effect on the vertical displacement at the abutment. The increase in vertical displacement by increasing spacing was more significant when applied pressure increased. Moreover, friction angle of backfill material effected on vertical displacement it was not as significant as effect of geosynthetic stiffness and spacing.

The composite behavior of GRS was studied by Pham [46]. He developed a two-dimension FE model using Plaxis2D software. The elastic-plastic and dilative behavior of backfill soil was simulated by a hyperbolic hardening model. The interface between geotextile reinforcement and backfill material was assumed fully bonded. The model was verified by results of a series of large-size Generic Soil-Geosynthetic Composite (GSGC) tests conducted by Pham [46]. In this study the following equation was developed to calculate the residual lateral stress in GRS mass due to compaction:

$$\Delta\sigma_3 = \Delta\sigma_{v.c.max} K_{i,c} F \left(1 + \frac{0.7 E_r}{E_s S_v - 0.7 E_r} \right) \quad (2)$$

where, $\Delta\sigma_{v,c,max}$ is the maximum vertical stress due to compaction loading, E_s and E_r are soil and reinforcement stiffness, respectively; and S_v is reinforcement spacing. $K_{i,c}$ is the coefficient of lateral earth pressure of a GRS mass for initial loading

$$F = 1 - \frac{(OCR - OCR^{\sin \phi})}{OCR - 1} \quad (3)$$

where, OCR is over-consolidation ratio. This study also showed that presence of reinforcement reduces the dilation of surrounding soil and improves the behavior of soil-geosynthetic composites.

Design and Analysis of GRS Structures

Numerous methodologies have been developed for design and construction of reinforced soil structures. Figure 33 shows the timeline of reinforced soil guidance and development since 1985. There was debates on over-conservatism of the early methods [2]. Figure 34 compares conservatism between multiple methods developed before the year 1998. Conservatism was assessed by examining the service loads (L) relative to resistance of the reinforcement (R). The ratio of L/R is plotted on the horizontal axis of Figure 34 [73].

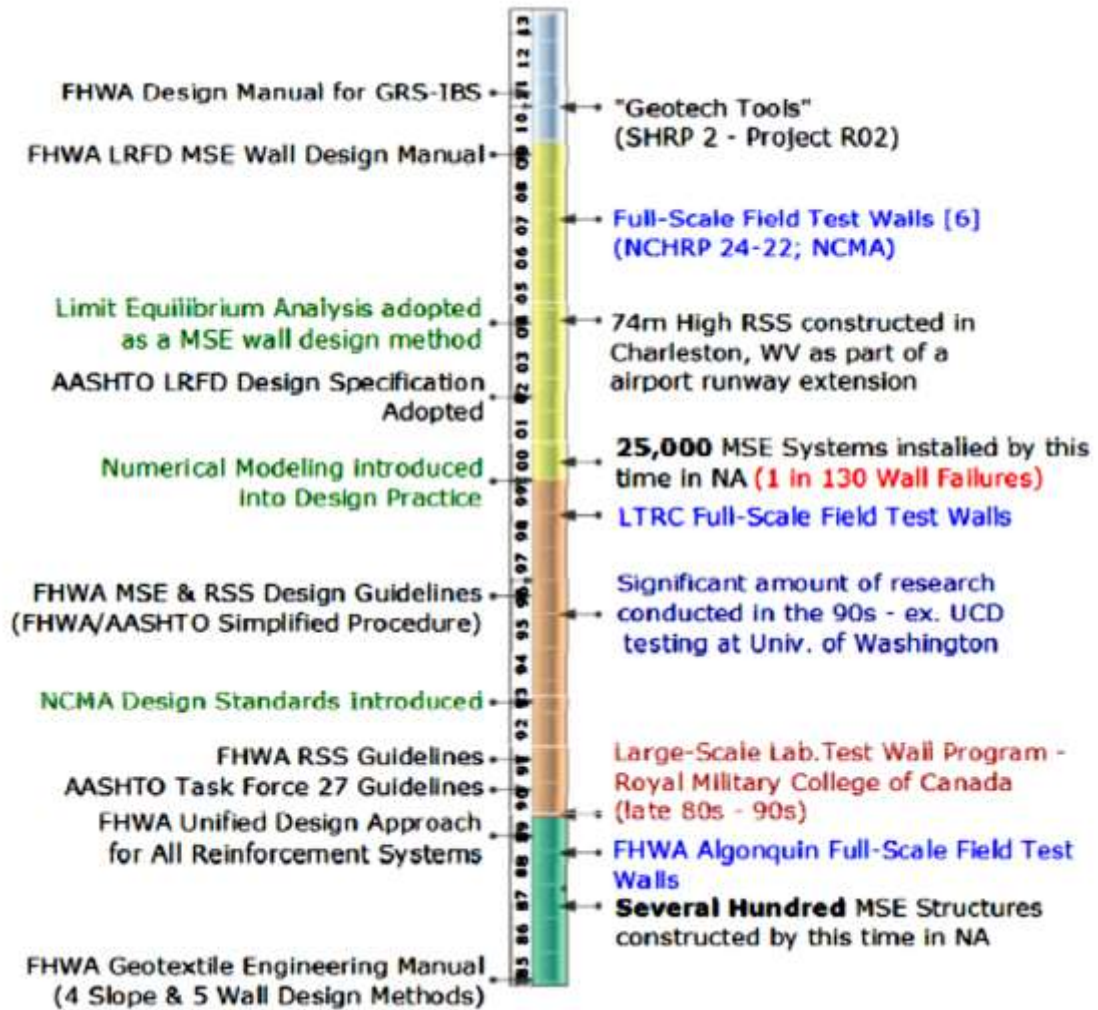


Figure 33

Timeline of development and advancement of reinforced soil design guidance [73]

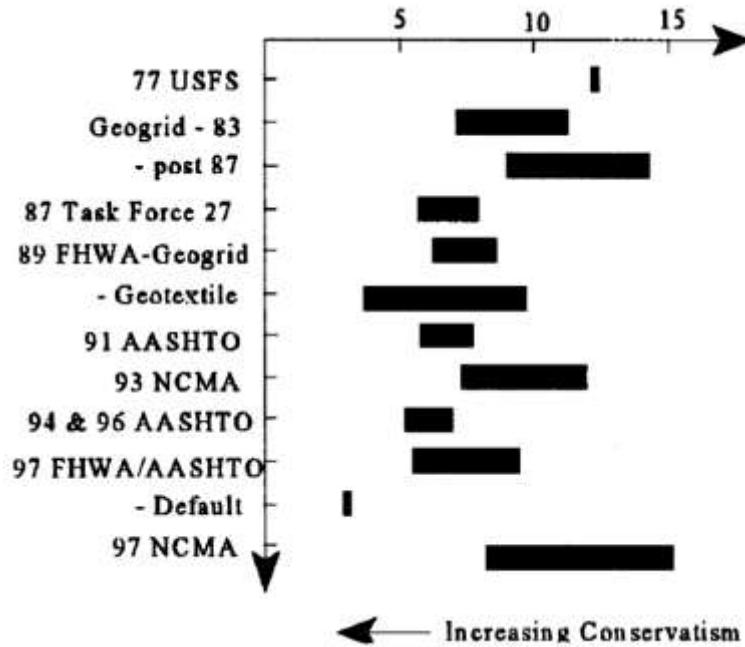


Figure 34

Conservatism of reinforcement soil design guidance [74]

The most commonly used design method for reinforced soil slopes (RSS) and MSEW in the US is the “FHWA LRFD MSE Wall Design Manual” published in 2009. This method is often called the “FHWA Simplified Procedure.” This method was adopted as the standard design guidance by AASHTO in 2012. The “FHWA Simplified Procedure” is the state of practice referenced for highway projects involving MSE and reinforced soil slopes (RSS). The design guidance is very comprehensive and provides guidelines to select, design, construct, and maintain MSE and RSS structures. The design guidance covers a wide range of reinforcement types, including geosynthetics. Additionally, design examples and equations are provided for bridge loading conditions imposed on an abutment wall. However, the code does not incorporate the defining characteristics of GRS technology, specifically the close reinforcement spacing [74].

In general, there are two different methodologies for designing of GRS systems: the tie back wedge approach (GMSE wall design) and composite design approach (GRS-IBS). The first approach is very comprehensive and covers various types of reinforcement (i.e., with steel or geosynthetic reinforcement). The primary application of GRS structures designed with this approach is highway projects involving mechanically stabilized earth and reinforced soil slopes. Examples of tie back wedge design approaches are the FHWA *LRFD MSE Wall Design Manual*, the AASHTO LRFD Bridge Design Specifications and the FHWA *Mechanically Stabilized Earth Walls Design and Construction Guidelines* [75]. LRFD is the load and resistance factor design. The second method

was developed specially for GRS-IBS Bridge [5]. This method reduces the conservatism of first approach for closely- spaced geosynthetic reinforced soil. This method is explained briefly in next section.

The other differences between the two methods have been described in a number of publications [44, 75]. The GRS- IBS design method is mainly focus on designing of GRS abutment structures and does not sufficiently cover design details of wing walls and walls supporting embankment [75]. The GMSE wall design was mainly developed for free standing structures such as footing supporting bridge, and wall supporting embankment slopes. The fundamental difference of decoupling the bridge from the supporting structure in the latter case does not account for the confining effect of the bridge on the wall and the composite strength that develops in the reinforced soil mass. It also does not consider the restraining effect of the bridge on the wall in the GRS-IBS system, which will significantly decrease lateral movement during loading. The other differences between the two design methods are shown in Table 6.

Some researchers proposed modifications and revisions to the GMSE design method regarding the design and construction of GRS walls. Wu suggested four modifications to AASHTO guidelines be included [76]:

- Lateral earth pressure on wall facing was proposed to be simulated by a “bin pressure” diagram on the wall facing of segmental GRS walls instead of the Rankine active earth pressure;
- Cumulated long-term reduction factor was proposed, which depends on backfill type and placement conditions, reinforcement spacing, and polymer type of the reinforcement;
- Truncated reinforcement length at wall base was proposed where excavation is needed as it is impractical to have full design length reinforcement. Yet, the external stability has to be checked when truncated base is adopted; and
- Embedment depth (measured from the leveling pad to the grade in front of the wall) is not necessary for GRS walls.

Table 6
Comparison between GMSE and GRS design methods [44]

Design Check	GMSE (AASHTO and FHWA GEC-11)	FHWA GRS-IBS Method
Reinforcement vertical spacing, S_v	$S_v \leq 0.8$ m (32 in.), but no lower limit. Can be equal to GRS requirements, but provides not advantage to do so (i.e. design strength directly proportional to spacing). $T_{max} = \sigma_h S_v$	$S_v \leq 0.3$ m (12 in.), with bearing bed reinforcement (minimum of 5 layers) placed beneath beam seat in between primary reinforcement at $S_v \leq \frac{1}{2}$ primary spacing. $T_{req} = \left[\frac{\sigma_h}{0.7 \left(\frac{S_v}{S_{vmax}} \right)} \right] S_v$
Reinforced fill (range)	100% < 100 mm (4 in.) to 100% < No. 4, sand to cobbles.	100% < 50 mm (2 in.), clean, open-graded crushed gravel and well-graded sandy gravel.
Reinforcement length, B	$B \geq 6.7$ m (22 ft.) for bridge structures, uniform. Allows non uniform with $0.4H$ at the base with an overall average of $0.7H$.	$B = 0.3H$ or 1.8 m (6 ft.) at the base, non-uniform with a minimum of $0.7H$ in upper reinforcements. Also includes a reinforced soil foundation (RSF), which increases base width B to $(B + 0.25B)$.
Vertical capacity	Vertical capacity is not determined; however, provides allowable load for serviceability limit and strength limit state, factored bearing resistance, based on limited field performance tests and monitored structures.	Vertical capacity is determined empirically (based on performance test results) or analytically. The capacity uses the same allowable load limit from AASTHO and GEC-11. $q_{ult,an} = \left[0.7 \left(\frac{S_v}{S_{vmax}} \right) \frac{T_f}{S_v} \right] K_{pr}$ $V_{allow,an} = \frac{q_{ult,an}}{FS_{capacity}} = \frac{q_{ult,an}}{3.5}$
Deformation	Chart provided for estimation of lateral movement during construction. Post construction not available.	Empirical (based on performance test and monitored structures). - Vertical Strain, $\epsilon_v \leq 0.5\%$, and - Lateral Strain, $\epsilon_l \leq 0.1\%$
Reinforcement rupture	$T_{al} = \frac{T_{ult}}{RF_{CR} \cdot RF_{ID} \cdot RF_D}$	$T_{ff} = \frac{0.9T_f}{2.5}$ With $T_{allow} \leq T_{act} \approx 2\%$
Reinforcement pullout	Required	No Criterion
Connection strength	Required	No Criterion
Friction angle	≤ 40 deg (Instrumented structures indicates that design model underestimate reinforcement loads at higher friction angles)	≥ 38 deg (**)
Limiting eccentricity	Required	No criterion

(**) Minimum required value reported by Adams et al. (2012)

FHWA GRS-IBS Design Method

The FHWA released a guide on the design and construction of the GRS bridge abutments [5]. The design method can be used for GRS structures with a vertical or near vertical face with height of 30 ft. or less. FHWA recommended that bridge span limits to 140 ft. and bearing stress on the GRS is limited to 4,000 lb/ft². The following will be focused on highlighting important aspects of

designing the GRS bridge abutments. The design of GRS-IBS is based on the following assumptions:

- A GRS mass is a composite material that is stabilized internally.
- Both the compacted granular fill and the reinforcement layers strain laterally together in response to vertical stress until the system approaches a failure condition.
- A GRS mass is not supported externally, and therefore, the facing system is not considered a structural element in design.
- Lateral earth pressure at the face of a GRS mass is not significant
- The facing elements of a GRS mass are frictionally connected to the geosynthetic reinforcement.
- Under the prescribed granular fill and reinforcement conditions, reinforcement creep is not a concern for the sustained loads. Therefore, individual reduction factors for reinforcement creep are not necessary. Creep can be accommodated safely within the factor of safety used for design.

External Stability Analysis

The external stability of GRS-IBS needs to be evaluated for possible failure modes such as the direct sliding (Figure 35), bearing capacity of the soil foundation (Figure 36), and global stability (Figure 37). The overturning failure about the toe unlikely occurs to the GRS abutment due to its relatively ductile nature and presence of deck or girder on the two abutments [5].

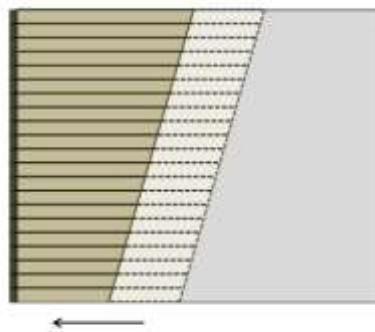


Figure 35
Direct sliding failure [5]

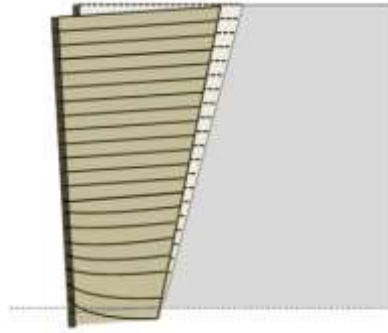


Figure 36
Bearing capacity failure [5]

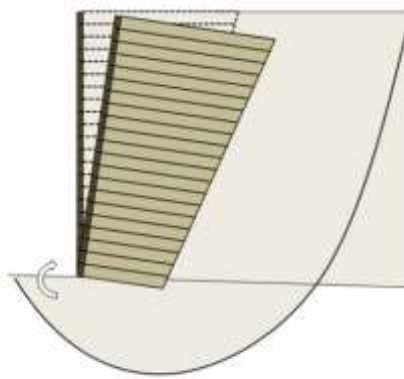


Figure 37
Global stability failure [5]

Direct Sliding. The total driving force (F_n) is calculated by the thrust forces behind the GRS abutment from the retained backfill (F_b), the road base (F_{rb}), and the roadway live load surcharge (F_t). The thrust forces are calculated according to following equations:

$$F_b = \frac{1}{2} \gamma_b K_{ab} H^2 \quad (4)$$

$$F_{rb} = q_{rb} K_{ab} H \quad (5)$$

$$F_t = q_t K_{ab} H \quad (6)$$

$$F_n = F_b + F_{rb} + F_t \quad (7)$$

where, γ_b is the unit weight of the retained backfill, K_{ab} is the active earth pressure coefficient for the retained backfill, H is the height of the wall including the clear space distance, q_{rb} is the road base dead load, and q_t is the roadway live load.

The resistance force (R_n) is calculated by following equation (8):

$$R_n = W_t \mu \quad (8)$$

where, W_t is the total resisting weight and μ is the friction factor between the wall base and the foundation. W_t is calculated by equation (9). The critical friction angle is interface friction angle between the soil and reinforcement which should be measured by an interface direct shear test according to ASTM D5321.

$$W_t = W + q_b b + q_{rb} b_{rb,t} \quad (9)$$

where, W is the weight of the GRS abutment and calculated according to equation (10), q_b is the bridge dead load, b is the width of the bridge load, q_{rb} is the road base dead load, and $b_{rb,t}$ is the width over the GRS abutment where the road base dead load acts.

$$W = \gamma_r H B \quad (10)$$

where, γ_r is the unit weight of the reinforced fill, H is the height of the GRS abutment including the clear space distance, and B is the base width of the GRS abutment not including the wall facing. Factor of safety against direct sliding is calculated by dividing the resisting force (R_n) to the total driving force (F_n). The factor of safety must be greater than or equal to 1.5.

Bearing Capacity. To check the factor of safety against bearing failure, the vertical pressure at the base of reinforced soil foundation is measured. The vertical pressure must be equal or less than allowable bearing capacity of the underlying RSF. The vertical pressure is function of the weight of the GRS abutment, the weight of the RSF, the bridge seat load, the live load on the superstructure, and the live load on the approach pavement.

$$\sigma_{v,base,n} = \frac{\Sigma V}{B_{RSF} - 2e_{B,n}} \quad (11)$$

where, $\sigma_{v,base,n}$ is the vertical pressure at the base, ΣV is the vertical load on GRS abutment, B_{RSF} is the width of RSF, and $e_{B,n}$ is the eccentricity of the resulting force at the base of the wall.

The bearing capacity of the foundation (q_n) can be calculated according to equation (12).

$$q_n = c_f N_c + \frac{1}{2} B' \gamma_f N_\gamma + \gamma_f D_f N_q \quad (12)$$

where, c_f is the cohesion of the foundation soil; N_c , N_γ , and N_q are dimensionless bearing capacity coefficients; γ_f is the unit weight of the foundation soil; B' is the effective foundation width; and D_f is the depth of embedment.

The factor of safety against bearing failure must be greater than or equal to 2.5. Factor of safety can be increase by reducing the width of GRS abutment and RSF, adding embedment depth, or using more competent soil for foundation.

Global Stability. Based on the FHWA manual, minimum factor of safety for global stability should be equal to 1.5. Global stability should be evaluated through slope stability analysis using either rotational or wedge analysis.

Internal Stability Analysis

The internal stability analysis for a GRS abutment involves analyzing the ultimate vertical load-carrying capacity, vertical and lateral deformations, and the required strength of the geosynthetics.

Ultimate Capacity. The ultimate capacity of GRS abutment can be determined either by empirical method or analytical analysis. For empirical method, a performance test should be conduct on GRS sample to determine stress-strain curve. The ultimate vertical capacity is defined as the stress corresponding to 5 % strain. If the designer decides to change the materials from those already tested, then a performance test can be performed to obtain an applicable stress-strain curve for the empirical method.

Alternatively, soil-geosynthetic composite capacity equation can be used to predict the ultimate capacity of GRS abutment. The analytical formula is shown in equation (13). The ultimate load-carrying capacity ($q_{ult,an}$) is a function of reinforcement spacing (S_v), maximum grain size of the reinforced backfill (d_{max}), and the ultimate strength of the reinforcement (T_f), and coefficient of passive earth pressure for the reinforced fill (K_{pr}).

$$q_{ult,an} = \left[0.7 \left(\frac{S_v}{6d_{max}} \right) \frac{T_f}{S_v} \right] K_{pr} \quad (13)$$

The total allowable pressure on the GRS abutment is the ultimate capacity found by either empirical or analytical method divided by a factor of safety of 3.5.

Deformation. The vertical deformation of a GRS bridge abutment is derived from the results of performance tests conducted on the GRS abutment sample. A vertical stress due to dead load is applied to sample to measure vertical strain. The vertical deformation of GRS abutment can be predicted by multiple the measured vertical strain from performance test to height of the wall or abutment. The vertical strain should be limited to 0.5%.

In order to predict the maximum lateral reinforcement strain and the maximum face deformation, FWHA method conservatively assumes a zero-volume change in the GRS abutment. Additionally, lateral deformation of wall is assumed to be triangular shape and vertical deformation is assumed

to be uniform (Figure 38). The maximum lateral displacement of the abutment face wall (D_L) and lateral strain (ϵ_L) can be estimated using equations (14) and (15), respectively.

$$D_L = \frac{2b_{q,vol} D_v}{H} \quad (14)$$

$$\epsilon_L = \frac{D_L}{b_{q,vol}} = \frac{2D_v}{H} = 2\epsilon_v \quad (15)$$

where, $b_{q,vol}$ is the width of the load along the top of the wall, D_v is the vertical settlement in the GRS abutment, H is the wall height including the clear space distance, and ϵ_v is the vertical strain at the top of the wall.

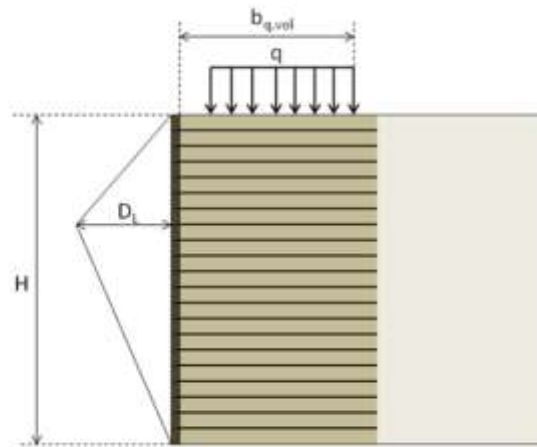


Figure 38
Lateral deformation of a GRS structure [5]

Correct numerical modeling offers the possibility to investigate the influence of a wide range of geometry and component material properties on structure performance. A challenge faced by modelers has been the treatment of the elastic-plastic properties of polymeric reinforcement materials and the interactions between reinforcement layers, soil and structural facings.

Advanced numerical methods hold promise as a design and research tool to investigate the entire response of reinforced soil retaining walls. An advantage of related computer codes is that appropriate constitutive models for polymeric materials and soils can also be implemented. Furthermore, numerical models can be used to carry out parametric analyses of the influence of wall geometry, facing type and mechanical properties of the constituent materials on wall behavior. Calibrated numerical models can also be used to extend the database of carefully instrumented field or laboratory-scale structures and hence contribute to the development of rational design methods based on conventional concepts of earth pressure theory.

Helwany et al. used the program DACSAR and calibrated their finite element model against the measured response of the Denver Test Wall (Figure 39) [12]. The nonlinear soil model proposed by Duncan et al. was used to model the soil [77]. A good agreement between the model simulation and the triaxial test results was obtained, as indicated in Figure 40 the stress-strain behavior of the geotextile reinforcement and the timber facing was simulated as linear elastic. They obtained satisfactory agreement between the measured results of facing lateral displacement and reinforcement strain and results from of the finite element simulation. Helwany et al. carried out parametric analyses to investigate the effects of wall height, backfill type and reinforcement stiffness on wall response using three different geosynthetic reinforcements and sixteen different backfills in the analysis of three different wall configurations [12]. They concluded that backfill type has the most profound effect on the behavior of the GRS retaining wall. They found that the stiffness of the geosynthetic reinforcement has an important influence on wall displacement response when the backfill shear strength and stiffness are low. Helwany et al. developed a series of design charts for selection of backfill type and reinforcement stiffness to meet code requirements for the performance of reinforced soil wall systems [12].

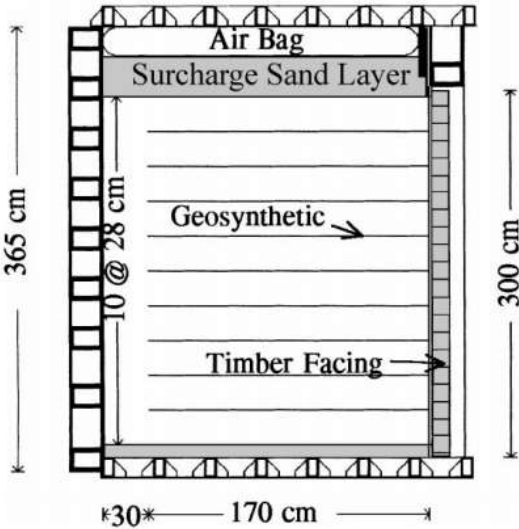


Figure 39
Schematic diagram of Denver wall [12]

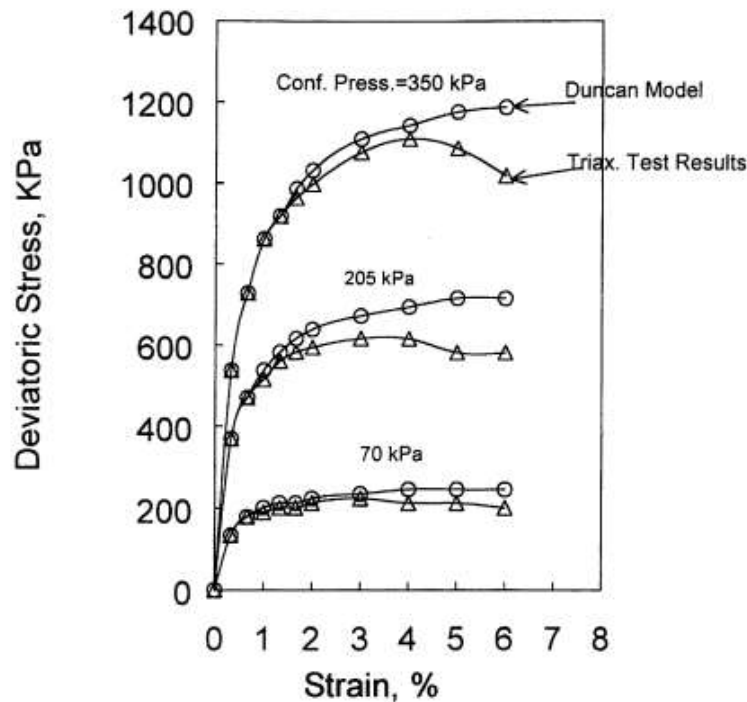


Figure 40

Comparison between FE predicted and results of triaxial compression tests for Ottawa sand [12]

Walters et al. used the program FLAC to calibrate the reinforced retaining walls constructed at Royal Military Collage of Canada (RMCC) [78]. They used the hyperbolic model proposed by Duncan et al. with Mohr-Columb failure criteria and non-associated flow rule to represent the soil elastic response [77]. Walters et al found good agreement between the measured wall response and predicted values from the FLAC program. However, the numerical results were very sensitive to the choice of interface properties assigned to the discrete block units during simulated construction.

Hatami and Bathurst developed a numerical model to predict the response of geosynthetic-reinforced soil modular block retaining walls during construction [79]. The backfill and facing modular blocks were modeled with continuum zones. The reinforcement layers were modeled with structural (cable) elements. Figure 41 shows the numerical grid used for the segmental retaining walls. They compared the predicted wall response results from the plane-strain numerical models with the measured responses of three 3.6 m high test walls constructed with sand backfill and different geogrid reinforcement stiffness and spacing. The numerical simulation was carried out using the finite-difference-based program, FLAC (Itasca Consulting Group 2001). They used a homogeneous, isotropic, nonlinear elastic-plastic material with Mohr-Coulomb failure criterion

and dilation angle (non-associated flow rule) to model the compacted backfill soil. They found that accurately predicting the response of the walls, which were constructed with a stiff facing column required a technique to account for compaction-induced stresses in the soil. A transient 1.16 psi vertical pressure was applied to the backfill surface at each stage during the simulation of wall construction. They found also that the magnitude of the horizontal compliance at the toe of the facing column have a major influence on wall response. They observed that a simple elastic–plastic soil model is sufficient for predicting wall deformation, footing reaction response, and peak strain values in reinforcement layers for strains of <1.5% provided that suitably selected values for the constant elastic modulus and Poisson’s ratio for the sand backfill soil are used. However, they observed that using nonlinear elastic-plastic soil models gave better fit to the measured data, since because the linear elastic-plastic model they used was shown to predict a contiguous zone of plasticity through the reinforced soil zone that was not consistent with measured results, and because of the stress level dependency of granular soils, the selection of a suitable single-value elastic modulus is problematic.

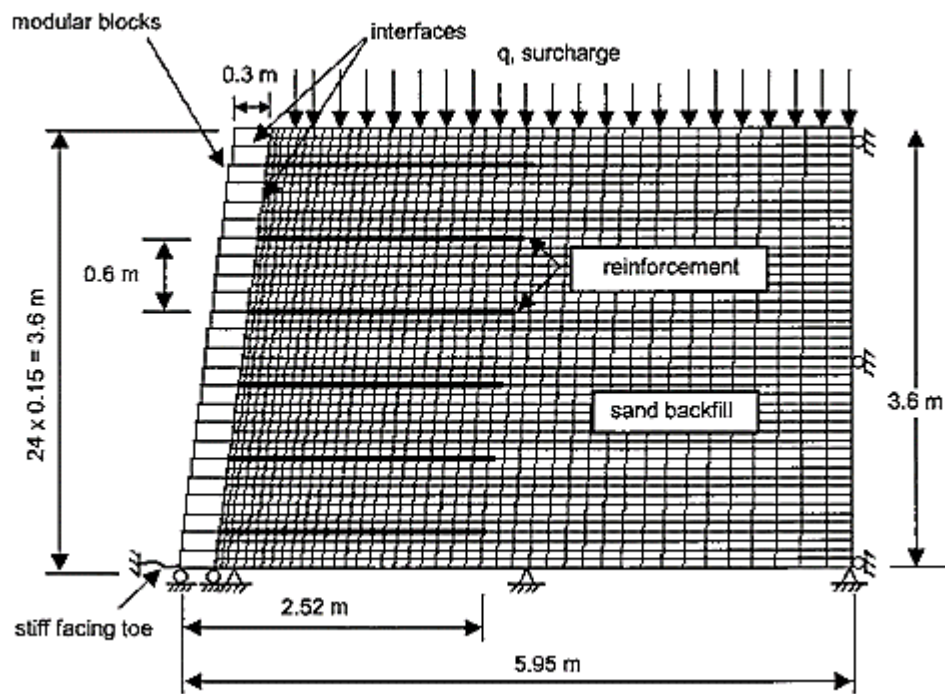


Figure 41
Details of FE numerical grid

Maree Michel GRS-IBS Bridge

Recognizing the potential benefits of using GRS-IBS for local bridges, the Louisiana Department of Transportation and Development (DOTD) decided to build GRS-IBS abutments for one single-span Bridge at Maree Michel. The Maree Michel Bridge is located in Route LA 91, Vermilion Parish (Figure 42). The new bridge is a replacement of an existing bridge that was nearing the end of its design life. The existing bridge was a 24-ft. by 59-ft. (7.3-m by 18-m) treated timber trestle, which replaced by a 65-ft. (20-m) steel girder span bridge. The new GRS-IBS Bridge had the same general footprint area as the previous bridge, carrying two lanes of traffic. The Average Daily Traffic (ADT) count on the bridge in 2013 was about 375, and it was estimated to be 450 vehicles in 2033.



Figure 42
Location of GRS-IBS project site

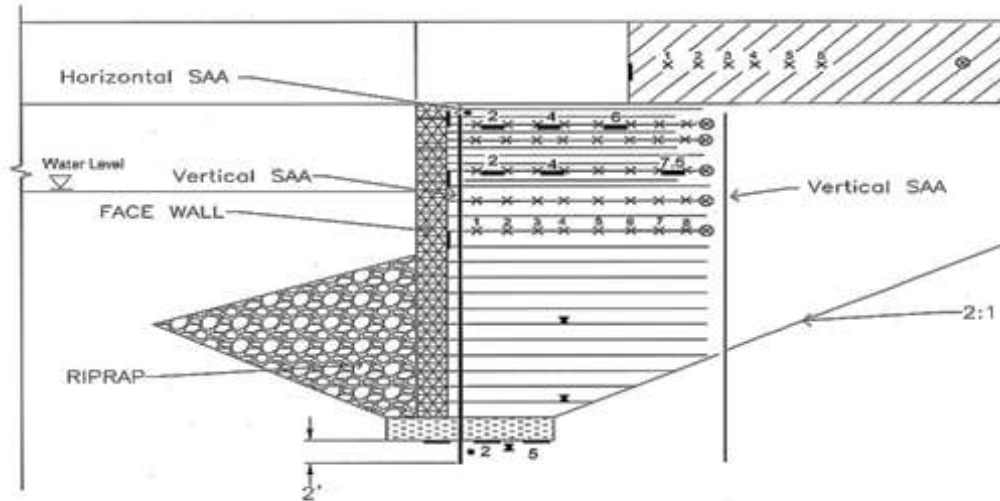
The maximum height of the GRS abutment is approximately 15.6 ft. (4.8 m) from the bottom of the RSF to the road pavement, the width of the abutment is 43 ft. (13 m), and the girder span is 72 ft. (22 m). The overall width of the bridge superstructure is 30 ft. (9.1 m). This bridge was built with a precast concrete superstructure, and its GRS abutments were constructed using locally available materials. The width of the beam seat bearing area on each abutment was determined to be 5 ft. (1.5 m) using the FHWA design procedure. The vertical spacing between the reinforcement layers of GRS was 8 in. However, for the top 5 layers of abutment, secondary reinforcement was added in the middle of each layer (spacing = 4 in.) to increase the load carrying capacity of abutment underneath the steel girders.

The three primary materials for GRS construction are a high quality granular fill, geosynthetic reinforcement, and facing elements. For this project, the abutment's structural fill consisted of an open-graded crushed rock with a maximum particle size of 0.5 in. and less than 5% passing the No. 16 sieve. The aggregate had a maximum dry density of 133 lb/ft³ and an angle of internal friction (ϕ) of 50.9° based on large-size direct shear test. The backfill material was compacted to a minimum of 95% of the maximum dry density according to AASHTO-T-99 (modified proctor). In the bearing bed and beam seat the backfill material was compacted to 100% of the maximum dry density. Small hand operated compaction equipment was used to compact the backfill materials near the facing wall. The RSF was constructed with the same backfill material as the abutment. The reinforcement for the abutment and the RSF consisted of woven polypropylene geotextile with an ultimate tensile strength of 4800 lb/ft (70 kN/m). Interface friction angle between geosynthetic and back fill material from direct shear test (ASTM D3080) is 40.4. Facing elements consisted of nominal 8-in. by 8-in. by 16-in. concrete masonry units (CMUs) with a compressive strength of 4000 psi (27.6 MPa).

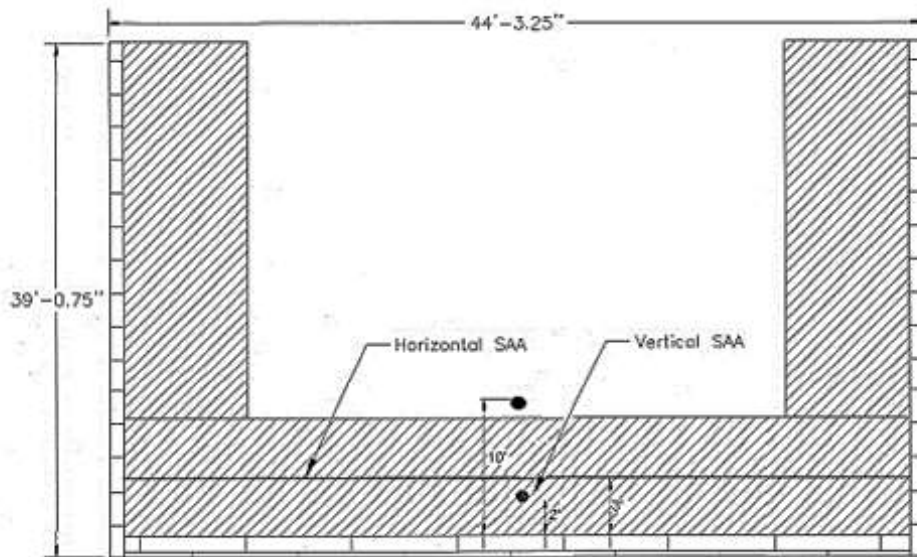
The design of the GRS abutment was performed using the Geosynthetic Reinforced Soil Integrated Bridge System Interim Implementation Guide. The factor of safety (F.S.) for the different types of failure modes are as following: F.S. against sliding = 1.5; F.S. against bearing failure = 2.5; F.S. against global failure = 1.5; tolerable vertical displacement = 0.5% wall height; and tolerable lateral displacement = 1.0% bearing width.

Instrumentation

In order to monitor and evaluate the performance of the GRS-IBS abutment, various types of instrumentations were installed in the south abutment of Maree Michel Bridge. An instrumentation plan was developed to measure the load-associated and environment-associated responses and the performance of the GRS-IBS abutment (Figure 43). The primary measurements were the vertical and horizontal deformations near the front wall, settlements due to the soil foundation and the GRS-IBS backfill, the distribution of stresses in the GRS-IBS abutments and below the reinforced soil foundation, and the distribution of strains along the geosynthetic reinforcements. Additionally, the pore water pressure and temperature were monitored by piezometers and thermocouples. Six different types of instrumentations were used to monitor the GRS-IBS bridge abutment: Shape Acceleration Array (SAA), horizontal and vertical earth pressure cells, strain gauges, piezometers, and thermocouples. Additionally, surveying was conducted at the bridge surface upon the completion of the construction.



a) Arrangement of Instrumentations in the GRS abutment section view



b) Arrangement of Instrumentations in the GRS abutment plan

- | | | | |
|---|--------------------------|---|--------------------------------|
|  | VERTICAL PRESSURE CELL |  | SHAPE ACCELERATION ARRAY (SAA) |
|  | HORIZONTAL PRESSURE CELL |  | PIEZOMETER |
|  | STRAIN GAUGE |  | THERMOCOUPLE |

Number denotes distance from facing wall (ft)

Figure 43
Instrumentation layout

Shape Acceleration Array (SAA). The GRS-IBS abutment is expected to experience settlements and deformations along with the construction progress and the time. The designed settlement for the Maree Michel Bridge is 3 - 4 in. The deformation characteristic of the GRS-IBS abutment is a critical indicator of the performance of the GRS-IBS abutment for internal and external stability, particularly the deformations near the facing wall. The shape acceleration array (SAA) is proposed to measure the GRS-IBS abutment deformations because of its reliability and successful applications for other geotechnical structures. The SSA consists of an array of triaxial accelerometers based on the micro-electromechanical system (MEMS) technology. The SAA measures the three-dimensional accelerations and deformations at each sensor node. Two sets of vertical shape acceleration array (SAA) are proposed to be installed at locations 2 ft. behind the face of the wall: one at the center of abutment and one 10 ft. away from the center (Figure 44). The bottom of the SAA will be located 2 ft. below the reinforced soil foundation while the top of SAA will be leveled with the backfill surface. These two sets of SAA will mainly measure the lateral deformations throughout the depth of the GRS-IBS abutment. Additionally, two sets of horizontal SAA are proposed to be installed: one at the location 3 ft. behind the face wall and 2 ft. below the GRS-IBS abutment surface and one at the location 1 ft. below the reinforced soil foundation (RSF). The upper horizontal SAA measured the total settlements across the GRS-IBS abutment while the lower horizontal SAA measured the settlements due to the soil foundation. The difference in the measurements between the upper and lower SAA was the settlements due to the GRS-IBS backfill. The SAA has options in segment length, i.e. the intervals between sensor nodes: 12 in and 19.7 in. The two vertical SAA used the segment length of 12 in. Since the horizontal profile of the GRS-IBS abutment settlement is expected to be approximately symmetric, the horizontal SAA will need less sensor nodes and have a segment length of 19.7 in.

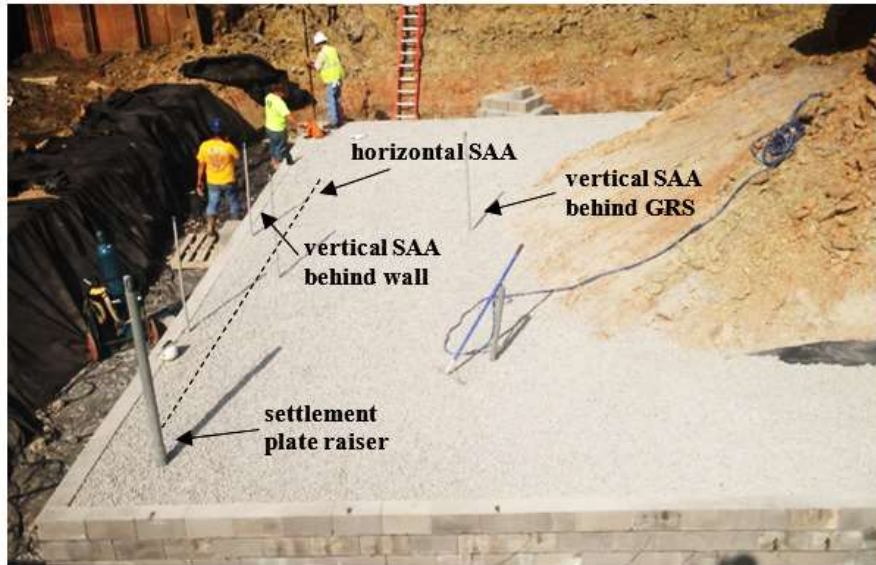


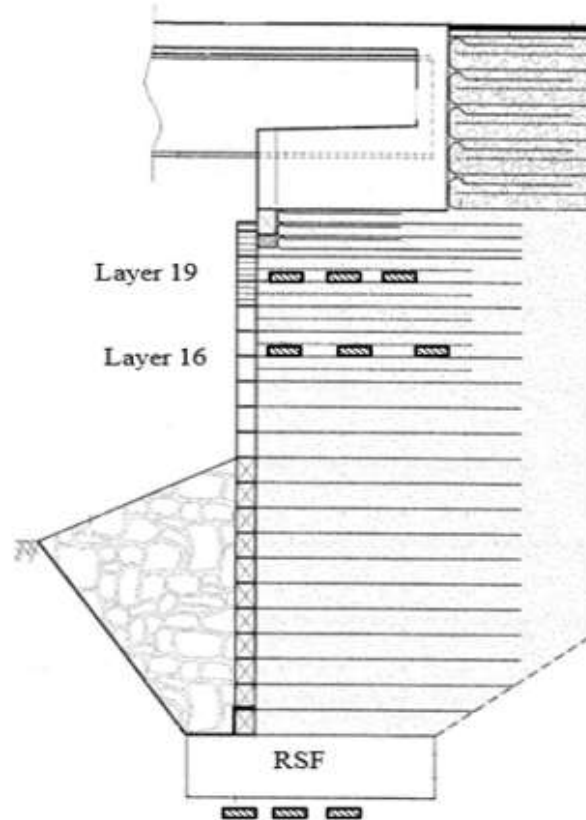
Figure 44

Arrangement of SAA for Maree Michel Bridge - GRS-IBS

Earth Pressure Cells. Hydraulic type earth pressure cells with semiconductor transducers are selected to measure the vertical and the horizontal total stresses (including thermal stresses) (Figure 45). The proposed pressure cells are capable of measuring both static and dynamic stresses. Seventeen (17) earth pressure cells were installed in the GRS-IBS abutment at different locations. Four pressure cells were installed behind the face wall to measure the horizontal total pressure. Nine pressure cells were installed in the bearing reinforcement zone to measure the distribution of the total vertical pressure within the zone. Measurements from the pressure cells provides important information on the stress distribution in the abutment, particularly in the bearing reinforcement zone in terms of improving the bearing capacity of the reinforced soil and redistribute the applied stresses to wider area. Additionally, one pressure cell was placed between the integrated approach and the bridge girder to monitor the variation of horizontal stresses due to the temperature change.



a) Installation of pressure cells



b) Location of pressure cells in abutment

Figure 45
Locations of earth pressure cells

Strain Gauges. Electrical resistance-type / foil-type strain gauges were attached onto the geosynthetic reinforcements to measure the developed strains along the geosynthetics. The reinforcement tensile forces developed in the geosynthetic reinforcement was estimated from strain measurements and the stiffness of the geosynthetic materials. A total of 69 strain gauges were installed on the geosynthetics in the abutment. Figure 46 shows the sketch of anticipated strain distributions along the geosynthetics at different heights in the GRS-IBS abutment. The locations of installing the strain gauges is arranged in a fashion such that strain gauge measurement could capture the strain distributions. The extensive instrumentation on geosynthetics provides the opportunity to quantify the mobilized tensile reinforcement forces and the distribution of the tensile in the geosynthetics and to help identify the critical load bearing zone for internal stability.

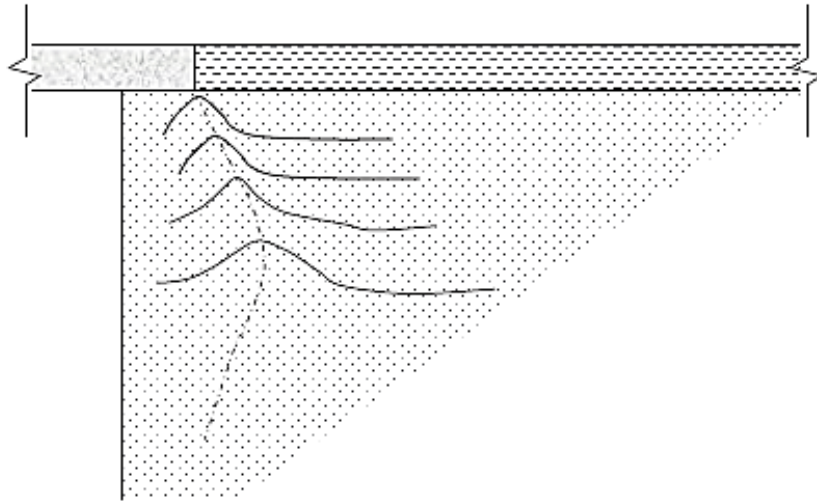


Figure 46
Anticipated strain distributions along the geosynthetics

Piezometers. Three piezometers with semiconductor type transducer were installed to measure the developed pore water pressures. Along with the measurement of total stresses from earth pressure cells, the measurement of pore water pressures can be used to calculate the effective stresses in the GRS-IBS abutment. The three piezometers were installed at the bottom, one-third and two-third of the height from the bottom of the GRS-IBS abutment, respectively.

Thermocouples. A total of seven K-type thermocouples are proposed to be installed inside and outside the abutment to monitor the variation of temperatures. One thermocouple will be installed on each layer of geosynthetics that are instrumented with strain gauges. One thermocouple will be installed on bridge girder. Comparison between temperature measurements and measurements from other instruments, mainly strain gauges will be conducted to examine the effects of thermal cycles on the abutment and bridge responses.

Data Logger. In addition to the instruments mentioned above, a data logger was used to collect the data in the field. The data logger was housed in a weather-proof enclosure with appropriate power supply using solar panel system.

PERFORMANCE MONITORING

Settlement and Deformation Measurements

The GRS-IBS abutment is expected to experience settlements and deformations along with the construction progress and time. The deformation characteristic of the GRS-IBS abutment is a critical indicator of the performance of the GRS-IBS abutment for internal and external stability, particularly the deformations near the facing wall. The bridge deformation was monitored, shortly after the beginning of construction (04/08/2015) to about two months after open to traffic (10/6/2015). Figure 47 shows the settlement profile of soil foundation measured during and after the construction. As expected, the maximum settlement was increased with lift placement, with more movements occurred near the center of abutment than the corners.

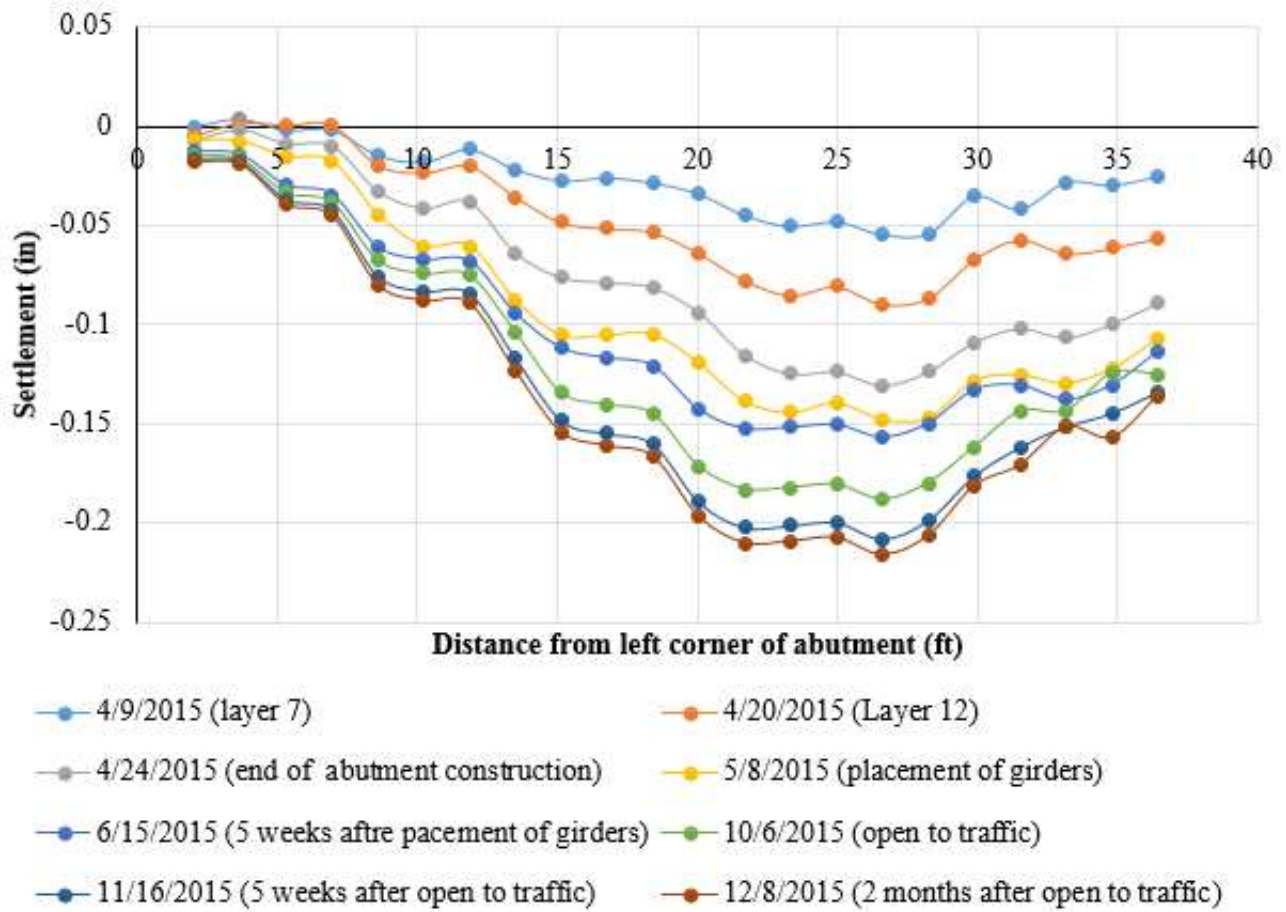


Figure 47
Settlement profile of soil foundation

The maximum deformation of the soil foundation as well as the GRS abutment is illustrated in Figure 48 shows the construction time schedule of the abutment layers. It took 18 days of construction time to complete GRS abutment. The foundation soil settlement increase was fast at the early stage of construction; however, the rate of increase in settlement decreased with time (Figure 49). The maximum deformation of the abutment was significantly less than the design value of 0.8 in. Measuring the deformation of abutment began five days following the end the abutment construction (4/29/2015). Figure 49 clearly shows the settlement due to the weight of the concrete deck. The bridge was opened to traffic on 10/6/2015, but this is not apparent in the settlement record. The deformation on the top abutment, from when the bridge was opened to traffic (0.31 in. on 10/6/2015) until one month after that (0.33 in. on 11/2/2015), was 0.02 in. Compared to the increase in deformation from 0.17 in. five days after end of abutment construction to 0.28 in. after casting the concrete deck on the steel girders, the settlement after open to traffic is minimal. The deformation measurements indicate that the maximum total settlements across the GRS abutment one month after trafficking was less than 0.35 in. About 70% of abutment deformation was due to settlement of foundation soil and less than 30% of total deformation experienced within the abutment and RSF. Majority of backfill deformations occurred by end of GRS construction (4/24/2015), which did not increase significantly with time. Overall, the GRS abutment performed satisfactory during the construction in terms of settlement and deformation measurements. The vertical strain of bridge abutment can be calculated by dividing the vertical deformation of GRS mass to the height of wall. The maximum vertical strain of 0.2 % was observed which is significantly less than tolerable limit of 0.5 % as stated by FHWA.

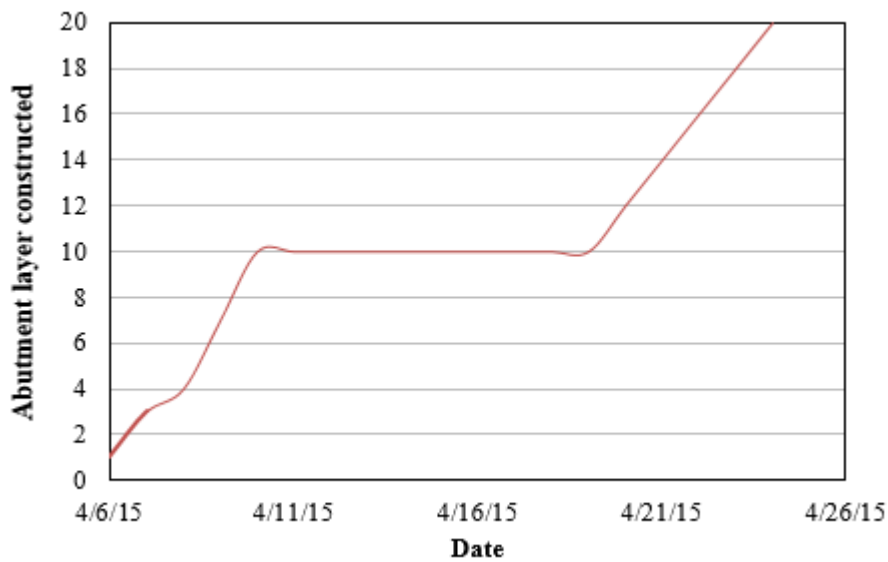


Figure 48
Construction of the GRS abutment with time

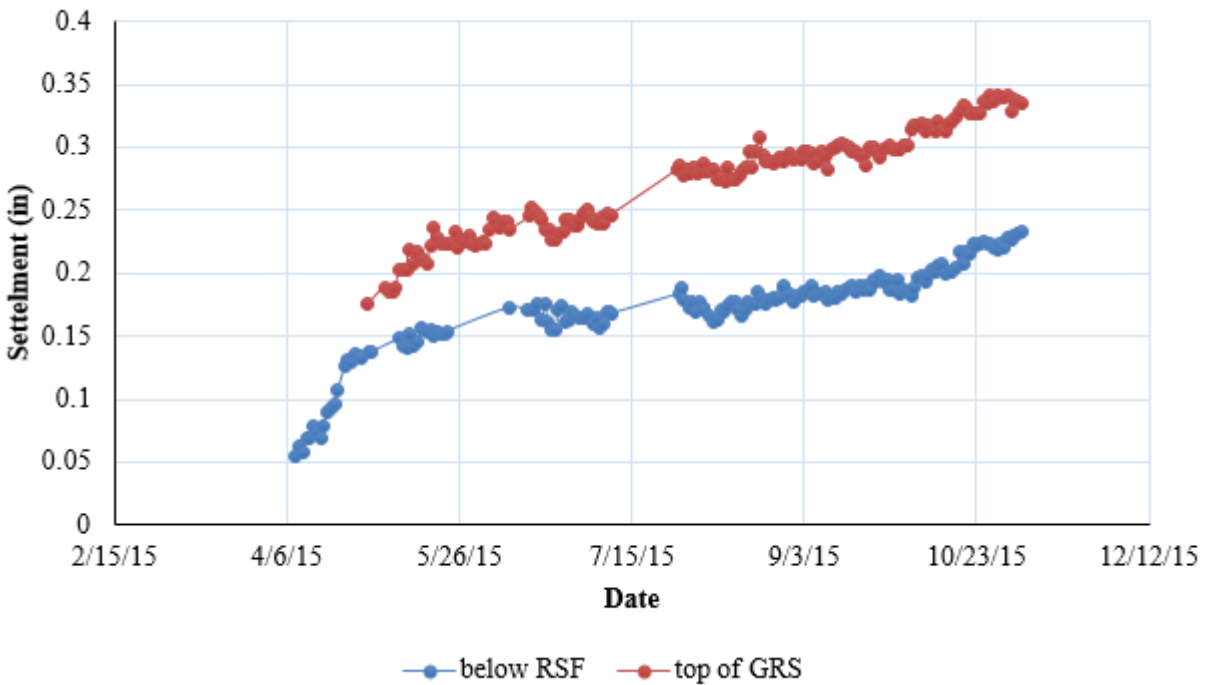


Figure 49

Settlement and vertical deformation during the construction of GRS abutment

Figures 50 and 51 present the lateral movements or deformations of the abutment at locations of 2 ft. and 10 ft. behind the facing wall, respectively. The positive value of deformation indicates movement toward the wall face and the negative value indicates deformation away from the wall. These figures demonstrate that the maximum lateral movement occurred near the top of the wall. Following the construction of bridge abutment, the facing wall experienced some outward (away from backfill) lateral displacements. After placing the steel girders (5/8/2015), the lateral movement close to the wall significantly increased from 0.01 (measured after completing the construction of GRS abutment on 4/24/2015) to 0.09 in. The measured lateral movement behind the GRS mas is very small and in the direction away from the wall. The maximum measured lateral movement was 0.015 in. at the top one third of the abutment mass.

The FHWA consider a zero volume change in the GRS mass to predict the lateral displacement of the abutment face wall. By assuming the volume lost at the top of abutment due to settlement equal to the volume gained at the face due to lateral deformation, FHWA provides the following equation to estimate the maximum lateral displacement (D_L):

$$D_L = \frac{2b_{q,vol}D_v}{H} \tag{14}$$

where, $b_{q,vol}$ is the width of the load along the top of the wall including the setback (6 ft), D_v is the vertical settlement in the GRS mass, and H is the wall height (13.65 ft.). The lateral strain can be measured by dividing lateral displacement to the width of the load. Table 7 provides the theoretical values and measurements of lateral displacement and strain during the monitoring period. In general, the theoretical method underpredicts the lateral movement of facing wall. The difference between measurement and theoretical values was more significant during the construction of bridge, however, after open the bridge to traffic (10/6/2015), the difference between the predicted and measured lateral deformations and strains were decreased. FHWA assumes a triangular lateral deformation and uniform vertical deformation and restricts the horizontal strain at the facing by 1.0%. Still, the measured strains during the monitoring period were significantly less than the FHWA criteria.

Table 7
Comparison between predicted and measured lateral facing deflection

Date	Vertical settlement in abutment (mm)	Maximum lateral displacement (mm)		Maximum lateral strain	
		Measurement	Theory	Measurement	Theory
05/8/2015	1.5	2.2	1.35	0.12%	0.07%
06/15/2015	1.9	2.7	1.67	0.15%	0.09%
10/06/2015	2.81	2.9	2.47	0.16%	0.13%
11/16/2015	2.79	3.0	2.46	0.16%	0.13%

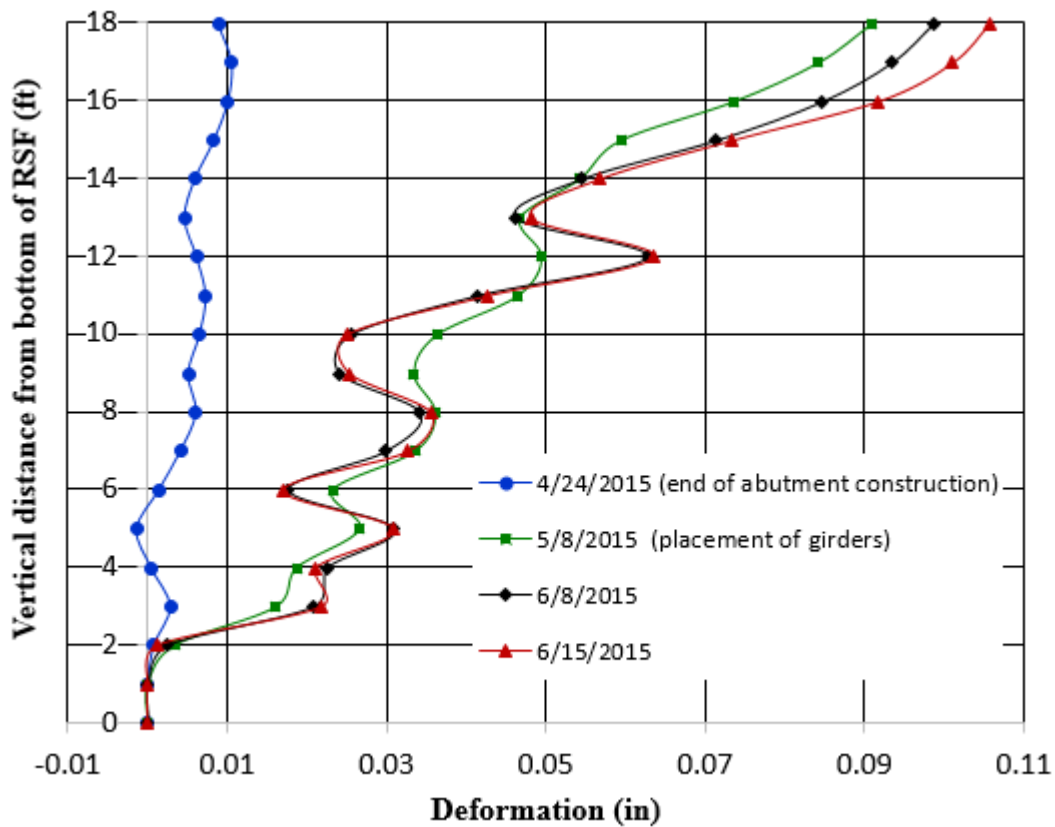


Figure 50
Lateral movements of the abutment 2 ft. behind the facing wall

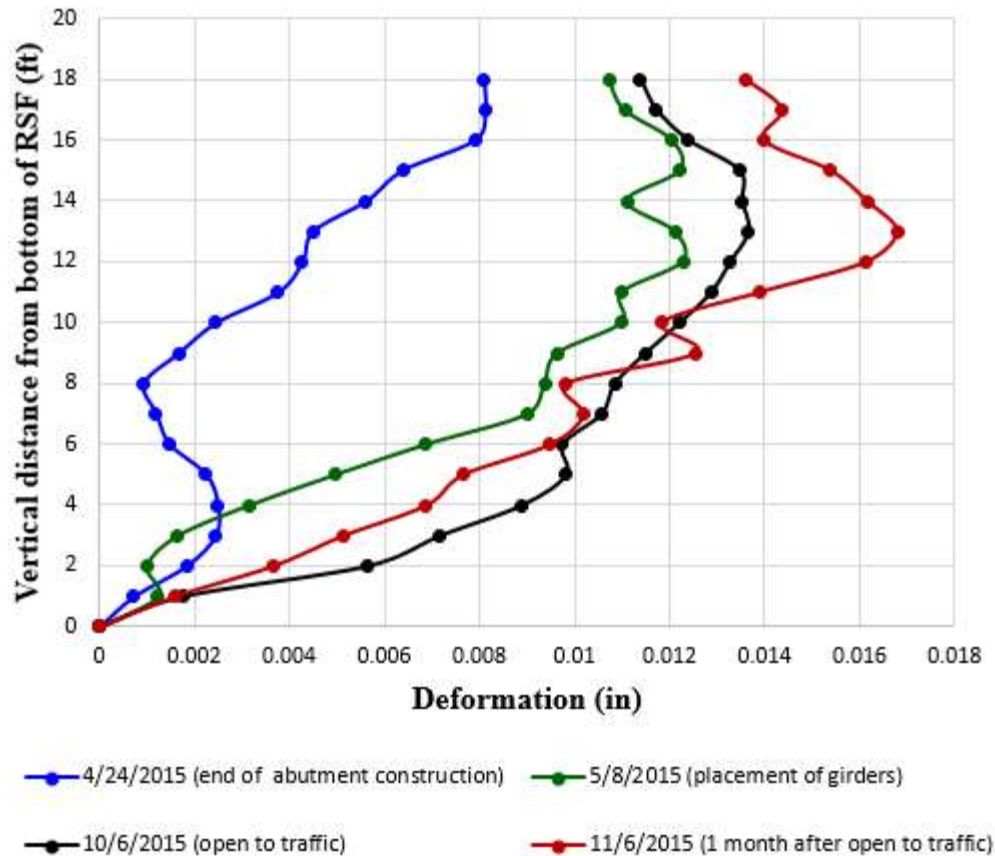


Figure 51
Lateral movements behind GRS mass

Measurement of Stresses

Figure 52 shows the measured vertical pressure at different elevations during and after the construction of GRS-IBS abutment. As expected, higher pressure was observed at lower levels of the abutment. The maximum vertical pressure of 16.7 psi was measured below the RSF after bridge opened to the traffic. Figure 52 shows that at the certain level, the vertical pressures from behind the wall up to 1.8 m away from wall are generally very close. However, the pressure cell located at 2.3 m away from wall on layer 16 shows significantly lower value than the pressure cell close to the wall. The measured vertical earth pressure at the end of abutment construction was compared to the theoretical values for verification. The theoretical value was calculated by multiplying the heights of the backfill above the cells by the average unit weight of backfill. The calculated theoretical pressure at the level below RSF, level 16 and level 19 are 12.2 psi, 2.3 psi, and 1.0 psi, respectively, which compare well with the measured values at the end of abutment construction. In overall, the maximum measured vertical pressure below the girders was less than FHWA bearing stress restriction of 27.8 psi. The horizontal total pressure on the wall was measured by

pressure cells attached vertically behind the wall. Three pressure cells were installed behind the facing wall on layers 13, 17, and 20 of the GRS abutment. Figure 53 depicts the measurements of the horizontal pressures. The maximum horizontal pressure was observed in the lower level (layer 13), which is about two times the measured horizontal pressures at upper layers. The higher value at layer 13 can be attributed to the reinforcement spacing. The addition of secondary reinforcement in the top 5 layers of abutment decreases the reinforcement spacing from 4 to 8 in. The measured horizontal pressures were used later in this paper to calculate thrust force on the facing wall. The measured lateral pressure at the end of abutment construction was compared to the theoretical values from Rankine theory.

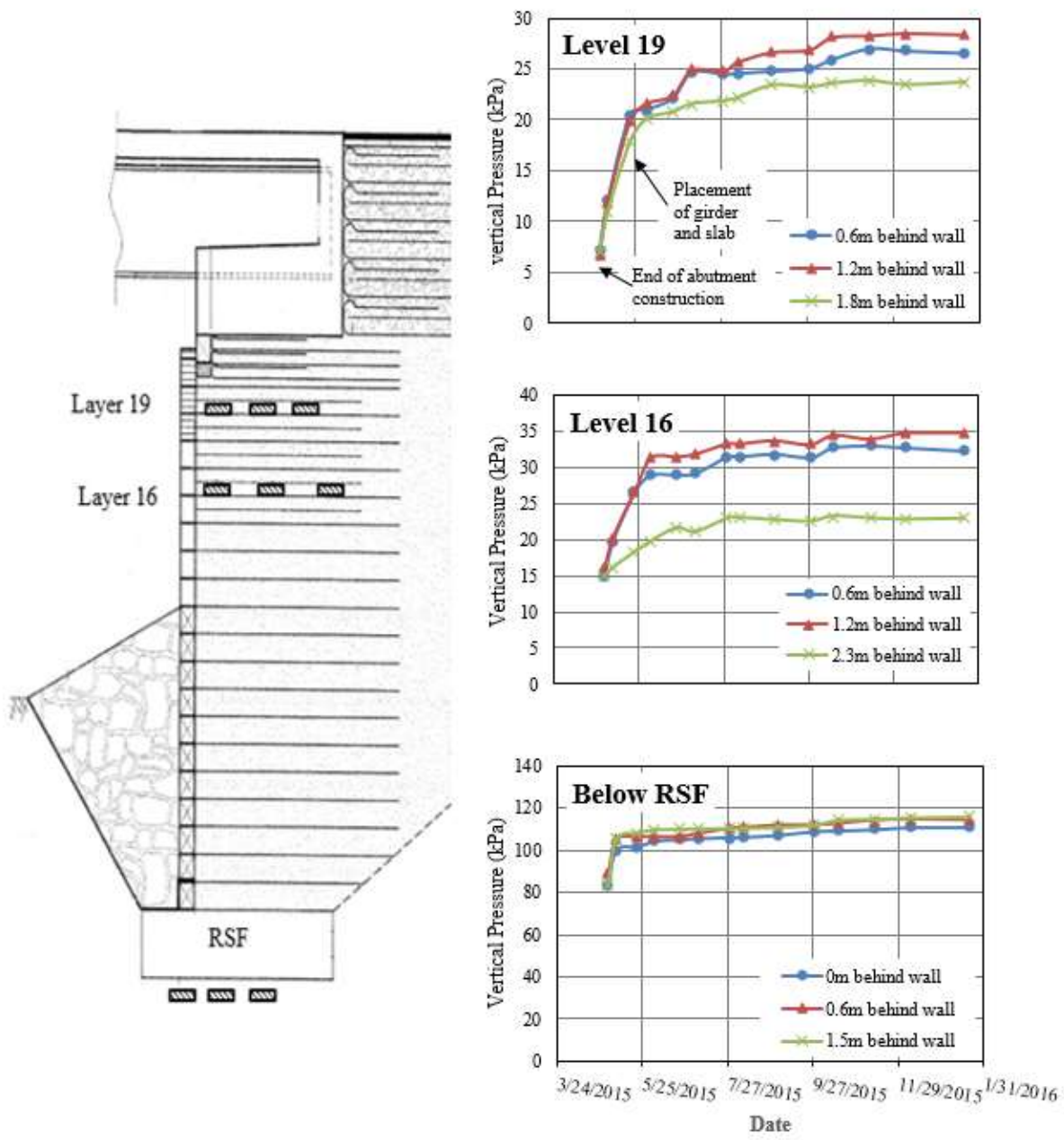


Figure 52
Measurement of vertical pressures

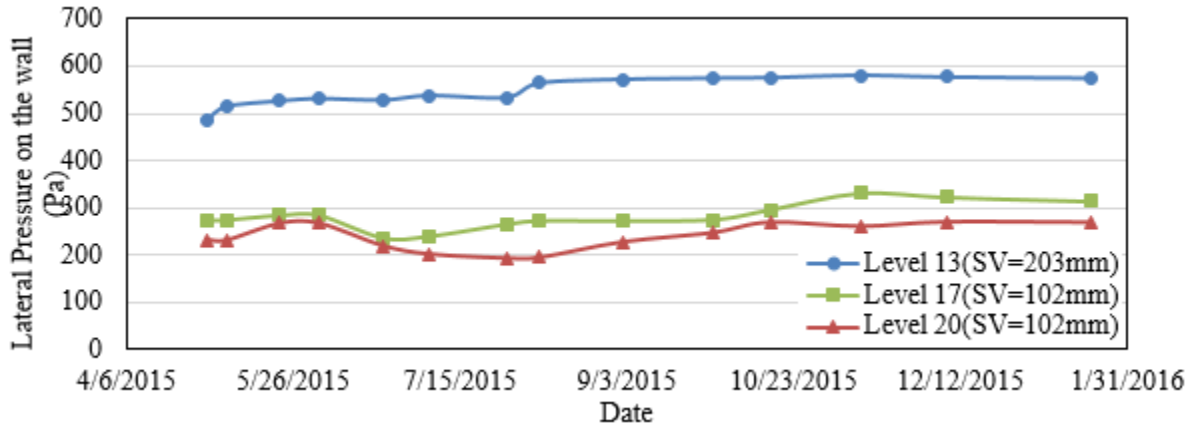


Figure 53
Measurements of lateral pressures on the wall

Measurement of Pore Water Pressure

Piezometer pore pressure readings were monitored from 4/30/2015 to 7/6/2015 (Figure 54). As expected, the pore water pressure was higher in the lower level of abutment and by reducing the water level height in upper levels, the pore water pressure decreased. During the construction, sheet piles were installed (as cofferdam) to divert the water flow in creek away from construction site. After completing the construction of GRS mass, the sheet piles were removed and the water level increased to about 12 ft. above the top of RSF. The jump in Figure 54 is due to increase in water level after the removal of sheet piles. After that, water level did not change significantly.

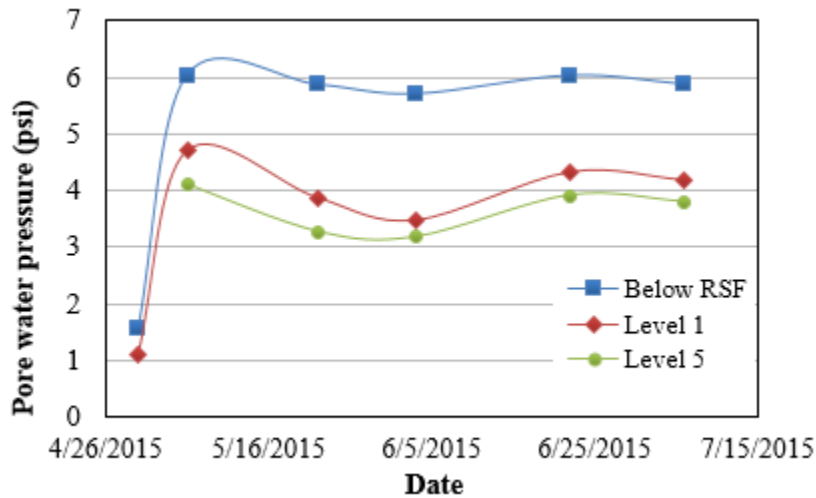


Figure 54
Measurements of pore water pressures

Strain Measurements along Geosynthetics

Electrical resistance-type/foil-type strain gauges were installed onto the geosynthetic reinforcements to measure the developed strains along the geosynthetics. A total of 55 strain gauges were installed on five different geotextile layers few weeks before the construction of GRS. 40 out of 55 strain gauges were installed along the centerline of the abutment and the rest 15 strain gauges were installed at 1-ft. offset from the centerline for redundancy. The installation locations of strain gauges were arranged in a fashion such that strain gauge measurements would be able to capture the strain distributions. The extensive instrumentation of geosynthetics provides the opportunity to quantify the mobilized tensile reinforcement forces and the distribution of the tensile strain along geosynthetics that help to identify the critical load bearing zone for internal stability.

The strain measurements of abutment reinforcements are shown in Figure 55. The figure presents the strain distribution along the reinforcements at different layers and the locus of maximum strains in the abutment. Before placement of the steel girders, the maximum strain was observed at lower levels. However, after placement of the steel girders (5/8/2015), the maximum strain spikes on the upper layers of abutment. During the construction period, the maximum strain of 1.1% was observed at level 19, which is less than the maximum strain of 2% specified by the FHWA.

Estimation of Failure Surface

The critical failure surface is assumed to be the surface connecting the locus of maximum strains in each layer. The location of maximum strains with depth are plotted in Figure 56. The figure shows that the maximum strains before placement of the steel girders (Figure 56a) formed a bilinear surface with an angle slightly lower than the theoretical K_a failure surface (line of $45 + \phi/2$ angle) up to 9 ft height, followed by a vertical surface. However, after placement of the steel girders, the distance of linear surface representing the locus of maximum strains increased with the abutment height up to a certain level before it decreased sharply (Figure 56b). The maximum distance of locus of maximum strains from the wall facing occurs at about two third the height of abutment.

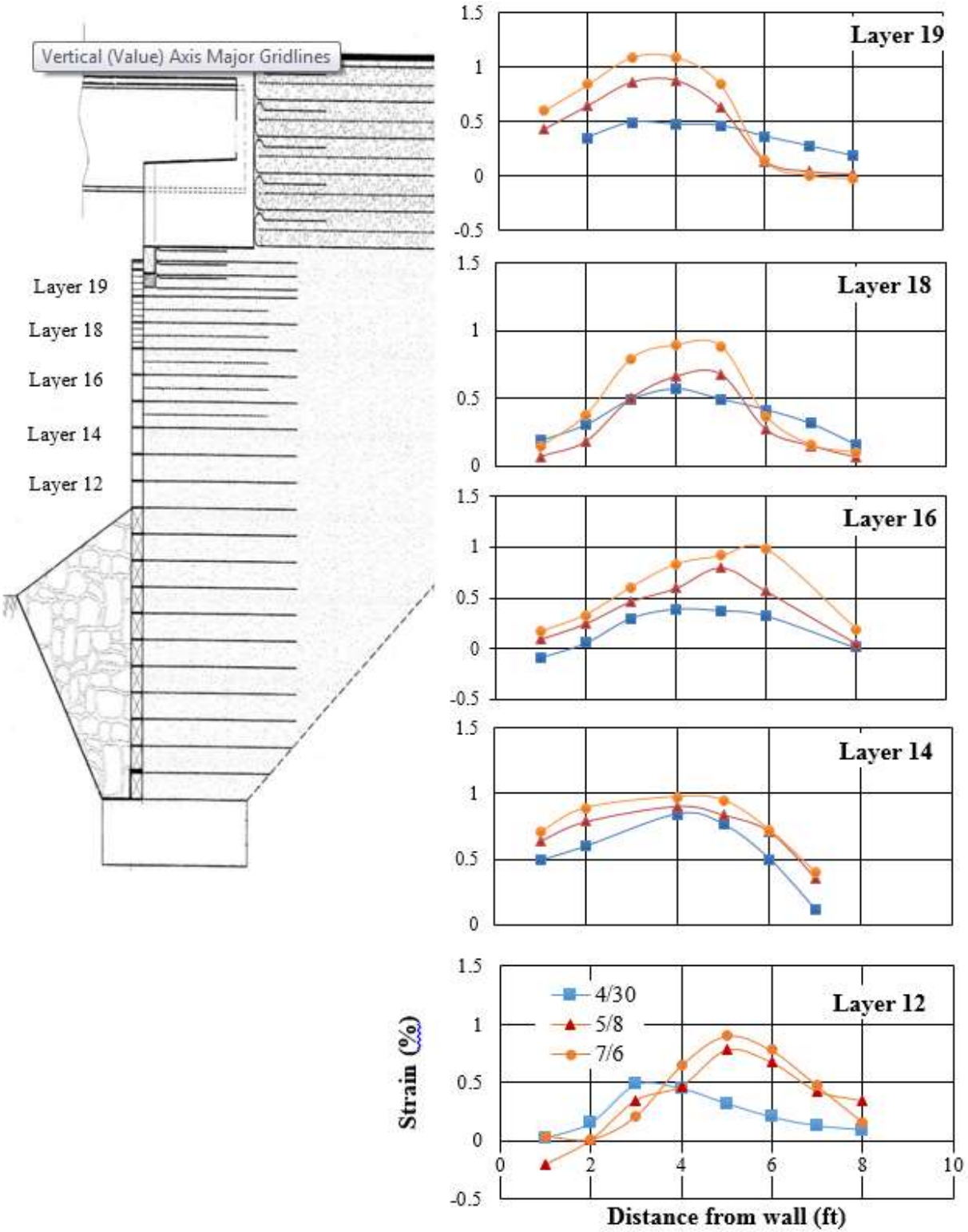
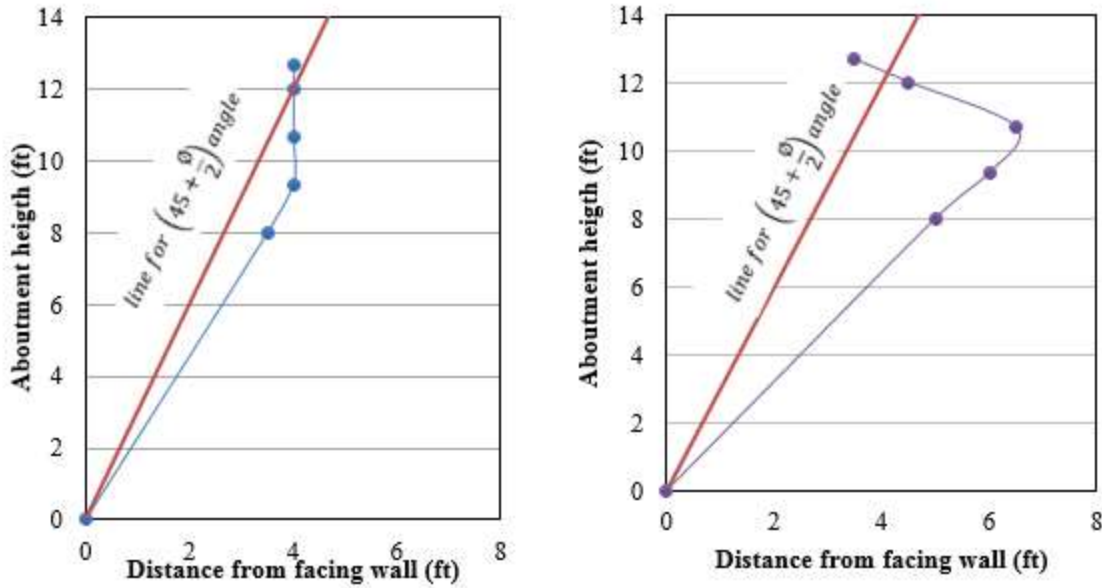


Figure 55
Measurement of strain distribution along geosynthetics



a) before placement of steel girders b) after placement of steel girders

Figure 56

Locations of maximum strain at various stages of construction

Estimation of Force against the Wall Face

Figure 57 presents the estimated thrust force on the wall face with time. These values were calculated from the vertical pressure cells that were attached against the inside face of the wall at layers 13, 17, and 20. The maximum measured force at the lower level (layer 13) of abutment was around 50 lb; while the maximum measured thrust forces in the upper layers of abutment (layers 17 and 20) were about half this value. The presence of secondary reinforcement layer within the upper five layers of the GRS mass (layers 16-20) reduced the reinforcement spacing and consequently the thrust force against the wall, in addition to lower overburden pressure. No significant change in thrust force was observed during the construction time, which can prove the FHWA assumptions. The FHWA assumes that when the reinforcement is capable of restraining lateral deformation of the soil immediately above and below it, the lateral earth pressure from the reinforced soil mass becomes independent of the wall height, surcharge or bridge loads. The validity of this assumption behavior is strongly dependent on the reinforcement spacing.

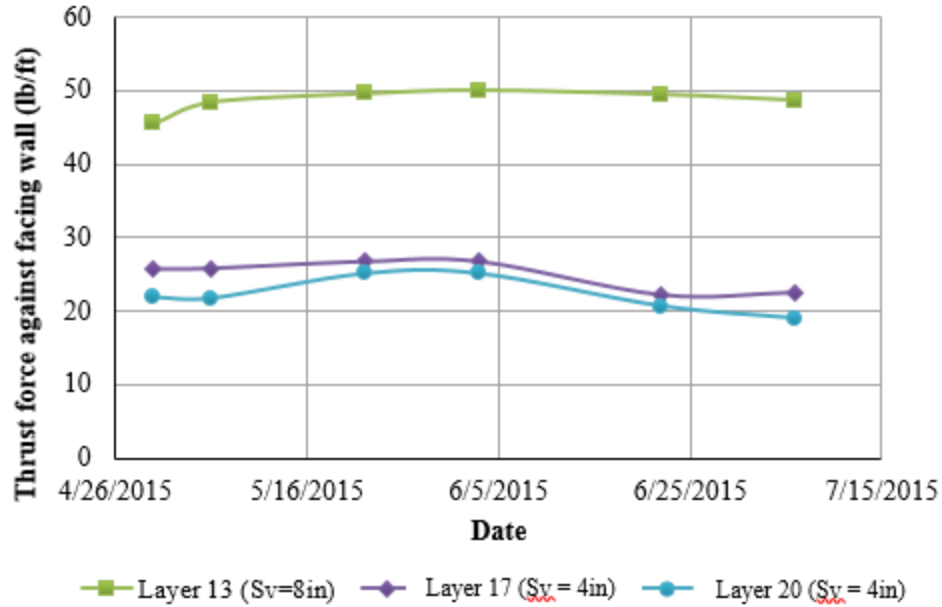


Figure 57
Measured thrust force at various stages of construction

Wu et al. suggested that the lateral pressure distribution between reinforcement layers is based on the bin pressure concept [4]. They developed an equation to calculate the thrust force that is only a function of reinforcement spacing and the strength parameter of fill material. This dependency is demonstrated in the following relationship:

$$F_{bin} = 0.72\gamma k_a s_v^2 \quad (16)$$

where, F_{bin} = thrust force against the wall face from bin theory, γ = unit weight of fill material, k_a = coefficient of active earth pressure, and s_v = vertical reinforcement spacing.

The comparison of the theoretical and measured thrust values are illustrated in Figure 58. The results indicate that the load predicted by the pressure theory were close to the measured thrust loads at layer 13 with 8 in. reinforcement spacing before placement of girder. However, the bin pressure theory under predicts the load at the layer 17 and 20 with reduced reinforcement spacing. The theoretical thrust values at the top layers with 4 in. reinforcement spacing are about half the thrust values measured using vertical pressure cells.

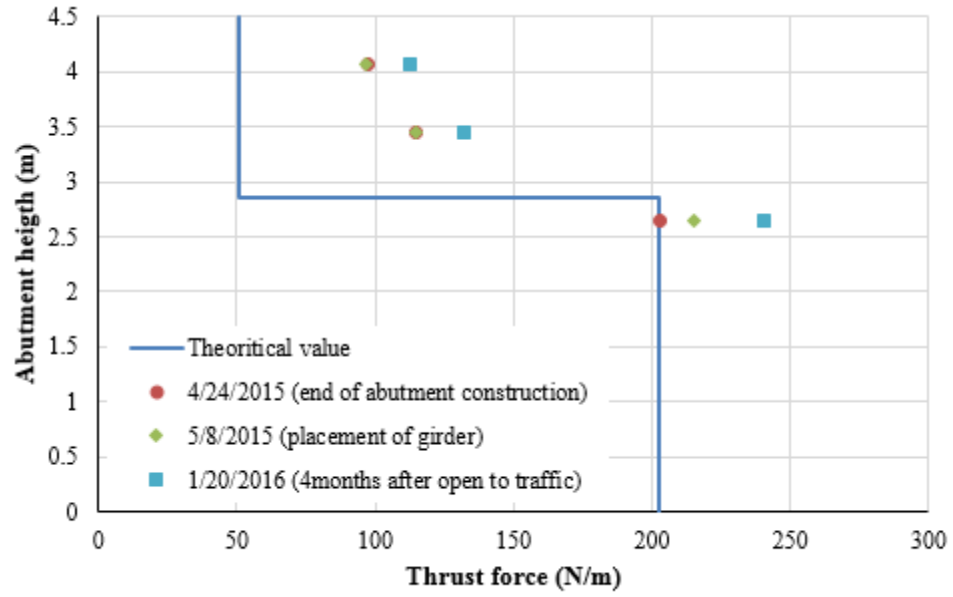


Figure 58
Measured and theoretical value of thrust force

FULL-SCALE STATIC LOAD TESTS

This section focused on the preliminary results of static load tests that were conducted on a geosynthetic reinforced integrated bridge system (GRS-IBS) in Louisiana. Sixteen loading cases, using two fully loaded trucks, were conducted on the instrumented GRS-IBS Bridge (Figure 59). The bridge was surcharge loaded to stress levels well in excess of working load conditions.



Figure 59
Static load test

Test Setup

The static load test was carried out in October 2015, about 4.5 months after the completion of bridge construction and before the bridge was opened to traffic. Sixteen static tests were conducted using heavy loaded trucks. The configurations of static distributed load tests are shown in Figure 60. Twelve tests (C1-C4; R1-R4; CC1-CC4) were performed using a 28.2-ton (56.5 kips) dump truck. In the rest of tests (D1-D4), in addition to dump truck, a 19-ton (38 kips) cone truck was added to increase the live load. Each test is labeled with a letter (C, R, CC, and D) and a number. The letters show the location of live load along traffic lanes. As illustrated in Figure 60, on C tests, dump truck was placed at the centerline of roadway, on tests CC, right wheels of dump truck were placed on the centerline of roadway. On tests R, dump truck was located on the middle of right lane. On tests D, dump truck was placed on the middle of left lane and cone truck placed on the middle of right lane.

In each series of load tests, the truck was located at four different locations along the bridge (Figure 61). At position 1, the center of tandem axle of truck was located on the approach slab and 1.5 ft. (0.46 m) behind beam seat. At position 2, the whole truck was placed on the bridge while tandem axle was 1ft away from end of the girder. At position 3 and 4, the truck was located at the one third and middle of bridge span. Each load test was maintained for a sufficient amount of time to allow the stress to be transferred to the entire bridge abutment. The time for placement of each static load test was decided based on the GRS displacements and stress measurements. In this study, measurements were started at least 20 minutes after placement of each static load test. The axle loads of the dump truck and cone truck used in tests are presented in Figure 62.

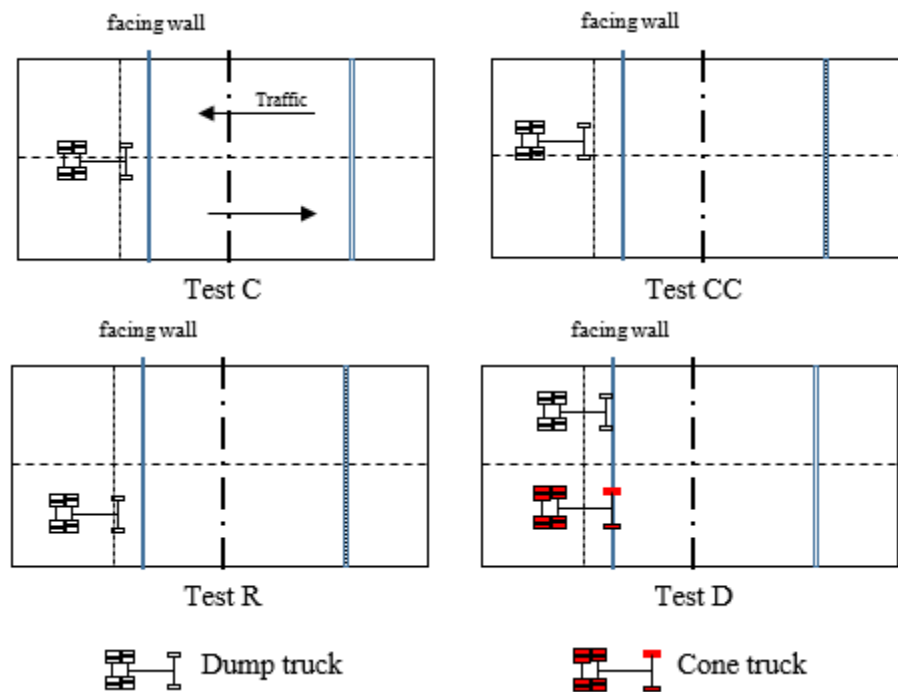


Figure 60
Location of trucks along roadway lanes

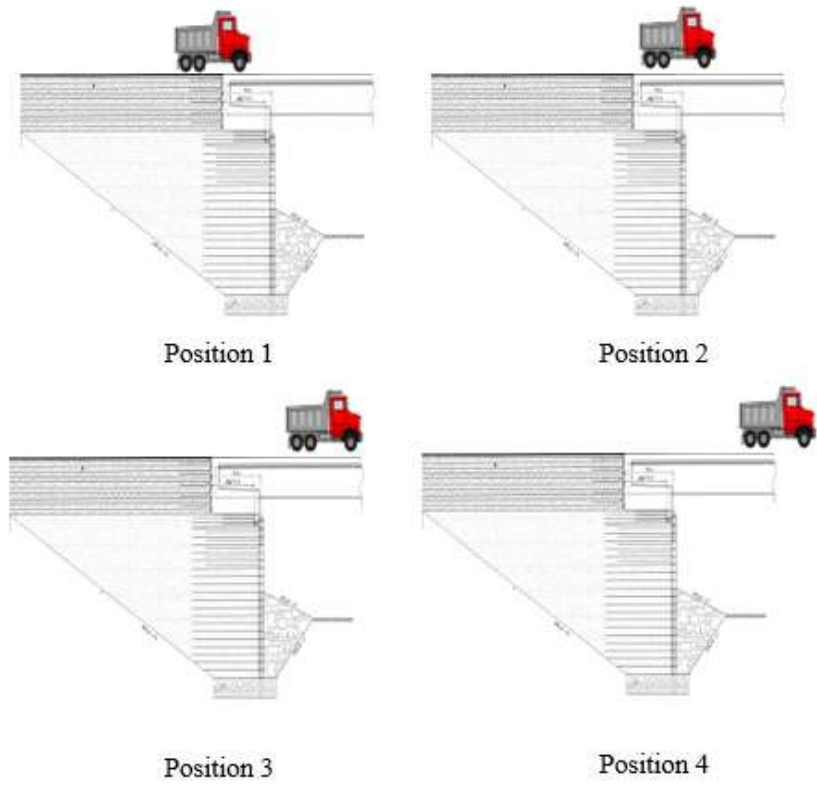


Figure 61
Location of trucks along bridge

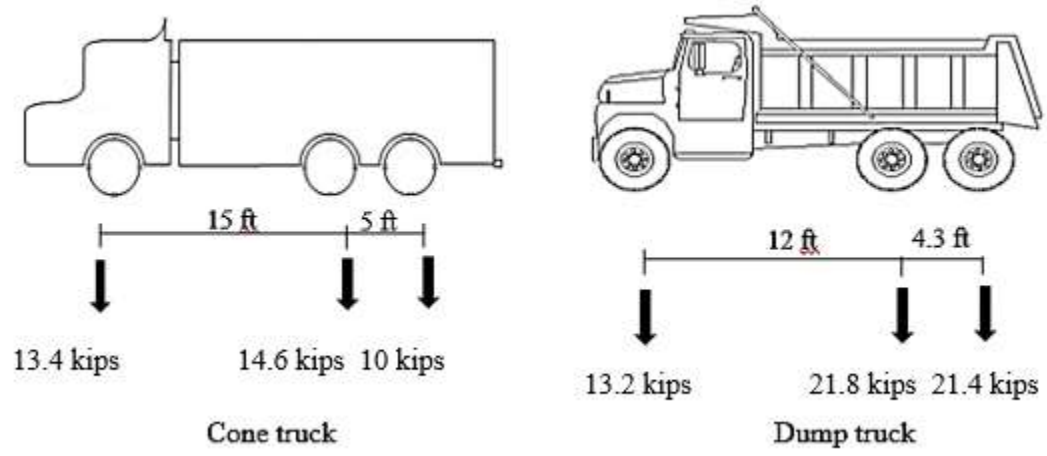


Figure 62
Axle loads of the dump truck and cone truck used in tests

Results of Field Static Load Tests

Settlement and Deformation Measurements

The bridge deformation was monitored under the static load tests. Figure 63 shows the vertical deformation profile on the top of GRS abutment due to only load test when trucks were positioned at planned locations. As expected, for similar load positions along the bridge, the vertical deformation was increased when the two trucks were placed on the bridge (D1-D4). The vertical deformation on the top of abutment was increased by moving the trucks from the approach pavement (position 1) to the bridge deck (position 2) and decreased when the truck moved the load toward the center of bridge span (position 3 and position 4). The lowest deformation observed when the truck was placed at the center of bridge span. Figure 64 shows the maximum total deformation of GRS abutment due to dead load and live load from static load tests. A maximum total deformation of 0.47 in. was observed when the two trucks were placed at position 2. However, more than 60% (0.3 in.) of deformation was due to the dead weight of bridge, less than 40% of total deformation occurred regarding to live load. After each test, trucks moved from bridge to measure the permanent deformation due to the live load. Measurements shows that plastic deformation was very small and negligible (less than 0.05 in.). Overall, the GRS abutment performed satisfactory during the load test in terms of settlement and deformation. The maximum vertical deformation of the abutment was significantly less than the design value of 0.8 in.

Figures 65 presents the lateral movements or deformations of the abutment at location of 2 ft. (0.6 m) behind the facing wall due to only truck loads. The positive value of deformation indicates movement toward the wall. This figure demonstrates that the maximum lateral movement occurred near the top of the wall. As seen in the figure, a maximum lateral deformation of 0.02 in. recorded at the top of the abutment when two trucks were placed on the bridge at location 2. Similar to vertical deformation, the critical load location in terms of lateral movement occurred when the truck is located at the beam seat and behind the facing wall. The measured lateral movement behind the GRS mass is very small and within the range of resolution limit of SAA sensors.

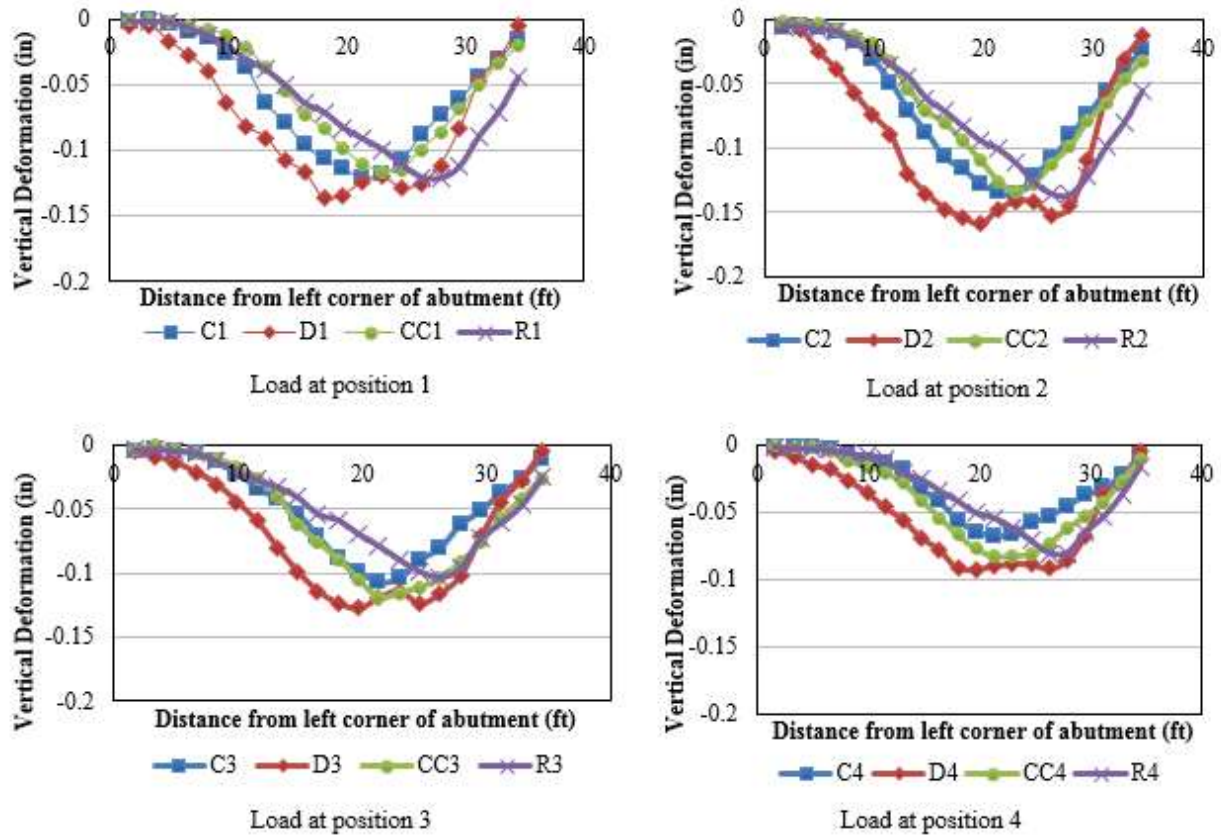


Figure 63
Vertical deformation of GRS abutment due to the trucks load

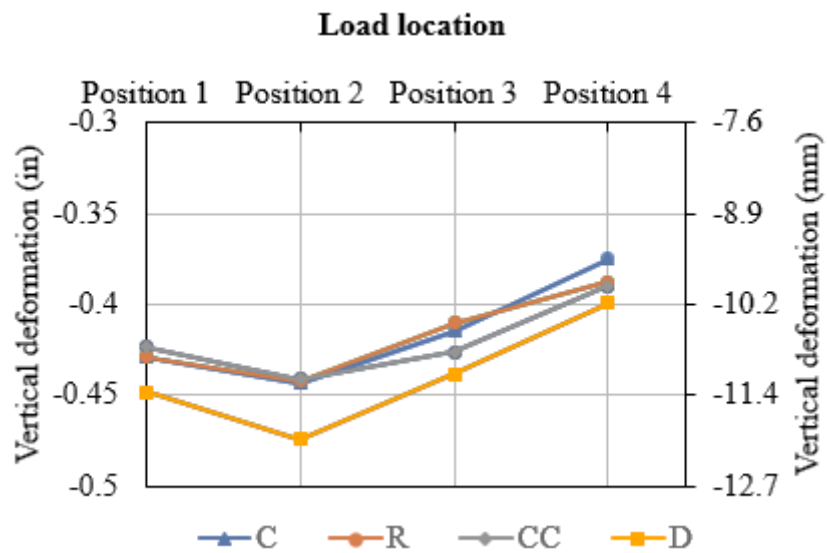


Figure 64
Maximum vertical deformation due to dead load and trucks load

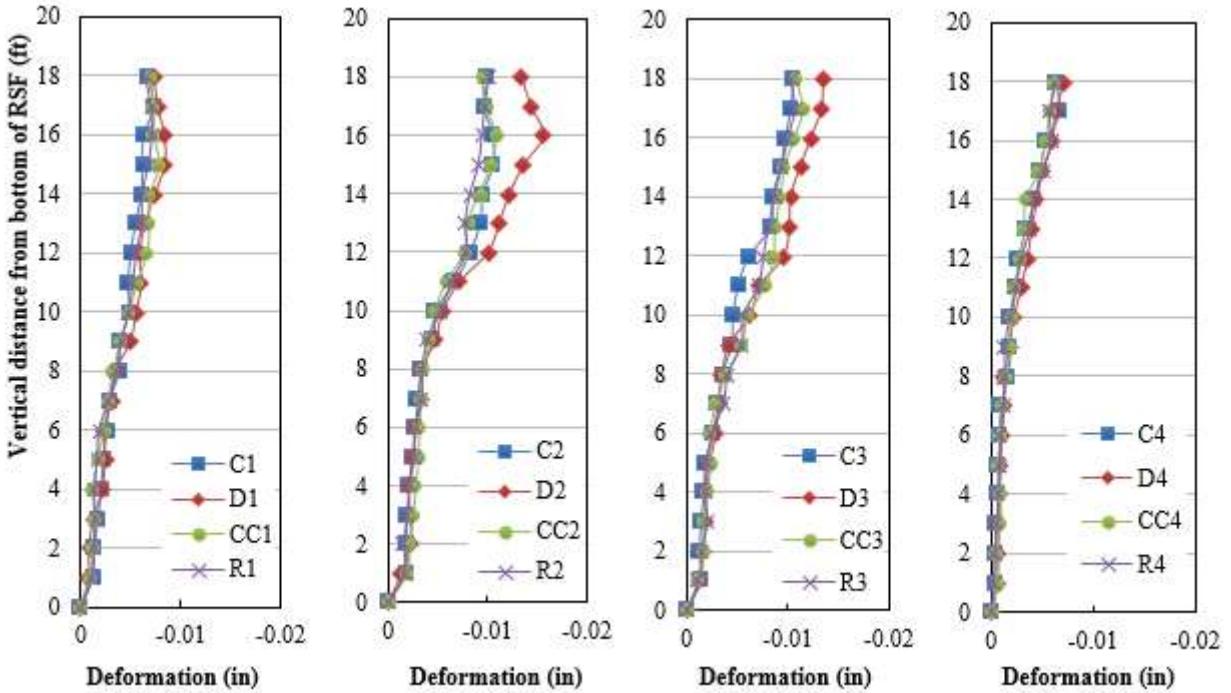


Figure 65
Profiles of lateral movements of the abutment behind the facing wall

The FHWA consider a zero volume change in the GRS mass to predict the lateral displacement of the abutment face wall [5]. By assuming the volume lost at the top of abutment due to vertical deformation is equal to the volume gained at the face due to lateral deformation, the following equation can be used to estimate the maximum lateral displacement (DL):

$$D_L = \frac{2b_{q,vol}D_v}{H} \tag{14}$$

where, $b_{q,vol}$ is the width of the load along the top of the wall including the setback, D_v is the vertical settlement in the GRS mass, and H is the wall height. Table 8 presents the comparison between the theoretical values and measurements of lateral displacement and strain due load tests as well as dead load of bridge. In general, the theoretical method is conservative and overpredicts the lateral movement of facing wall. The difference between measurement and theoretical values was more significant when the surcharge load was applied. Assuming a triangular lateral deformation and uniform vertical deformation, the maximum horizontal strain at the facing is restricted by 1.0%. However, the measured strains during load tests were significantly less than the FHWA criteria.

Table 8
Comparison between predicted and measured lateral deformation of facing wall

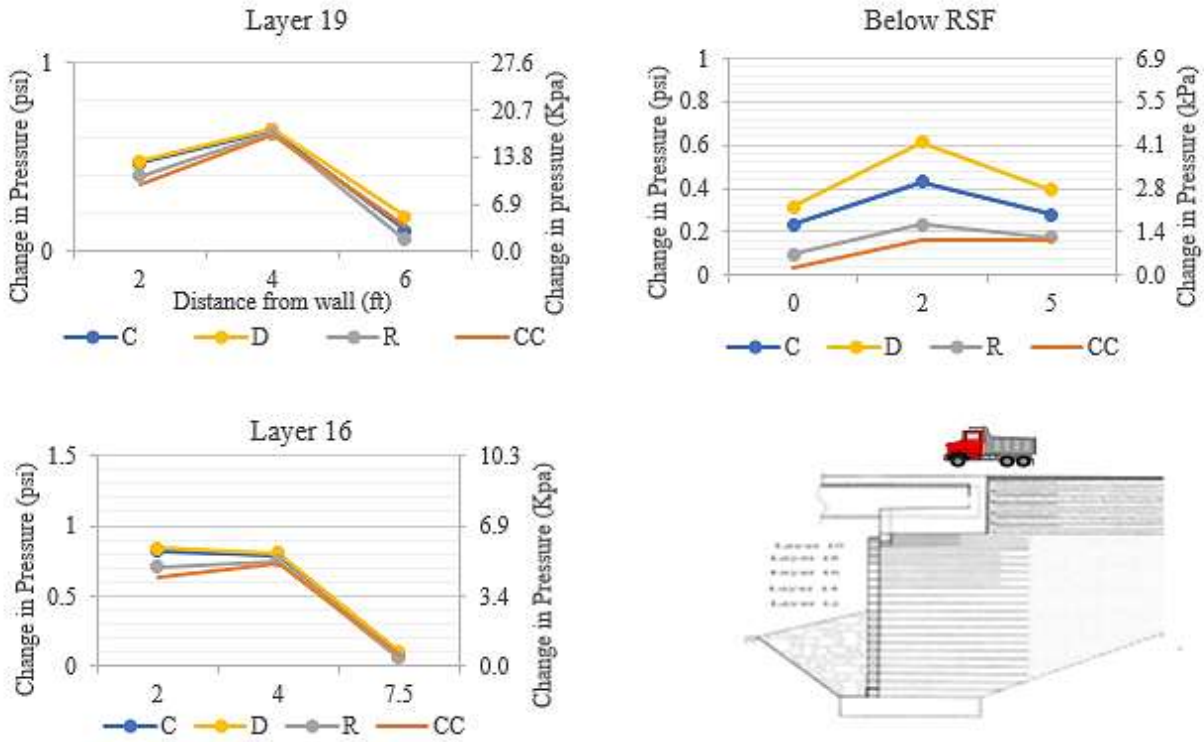
Date	Vertical settlement in abutment (in)	Maximum lateral displacement (in)		Maximum lateral strain	
		Measurement	Theory	Measurement	Theory
Dead load	0.307	0.157	0.270	0.21%	0.37%
C1	0.429	0.165	0.377	0.22%	0.51%
C2	0.443	0.168	0.390	0.23%	0.53%
C3	0.414	0.168	0.364	0.23%	0.49%
C4	0.375	0.164	0.329	0.22%	0.45%
D1	0.448	0.166	0.394	0.22%	0.53%
D2	0.474	0.173	0.417	0.23%	0.56%
D3	0.438	0.171	0.385	0.23%	0.52%
D4	0.399	0.165	0.351	0.22%	0.48%
CC1	0.423	0.165	0.372	0.22%	0.50%
CC2	0.442	0.168	0.388	0.23%	0.53%
CC3	0.426	0.169	0.375	0.23%	0.51%
CC4	0.390	0.164	0.343	0.22%	0.46%
R1	0.429	0.165	0.377	0.22%	0.51%
R2	0.442	0.168	0.389	0.23%	0.53%
R3	0.410	0.168	0.361	0.23%	0.49%
R4	0.388	0.164	0.341	0.22%	0.46%

Measurement of Soil Stresses

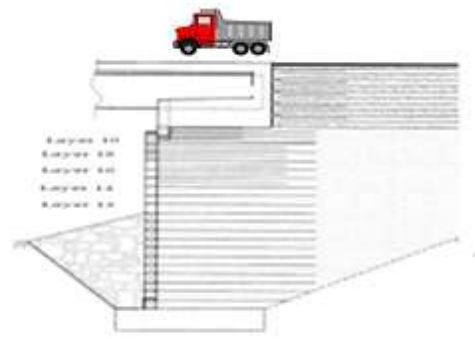
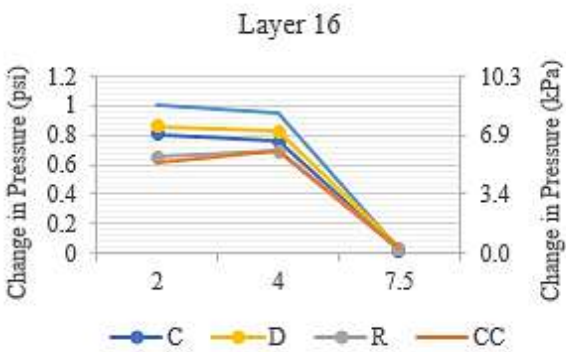
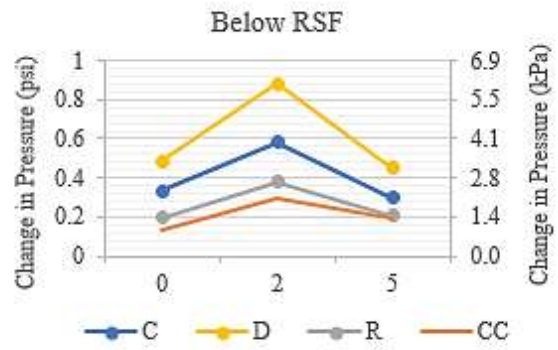
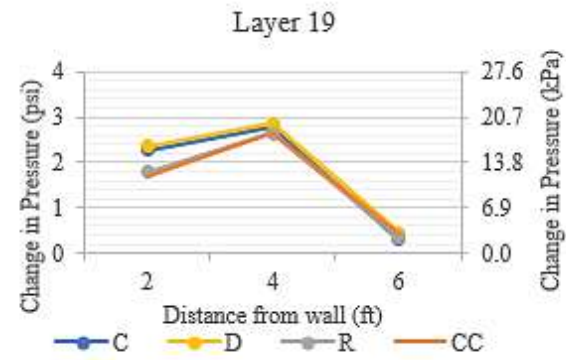
The distribution of vertical pressure within the GRS-IBS Bridge was measure by nine pressure cells installed in the bearing reinforcement zone. Figure 66 shows the increase of vertical pressure at different elevations due to static load tests for different truck positions. As expected, pressure increase more at higher levels of the bridge and was distributed on wider area at the lower levels. The maximum vertical pressure of 2.9 psi was measured at layer 19 of abutment due to double trucks placed at the beam seat (position 2). Figure 66 also shows that at the certain level, the vertical pressures from behind the wall up to 6 ft. behind wall are generally very close. However, the pressure cell located at 7.5 ft. away from wall on layer 16 shows significantly lower value than the pressure cell close to the wall. At load tests C1 to C4, the truck was placed on the centerline of bridge, where pressure cells were located. Therefore, at the top layers the vertical pressure due

to single truck (test C) is close to pressure measurements due to two trucks. However, at the bottom layer, higher pressure was measured when the two trucks were used.

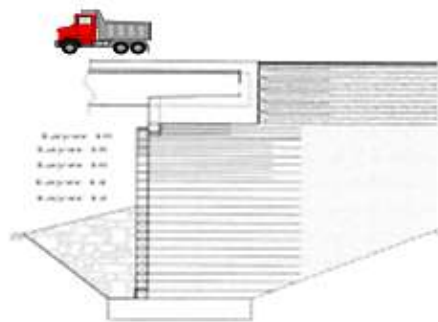
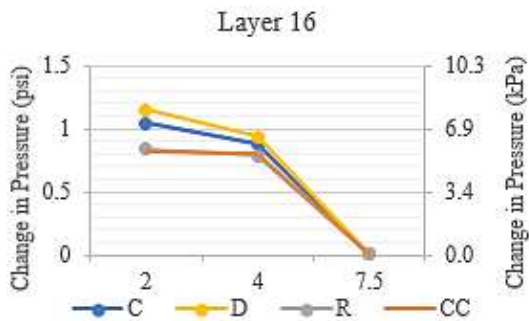
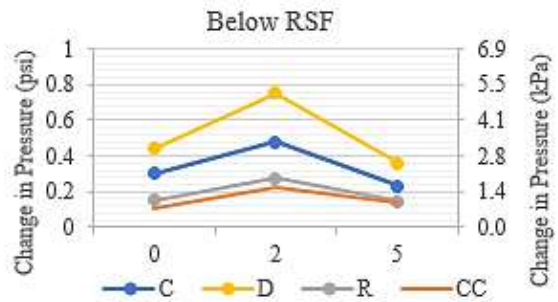
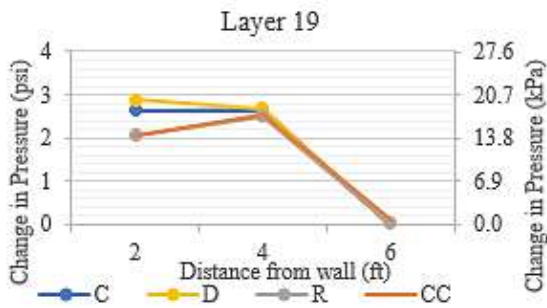
It should be noted here that the maximum total vertical stress at layer 19 (2.7 ft. below the strip footing) due to both dead load and static truck loads is about 7.5 psi (4.6 psi + 2.9 psi), or 1080 psf. Accordingly, it is expected that the maximum vertical stress below strip footing will be far less than the 4000 psf, as recommended by FHWA.



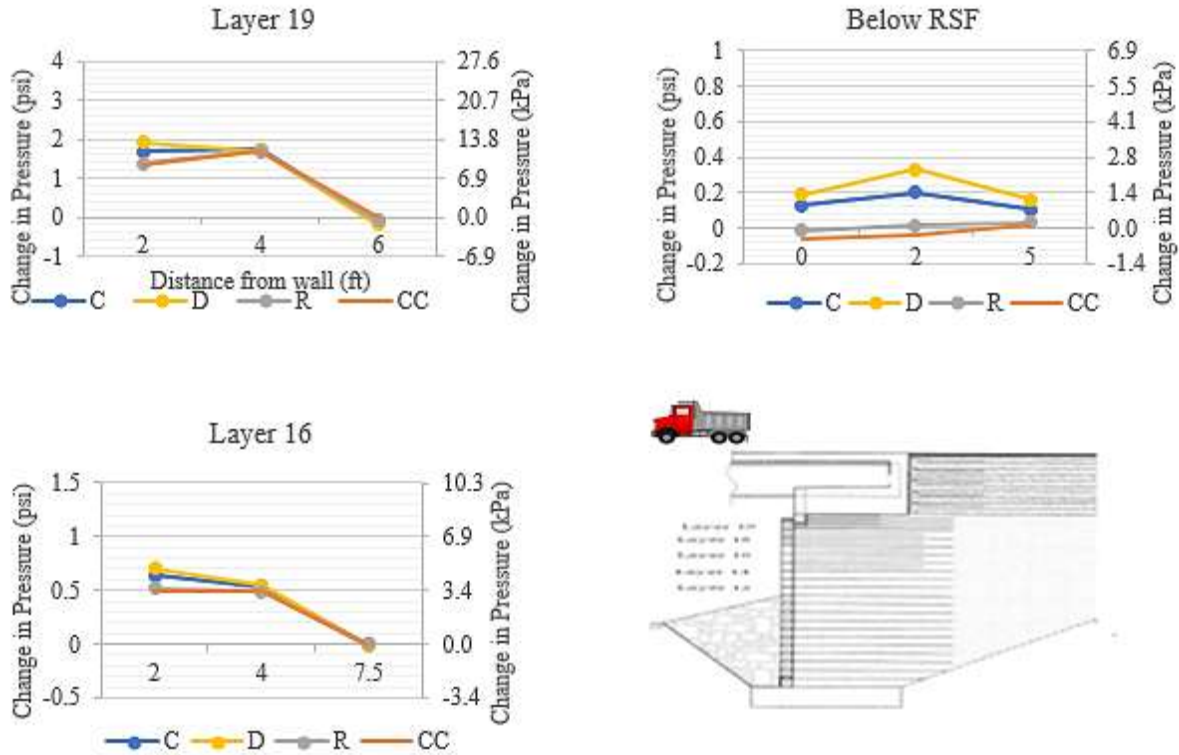
(a) Load placed at position 1



(b) Load placed at position 2



(c) Load placed at position 3



(d) Load placed at position 4

Figure 66
Vertical earth pressure measurements

The horizontal pressure on the wall was measured by pressure cells attached vertically behind the wall. Three pressure cells were installed behind the facing wall on layers 13, 17, and 20 of the GRS abutment. Table 9 shows the measurements of the total horizontal pressures due to dead load and load tests. The horizontal pressure on concrete slab was significantly higher than facing wall. The maximum horizontal pressure on wall was observed in the lower level (layer 13), which is about two times the measured horizontal pressures at upper layers. The higher value at layer 13 can be attributed to the reinforcement spacing. The addition of secondary reinforcement in the top 5 layers of abutment decreases the reinforcement spacing from 8 to 4 in. which results in less lateral pressure in upper layers. In all three layers, the pressure did not change significantly by applying live loads, which supports the FHWA assumption.

Table 9
Measurement of total lateral pressure on the facing wall

TEST ITEM	LAYER 13		LAYER 17		LAYER 20		APPROCH SLAB	
	psi	kPa	psi	kPa	psi	kPa	psi	kPa
DEAD LOAD	0.76							
		5.24	0.35	2.41	0.30	2.07	2.44	16.84
C1	0.90	6.23	0.51	3.50	0.73	5.00	14.20	97.90
C2	1.07	7.38	0.70	4.79	0.78	5.38	14.69	101.32
C3	1.05	7.22	0.68	4.69	0.78	5.37	14.01	96.62
C4	0.97	6.68	0.60	4.11	0.69	4.74	12.94	89.20
CC1	0.90	6.22	0.51	3.53	0.72	4.99	14.19	97.83
CC2	1.07	7.37	0.70	4.80	0.79	5.44	14.68	101.24
CC3	1.06	7.28	0.68	4.70	0.78	5.39	14.06	96.94
CC4	0.97	6.72	0.61	4.18	0.71	4.90	12.88	88.78
R1	0.90	6.19	0.51	3.49	0.70	4.82	13.97	96.31
R2	1.07	7.35	0.68	4.69	0.79	5.43	14.59	100.60
R3	1.06	7.28	0.70	4.80	0.77	5.29	13.96	96.27
R4	0.98	6.75	0.59	4.09	0.71	4.87	12.90	88.96
D1	0.92	6.33	0.52	3.57	0.70	4.83	14.13	97.45
D2	1.08	7.47	0.71	4.91	0.80	5.53	14.95	103.09
D3	1.07	7.38	0.70	4.84	0.78	5.39	14.19	97.81
D4	0.99	6.81	0.64	4.43	0.71	4.92	13.03	89.86

Estimation of Force against the Wall Face

Wu et al. suggested that the lateral pressure distribution between reinforcement layers is based on the bin pressure concept [4]. They developed an equation to calculate the thrust force that is only a function of reinforcement spacing and the strength parameter of fill material. This dependency is demonstrated in the following relationship:

$$F_{bin} = 0.72\gamma k_a S_v^2 \quad (17)$$

where, F_{bin} = the thrust force against the wall face from bin theory, γ = Unit weight of fill material, k_a =Coefficient of active earth pressure, and S_v =Reinforcement spacing.

The comparison of the theoretical and measured thrust values are shown in Table 10. The measured values were calculated from the vertical pressure cells that were attached against the inside face of the wall at layers 13, 17, and 20. The maximum measured thrust force at the lower level (layer 13) of abutment was between 4.5-4.74 lb/ft; while the maximum measured thrust forces in the upper layers of abutment (layers 17 and 20) were about half this value. The presence of secondary reinforcement layer within the upper five layers of the GRS mass (layers 16-20)

reduced the reinforcement spacing and consequently the thrust force against the wall, in addition to lower overburden pressure. No significant change in thrust force was observed due to the application of surcharge load, which can verify the FHWA assumptions.

Table 10
Measured and theoretical value of thrust force (l b/ft)

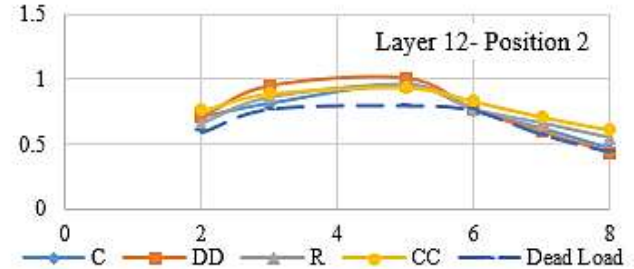
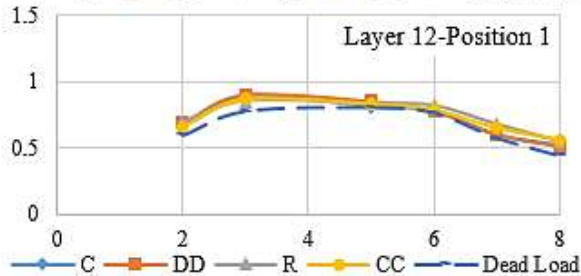
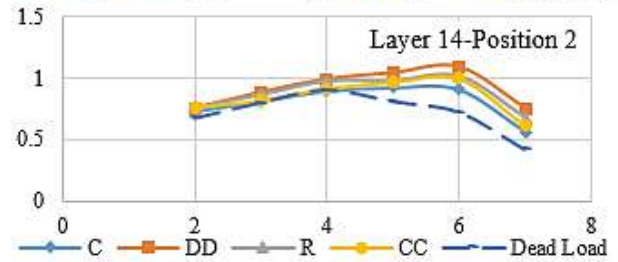
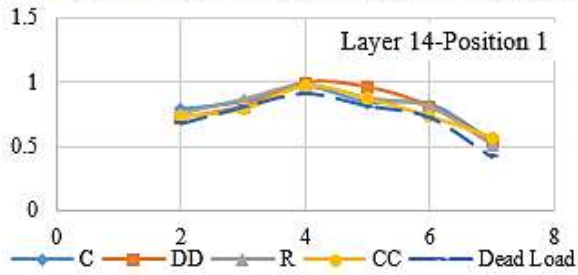
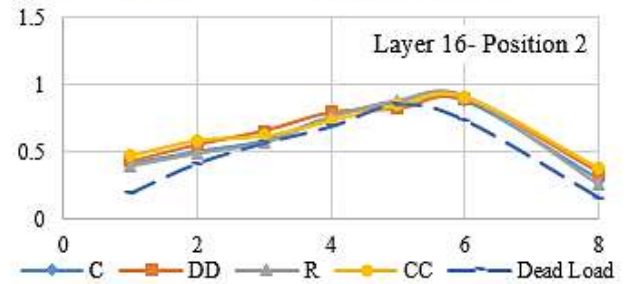
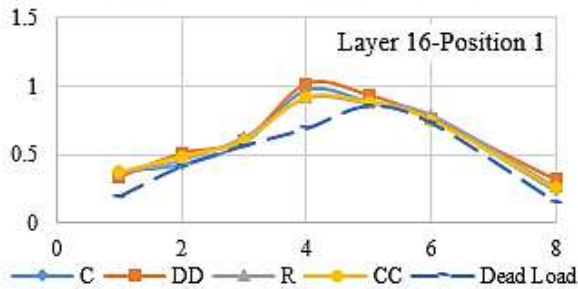
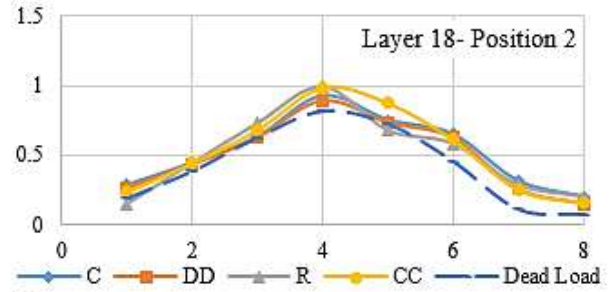
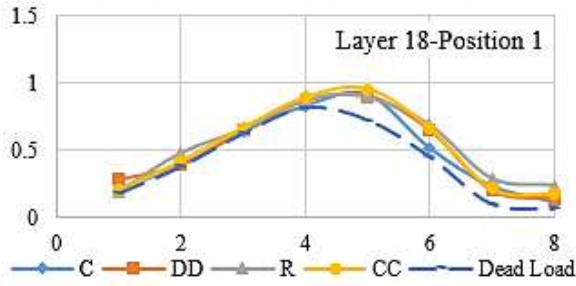
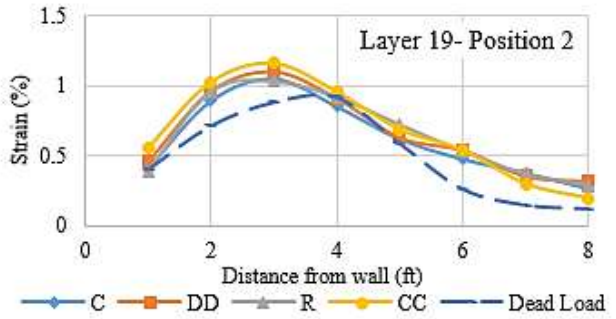
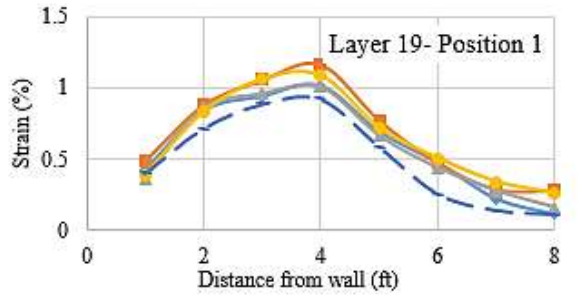
Test Item	Layer 13 ($S_v=8$ in)	Layer 17 ($S_v=4$ in)	Layer 20 ($S_v=4$ in)
Dead load	4.50	2.47	2.21
C1	4.51	2.47	2.32
C2	4.65	2.48	2.33
C3	4.64	2.48	2.33
C4	4.57	2.48	2.34
CC1	4.52	2.48	2.38
CC2	4.67	2.48	2.41
CC3	4.70	2.48	2.36
CC4	4.60	2.48	2.36
R1	4.57	2.49	2.40
R2	4.70	2.48	2.41
R3	4.70	2.48	2.40
R4	4.63	2.49	2.40
D1	4.57	2.48	2.27
D2	4.71	2.49	2.42
D3	4.74	2.49	2.41
D4	4.61	2.48	2.36
Theoretical value	5.32	1.34	1.34

The comparison between measured and predicted trust force for dead load only and different truck load conditions indicates that the load predicted by the pressure theory over predicts thrust loads at layer 13 with 8 in. reinforcement spacing. However, the bin pressure theory under predicts the load at the layer 17 and 20 with reduced reinforcement spacing. The FHWA assumes that when the reinforcement is capable of restraining lateral deformation of the soil immediately above and below it, the lateral earth pressure from the reinforced soil mass becomes independent of the wall height, surcharge or bridge loads. The validity of this assumption behavior is strongly dependent on the reinforcement spacing. The measurements showed that, increase in thrust force due to surcharge load was less than 10%, which is in agreement with the FHWA assumption.

Strain Measurements along Geosynthetics

Strain gauges were installed onto the geosynthetic reinforcements to measure the developed strains along the geosynthetics. A total of 55 strain gauges were installed on five different geotextile layers. Forty out of the 55 strain gauges were installed along the centerline of the abutment and the remaining 15 strain gauges were installed at 1-ft. offset from the centerline for redundancy. The locations of strain gauges were arranged in a fashion such that strain gauge measurements would be able to capture the strain distributions. All strain gauges were installed on geotextile layers at laboratory based on the method described by Brandon et al. [80]. The extensive instrumentation of geosynthetics provides the opportunity to quantify the mobilized tensile reinforcement forces and the distribution of the tensile strain along geosynthetics, which can help to identify the critical load bearing zone for internal stability.

The strain measurements of abutment reinforcements are shown in Figure 67. The figure presents the total strain distribution along the reinforcements at different layers and the locus of maximum strains in the abutment. In all tests, strain on reinforcement layers was less than FHWA criteria of 2%. The critical failure surface is assumed to be the surface connecting the locus of maximum strains in each reinforcement layer. The location of maximum strains with depth are plotted in Figure 68. The figure shows that when the surcharge load was placed on the approach slab (position 1) the maximum strains formed a bilinear surface with an angle slightly lower than the theoretical K_a failure surface (line of $45 + \Phi/2$ angle). When the load was placed on the bridge (position 2-4), the distance of linear surface representing the locus of maximum strains increased with the abutment height. The maximum distance of locus of maximum strains from the wall facing occurs at about two third of the abutment height.



a) Load placed at position 1

b) Load placed at position 2

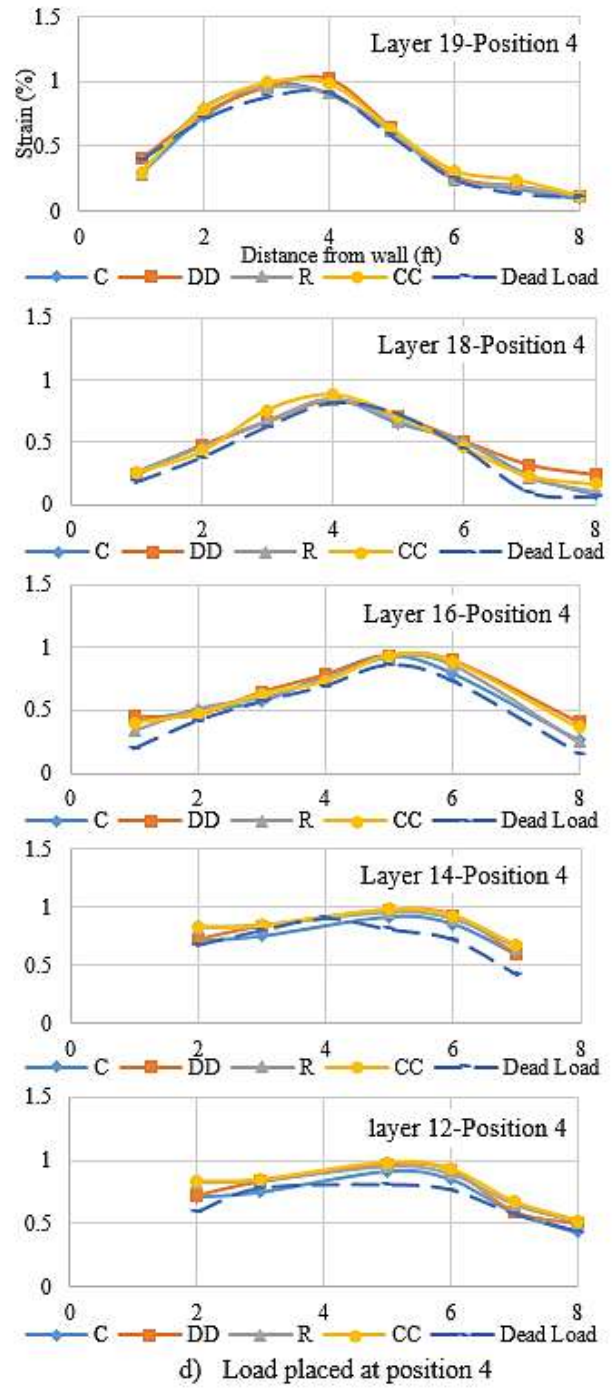
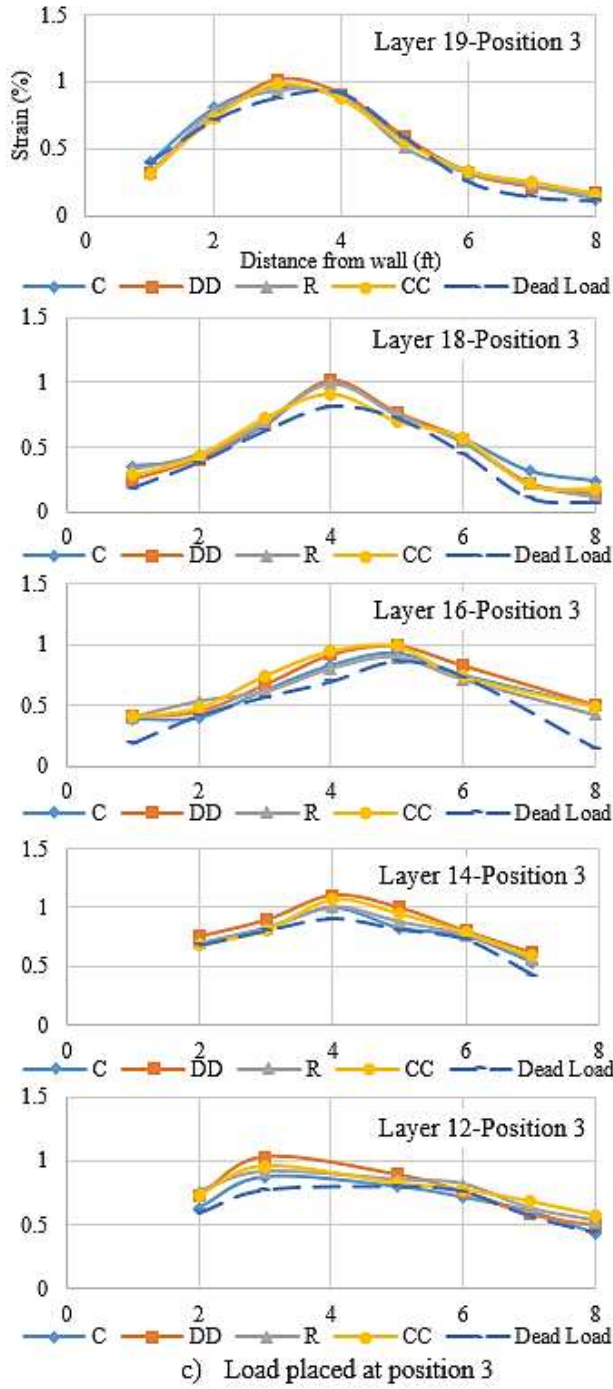


Figure 67
Strain distribution under static load test

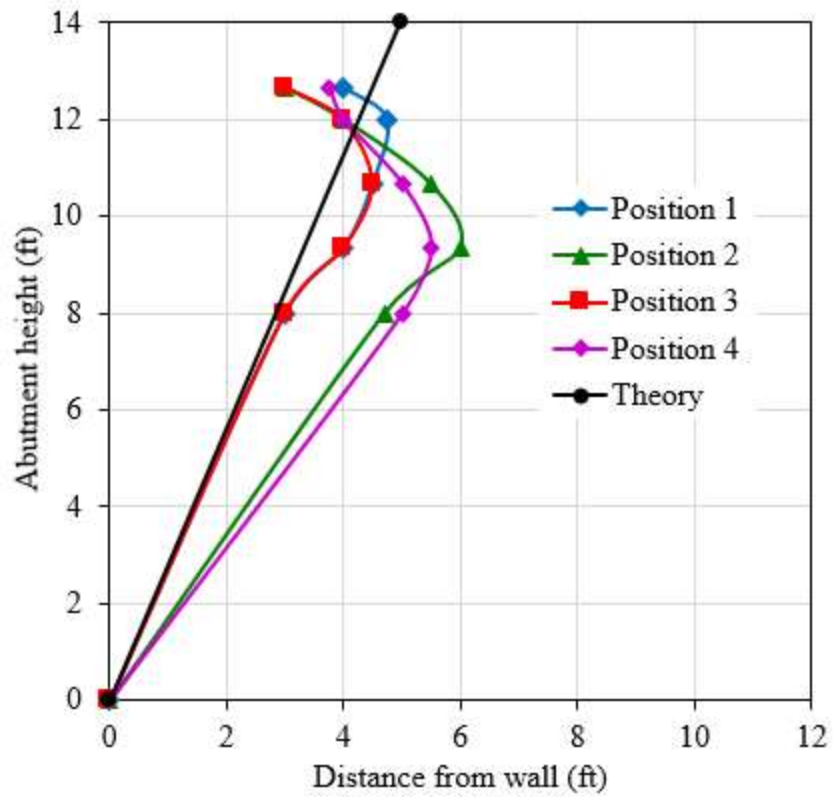


Figure 68
Locations of maximum strain at various load tests

FINITE ELEMENT ANALYSIS OF GRS-IBS AT MAREE MICHEL BRIDGE

Introduction

Plane strain FE analysis was developed and verified using the results from the field monitoring of the fully instrumented GRS-IBS bridge abutment at Maree Michel Bridge in Louisiana. The PLAXIS 2D 2016 was selected for the numerical analysis of this study. In the FE model, the soil and the facing block were represented by a plane strain fourth-order 15-noded triangle elements to describe the stress-deformation behavior. The geotextile was represented by a special tension 5-noded elements (Note that the geotextile elements are automatically taken to be compatible with the soil element type) to describe the axial forces. The interface between the backfill soil and geosynthetic was simulated using joints elements to model the soil-structure interface behavior, which is represented by 5-pair joint element (also compatible with the soil element) to simulate the thin zone of intensely shearing at the contact between the geotextile and the surrounding soil.

PLAXIS 2D 2016 also offers a linear elastic model with Mohr–Coulomb failure criterion option to simulate the mechanical behavior of the interface between dissimilar materials by using a reduction factor ($R_i \leq 1.0$) applied to the soil material when defining soil property values ($R_i = 1.0$, for a fully-bonded interface). Hence, the interface property values are directly related to the mechanical properties of the soil forming the interface (e.g. $C_i = R_i * C_{soil}$). These interfaces have properties of friction angle, cohesion, dilation angle, tensile strength, Young's modulus (E), and Poisson's ratio (ν).

Figure 69 presents the FE mesh for the GRS-IBS of Maree Michel Bridge abutment (252932 nodes and 30229 elements). Mesh sensitivity was first carried out to select the proper size of FE mesh that is not affecting the FE results. A fixed boundary condition was applied at the bottom of the FE model. Roller boundary conditions was used on both sides of the FE model.

The total height of the GRS-IBS wall is 12.5 ft. from the top of the RSF was divided into twenty layers to simulate the field construction process by using the staged construction mode in PLAXIS 2D 2016, which allows for simulation of construction and excavation processes. A 9-psi distribution load at the top and bottom of each soil layer was applied during the staged construction process to simulate the soil compaction. This approach is based on the procedure introduced by Dantas and Morrison et al. to consider the induced stress on the backfill soil due to compaction, which was also adopted later by Ehrlich and Mirmoradi, Mirmoradi and Ehrlich and Riccio et al. [81-85].

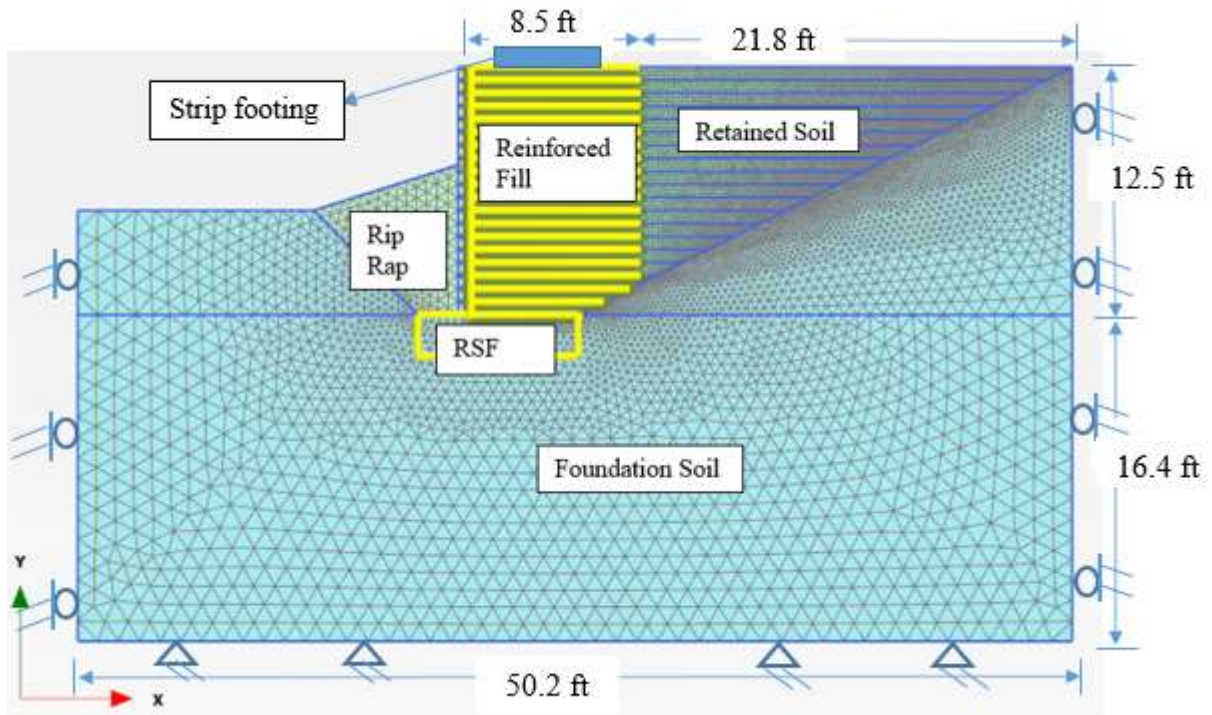


Figure 69

FE Mesh of the GRS-IBS and locations of the applied boundary conditions

Two-Dimensional Finite Element (2D-FE) Analysis

2D-FE Numerical Model

Plane strain FE analysis was developed and verified using the results from the field monitoring of the fully-instrumented GRS-IBS bridge abutment at Maree Michel Bridge, in Louisiana. The PLAXIS 2D 2016 was selected for the numerical analysis of this study. In the FE model, the soil and the facing block were represented by a plane strain fourth-order, 15-noded triangle elements to describe the stress-deformation behavior. The geotextile was represented by a special tension 5-noded elements to describe the axial forces (Note that the geotextile elements are automatically taken to be compatible with the soil element type). The interface between the backfill soil and geosynthetic was simulated using joints elements to model the soil-structure interface behavior, which is represented by 5-pair joint element (also compatible with the soil element) to simulate the thin zone of intensely shearing at the contact between the geotextile and the surrounding soil.

PLAXIS 2D 2016 offers a range of constitutive models including the second order hyperbolic elastoplastic hardening soil model that was selected to simulate the behavior of granular backfill materials in this study [1]. The hardening model implies friction hardening to model the plastic

shear strain in deviatoric loading and cap hardening to model the plastic volumetric strain in primary compression. The model is also capable of simulating the soil dilation, non-linear stress-strain behavior of the backfill soil, stress dependency, and unloading-reloading behavior. The formulation and verification of the Hardening Soil Model (HSM) was explained by Schanz et al. and Brinkgreve in details [1, 86]

PLAXIS 2D 2016 also offers a linear elastic model with the Mohr–Coulomb failure criterion option to simulate the mechanical behavior of the interface between dissimilar materials by using a reduction factor ($R_i \leq 1.0$) applied to the soil material when defining soil property values ($R_i = 1.0$). This means that the interface should not have a reduced strength with respect to the strength of the surrounding soil). Hence, the interface property values are directly related to the mechanical properties of the soil forming the interface (e.g., $C_i = R_i * C_{soil}$). These interfaces have properties of friction angle, cohesion, dilation angle, tensile strength, Young’s modulus (E), and Poisson’s ratio (ν).

The backfill material was a crushed diabase open-graded aggregate soil with a maximum particle size of 3/4 in. Three triaxial tests were conducted to evaluate the stiffness of the backfill materials at confining pressures of 30 psi, 50 psi, and 70 psi. The soil specimen was 0.5 ft. in diameter and 1.0 ft. in height. Figure 70 presents the stress-strain curve for the backfill materials. Three large direct shear tests were conducted to evaluate the strength of the backfill materials at normal stresses of 7 psi, 17.4 psi, and 27.84 psi. The soil specimen was $1.0 \times 1.0 \times 0.5$ ft. The peak stress was found to be 12.11 psi, 20.88 psi, and 27.7 psi for the previous normal stresses, respectively. The dilation angle was estimated using Bolton [87]:

$$\phi_p = \phi_{cv} + 0.8\psi \quad (18)$$

where, ϕ_p = peak friction angle = 51° ; ϕ_{cv} = critical state friction angle = 34° ; and ψ = dilation angle.

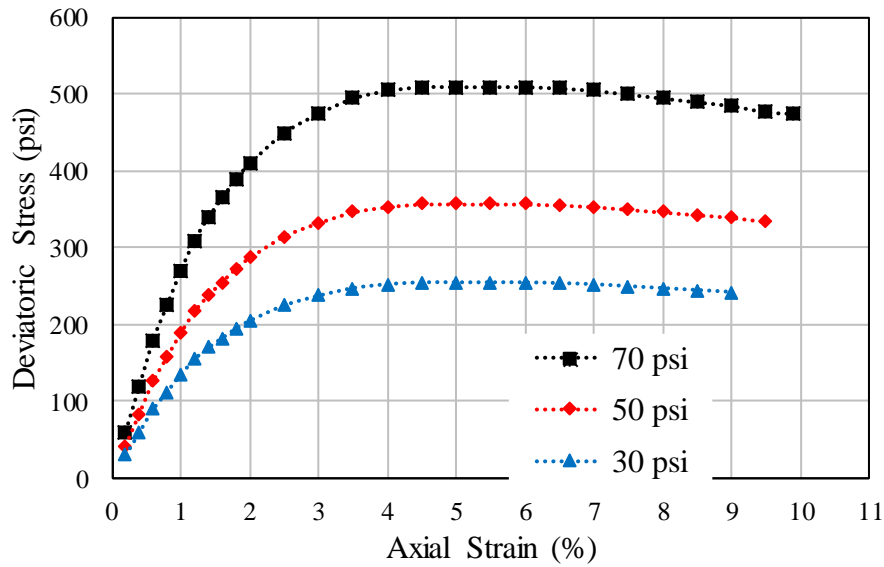


Figure 70
Stress-strain curves of backfill at 115 lb/ft³ dry density

A cone penetration test (CPT) was conducted to evaluate the foundation soil properties. The geotextile and facing block properties were provided from the manufacturer (note that the strain-rate in the field is less than the strain-rate described in the ASTM D 4595, which is 10% strain min⁻¹. However, the manufacturer does not provide the axial stiffness parameter, which is the only input parameter required to model the geotextile as elastic, instead the axial stiffness of geotextiles was calibrated from laboratory experiment test data). A summary of the parameters used in FE modeling is provided in Table 11.

The FE mesh for the GRS-IBS of the Maree Michel Bridge abutment (252932 nodes and 30229 elements). Mesh sensitivity was first carried out to select the proper size of FE mesh that is not affecting the FE results. A fixed boundary condition was applied at the bottom of the FE model. Roller boundary conditions were used on both sides of the FE model. The dimensions of the soil body are determined by finding the least dimension at which the deformation in the boundary elements is negligible.

Table 11
Material Properties

Category	Description
Facing Block	Linear elastic model; $E = 626.5 \times 10^6$ psf; $\gamma = 80$ lb/ft ³ ; dimensions, 16×8×8 in; Poisson's ratio, $\nu = 0$
Geotextile	linear elastic perfectly plastic model; Tensile strength @ 2% = 75×100 lb/in, Tensile strength @ 5% = 200×230 lb/in; $T_{ult} = 456$ lb/in; reinforcement spacing = 8 in; Axial stiffness, EA= 41 k/ft.
Backfill Material	Hardening soil model; dry unit weight, $\gamma_d = 114.6$ lb/ft ³ ; wet unit weight, $\gamma_t = 121$ lb/ft ³ ; cohesion, $c = 418$ psf; friction angle, $\phi = 51^\circ$; dilation angle $\Psi = 21^\circ$; $E_{50}^{ref} = 710 \times 10^3$ psf, $E_{ur}^{ref} = 2015.5 \times 10^4$ psf, $E_{oed}^{ref} = 551 \times 10^3$ psf, $\nu = 0.2$; power, $m = 0.5$
Foundation Soil	Soil model, Mohr-Coulomb model; dry unit weight, $\gamma_d = 97$ lb/ft ³ ; wet unit weight, $\gamma_w = 119$ lb/ft ³ ; cohesion, $c = 370$ psf; $\phi = 27^\circ$; $E = 626.5 \times 10^3$ psf; $\nu = 0.2$.
Interface (backfill and geotextile)	linear elastic with Mohr-Coulomb failure criterion; adhesion, $c = 180$ psf; interface friction angle $\delta = 40.4^\circ$
Interface (block and geotextile)	linear elastic with Mohr-Coulomb failure criterion; cohesion, $c = 146$ psf; friction angle $\phi = 34^\circ$
Girder	Linear elastic model; $E = 2900$ ksi; $\gamma = 75.5$ lb/ft ³ ; $\nu = 0.2$

The total height of the GRS-IBS wall is 12.5 ft. from the top of the RSF and was divided into 20 layers to simulate the field construction process by using the staged construction mode in PLAXIS 2D 2016, which allows for simulation of construction and excavation processes. A 9-psi distribution load at the top and bottom and exposed faces of each soil layer was applied during the staged construction process to simulate the soil compaction. This approach is based on the procedure introduced by Dantas and Morrison et al. to consider the induced stress on the backfill soil due to compaction, which was also adopted later by Ehrlich and Mirmoradi, Mirmoradi and Ehrlich, and Riccio et al. [81 - 85].

Results and Discussion

Four different loading cases were considered in this study: (a) end of bridge construction, which is equal to the total dead loads on the abutment (case 1 = 14.5 psi); (b) truck loading, which is equal to the total dead loads and the load of a dump truck (case 2 = 18.85 psi); (c) service loading, which is equal to the total dead loads and the bridge live loads (case 3 = 25.7 psi); and (d) abnormal loading, which is equal to the total dead loads and three times the service loading (case 4 = 48 psi).

Note that abnormal loading is totally hypothetical loading assuming a linear elastic behavior for the reinforcement under these loading. The equivalent roadway live load was considered 1.74 psi and the equivalent roadway dead load was 2.61 psi. The field measurements during monitoring of the GRS-IBS at the Maree Michel bridge were used to verify the FE model, and then the verified FE model was used to generate the vertical and lateral deformations, horizontal and vertical earth pressures, the axial force and strain in the reinforcement, and the interface shear strength between the reinforcement and backfill materials due to the four loading cases.

Vertical and Lateral Deformations

According to FHWA, the vertical strain deformation should be less than 0.5% of the abutment height [5]. The maximum lateral deformation at the face can be calculated using the assumption of the composite behavior of properly constructed GRS-IBS mass such that the reinforcement and soil strain extend laterally together [5]. With that being said and assuming a zero-volume change in the GRS-IBS abutment due to vertical loading, the lateral strain according to FHWA is two times the vertical strain and should be less than 1% of the abutment height [5].

Figure 71 presents the comparison profiles of the lateral deformations at the face of the GRS-IBS wall determined from FE analysis at the end of abutment construction and the end of bridge construction and field measurements. It can be seen that there is a good agreement between the field measurements and FE numerical results. The maximum lateral deformation was found to be 0.02 in. and 0.1 in. for the end of abutment construction and at the end of bridge construction, respectively. It is interesting to notice that these results are much lower than the FHWA recommendations (less than 1%, 0.8 in. for the width of the load along the top of the wall including the setback, which is equal to 6.82 ft.) [5].

Figure 72 presents the comparison profiles of the settlement distribution under the RSF predicted by FE analysis at the end of abutment construction and the end of bridge construction and field measurements. The maximum footing settlements due to service load and abnormal load are 0.4 in. (0.3%) and 0.9 in. (0.6%), respectively, which is acceptable for both the service load and the abnormal load according to FHWA recommendation. The reason that the field measurements are lower than those predicted by the FE analysis are most probably due to the over consolidated soil caused by the old bridge [5].

Figure 73 presents the lateral deformation profile of the GRS-IBS wall face, which shows that the maximum lateral deformations are 0.02, 0.08, 0.25, 0.36, and 0.5 in. at the end of abutment construction, the end of bridge construction, the truck loading, the service loading, and abnormal loading, respectively.

Horizontal and Vertical Stresses

Figure 74 presents the profile comparison of the lateral stress at the face of the GRS-IBS abutment wall predicted by the FE analysis and the field measurements at the end of bridge construction. The figure also presents the lateral stresses predicted by FE analysis for the truck loading, service loading, and abnormal loading. It can be noted that the lateral earth pressure at the face of the GRS-IBS wall is somehow uniform with depth and much less than the lateral earth pressure estimated by Rankine method as in the case of MSE walls, which is in agreement with the composite behavior of closely reinforced soil as demonstrated by Adams et al. [88]. The maximum lateral earth pressure was found to be 0.725 psi, 1.16 psi, 1.45 psi, and 1.74 psi, for Case 1, Case 2, Case 3, and Case 4, respectively. The composite behavior of the GRS-IBS wall plays an important role in reducing the lateral earth pressure at the face as shown in Figure 74. The presence of closely reinforcement in a soil mass has proved to reduce the lateral stresses when subjected to vertical loading because the reinforcement is capable of restraining the lateral deformation of the soil around it [42].

For instance, the active lateral earth pressure at the facing would be 2.17 psi for backfill material having internal friction angle 51° (using the MSE design criteria where the internal friction angle is capped at 40°) and 12.6 psi after adding 48 psi to the GRS-IBS abutment using Rankine method without reinforcement, which is used for MSE wall design criteria. For the purpose of comparison, the theoretical active earth pressure using Rankine method for Case 1 loading is also presented in Figure 74 to give the reader an indication of the major differences between the internally (GRS-IBS) and externally (MSE) supported structure.

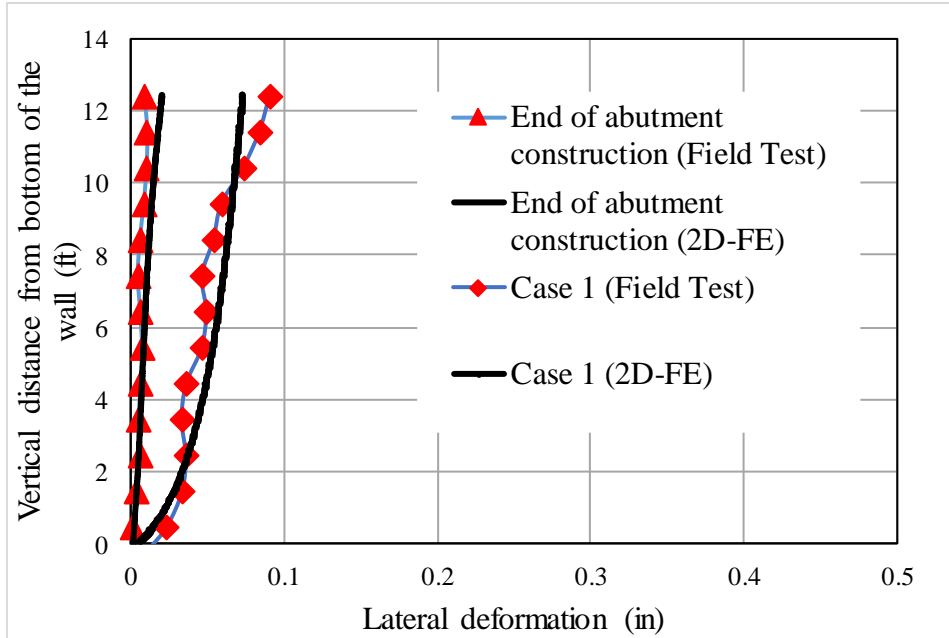


Figure 71

Comparison between measured and predicted lateral deformation profiles along the wall face

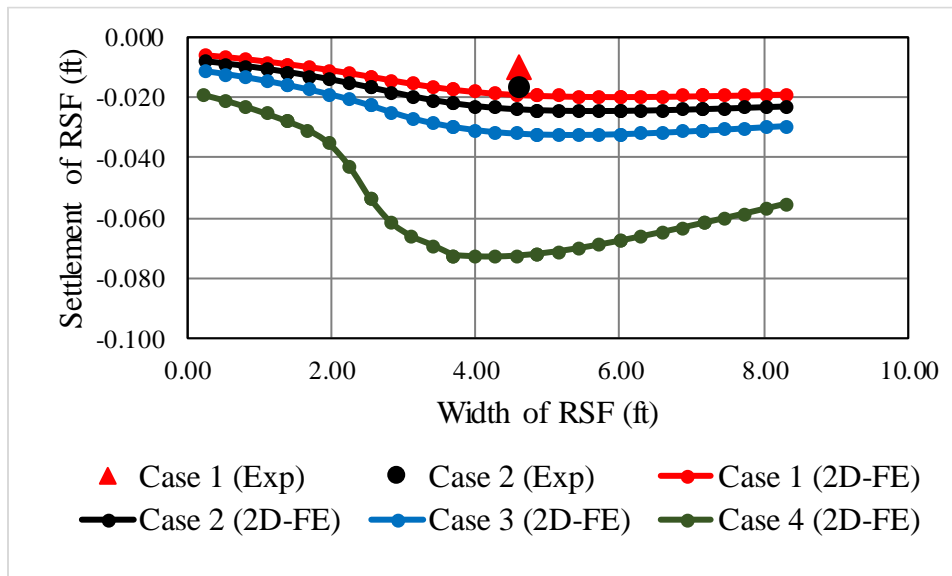


Figure 72

Comparison between measured and predicted RSF settlement distribution

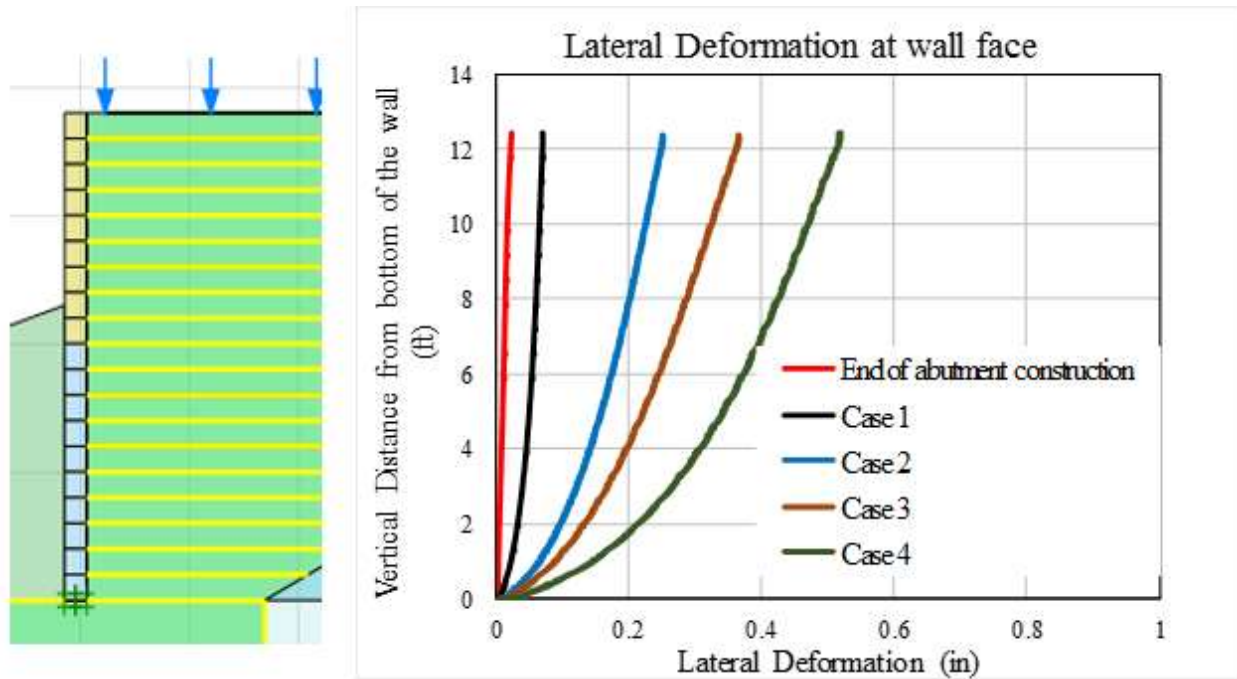


Figure 73

Profiles of prediction lateral deformation along the wall face at different loading conditions using FE analysis

Figure 75 presents the predicted vertical stresses at different layers at the end of bridge construction, truck loading, service loading, and abnormal loading for the upper third of GRS-IBS abutment. The distribution of the stresses changes with the depth. A symmetrical stress distribution was noted in layer 19 and 18 right under the footing and a biased stress distribution toward the facing was noted in layers 16, 14, and 12. The symmetrical stress distribution right under the footing can be explained due to the short distance between these layers and the strip footing.

Reinforcement Strain Distribution and Axial Force

For the purpose of comparison and verification, the distribution strain of geotextile reinforcement obtained from the FE analysis were compared with those obtained from field strain measurements at the end bridge construction (Case 1) as presented in Figure 76. It can be noted that the maximum strains predicted by the FE analysis are a little lower than the measured strains in the field, which researchers believe are in good agreement and within the acceptable range.

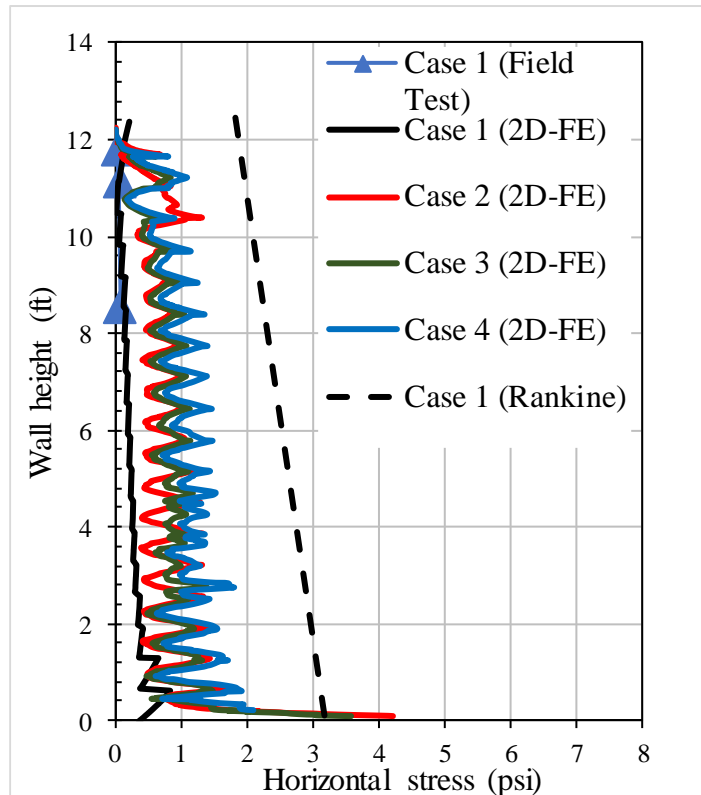


Figure 74

Measured and FE predicted lateral earth pressure distribution at the GRS-IBS abutment face

Figure 77 presents the predicted strains generated by the FE analysis for the end of bridge construction, truck loading, service loading, and abnormal loading. The highest reinforcement strain was found to be 1.5% for abnormal loading (48 psi), while the lowest strain was 0.4% at the end of abutment construction. The maximum strain for the service loading is 1.2%. The strain predicted by the FE analysis were close for the top two geotextile layers (layers 18 and 16) and slightly increases in the fourth and fifth layer from the top (layer 14). It can be seen that the locus of maximum strain was varied with depth. The maximum strain at the top four layers were located at about 20% of the reinforcement length from the wall face, and then moved to about 40% for the next six layers, and finally, the location goes back up to about 10% for the remaining lower eight layers. This is mainly due to the presence of rip rap as described in Figure 77.

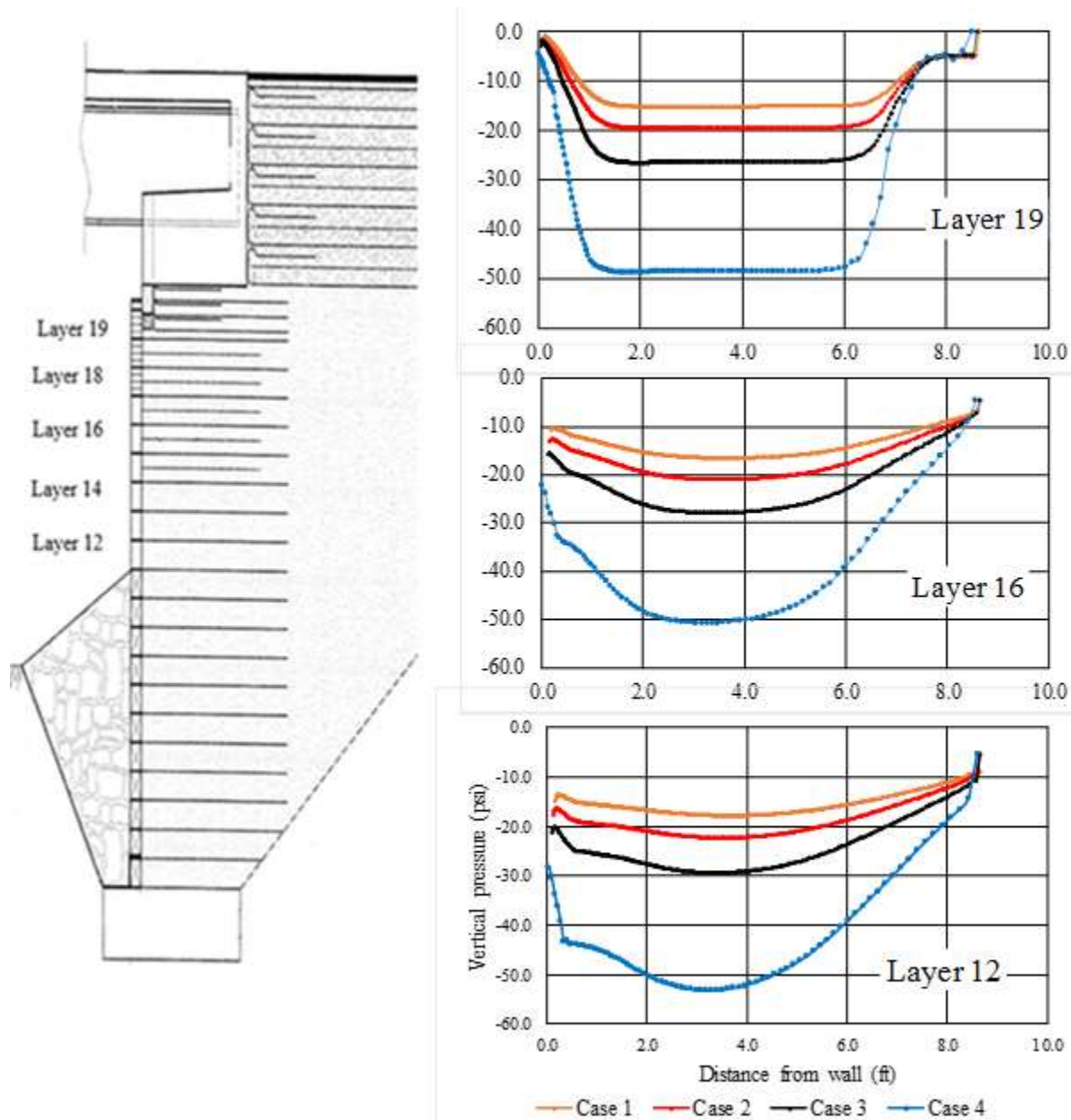


Figure 75

FE predicted vertical stress distribution at different layers in the GRS abutment

Table 12 compares the axial force in the reinforcement and the interface shear stress between the reinforcement and backfill materials as predicted by the FE analysis, the FHWA method and Mohr-Coulomb analytical methods for the service loading and the abnormal loading [5].

It can be seen in Table 12 that the strength of the geotextile reinforcement predicted by the FHWA method are 1.5-2.5 times higher than those predicted by the FE analysis, depending on the loading condition and reinforcement location. It should be noted that the FHWA method is a design

guideline that have built-in safety factors and conservatism, and therefore it is expected that the predictions by FHWA would be higher than the results of FE analysis. It was noted that the deviation decreases with increasing the loading. The highest predicted axial force is 746 lb/ft and 1076 lb/ft for the service loading and the abnormal loading, respectively. The most important notice is that the axial forces remain constant through the entire GRS-IBS abutment in all different loading cases except for case 4 (abnormal loading), this explains the main difference between the internally supported structures (GRS-IBS) and externally supported structures (MSE walls) as the axial forces in the latter (MSE walls) increases with depth according to the conventional Rankine or Coulomb method.

It was also noted in Table 12 that the interface shear stress predicted by the FE analysis is very close to those predicted by Mohr-Coulomb analytical method which indicates the using 0.8 as an interface friction value that was found between the reinforcement and backfill using the direct shear test is accurate.

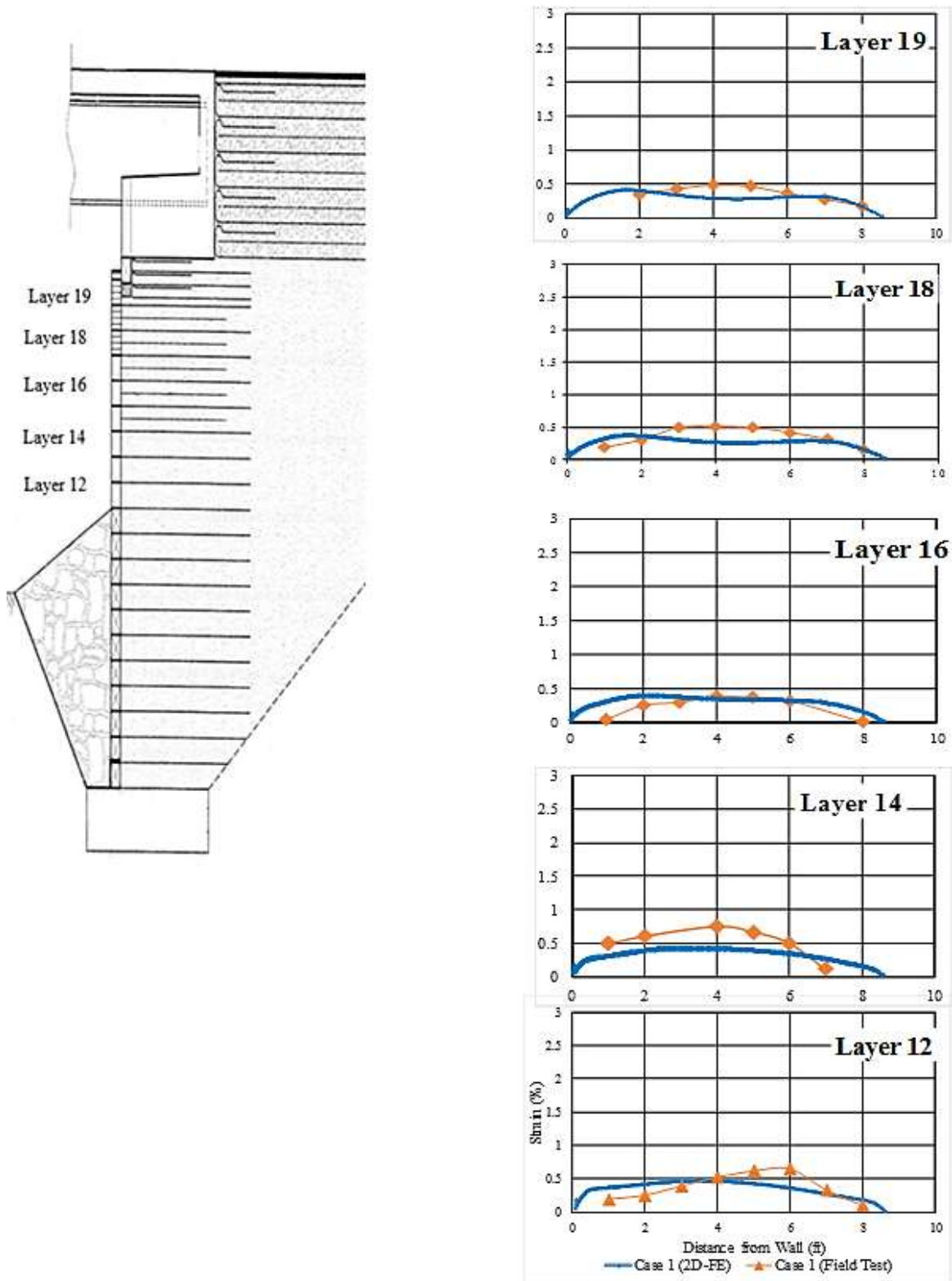


Figure 76
Measured versus FE predicted strain distribution along geosynthetics for Case 1

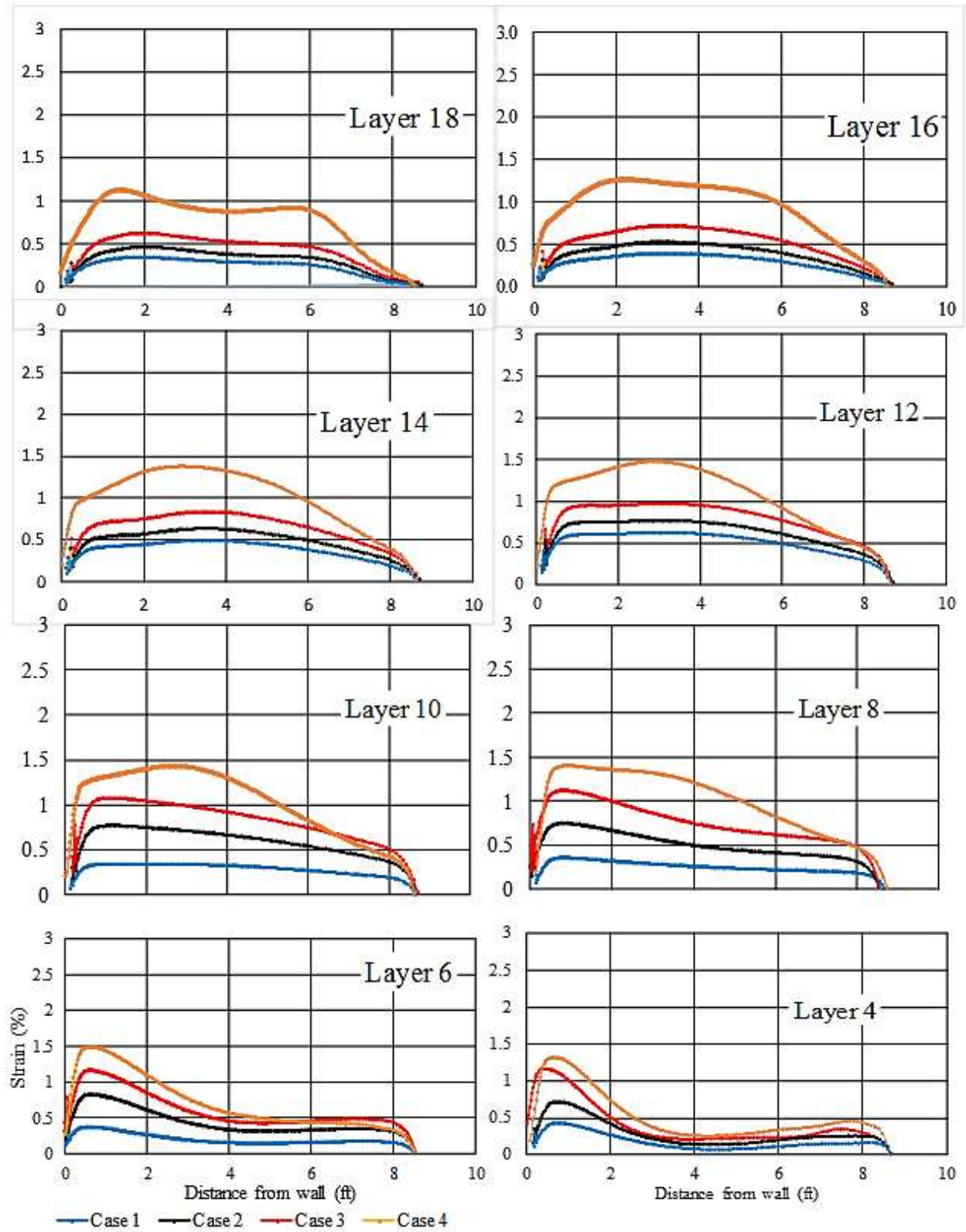


Figure 77

FE Predicted strain distribution along geosynthetics for the four cases of loading

Table 12
Axial force in the reinforcement and the interface shear stress

Layer #	Case 3				Case 4			
	Axial Force FE (lb/ft)	Axial Force FHWA (lb/ft)	Max Shear Stress FE (psi)	Max Shear Stress Analytical (psi)	Axial Force FE (lb/ft)	Axial Force FHWA (lb/ft)	Max Shear Stress FE (psi)	Max Shear Stress Analytical (psi)
1	363	675	46	44	740	824	90	79
2	329	672	39	38	678	829	77	65
3	308	671	37	36	630	835	63	60
4	295	670	35	34	610	843	60	57
5	281	670	34	33	596	854	58	55
6	274	672	33	32	576	867	56	53
7	267	675	33	31	569	883	55	52
8	260	680	32	30	562	903	55	52
9	267	688	31	29	562	927	53	50
10	281	697	30	28	582	955	52	49
11	288	710	30	28	610	989	51	48
12	283	726	30	27	605	1028	52	48
13	265	746	31	28	567	1076	52	48
14	253	384	31	28	561	562	53	48
15	239	404	31	28	518	596	53	49
16	233	411	31	28	501	637	53	48
17	221	432	30	27	489	672	53	48
18	204	432	30	27	460	669	52	48

Bold: double reinforcement (layers 14-18)

Figure 78 presents the comparison between the locations of maximum strain envelope with depth obtained from FE analysis for cases 1 and 2 and those obtained from field measurements. The figure also presents the location of maximum strain envelope with depth obtained from FE analysis for other loading cases (3 and 4). The FE analysis demonstrates that the maximum strain location is load dependent, i.e., by increasing the applied load, the maximum strain location moves toward the GRS-IBS abutment face. It is also noted that the presence of riprap (6.56 ft. from the bottom of the GRS-IBS abutment) affects the maximum strain location for the bottom reinforcement layers due to the lateral pressure that is created by the riprap in front of the GRS-IBS abutment.

For the purpose of comparison between the MSE wall and GRS-IBS design philosophies, the Rankine active failure surface envelope through the reinforced soil slopes (i.e., $45^\circ + \phi/2$) is also

drawn in Figure 78. It can be seen that the active failure assumption is not valid for the case of GRS-IBS abutment (internally supported structure due to the composite behavior of closely reinforcement) and that the failure envelope extends beyond this assumption up to 40% extra. In MSE walls, the reinforcements extend beyond the assumed active failure surface, and their reinforcement mechanism is considered to be tension-resistant tieback (fully bonded to the facing structure) for the assumed failure wedge. This analysis is commonly referred to as tieback wedge analysis, while in GRS-IBS the reinforcement mechanism is not considered as a tieback instead it is considered to be part of a composite material due to the interaction between closed spaced reinforced and backfill material.

Figure 79 depicts the relative shear stress τ_{rel} as determined from FE analysis for the GRS-IBS under service loading (Case 3) and abnormal loading (Case 4), respectively, which gives an indication of the proximity of the stress to the failure envelope. τ_{rel} is defined as:

$$\tau_{rel} = \frac{\tau_{mob}}{\tau_{max}} \tag{19}$$

where, τ'_{max} is the maximum projected value of shear stress where the Mohr's circle is expanded to touch the Coulomb failure envelope while keeping the center of Mohr's circle constant, which is different than the shear strain at failure τ_{ult} , and τ_{mob} is the maximum value of shear stress (i.e., the radius of the Mohr stress circle).

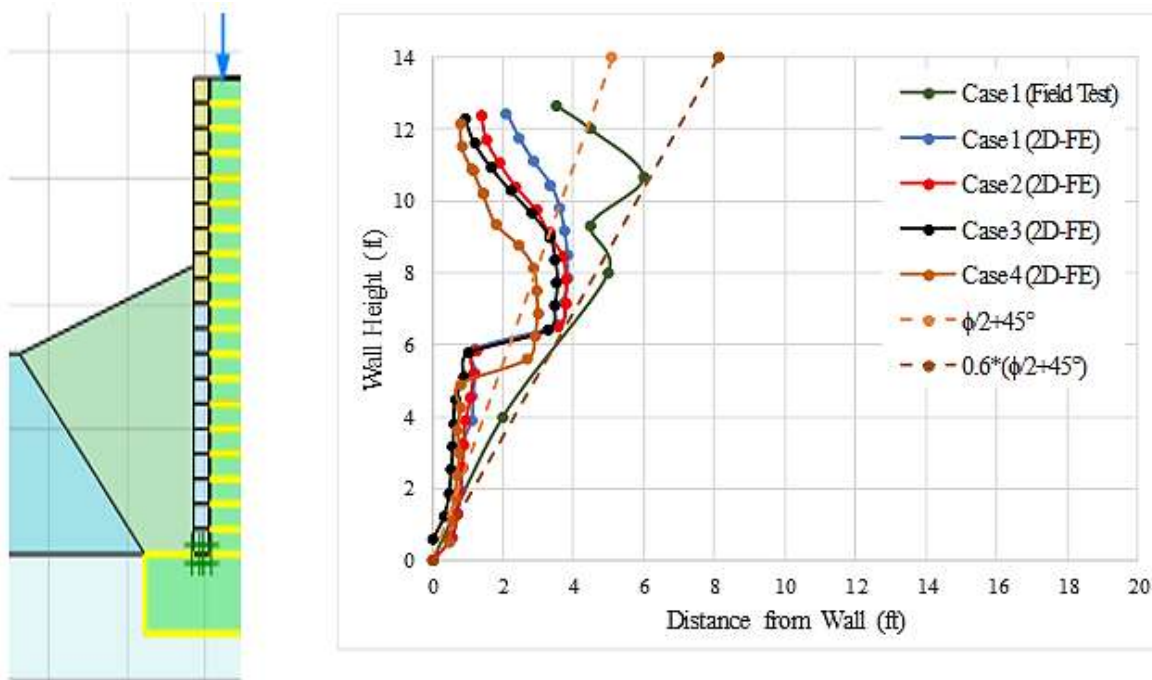


Figure 78
Maximum strain envelope for field and FE results at different loading

It can be seen that the maximum relative shear stress envelope is consistent with the previous discussions as with increasing the applied load on top of the GRS-IBS abutment, the failure envelope slopes less. It is also noted that the reinforced-zone is subject to higher shear stress as compared to the retained soil, which indicates that potential critical failure surface lies within the reinforced-zone with a slope of about $(45^\circ + \frac{\phi}{2}) \times 0.6$ up to 3 m from the top of the RSF, then moves toward the wall.

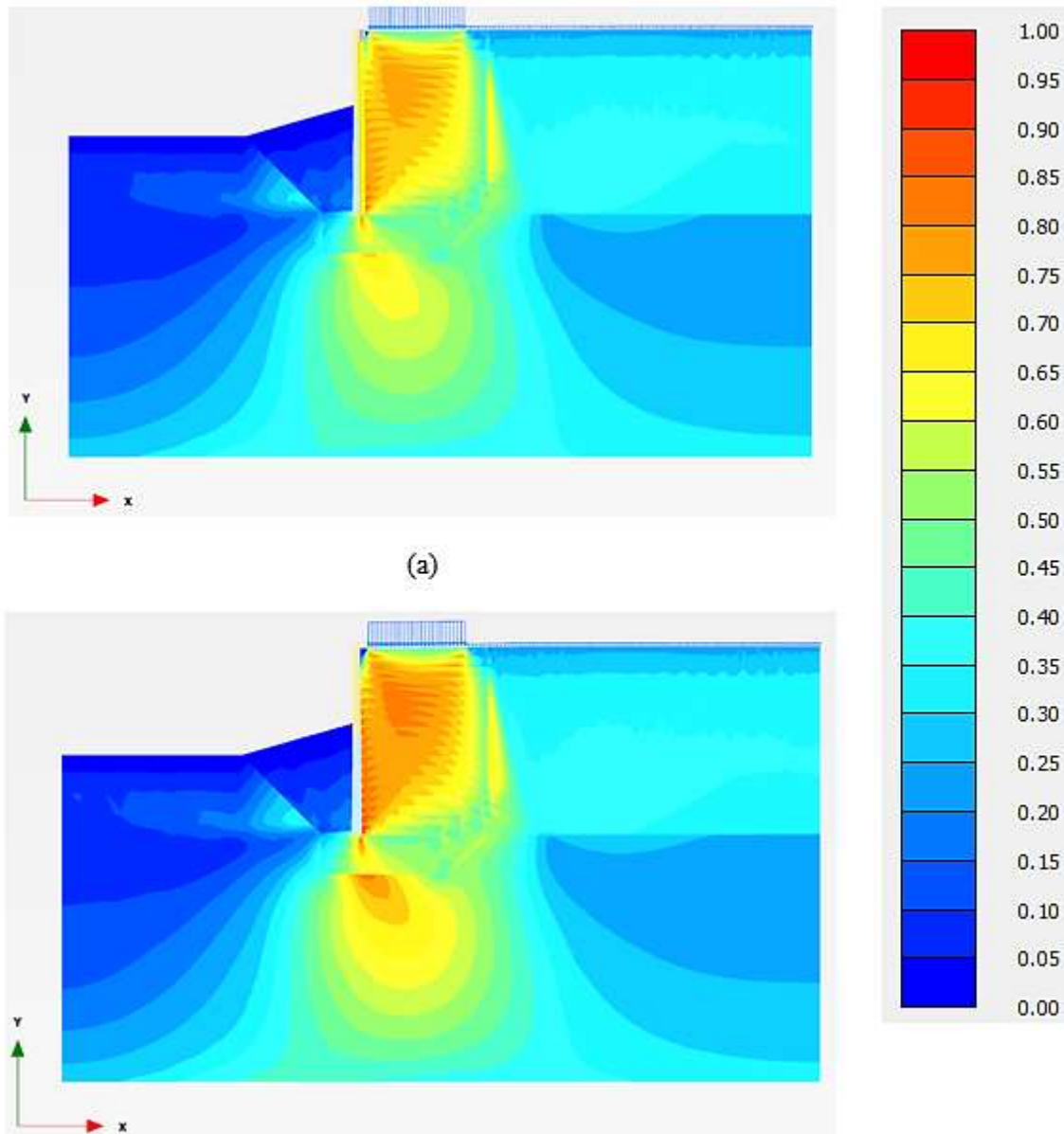
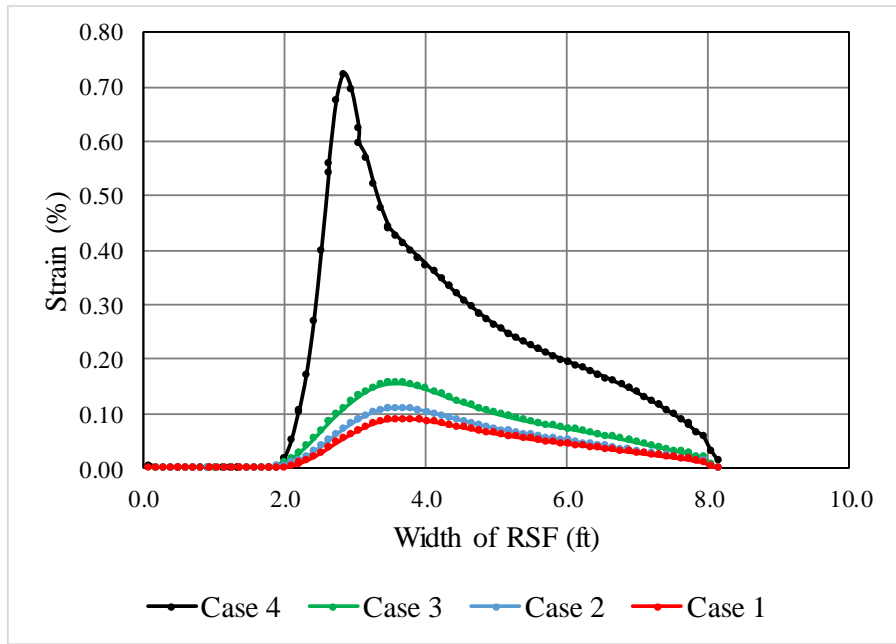


Figure 79

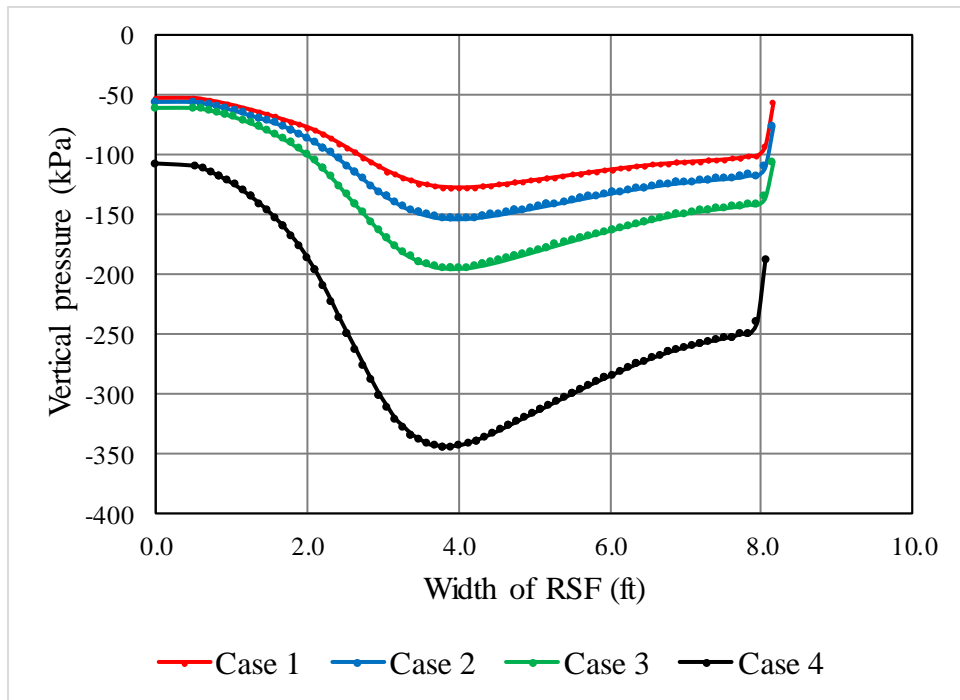
The distribution of relative shear stress, τ_{rel} , as determined from FE analysis for the GRS-IBS under service loading: a) service loading Case 3, and b) abnormal loading Case 4

Strain Distribution and Vertical Pressure Distribution under RSF

Figure 80a presents the strain distribution along the geotextile reinforcement of the RSF and Figure 80b presents the vertical pressure distribution under the RSF as predicted by the FE analysis at the four loading cases: end of the bridge construction (Case 1), truck loading (Case 2), service loading (Case 3), and abnormal loading (Case 4). Figure 80a shows that the maximum reinforcement strain is less than half of the strain developed in reinforced layers within the GRS-IBS abutment, with 0.16% and 0.72% values obtained for the service load (Case 3) and the abnormal load (Case 4), respectively. It can be seen that the maximum vertical pressure under the RSF is very close to those values under the bridge footing in the top third of the GRS-IBS abutment. Figure 80 demonstrates that the shape of reinforcement strain distribution and the vertical pressure distribution are different from those shown in Figures 76 and 77 in the GRS-IBS abutment, with the peak values are located immediately below the GRS-IBS wall facing and decreases in both directions as shown in Figure 78.



(a)



(b)

Figure 80

(a) Strain distribution along RSF reinforcement, (b) vertical stress distribution below RSF

Three-Dimensional Finite Element (3D-FE) Analysis

3D-FE Numerical Model

A three-dimensional FE model was developed and verified by using the measured results from the field monitoring of the fully-instrumented GRS-IBS bridge abutment at Maree Michel Bridge, in Louisiana. For the numerical analysis of this study, PLAXIS 3D 2016 was selected to simulate the three-dimensional behavior of GRS-IBS system. In the FE model, the soil was represented by 10-node tetrahedral elements to simulate the stress-strain behavior. To simulate the axial force along the geotextile, PLAXIS offers special tension 6-node triangular surface elements with three translational degrees of freedom per node (U_x , U_y , and U_z) to represent the geosynthetic materials (Note that the geotextile elements are compatible with the soil element type). The Interfaces between the geotextile and the backfill material and the facing blocks were simulated using joints elements to model the soil-structure interface behavior, which is represented by 10-node interface element (also compatible with the soil element) to simulate the thin zone of intensely shearing at the contact between the geotextile and the surrounding geomaterial.

The second order hyperbolic elastoplastic hardening soil model, which is a built-in constitutive model in PLAXIS 3D 2016, was selected to simulate the granular backfill material in this study [1]. The hardening soil model (HSM) implies friction hardening to model the plastic shear strain in deviatoric loading and cap hardening to model the plastic volumetric strain in primary compression. The HSM is also capable of simulating the non-linear stress-strain behavior of the backfill soil, stress dependency, soil dilation, and unloading-reloading behavior. For more details about the formulation and verification of the Hardening Soil Model (HSM), the reader can refer to Schanz et al. and Brinkgreve [1, 86]. A built-in linear elastic model with Mohr–Coulomb failure criterion model was selected to simulate the mechanical behavior of the interface between the backfill material and geotextile and the facing blocks by applying a reduction factor ($R_i \leq 1.0$) to the backfill material when defining soil property values ($R_i = 1.0$, for a fully-bonded interface). The interface property values are directly related to the mechanical properties of the backfill forming the interface (e.g., $C_i = R_i * C_{soil}$). These interfaces have properties of friction angle, dilation angle, cohesion, Young's modulus (E), tensile strength, and Poisson's ratio (ν).

A summary of the parameters used in 3D-FE modeling is provided in Table 11. Soil parameters were evaluated using the laboratory and in-situ testing. The geotextile and facing block properties were provided from the manufacture.

Figure 81 presents the 3D-FE mesh for the GRS-IBS of Maree Michel Bridge abutment (326270 nodes and 193983 elements). Mesh sensitivity was first carried out to select the proper size of FE mesh that is not affecting the FE results. For the purpose of comparison, 2D-FE analysis was also conducted using the same parameters and dimensions.

To simulate the field construction process, PLAXIS offers a staged construction mode, which is enable a realistic simulation of construction and excavation processes by activating and deactivating cluster of elements and load applications. To take into account the induced stress on the backfill soil due to soil compaction, a 9psi distribution load were applied at the top and bottom of each soil layer during the staged construction process according to the procedure introduced by Dantas and Morrison et al., which was also adopted later by Ehrlich and Mirmoradi, Mirmoradi and Ehrlich, and Riccio et al. [81- 83, 85].

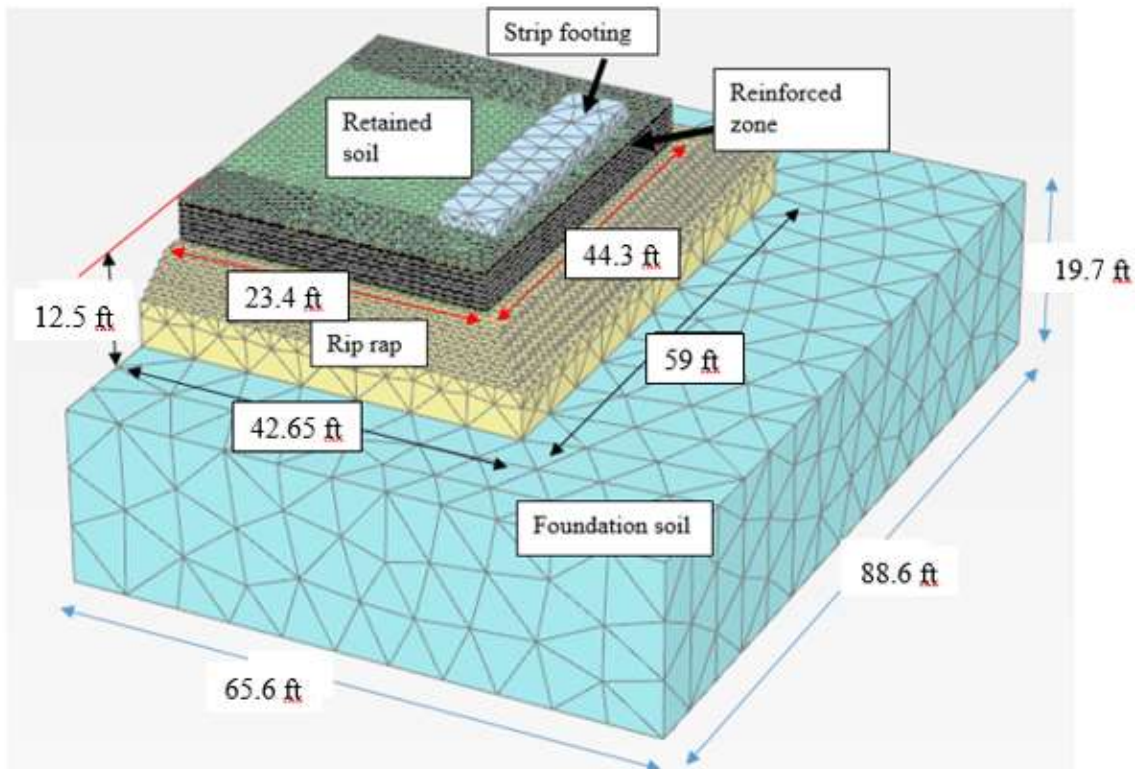


Figure 81

3D FE mesh of the GRS-IBS and locations of the applied boundary conditions

Results and Discussions

In this section, a comprehensive FE analyses in terms of reinforcement strain, lateral and vertical deformation, and horizontal and vertical pressure were carried out to evaluate the performance of the GRS-IBS system at Maree Michael Bridge. Results of 3D-FE analyses were compared with field measurements during monitoring program and with 2D-FE analyses. Three different loading conditions were considered in this study: at the end of bridge construction (Case 1), which is equal to the dead load of the bridge structure; service loading (Case 2), which is equal to the dead load

of the bridge structure plus the equivalent live traffic load; and at abnormal loading (Case 3), which is equal to the dead load of the bridge structure plus three times the traffic loading.

Lateral and Vertical Deformation. According to FHWA, the lateral facing deformation can be determined by conducting a performance test, in which the materials used in the performance test are the same materials to be used in constructing the GRS-IBS abutment [5]. The vertical strain deformation (settlement of GRS-IBS abutment) can be calculated by multiplying the vertical strain from the performance test by the total height of the GRS-IBS abutment, which should be less than 0.5% of the abutment height. In order to determine the maximum lateral deformation at the face, a zero-volume change is assumed in the GRS-IBS abutment due to vertical loading. The FHWA [5] defined the lateral strain to be two times the vertical strain and should be less than 1% of the abutment height.

Figures 82 and 83 depict the results of vertical and lateral deformations of the GRS-IBS due to the abnormal loading (Case 3). It can be seen that the reinforced-zone (GRS-IBS abutment) experienced the most vertical and lateral deformations due to the applied load from steel girders. A zero or very low deformation occurs behind the reinforced-zone.

The profiles of lateral deformations at the face of the GRS-IBS wall determined using the 3D-FE and 2D-FE analyses at the end of abutment construction and the end of bridge construction were compared with field measurements as shown in Figure 84. It can be seen that the prediction results by the 2D-FE and 3D-FE analyses are very close to each other and are in a good agreement with the field measurements. It was also noted that the 3D-FE analysis predicts a little higher lateral deformation than the 2D-FE analysis. The maximum lateral deformations predicted using the 3D-FE analyses were found to be less than 0.02 in. and 0.08 in. at the end of abutment construction and at the end of bridge construction, respectively.

The 3D-FE model was used to predict the lateral deformation profile of the GRS-IBS wall face for the three loading conditions (Case 1, 2, & 3) as presented in Figure 85, which shows that the maximum lateral deformations are 0.08, 0.12, and 0.27 in. at the end of bridge construction (Case 1), the service loading (Case 2), and abnormal loading (Case 3), respectively. The predicted maximum lateral deformations are less than the values recommended by the FHWA [5].

Since the GRS-IBS abutment was built using granular materials, most of the vertical deformation within the abutment occurs immediately after adding the load. Distinguish must be made here between the GRS-IBS abutment vertical deformation and the settlement of underlying foundation soils (RSF). With that being said, the comparison profiles of the settlement distribution under the RSF predicted using the 2D-FE and 3D-FE analyses at the end of abutment construction and the end of bridge construction and the comparison with the field measurements are presented in Figure

86 in both the cross-section direction and the longitudinal direction. The maximum footing settlement due to service load (case 2) and abnormal load (case 3) are around 0.2 in. and 0.4 in., which is acceptable for the service load but not acceptable for the abnormal load according to FHWA recommendations [5].

Strain Distribution under RSF. Figure 87a presents the predicted 3D-FE strain distributions along the geotextile reinforcement under the RSF in the cross-section direction; and Figure 87b presents the predicted 3D-FE strain distribution along the geotextile reinforcement under the RSF in the longitudinal direction. Figure 87a shows that the maximum reinforcement strain predicted by the 3D-FE analysis for cases 1 and 2 are very close in magnitude to those predicted by 2D-FE analysis (Figure 80a), but with a little different in the location of those maximum strains.

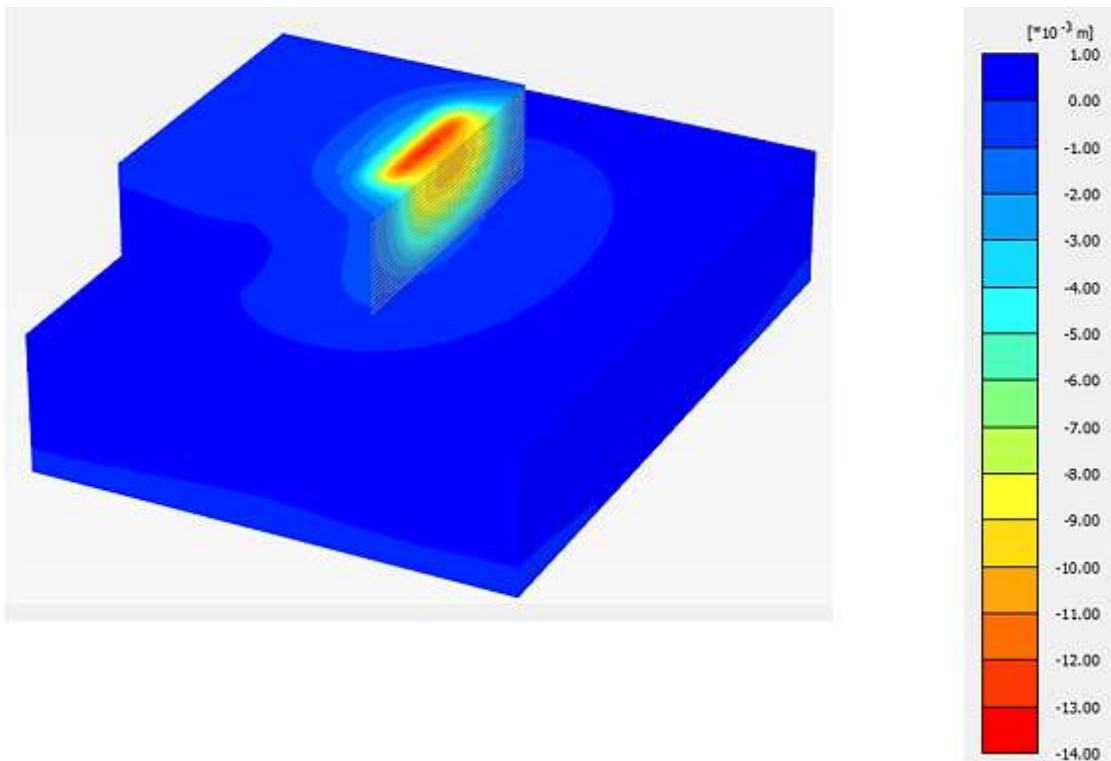


Figure 82
Predicted settlement of GRS-IBS due to abnormal loading (Case 3)

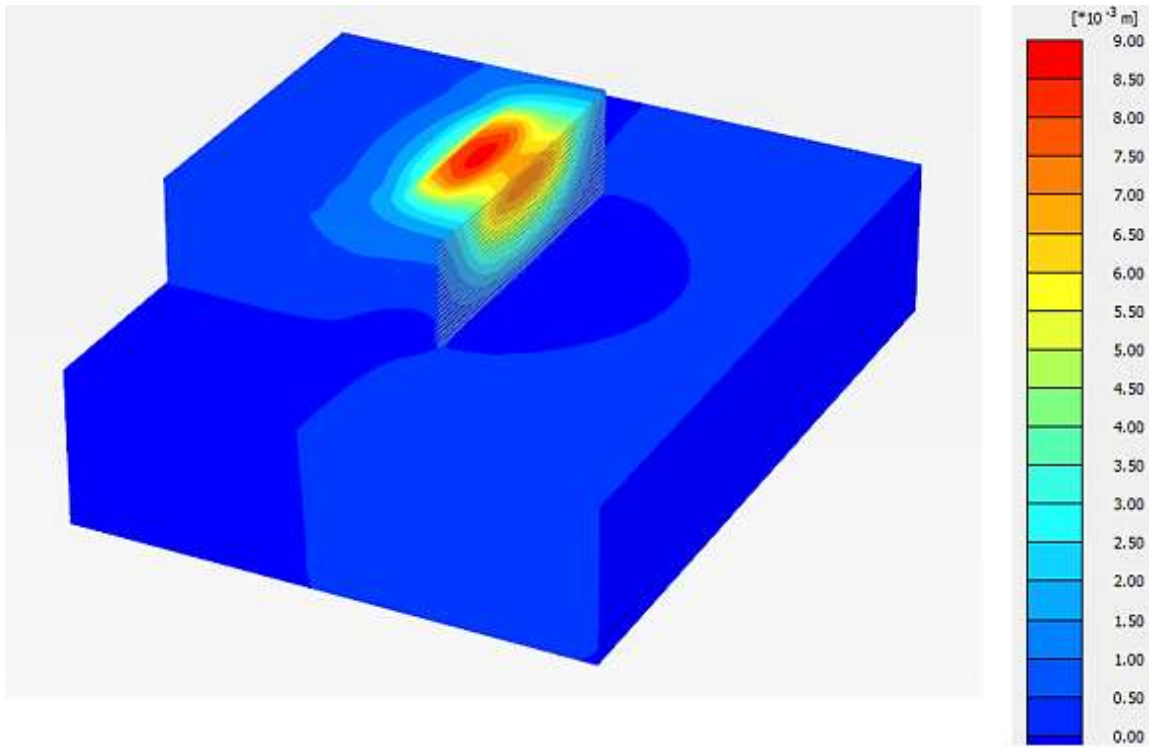


Figure 83
Predicted lateral deformation of GRS-IBS due to abnormal loading (Case 3)

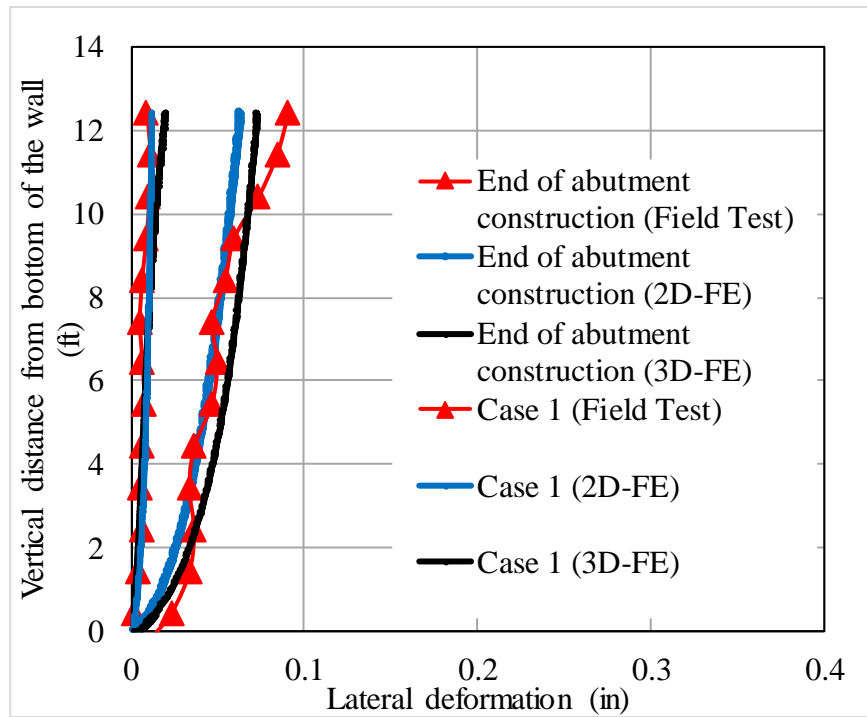


Figure 84
Comparison of measured and FE predicted lateral deformation profiles along the wall face

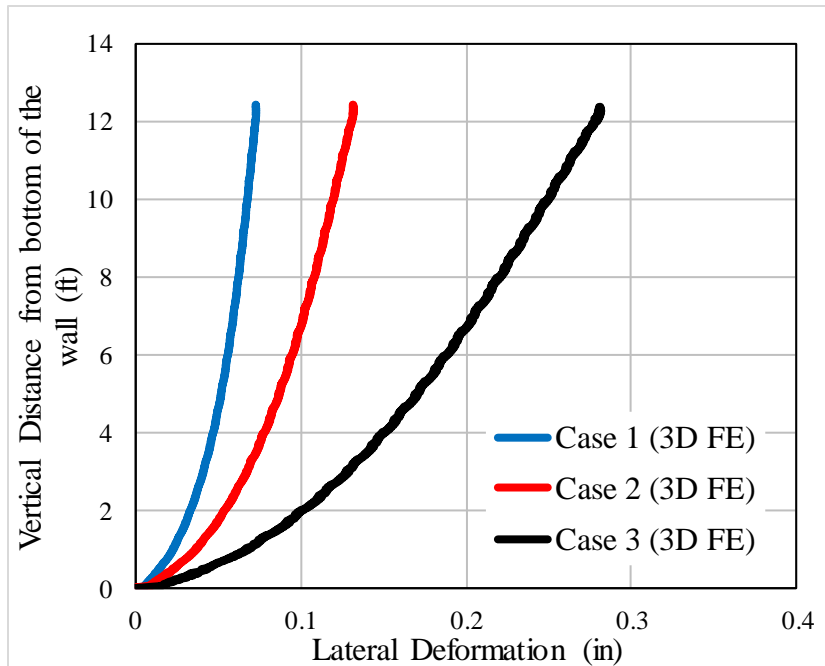


Figure 85

3D-FE predicted lateral deformation profile along the face at different loading conditions

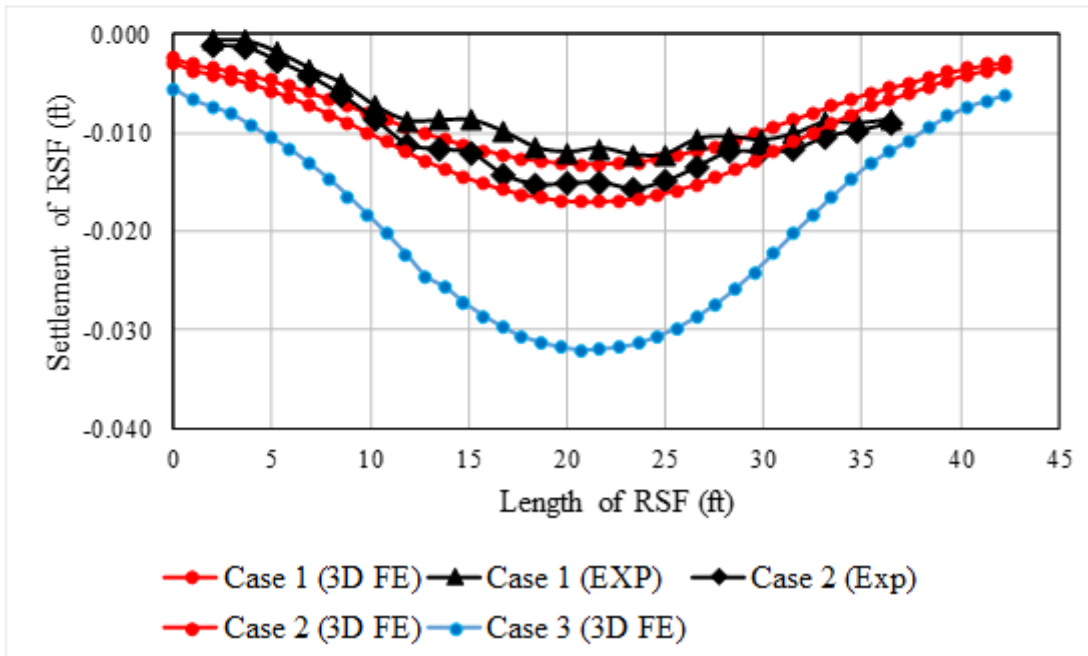
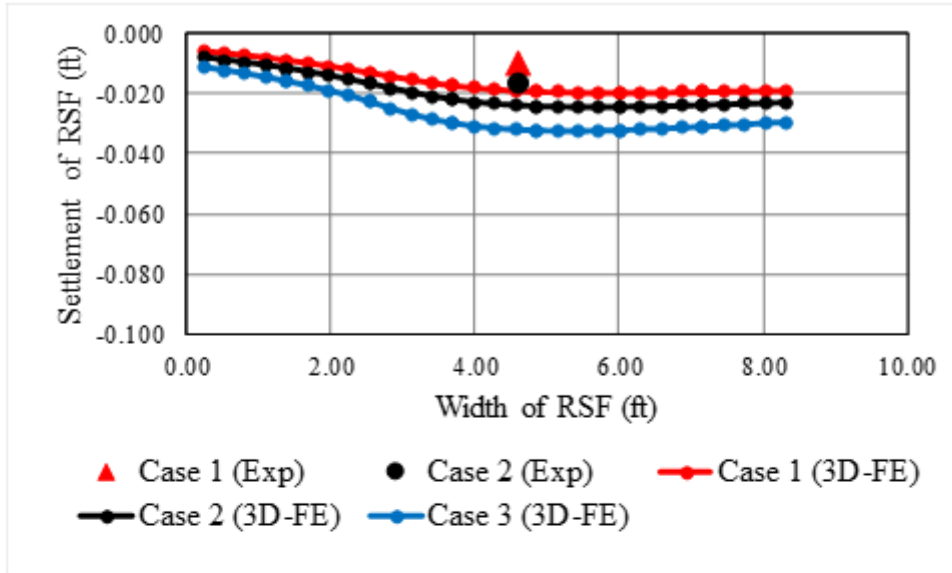


Figure 86

Comparison between measured and FE predicted of RSF settlement distribution

Strains values of around 0.16% and around 0.5% were obtained for the service load (Case 2) and the abnormal load (Case 3), respectively. The shapes of distribution of reinforced strains under the RSF are different from those reinforcements within the GRS-IBS abutment as will be discussed later.

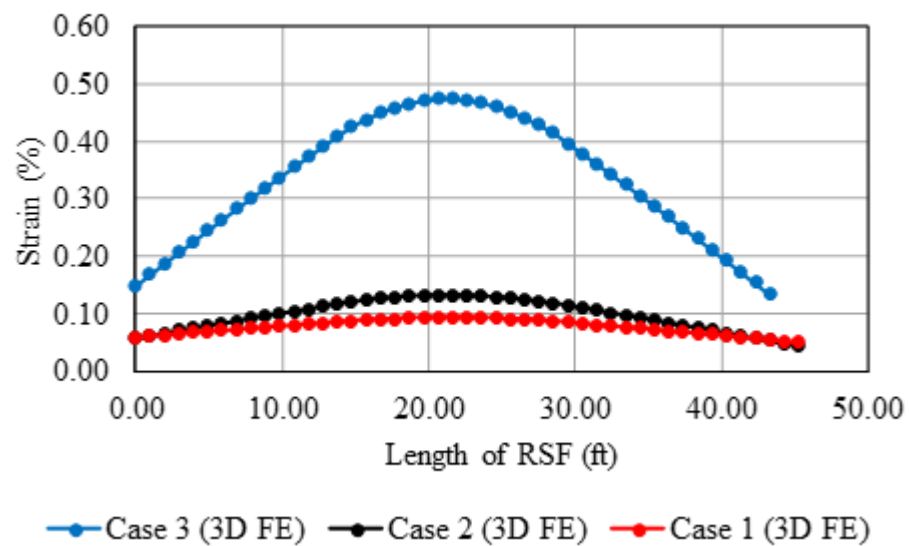
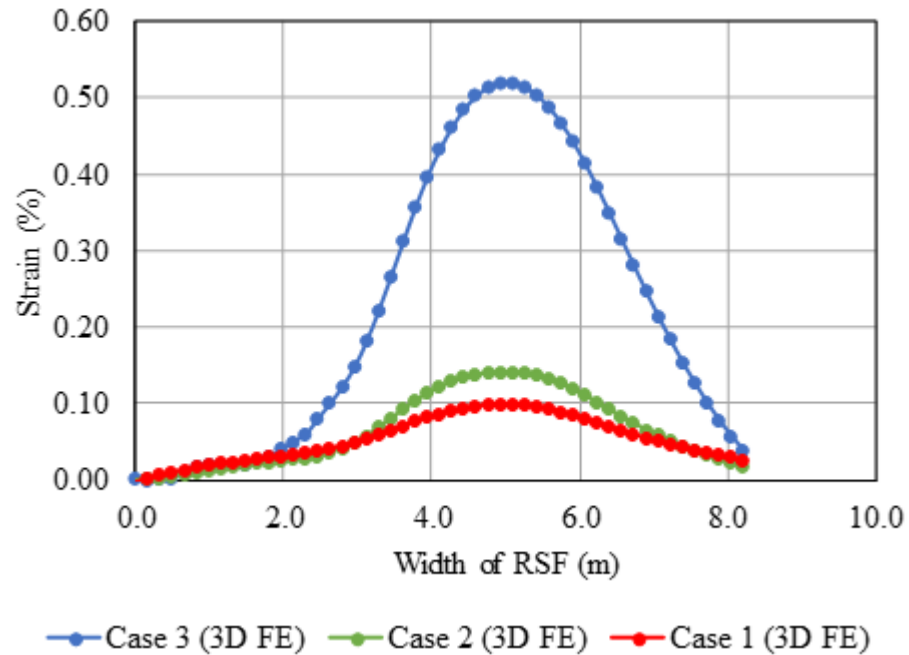


Figure 87
Strain distribution along RSF geosynthetic reinforcement

Vertical and Lateral Stresses within GRS Abutment. Figures 88 and 89 present the vertical stresses distribution under three different loading conditions along the cross-section and longitudinal direction of GRS-IBS, respectively. It was noted that the vertical stresses in the longitudinal direction are symmetrically distributed under the applied loads. On the other hand,

the vertical stresses along the cross-section direction are biased toward the front wall face direction as it is expected. It is also noted that the distribution of vertical stresses for the top five to six layers are very close within the bearing bed zone under the same loading conditions.

Figure 90a presents the comparison between the lateral pressures on the wall face predicted using the 3D-FE and 2D-FE analyses and the field measurements at the end of bridge construction (case 1); and Figure 90b presents the predicted lateral pressures using the 3D-FE analyses for three different loading cases (case 1, 2, and 3). It can be seen that there is a good agreement between both the 3D-FE and the 2D-FE analyses and the field measurements. For the purpose of comparison, the lateral stresses as predicted by Rankine method is also presented in Figures 90a and 90b. It was noted that the predicted and measured lateral pressure are much less than the Rankine lateral earth pressure. This is mainly attributed to the composite behavior of closely-spaced reinforced layers.

Wu proposed the bin pressure theory to evaluate the performance of the GRS walls in terms of lateral facing pressure, in which the smaller reinforcement spacing results in significant reduction in lateral earth pressure on the face [76]. The FE analysis and the field measurements results showed the main difference between the MSE walls and GRS in terms of lateral earth pressure. In the MSE walls, the current design methods use Rankine or Coulomb lateral earth pressure theories, which assume the stresses on the wall-face increases linearly with depth. Obviously, this is not valid in case of GRS (internally supported structure).

Reinforcement Strain Distribution and Axial Force. For the purpose of comparison and verification, the distribution strain of geotextile reinforcement obtained from the 3D-FE analysis were compared with those obtained from the 2D-FE analysis and from the field strain measurements at the end bridge construction (Case 1) as shown in Figure 91. It can be noted that the maximum strains predicted by the 3D-FE and 2D-FE analysis are very close to each other in the plain strain direction, which are slightly lower than the measured strains in the field. The figures demonstrate that the shape of reinforcement strain distribution is different than those in the GRS-IBS abutment in Figure 91, with the peak values are located immediately below the GRS-IBS wall facing and decreases in both directions. Figure 92 presents the predicted strains generated by the 3D-FE analysis in the cross-section direction at the end of bridge construction (Case 1), service loading (Case 2), and abnormal loading (Case 3). The highest reinforcement strain was found to be 1.6% for abnormal loading (48 psi) in layer number 12; while the lowest strain was 0.4% at the end of bridge construction in layer number 18. The maximum strain for the service loading is around 1%. The strain predicted by the 3D-FE analysis were close for the top three geotextile layers (layers 18, 16, and 14) within the bearing bed zone and slightly increases in the fifth layer from the top (layer 12). Figure 93 presents the predicted strains generated by the 3D-FE analysis in the longitudinal-direction, It can be seen that the maximum strains predicted by the 3D-FE

analysis in the longitudinal direction are distributed symmetrically in which the highest values are located under the strip footing and decreases toward the edges.

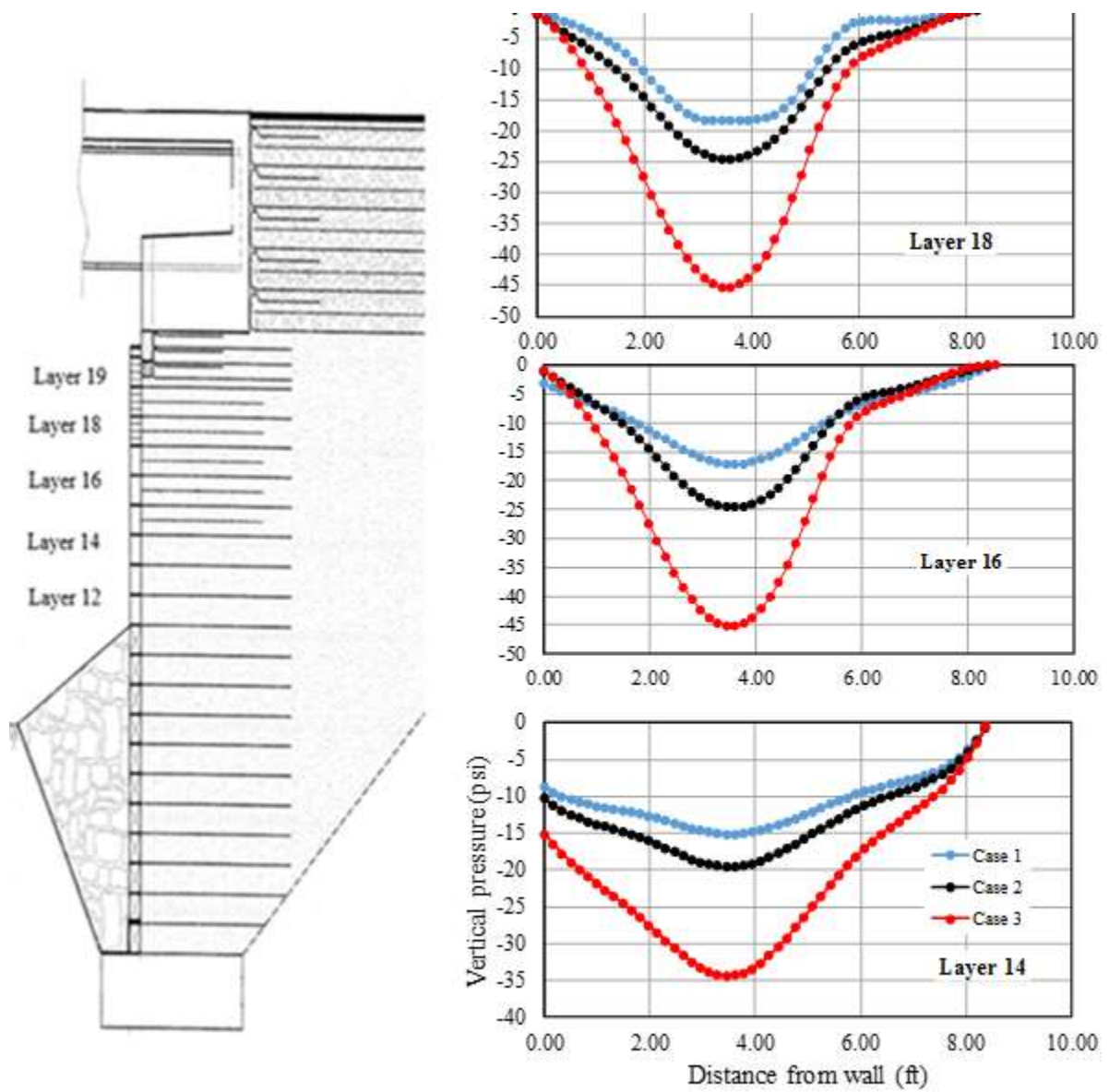


Figure 88
Predicted vertical stress distribution along cross-section at different layers in the GRS abutment

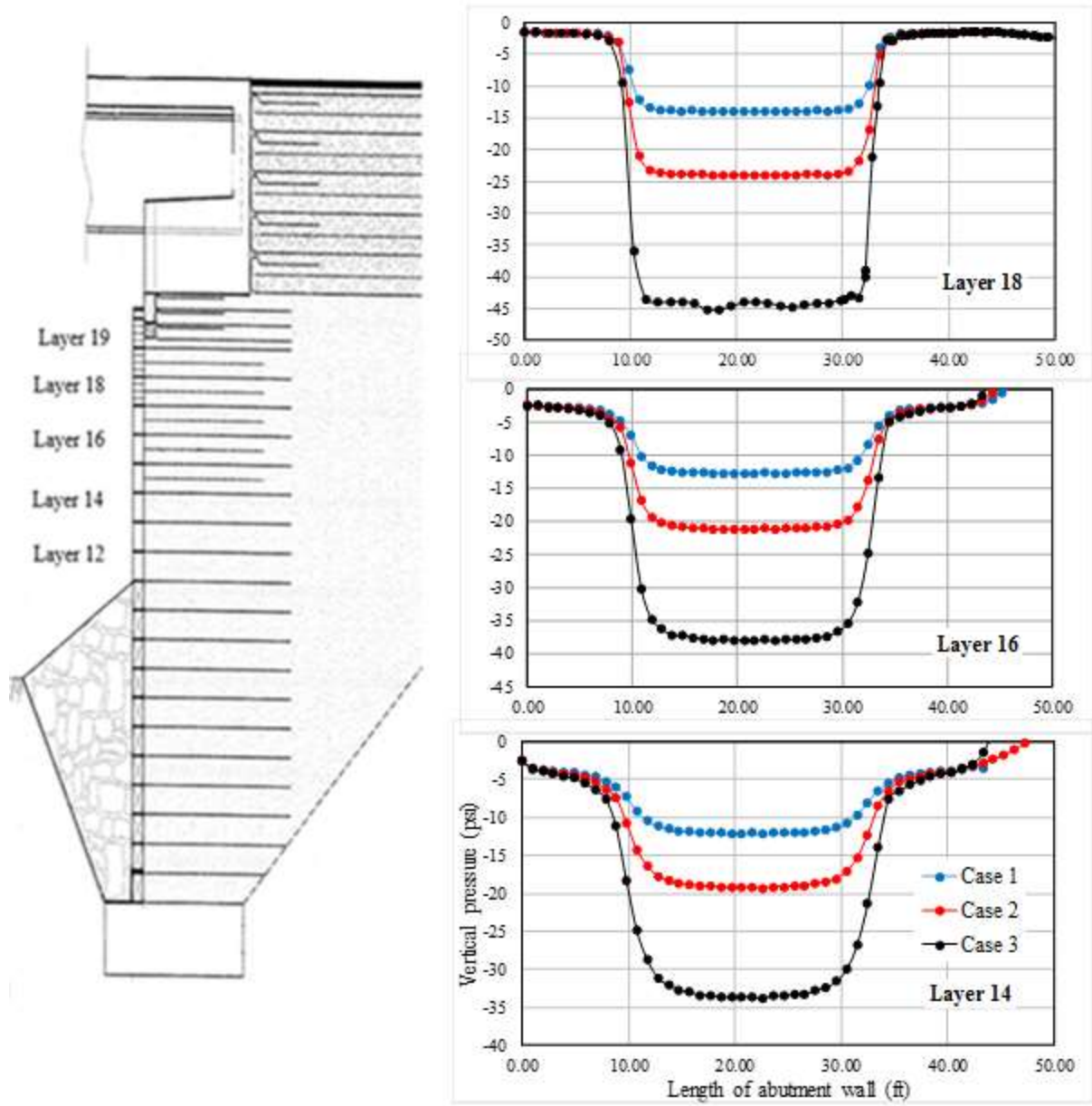
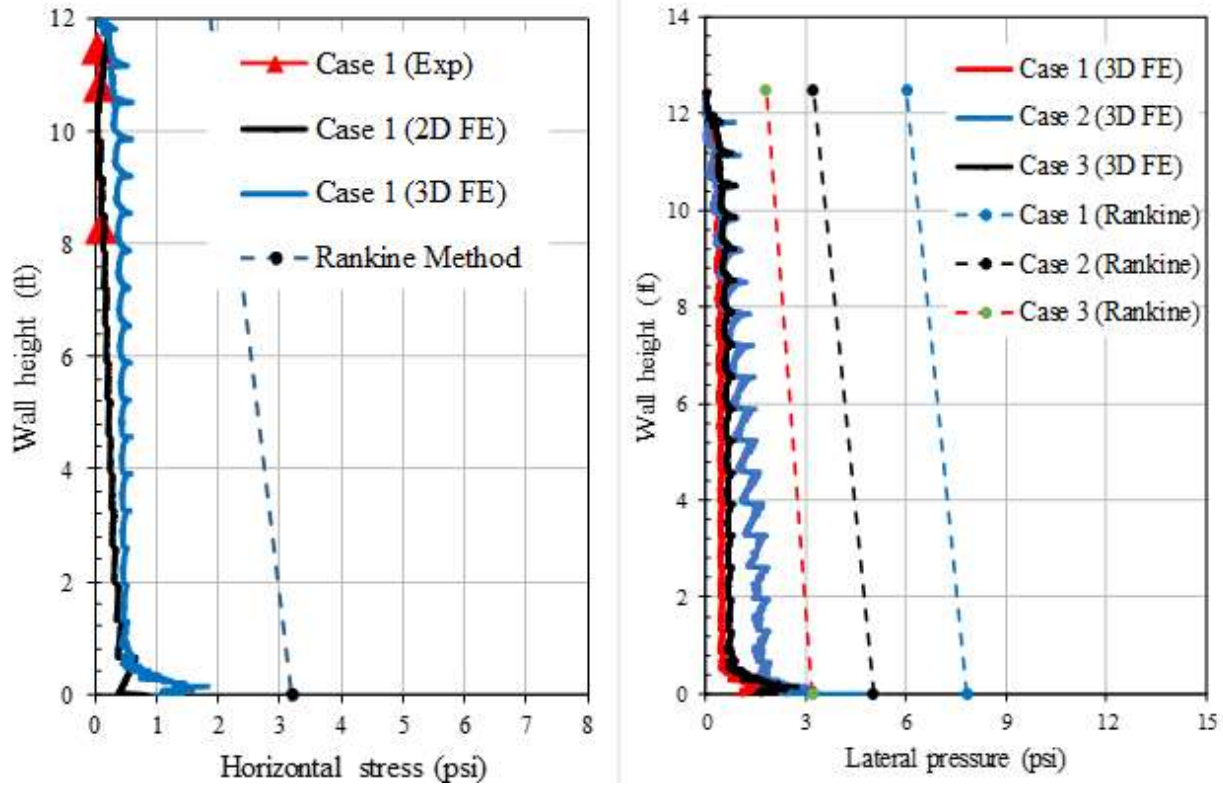


Figure 89
Predicted vertical stress distribution along longitudinal-section at different layers in the GRS abutment



(a) under service load

(b) under different load conditions

Figure 90

Measured and FE predicted lateral pressures on wall face under different load conditions

Table 13 compares the interface shear stress between the reinforcement and backfill materials as predicted by the 2D-FE and 3D-FE analysis, and estimated using the Mohr-Coulomb (equation 20) analysis method for the service loading (Case 2) and the abnormal loading (Case 3). The table also compares between the axial force in the reinforcement predicted by the 2D-FE and 3D-FE analyses and the estimated values by the FHWA method (equation 21) for the same cases [5].

$$\tau_{max} = c_a + \sigma_n \tan \delta \tag{20}$$

where, τ_{max} is the maximum interface shear stress at interface; σ_n is the normal stress; δ is the interface friction angle of backfill; and c_a is the cohesion of the backfill.

$$T_{req} = \left[\frac{\sigma_h}{0.7(\delta d_{max})} \right] S_v \tag{21}$$

where, T_{req} is the required reinforcement strength; σ_h is the lateral earth pressure; S_v is the reinforcement spacing; and d_{max} is the maximum grain size of backfill which is 0.75 in. in this study.

It can be seen in Table 13 that the axial forces in the geotextile reinforcement predicted by 2D-FE and those predicted by 3D-FE analysis are within acceptable range. It was also noted that the highest deviation comes from the bottom layers where the maximum reinforcement strain strains are less than 1% for the service loading. For the purpose of comparison, the predicted axial forces by the FE analysis were also compared with the FHWA analytical method. It was noted that the axial forces in the geotextile reinforcement predicted by the values estimated by the FHWA analytical method are 1.5-2.0 times higher than those predicted by 2D-FE and 3D-FE analysis, depending on the loading condition and reinforcement location. It was noted that the deviation also decreases with increasing the loading. The highest predicted axial force by FHWA method is 746 lb/ft. and 1076 lb/ft. for the service loading and the abnormal loading, respectively. On the other hand, the highest predicted axial forces by 2D-FE analysis for the same layer are 265 lb/ft. and 567 lb/ft. for the service loading and the extreme loading, respectively. The corresponding predicted values by 3D-FE are 383 lb/ft. and 562 lb/ft. for the service loading and the abnormal loading, respectively. The predicted axial forces remain almost constant through the entire GRS-IBS abutment for all different loading cases. This explains the main difference between the internally supported structures (GRS-IBS) and the externally supported structures (MSE walls) as the axial forces in the later (MSE walls) increases with depth according to the conventional Rankine or Coulomb methods. The results support the assumption by Adams et al. that the facing is not a structural element but it is rather aesthetic component [5]. It was also noted in Table 13 that the interface shear stresses predicted by the 2D-FE and 3D-FE analyses are very close to each other and to those predicted by Mohr-Coulomb analytical method, which indicates that using coefficient of interface ($\mu = 0.8$) as an interface friction value that was obtained between the reinforcement and backfill from the direct shear test is accurate.

Figure 94 presents the comparison between the locations of maximum strain envelope with depth obtained from the 3D-FE and the 2D-FE analysis for cases 2 and 3 and those obtained from field measurements for case 1. The FE analysis demonstrates that both the 3D-FE and 2D-FE analyses can predict the location of maximum strain for the upper half of GRS-IBS abutment. However, it was noted that the location of maximum strain varies between the 3D-FE and 2D-FE for the lower half where the riprap is located and this is might due to the 3D boundary effects. The figure demonstrates that the locations of maximum strain is load dependent, i.e., by increasing the applied load, the location of maximum strain moves toward the GRS-IBS abutment face.

The distinction must be made here between the MSE wall (externally supported structure due to the tension resistant tieback) and the GRS-IBS (internally supported structure due to the composite behavior of closely reinforcement) design philosophies. The most used methods for MSE wall are Coherent Gravity Method and Tie Back Wedge Method. According to Coherent Gravity Method, the failure wedge is determined by assuming a bi-linear envelope of the maximum axial forces, in

which three points are required to draw the failure envelope $(H, 0.3H)$, $(H/2, 0.3H)$, and $(0,0)$ as shown in Figure 94. On the other hand, the failure envelope in the Tie Back Wedge Method can be drawn according to Rankine active failure surface envelope through the reinforced soil slopes (i.e., $45^\circ + \phi/2$), which is also drawn in Figure 94. As the FE analyses and field measurements results indicated in Figure 94, both methods fail to predict the failure assumption for the case of GRS-IBS abutment. The failure envelope extends beyond the Coherent Gravity Method assumption up to 33% extra, in which the three points are required to draw the failure envelope; $(H, 0.4H)$, $(H/2, 0.4H)$, and $(0,0)$ as shown in Figure 94. In MSE walls design criteria, the reinforcements extend beyond the assumed active failure surface, and their reinforcement mechanism is considered to be tension-resistant tieback (fully bonded to the facing structure) for the assumed failure wedge. This analysis is commonly referred to as tieback wedge analysis; while in the GRS-IBS the reinforcement mechanism is not considered as a tieback instead it is considered to be part of a composite material due to the interaction between closed spaced reinforced and backfill material.

Figure 95 presents the predicted distribution of the shear strain using the 3D-FE analyses for the service loading condition (Case 2). The figure shows that the maximum shear strain occurs directly below the strip footing at the bottom center of the GRS-IBS abutment and decreases in all other directions.

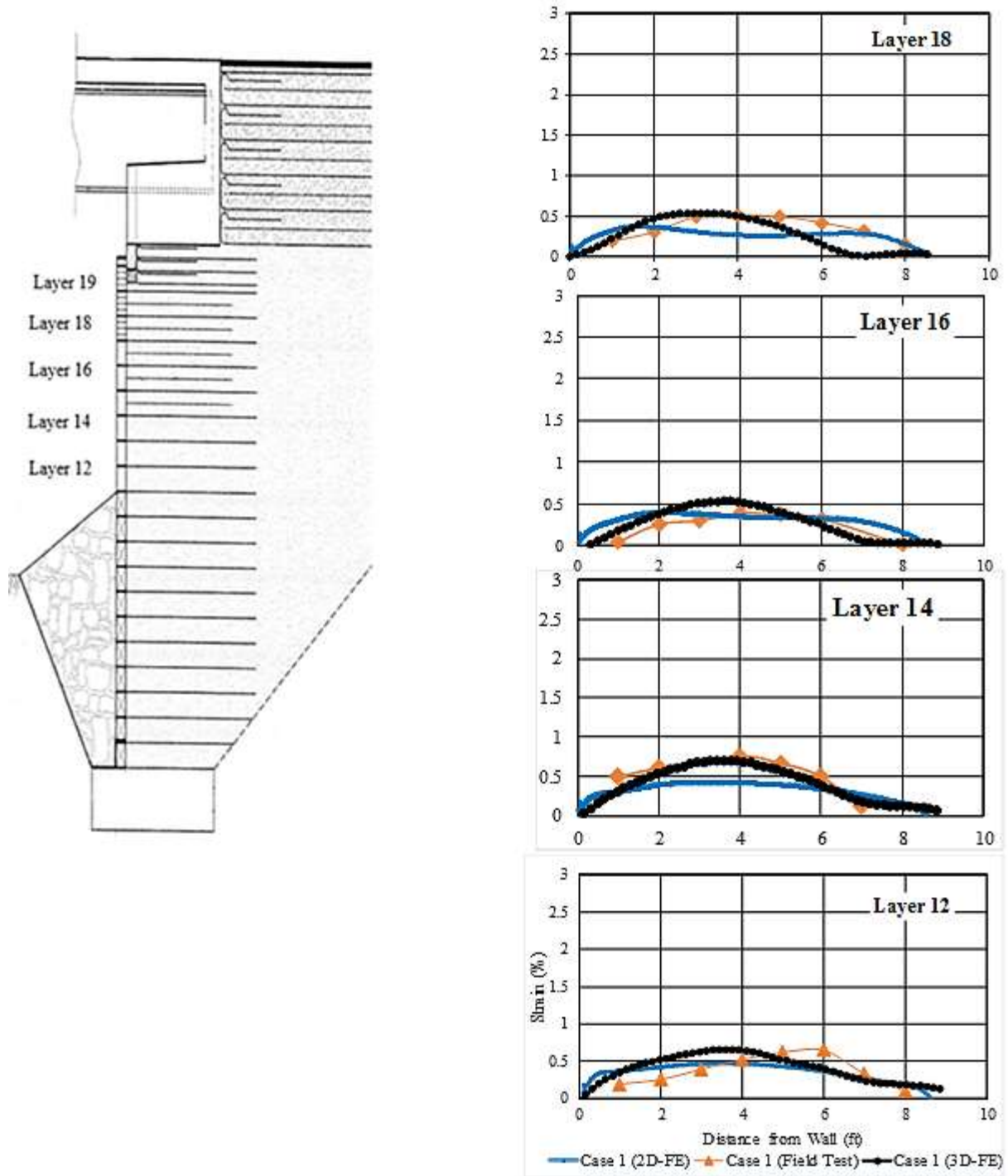


Figure 91
Comparison of strain distribution along geosynthetics for Case 1 in the transverse direction

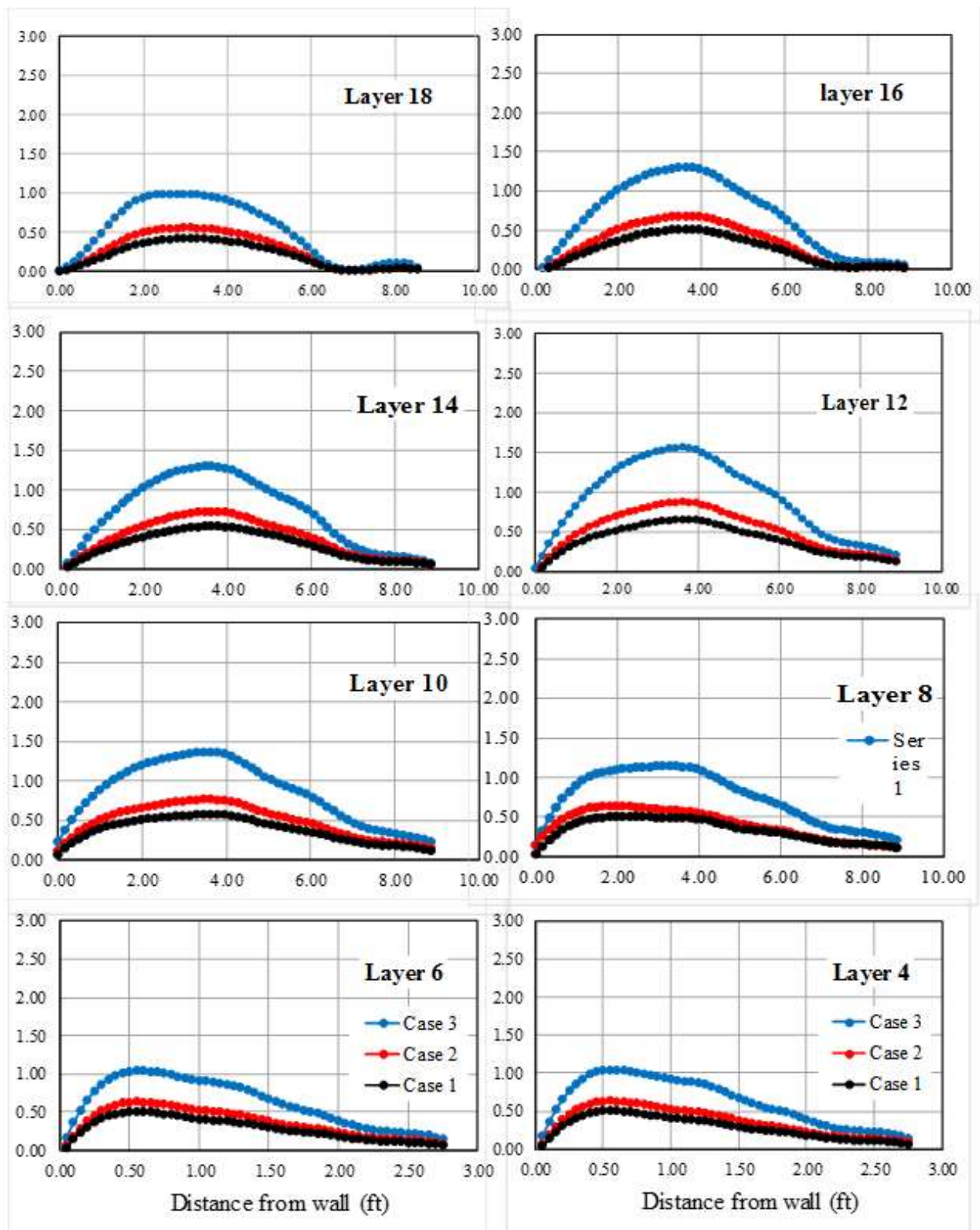


Figure 92

Predicted strain distribution along geosynthetics for the three cases of loading in the transverse direction

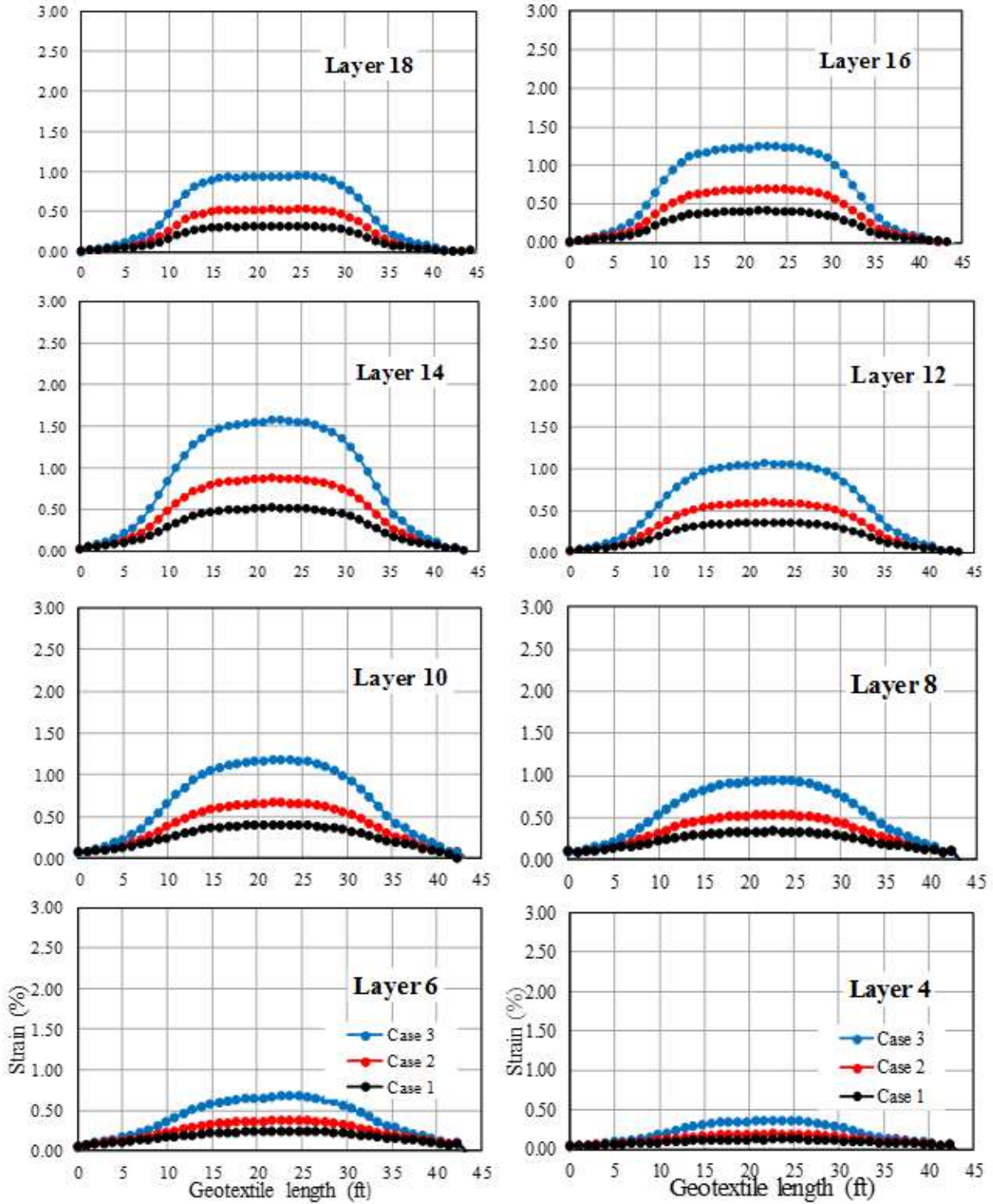


Figure 93
Predicted strain distribution along geosynthetics for the three cases of loading in the longitudinal direction

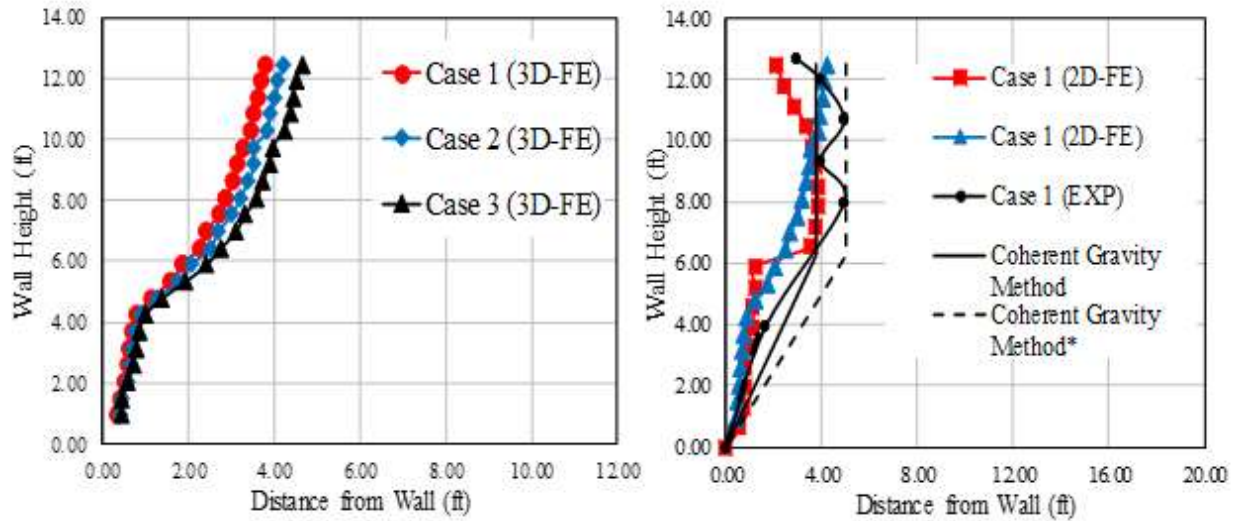


Figure 94

a) Maximum strain envelope at different loading conditions; b) Comparison of maximum strain envelope between field and FE results

Table 13

FE predicted axial force in the reinforcement and the interface shear stress

Layer #	Case 2						Case 3					
	Axial Force FE-2D (lb/ft)	Axial Force FE-3D (lb/ft)	Axial Force FHWA (lb/ft)	Max Shear Stress FE-2D (psi)	Max Shear Stress FE-3D (psi)	Max Shear Stress Analytical (psi)	Axial Force FE-2D (lb/ft)	Axial Force FE-3D (lb/ft)	Axial Force FHWA (lb/ft)	Max Shear Stress FE-2D (psi)	Max Shear Stress FE-3D (psi)	Max Shear Stress Analytical (psi)
2	329	244	672	39	38	38	678	433	829	77	63	65
3	308	269	671	37	35	36	630	380	835	63	59	60
4	295	235	670	35	34	34	610	449	843	60	55	57
5	281	283	670	34	33	33	596	432	854	58	52	55
6	274	267	672	33	31	32	576	488	867	56	48	53
7	267	299	675	33	29	31	569	460	883	55	45	52
8	260	275	680	32	28	30	562	509	903	55	43	52
9	267	302	688	31	27	29	562	527	927	53	41	50
10	281	292	697	30	26	28	582	580	955	52	40	49
11	288	319	710	30	25	28	610	614	989	51	39	48
12	283	338	726	30	24	27	605	656	1028	52	41	48
13	265	383	746	31	25	28	567	562	1076	52	42	48
14	253	295	384	31	25	28	561	576	562	53	48	48
15	239	306	404	31	26	28	518	576	596	53	42	49
16	233	314	411	31	28	28	501	555	637	53	53	48
17	221	307	432	30	29	27	489	500	672	53	51	48
18	204	270	432	30	31	27	460	435	669	52	50	48

Bold: double reinforcement (layers 14-18)

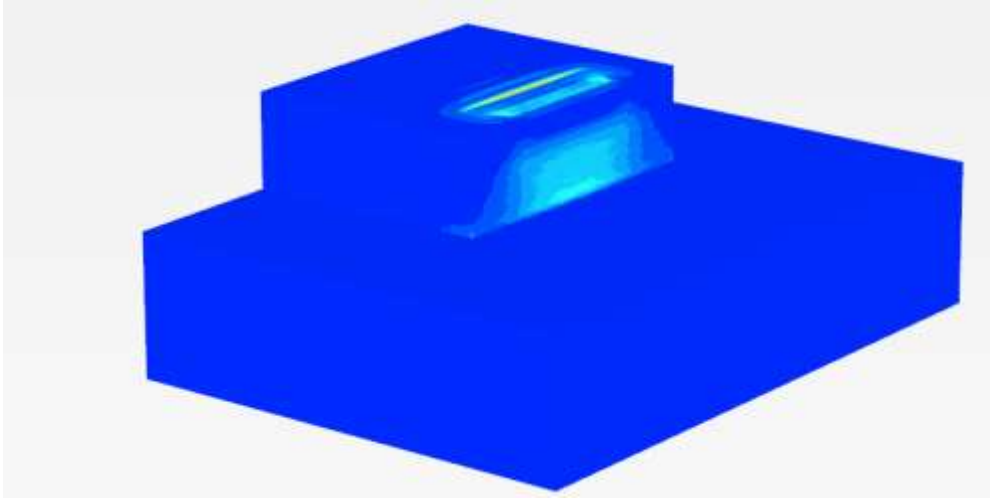


Figure 95
Shear strain (Service Load)

FINITE ELEMENT PARAMETRIC STUDY

FE Numerical Model

The two-dimensional FE program PLAXIS 2D 2016 was used in the current study to evaluate the effect of different parameters on the performance of GRS-IBS [86]. The FE grid and boundary conditions are shown in Figure 96. Mesh refinement was first conducted to find the optimum mesh-size where the numerical results are not mesh-size dependent. The dimensions of the model domain were selected far enough to minimize the effect of boundary conditions on the model response. The lateral boundaries were fixed by roller support to prevent the soil movement in the horizontal direction. The bottom of soil foundation was fixed using bin support to prevent the soil from movement in both the horizontal and vertical directions.

In the current study, the configuration of the GRS-IBS numerical model is selected according to the FHWA design criteria recommendation [5]. Figure 96 presents the configuration of the GRS-IBS model that was adopted to perform the parametric study. The height of bridge abutment H was selected with a minimum span length L_{span} larger than 25 ft., the minimum base width B_{total} is the greater value of 6 ft. or $0.3H$. The width of the reinforced soil footing (RSF) B_{rsf} is equal to $B_{total} + 0.25B_{total}$, assuming the bridge span to depth ratio = $L_{span}/D = 24$ as reported by Zheng and Fox, and the depth of the RSF D_{rsf} is equal to $0.25 B_{total}$ [35]. The setback distance between the back of the face and the footing a_b is equal to 8 in. The minimum clear space d_e , the distance from the top of the facing block to the bottom of the superstructure, is equal to 3 in. or 2% of the abutment height, whichever is greater. The width of the beam seat (strip footing in this study) b was selected equal to 4 ft. with a thickness of 2 ft. (note that the minimum width of the beam seat for a span length greater than 25 ft. is 2.5 ft. and the minimum thickness is 8 in.). The minimum reinforcement length L_r at the bottom of the bridge abutment should be $0.3H$ or B_{total} , whichever is greater, which increases linearly up to $0.7H$. The bearing bed reinforcement zone was extended from the top reinforcement layer for six consecutive layers. The length of the bearing bed reinforcement L_{rb} is equal to $2a_b + b$.

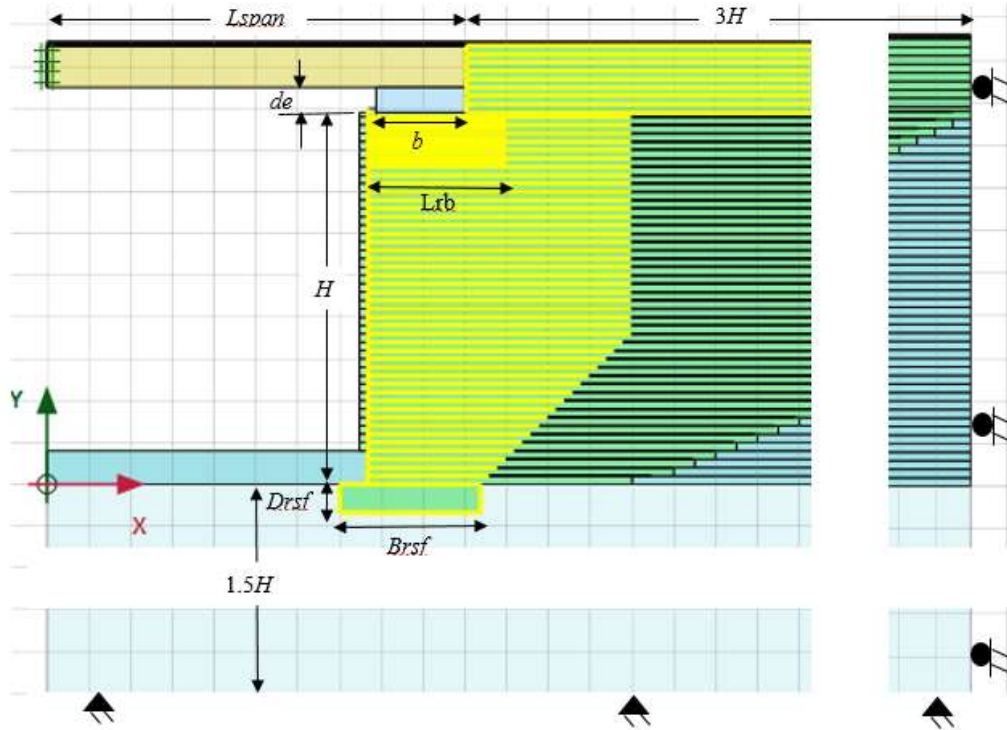


Figure 96

GRS-IBS FE numerical model with geometry and boundaries conditions

A crushed diabase opened graded backfill materials having maximum particle size D_{max} of (3/4 in) was selected in this study similar to the backfill materials used for the construction of the GRS-IBS at Maree Michel bridge site [36]. The properties of the backfill materials are listed in Table 11, which were determined and calibrated in a previous study [36].

A review of the recent literature shows that the hardening soil model has been used successfully to simulate the non-linear stress strain behavior of backfill materials [20, 31, 34, 36, and 42]. The hardening soil model developed by Schanz et al. is an elasto-plastic type hyperbolic model [1]. An isotropic hardening is assumed with associated plastic flow rule for the cap hardening and a non-associated flow rule is used for the frictional hardening. The hardening soil can simulate the soil dilation and plastic yielding. It accounts for stress history and stress dependent stiffness, in which the total strains are calculated using a stress-dependent stiffness, which is different for loading and unloading/reloading conditions. The hardening soil model can be used to simulate the behavior of sands and gravels as well as the softer soils (e.g., clay and silt). Formulation and verification of the hardening soil model is well described in Schanz et al. [1]. Nine input parameters are required to describe the hardening soil model: the secant stiffness parameter at 50% strain, E_{50}^{ref} obtained

from the triaxial test as well as the unloading/reloading stiffness parameter E_{ur}^{ref} , which is assumed to be equal to $3E_{50}^{ref}$ [89]; and the stiffness parameter E_{oed}^{ref} is assumed to be equal or less than E_{50}^{ref} as recommended by Schanz et al. [1]. The strength parameters, cohesion c , friction angle ϕ , and dilation angle Ψ are obtained from either the triaxial test or large direct shear test. The power m for stress level dependency of stiffness ranges from 0.5-1.0 (e.g., 0.5 for hard soil such as granular materials and 1.0 for very soft soil) Schanz et al. [1]. The failure ratio R_f , which is equal to the ultimate deviatoric stress divided by the asymptote deviatoric stress, has a default value is 0.9; and the Poisson's ration for the unloading/reloading, ν_{ur} , has a default value of 0.2.

The interfaces were simulated using the linear elastic Mohr-Coulomb frictional model. The role of the interface is to transfer the shear and normal stresses from the soil to the structure. The shear strength is governed by the Mohr-Coulomb failure criterion. The properties of the interfaces in PLAXIS can be set by using a reduction factor ($R_i \leq 1.0$) applied to the soil material when defining soil property values (i.e., $R_i = 1.0$, meaning the interface should not have a reduced strength with respect to the strength of the surrounding soil). Hence, the interface property values are directly related to the mechanical properties of the soil forming the interface (e.g., $C_i = R_i * C_{soil}$). These interfaces have properties of friction angle, cohesion, dilation angle, tensile strength, Young's modulus (E), and Poisson's ratio (ν). For more details about modeling the interfaces in PLAXIS or FLAC, refer to Yu et al. [90].

The linear elastic model was selected to simulate the reinforcement, facing blocks, and the strip footing. The Mohr-Coulomb model was selected to simulate the foundation soil. The soil layer was modeled using a 15-noded triangle element, which provides a fourth order interpolation of displacements (note the structure and interface element is automatically taken to be compatible with the soil element). The 5-noded geogrid element was used to simulate the behavior of the geotextile reinforcement, which is composed of line element with two transitional degree of freedom in each node (u_x, u_y). A zero-thickness interface element was selected to simulate the interfaces between the backfill materials and the reinforcement, and the interfaces between the facing blocks and the reinforcement. When using a 15-noded soil element, the corresponding interface elements are defined by 5-pairs of nodes to be compatible with the soil elements.

Results of FE Parametric Study

Four different parameters were considered in this study to evaluate the performance of the GRS-IBS under service loading condition in terms of lateral displacement of facing, settlement of RSF, reinforcement strain, and location of possible failure locus. The selected parameters are: abutment height, H , span length, L_{span} , reinforcement spacing, S_v , and reinforcement stiffness. A 23 ft. abutment height, 120 ft. span length, 8 in. reinforcement spacing, and 41 k/ft axial stiffness were

considered in this study the reference section subjected to an equivalent distributed roadway live load of 1.74 psi. The bridge girders were modeled as solid blocks ($L_b \times D \times 1$), assuming the bridge span to depth ratio = $L_{span}/D = 24$, composed of elastic elements with an equivalent unit of 75.5 lb/ft³. This procedure was adopted from a previous study by Zheng and Fox [35].

Effect of Abutment Height (H)

Three different abutment heights, H , were considered and evaluated in this study: 17 ft., 23 ft., and 30 ft. Figure 97 presents the effect of abutment height on the strain distribution along the geosynthetic reinforcement at 40 and 60% of the abutment height as measured from the bottom of the abutment. It can be seen that the maximum strain is affected by abutment height, in which the reinforcement layers at the bottom have higher strains than those in the top layers (e.g., the maximum strain decreases from 1.1% at 60% of the abutment height to 0.7% at the same location when decreasing the abutment height from 30 ft. to 17 ft.). Figure 99a presents the effect of the abutment height on the lateral facing displacement. The lateral facing displacement increases from about 1 in. for abutment height of 17 ft. to around 1.4 in. for abutment height of 30 ft., which indicates that increasing the abutment height will increase the lateral facing displacement. However, the location of the maximum lateral displacement unchanged. For the same span length (120 ft.) and the same location under the service loading condition, the figures indicate that the abutment height has a medium impact on the GRS-IBS performance in terms of the strain distribution along the reinforcement and a high impact on the lateral facing displacement.

Effect of Span Length (L_{span})

Five different span lengths, L_{span} , were considered and evaluated in this study: 40 ft., 60 ft., 80 ft., 100 ft., and 120 ft., which is corresponding to applied loads on top of GRS-IBS equal to 10.73, 15.66, 21, 26.1, and 31.3 psi, respectively. Figure 98 presents the effect of span length on the strain distribution along the reinforcement at 20, 40, 60, and 80% of the abutment height as measured from the bottom of the abutment. It can be seen that the maximum strain envelope is located near the abutment face at $0.2 H$ and moving about 4 ft. away from the abutment face at $0.8 H$ for all cases. It can be seen that increasing the span length does not affect the shape of the strain distribution; and at the same time slightly shifting the locus of maximum strain to the left. However, increasing the span length results increasing the magnitude of strain. The maximum strain increases from 0.4% for span length of 40 ft. to around 0.9% for a span length of 120 ft. at $0.6 H$ and $0.6 H$ above the bottom of the abutment. Figure 99b presents the effect of span length on the lateral displacement of wall facing. It can be seen that by increasing the span length, the lateral facing displacement increases, and the location of maximum displacement shifts up. The lateral facing displacement increases from around 1 in. for the 40 ft. span length to 1.2 in. for the

120 ft. span length. The figures indicate that the span length has a significant effect on the GRS-IBS performance in terms of the strain distribution along the reinforcement and the lateral displacement of wall facing for the same abutment height (23 ft.) under service loading condition.

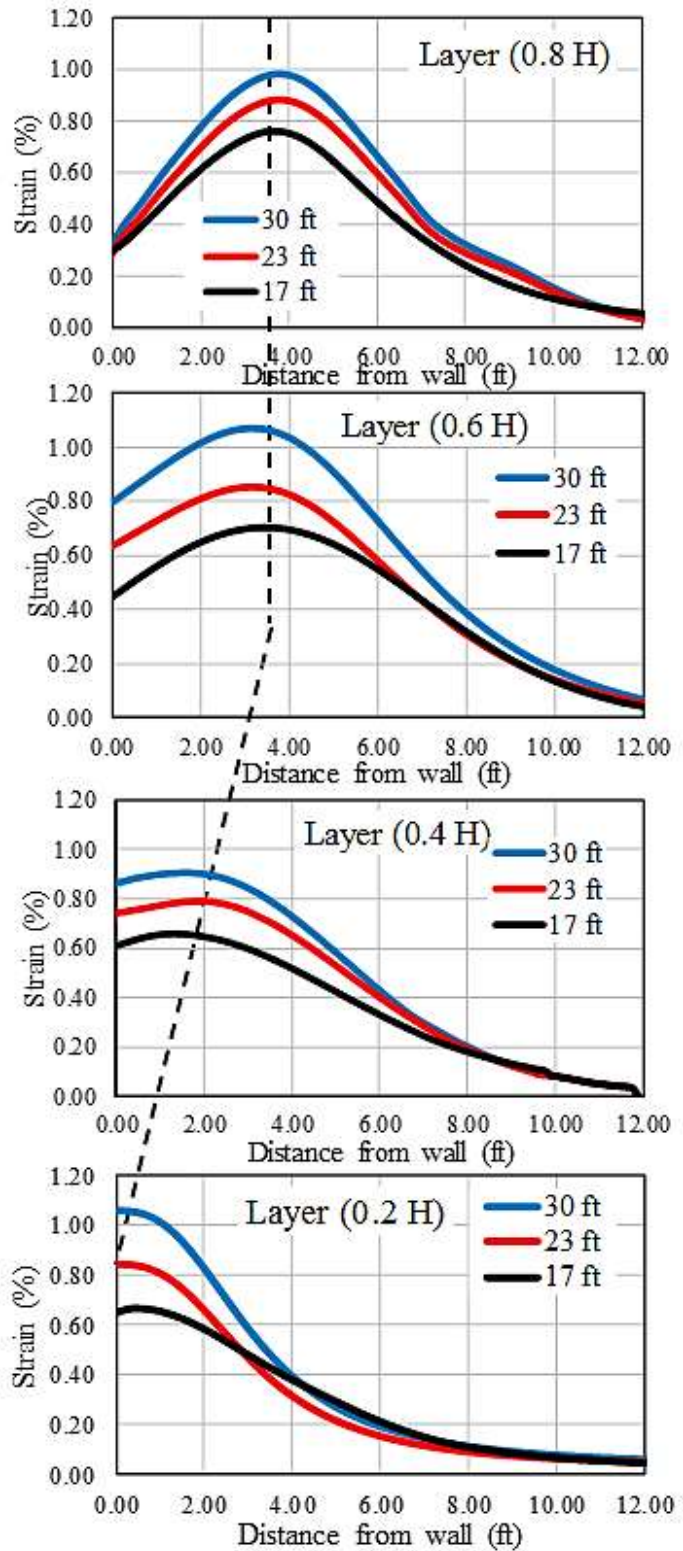
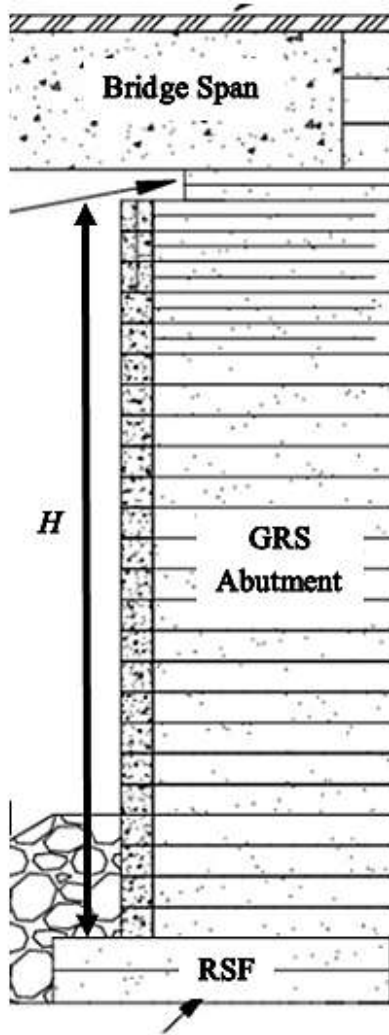


Figure 97

Effect of abutment height on the strain distribution along geosynthetics

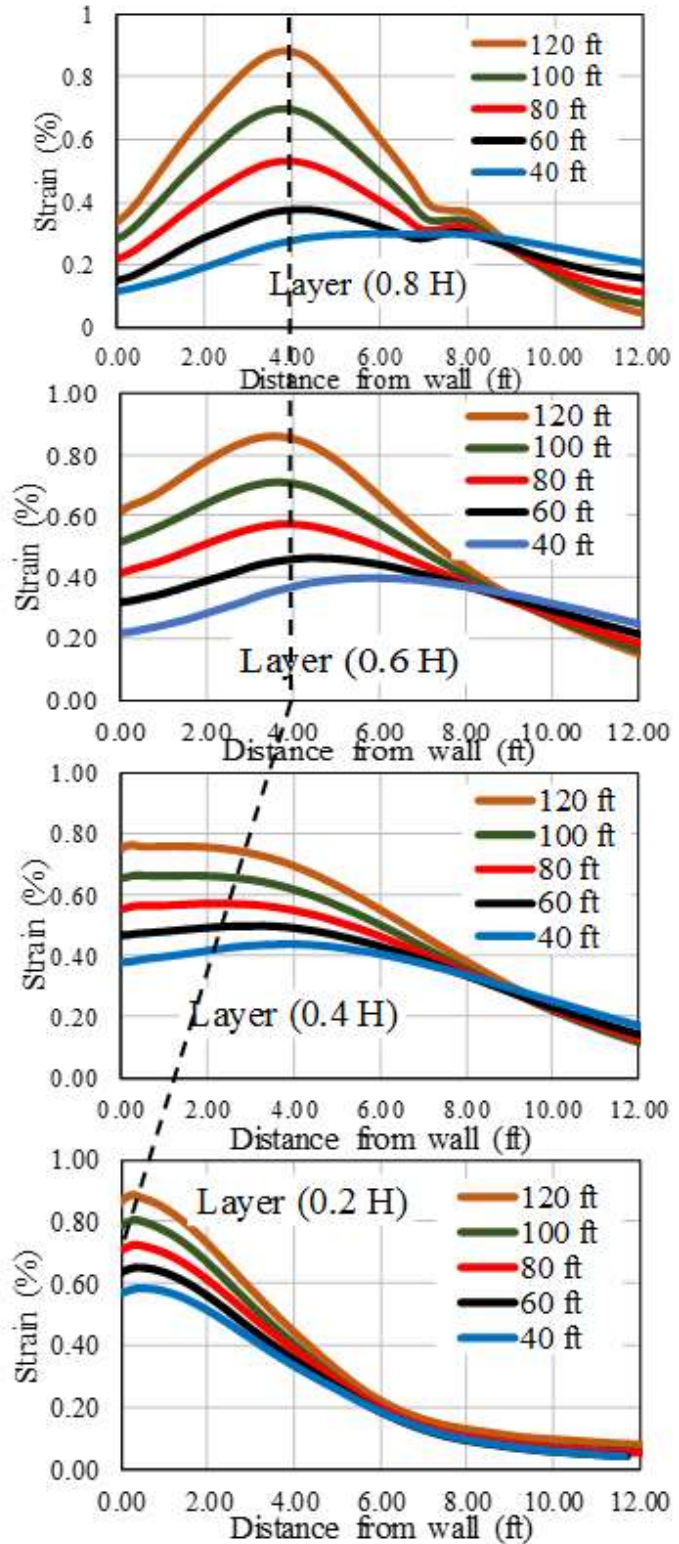
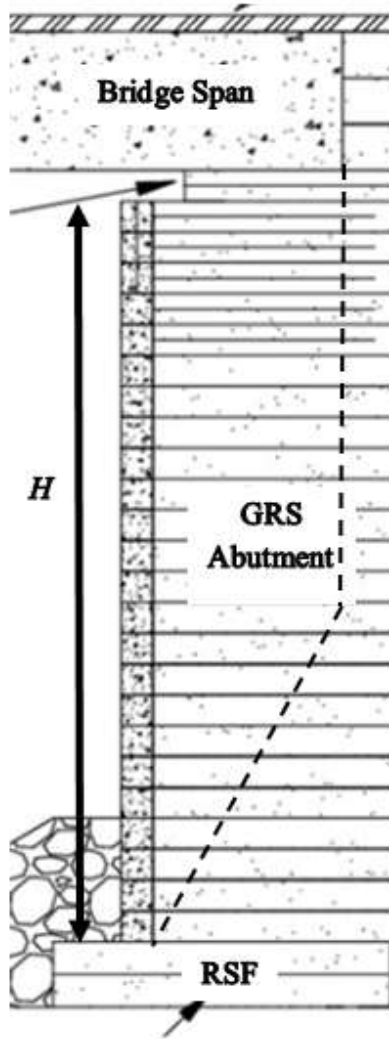


Figure 98

Effect of span length on the strain distribution along geosynthetics

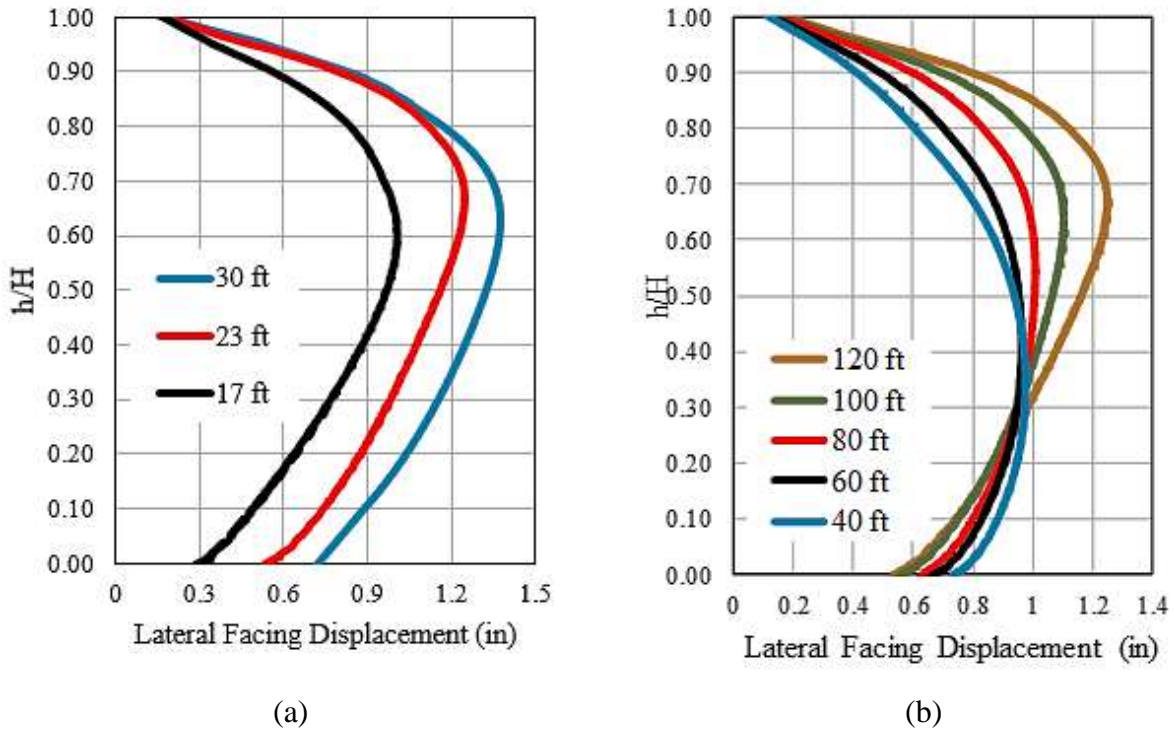


Figure 99

Effect of (a) abutment height; (b) span length on the lateral facing displacement

Effect of Reinforcement Spacing (S_v)

Four different reinforcement spacings, S_v , were considered and evaluated in this study: 4 in., 8 in., 12 in., and 16 in. Figure 100a presents the effect of the reinforcement spacing on the lateral facing displacement. The maximum lateral facing displacement increases from 1.1 in. for a reinforcement spacing of 4 in. to about 1.6 in. for a reinforcement spacing of 16 in. Figure 101 presents the strain distribution along the reinforcement at 20 and 80% of the abutment height as measured from the bottom of the abutment. It can be seen that for all cases the maximum strain envelope is located very close to the abutment face at $0.2 H$ of the abutment height and moves to about 4 ft. away from the abutment face at $0.8 H$. However, the magnitude of maximum strain increases with increasing the reinforcement spacing. The maximum strain increases from 0.62% for a reinforcement spacing of 4 in. to 1.63% for a reinforcement spacing of 16 in. at $0.8 H$ from bottom of abutment. The figures indicate that the reinforcement spacing has a significant influence on the strain distribution along the reinforcement and the lateral facing displacement for the same span length (120 ft.) and same abutment height (23 ft.) under the service loading condition (Figure 100b).

Effect of Reinforcement Stiffness (EA)

Five different reinforcement stiffness measurements, EA , were considered and evaluated in this study: 20.5, 41, 61.5, 82, and 102.5 k/ft. Figure 102 presents the strain distribution along the reinforcement at 20, 40, 60, and 80% of the abutment height as measured from the bottom of abutment. Similar to the effect of reinforcement spacing, reinforcement stiffness affects the magnitude of the strain but does not affect either the shape of the strain distribution or the location of maximum strain. The maximum strain decreases from about 1.3% for a reinforcement stiffness of 20.5 k/ft to about 0.5% for a reinforcement stiffness of 102.5 k/ft. It can be seen that increasing the reinforcement stiffness from 20.5 k/ft to 61.5 k/ft has significant effect on the reinforcement strain (e.g., the strain decreases from 1.3% to 0.7% at 0.8 H). However, after that, the effect of reinforcement stiffness tends to decrease (e.g., the strain decreases from 0.7% to 0.5% when the reinforcement stiffness increases from 61.5 k/ft to 102.5 k/ft at 0.8 H). Figure 100b presents the effect of reinforcement stiffness on the lateral displacement of wall facing. The maximum lateral facing displacement decreases from 1.45 in. for a reinforcement stiffness of 20.5 k/ft to 1 in. for a reinforcement stiffness of 102.5 k/ft.

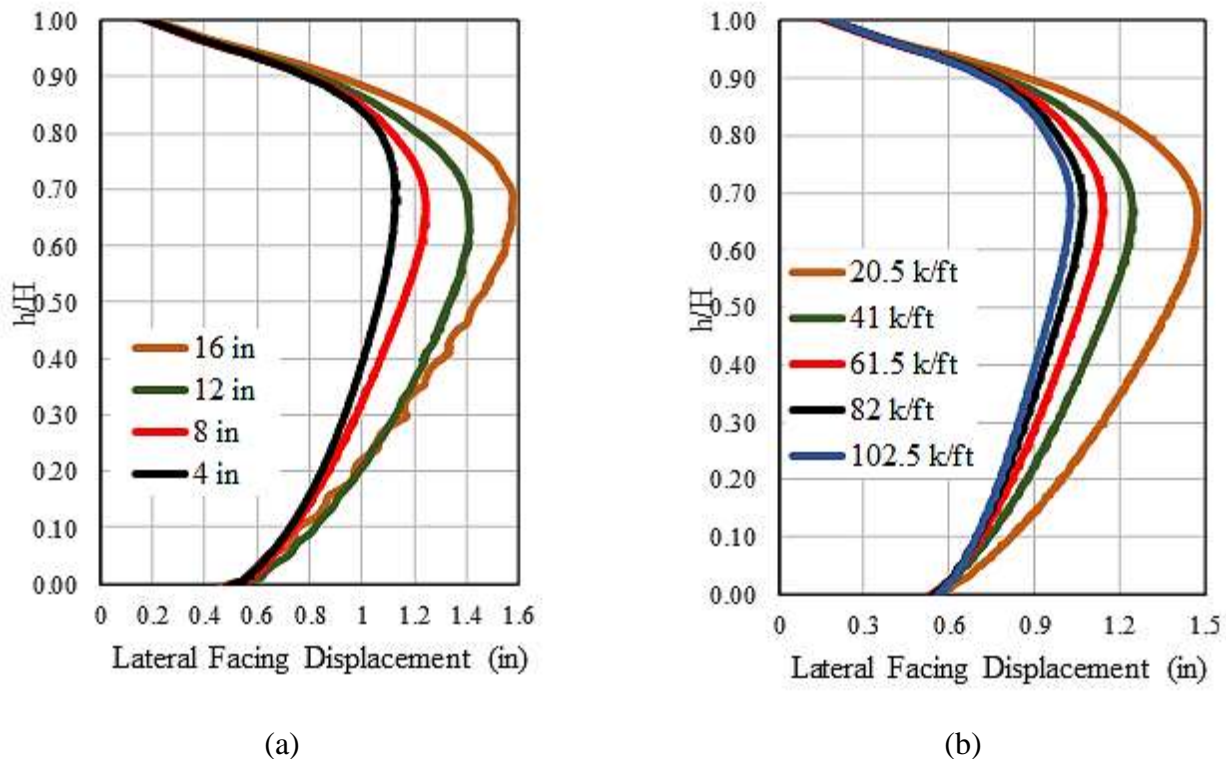


Figure 100
Effect of reinforcement a) spacing; b) stiffness on the lateral facing displacement

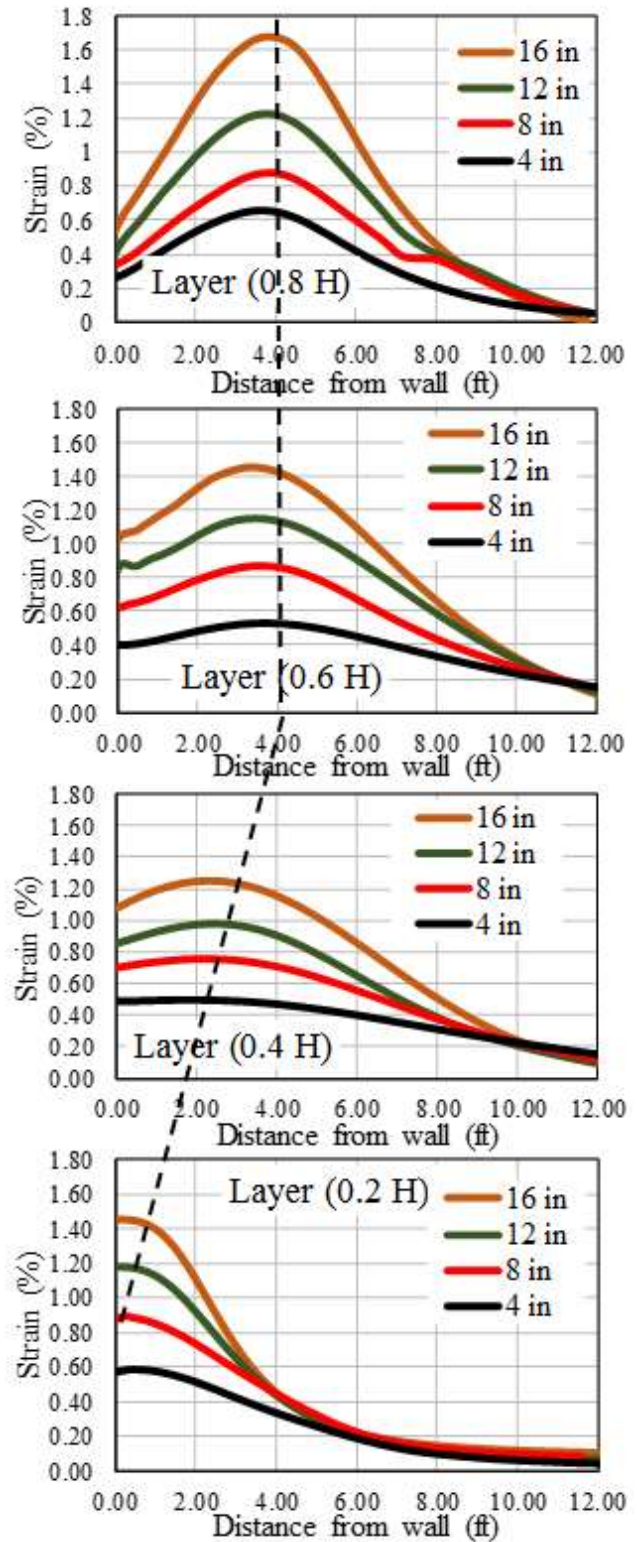
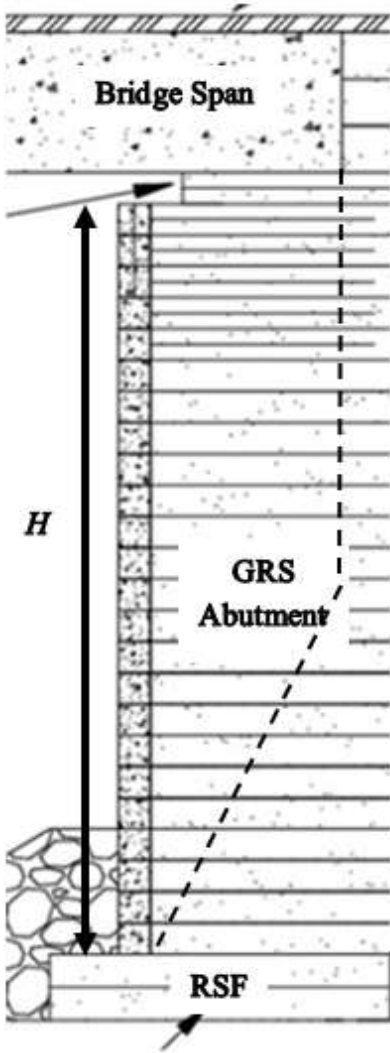


Figure 101
Effect of reinforcement spacing on the strain distribution along geosynthetics

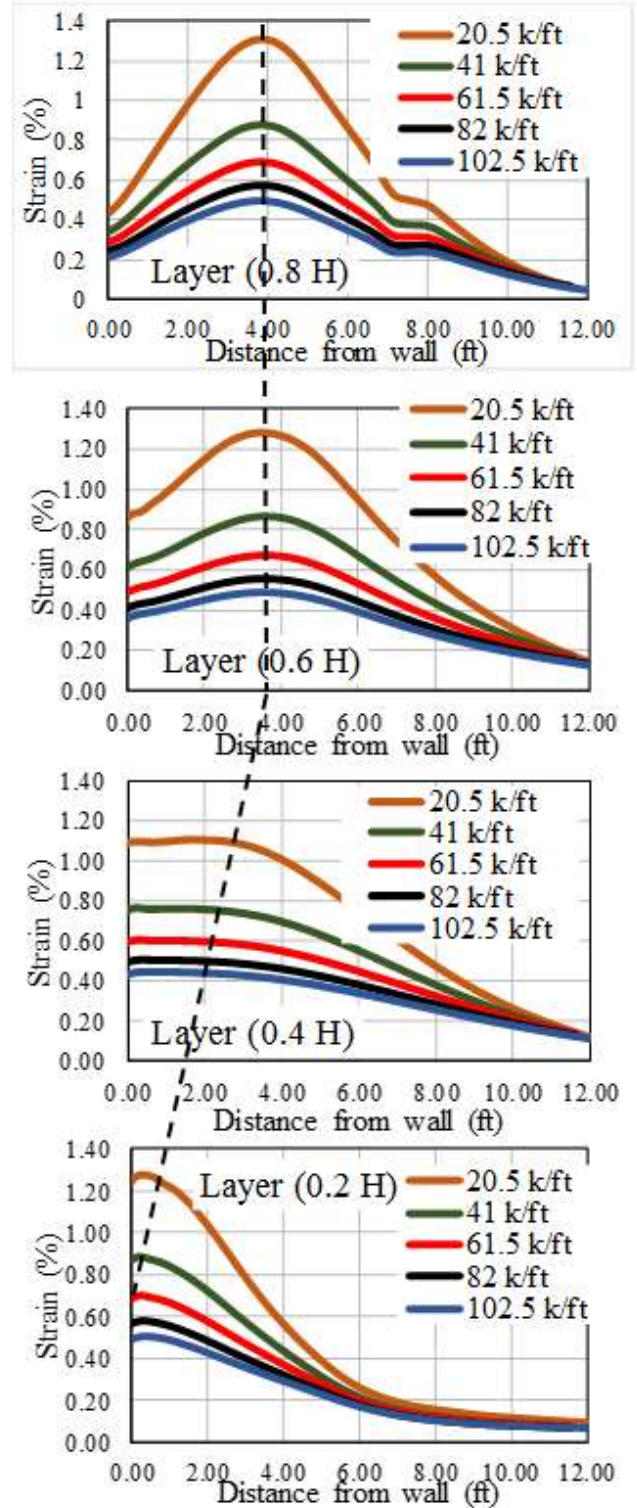
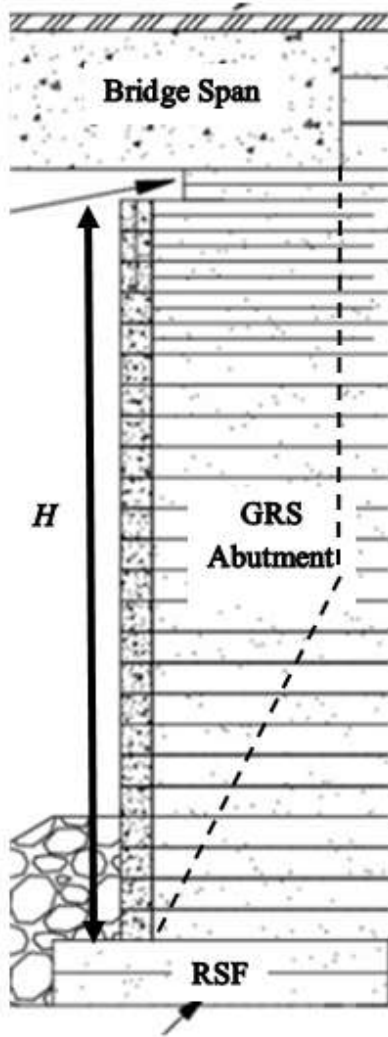


Figure 102
Effect of reinforcement stiffness on the strain distribution along geosynthetics

Effect of Internal Friction Angle (ϕ)

Four different internal friction angles of the backfill materials, ϕ , were considered and evaluated in this study: 35° , 40° , 45° , and 50° . Figure 103 presents the strain distribution along the reinforcement at 20 and 80% of the abutment height as measured from the bottom of the abutment. It can be seen that for all cases the maximum strain envelope is located very close to the abutment face at $0.2 H$ of the abutment height and moves to about 4 ft. away from the abutment face at $0.8 H$. However, the magnitude of maximum strain decreases with increasing the friction angle. The maximum strain increases from 0.85% for a friction angle of 50° to 1.30% for a friction angle of 35° at $0.8 H$ from bottom of abutment. Figure 105a presents the effect of the friction angle on the lateral facing displacement. The maximum lateral facing displacement increases from 1.3 in. for a friction angle of 50° to about 2.1 in. for a friction angle of 35° . The figures indicate that the friction angle has a medium impact on the strain distribution along the reinforcement and a significant impact on the lateral facing displacement for the same span length (120 ft.) and same abutment height (23 ft.) under the service loading condition.

Effect of Length of Reinforcement (L_r)

Four different reinforcement lengths, L_r , were considered and evaluated in this study: $L_r = 0.3 H$, $0.5 H$, $0.7 H$, and $1.0 H$. Figure 104 presents the effect of reinforcement length on the strain distribution along the geosynthetic reinforcement at 20, 40, 60 and 80% of the abutment height as measured from the bottom of the abutment. It can be seen that the maximum strain is not affected by reinforcement length. Figure 105b presents the effect of the reinforcement length on the lateral facing displacement. Reinforcement length has low impact on the lateral facing displacement, especially for $L_r \geq 0.5 H$. The lateral facing displacement increases from around 1.2 in. for $L_r \geq 0.5 H$ to around 1.4 in. for $L_r = 0.3 H$, which indicates that increasing the reinforcement length will not decrease the lateral facing displacement.

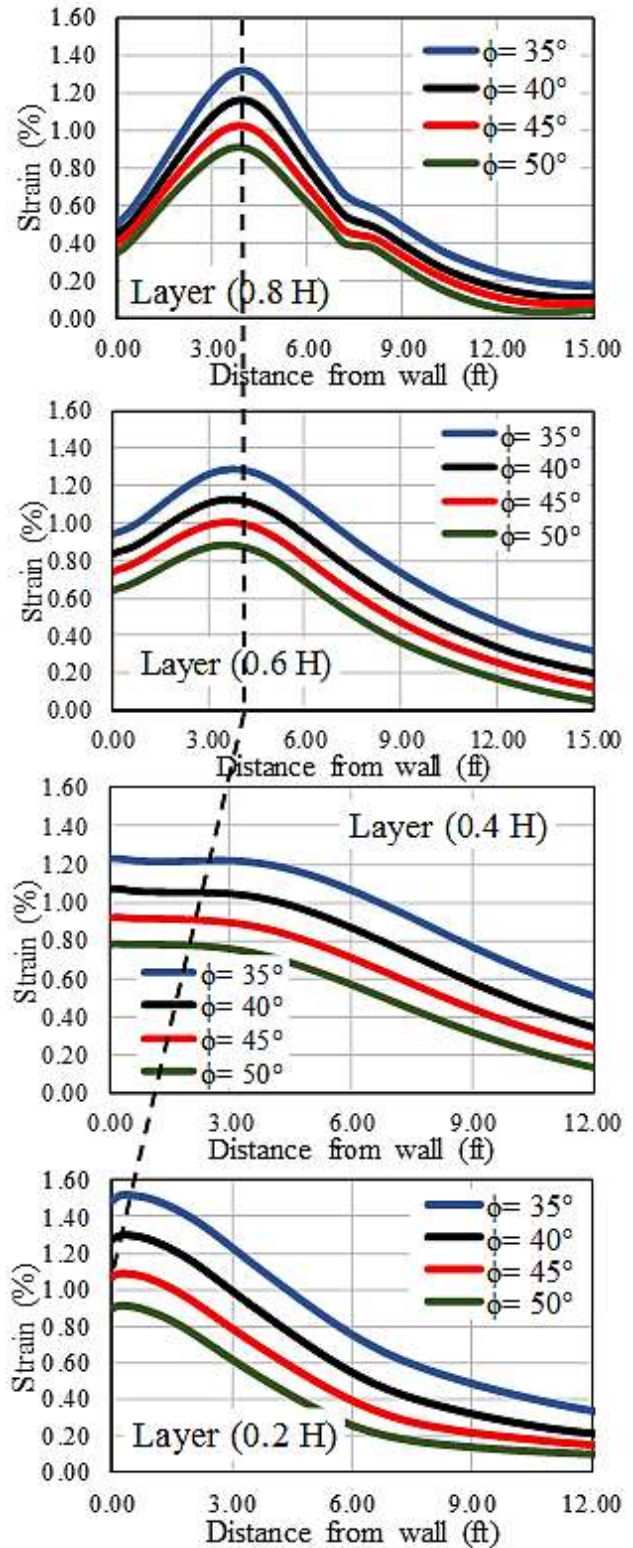
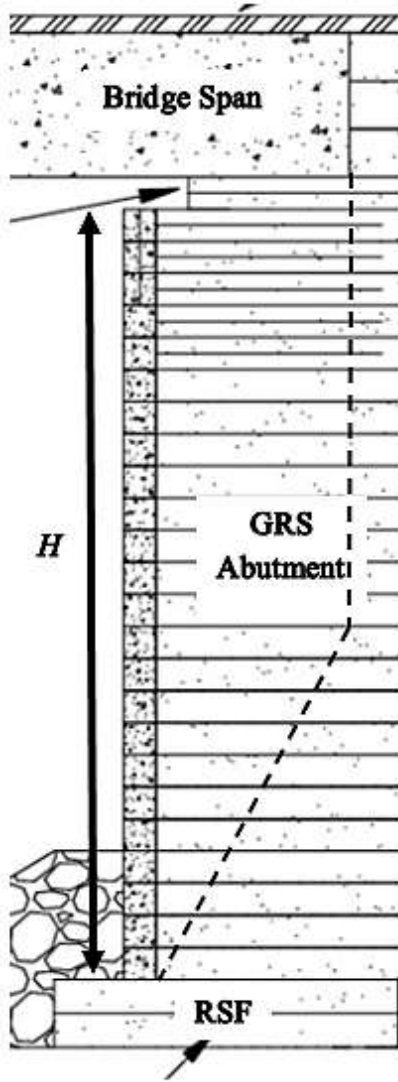


Figure 103

Effect of internal friction angle on the strain distribution along geosynthetics

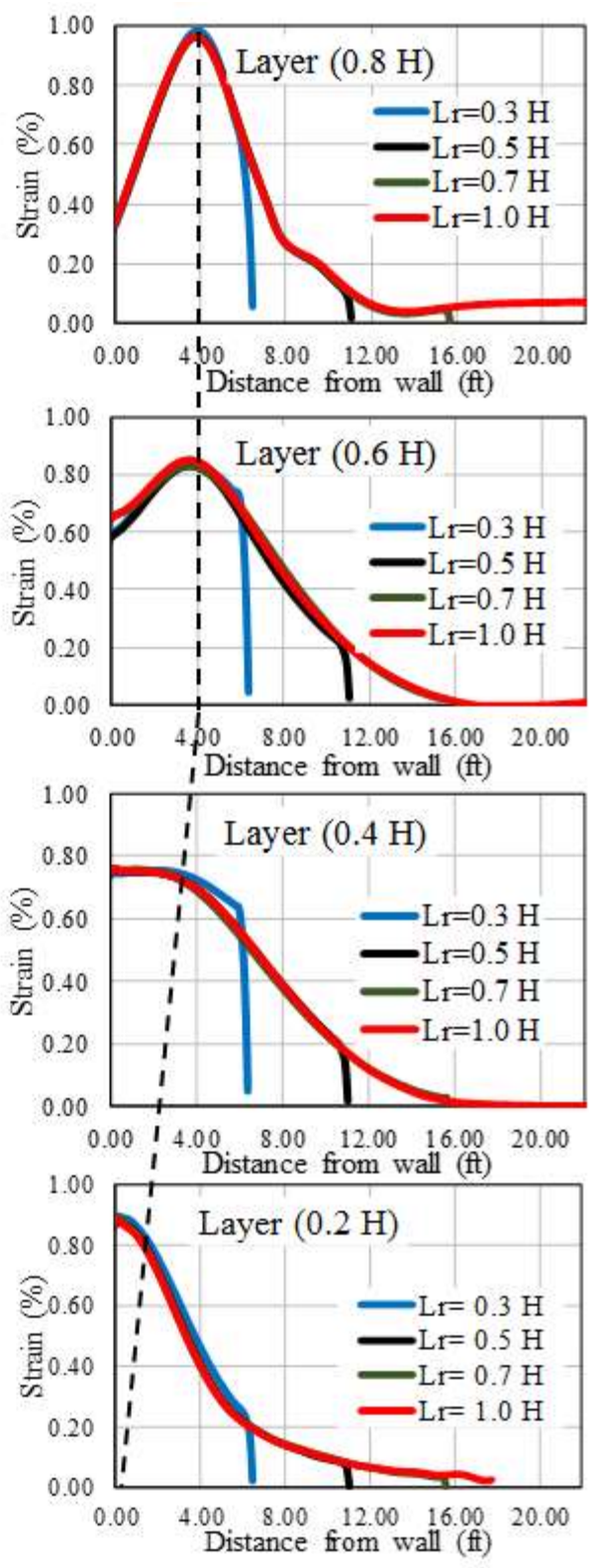
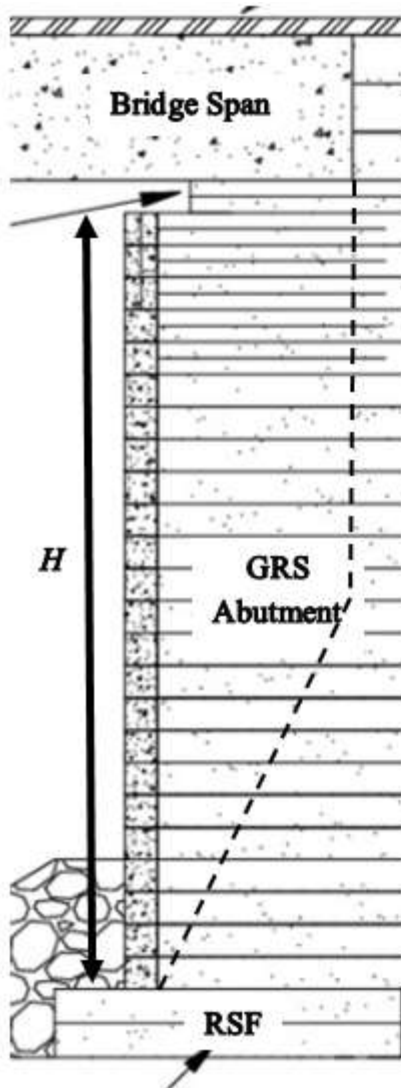


Figure 104
Effect of reinforcement length on the strain distribution along geosynthetics

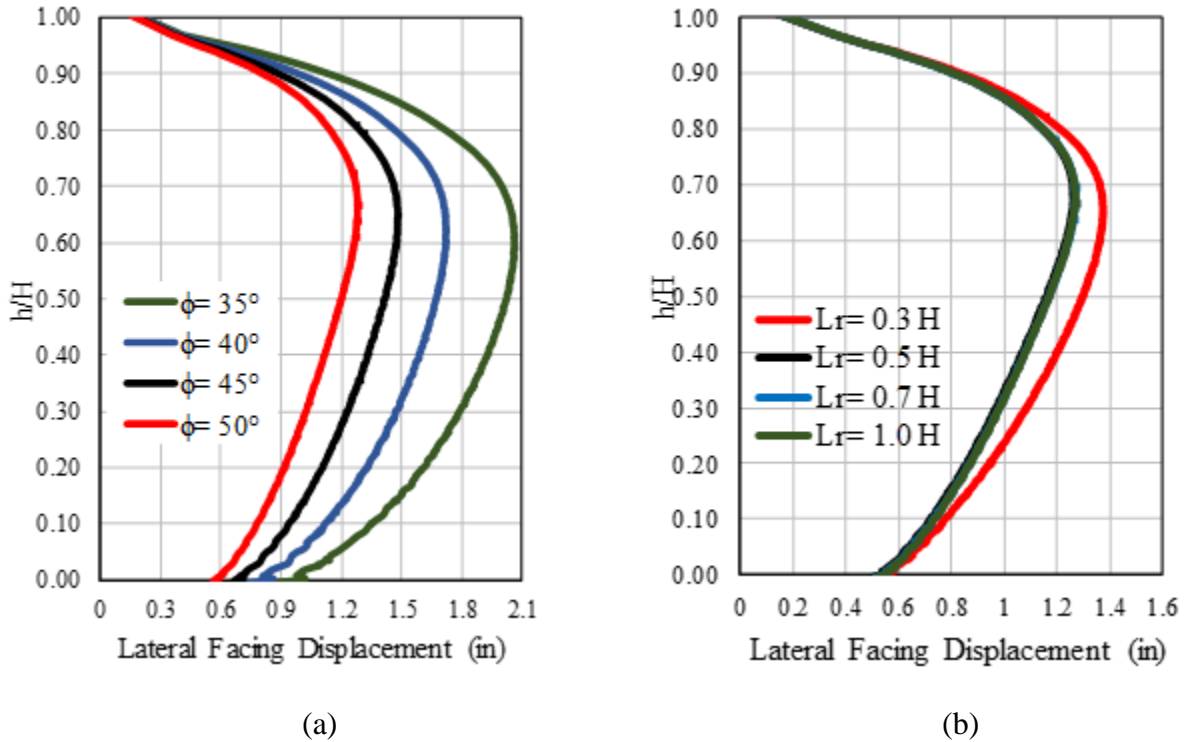


Figure 105

Effect of a) friction angle; b) reinforcement length on the lateral facing displacement

Effect of Width of Reinforced Soil Footing (B_{RSF})

According to the FHWA, the total width of the RSF should extend beyond the base (B) of the GRS abutment by one-fourth the width of the base. In this section, three different widths of RSF, B_{RSF} , were considered and evaluated: $B_{RSF} = 1.0 B$, $1.25 B$, and $1.5 B$. Figure 107 presents the effect of RSF width on the strain distribution along the geosynthetic reinforcement at 20, 40, 60, and 80% of the abutment height as measured from the bottom of the abutment. It can be seen that the maximum strain is not affected by RSF width. Figure 106a presents the effect of the RSF width on the lateral facing displacement. The width of RSF has minimal effect on the lateral facing displacement, which also indicates that increasing the width of RSF will not affect the lateral facing displacement.

Effect of Secondary Reinforcement (Bearing Bed Reinforcement)

Simulations were conducted with bearing and without bed reinforcement layers placed underneath the bridge seat (or strip footing). Figure 108 presents the effect of secondary reinforcement on the strain distribution along the reinforcement at 20, 40, 60, and 80% of the abutment height as measured from the bottom of the abutment. It can be seen that the maximum strain envelope is located near the abutment face at $0.2 H$ and moving about 4 ft. away from the abutment face at $0.8 H$

H for all cases. It can be seen that the maximum strain along the reinforcement at 20, 40, and 60% of the abutment height as measured from the bottom of the abutment decreases slightly when bearing bed reinforcement is included. However, the magnitudes of maximum strains along the reinforcement at 80% of the abutment height as measured from the bottom of the abutment (i.e., within bearing bed zone) increased by about 20% for reinforcements, which are still less than the recommended value by FHWA (2%). The FE results indicate that the secondary reinforcement has slightly effect on the performance of GRS-IBS in terms of lateral deformation of wall face. Figure 106b shows that the lateral facing deformation is slightly decreasing when the bearing bed reinforcement is included except for a span length of 60 ft. The figures indicate that the secondary reinforcement has a significant effect only on the strain distribution along the reinforcement at 80% of the abutment height as measured from the bottom of the abutment.

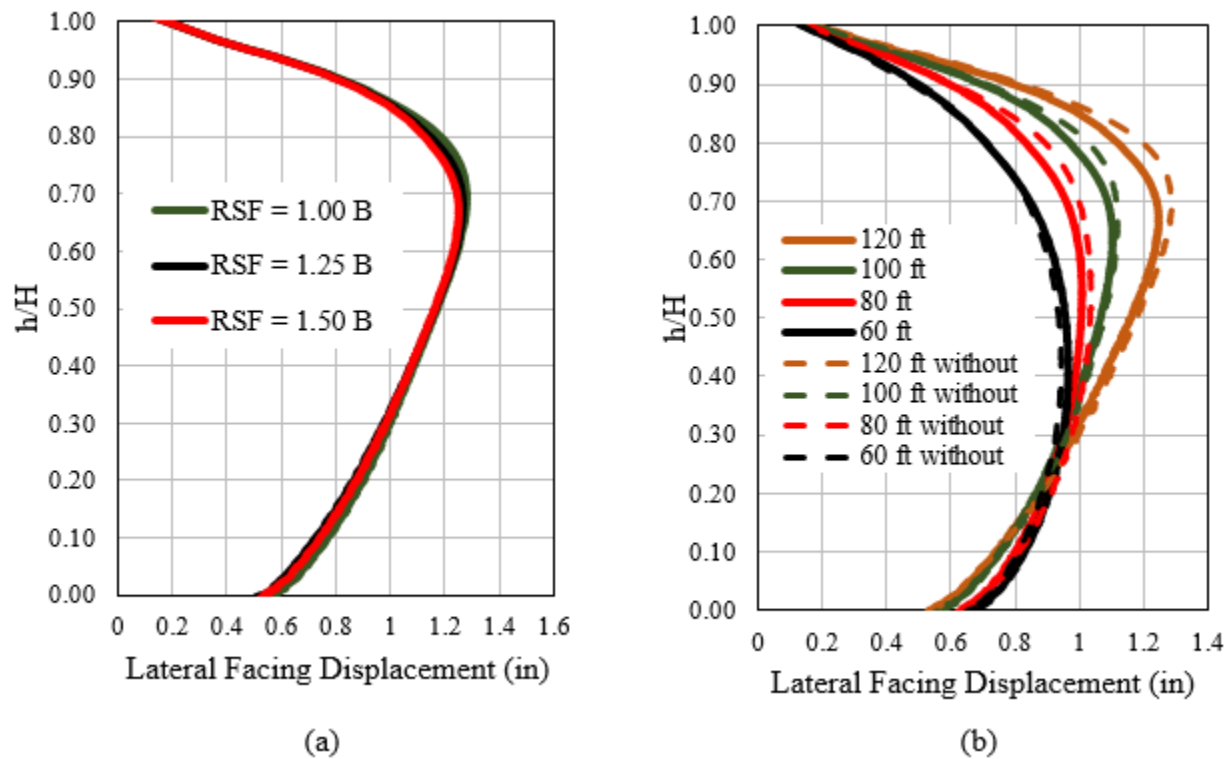


Figure 106

Effect of (a) width of RSF; (b) secondary reinforcement on the lateral facing displacement

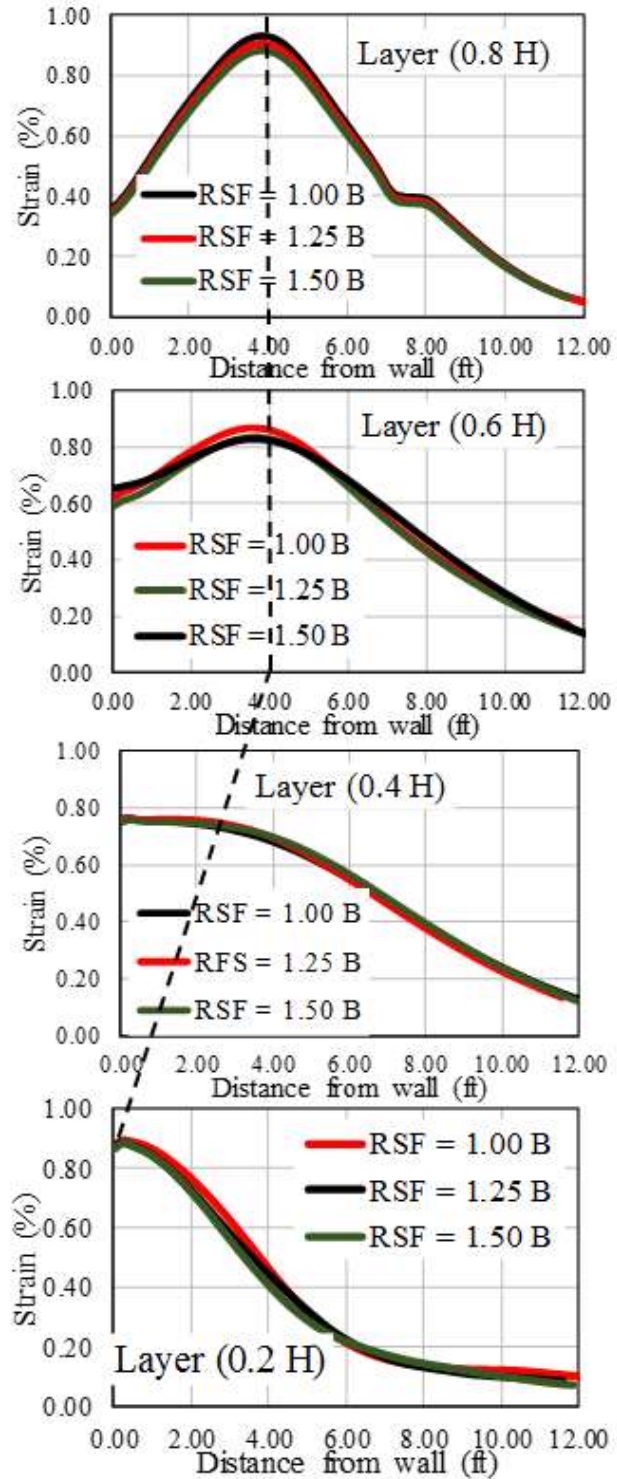
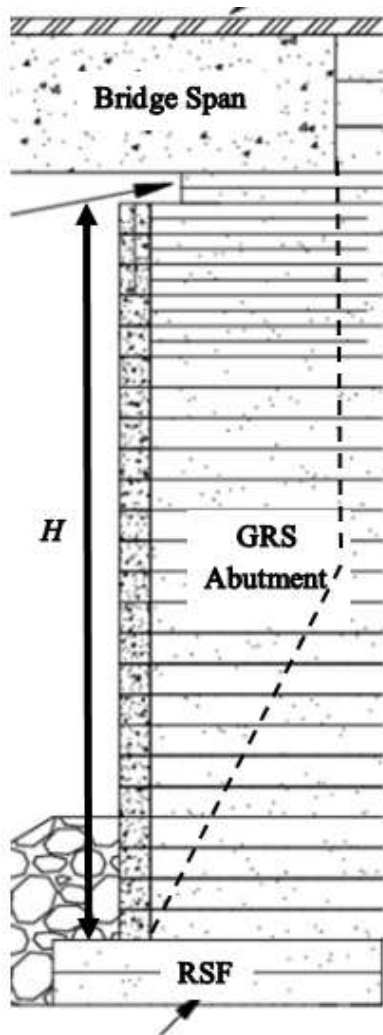


Figure 107
Effect of width of reinforced soil footing (B_{RSF}) on the strain distribution along geosynthetics

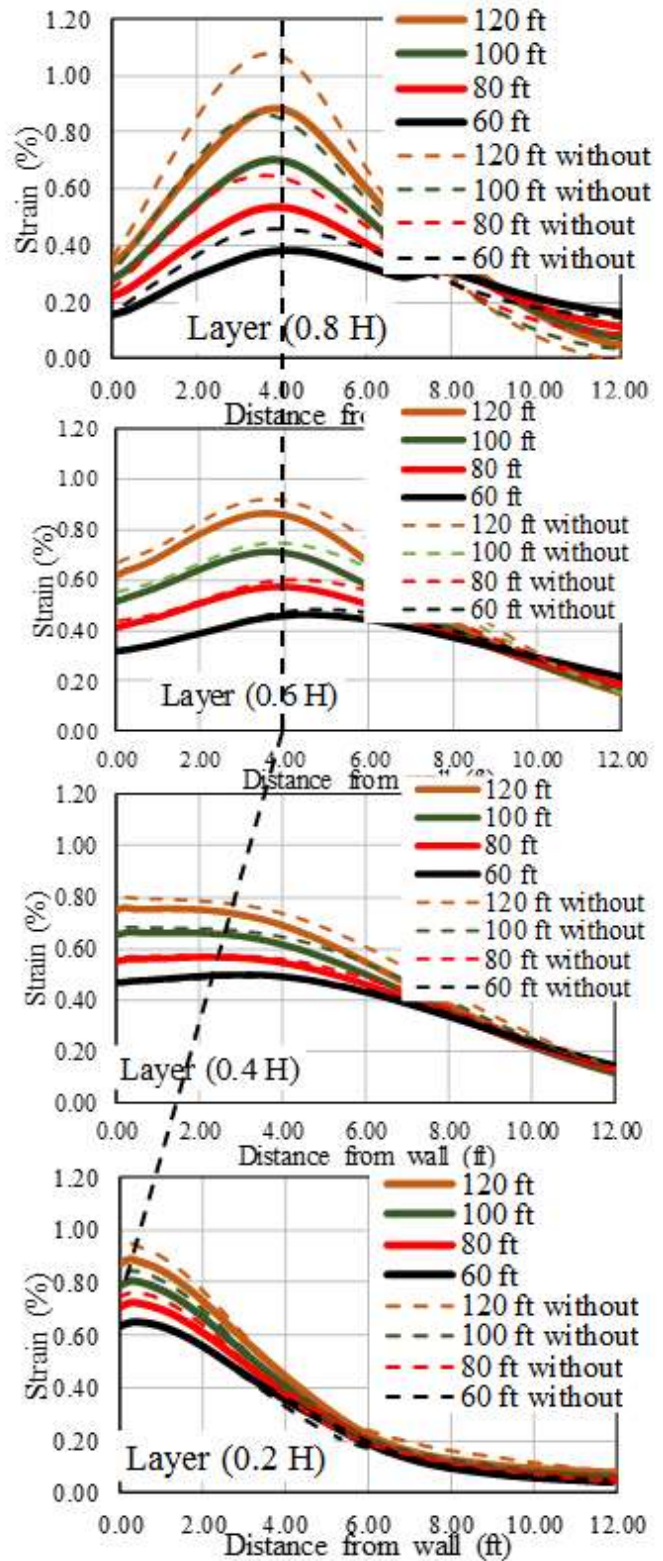
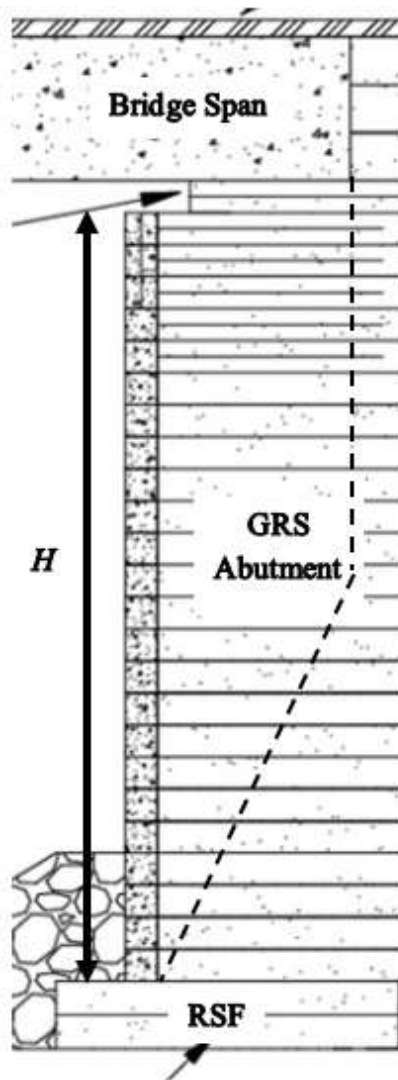


Figure 108

Effect of secondary reinforcement on the strain distribution along geosynthetics

Effect of Setback Distance (a_b)

Simulations were conducted for five different setback distance $a_b = 8, 16, 24, 32,$ and 40 in. from the abutment face. Figure 109 presents the effect of the setback distance on the strain distribution along the reinforcement at 20, 40, 60, and 80% of the abutment height as measured from the bottom of the abutment. It can be seen that the maximum strain along the reinforcement slightly increases by increasing the setback distance away from the abutment face and the location of maximum strain shifts to right due to increasing the span length associated with increasing the setback distance. Figure 112a shows that the lateral facing deformation is slightly increasing when the setback distance is increased. The figures indicate that increasing the setback distance will not necessary improve the GRS-IBS performance.

Effect of Foundation Type

Three different foundation types were simulated using the Modified Cam clay model. The parameters were selected from previous work by Nazzal to represent weak, medium and stiff subgrades. The parameters are presented in Table 14 [91]. Figure 110 presents the effect of foundation type on the strain distribution along the geosynthetic reinforcement at 20, 40, 60, and 80% of the abutment height as measured from the bottom of the abutment. It can be seen that the maximum strain is significantly affected by conditions of subgrade soil. The maximum strain increases from 0.5% for stiff subgrade soil to around 0.9% for a weak soft subgrade soils at $0.6 H$ above the bottom of the abutment. Figure 112b shows that the lateral facing displacement is highly affected by the subgrade soil conditions. The lateral facing displacement increases from around 1.0 in. for a stiff subgrade soil to around 1.3 in. for weak subgrade soil, which indicates that care must be taken when designing a GRS abutment on soft subgrade soils to avoid excessive lateral facing deformation.

Table 14
Modified Cam-Clay Model parameter for different subgrade soils

Subgrade	G (psi)	M	λ	κ	e_0	CBR
Soft	750	0.65	0.225	0.11	1.35	1.5
Medium	2900	1	0.11	0.084	0.95	7
Stiff	5076	1.56	0.022	0.005	0.54	15

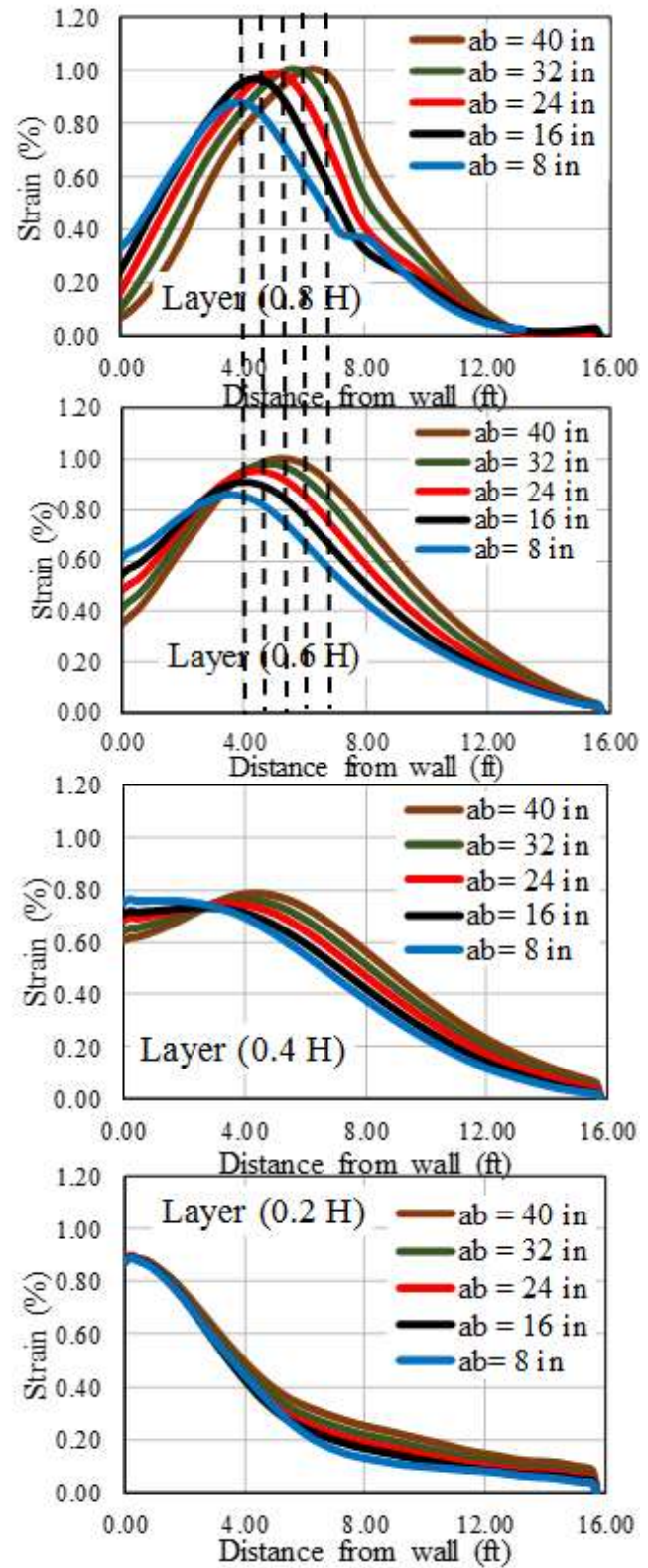
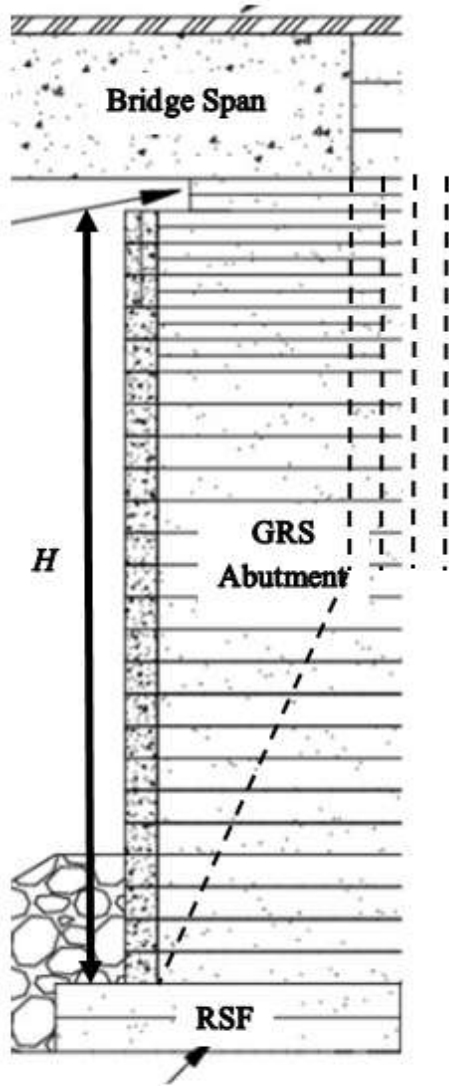


Figure 109

Effect of setback distance on the strain distribution along geosynthetics

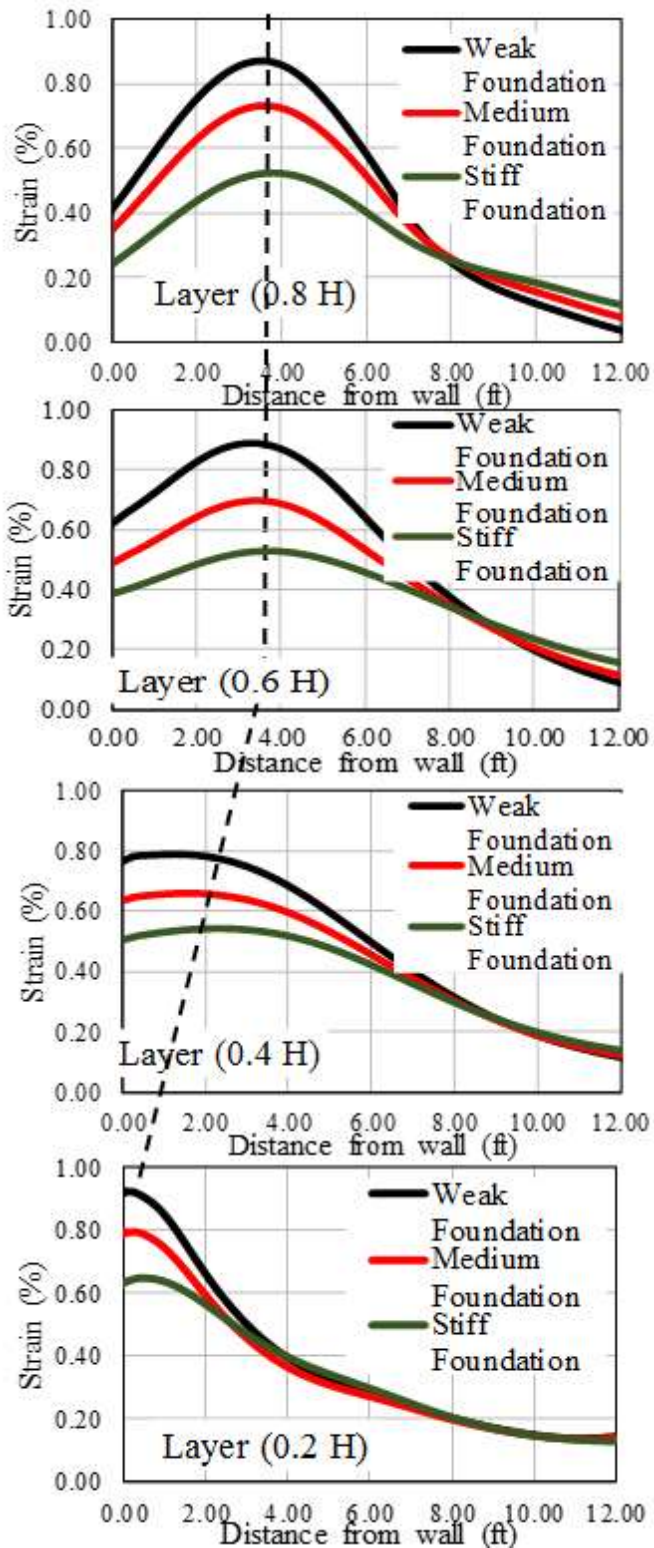
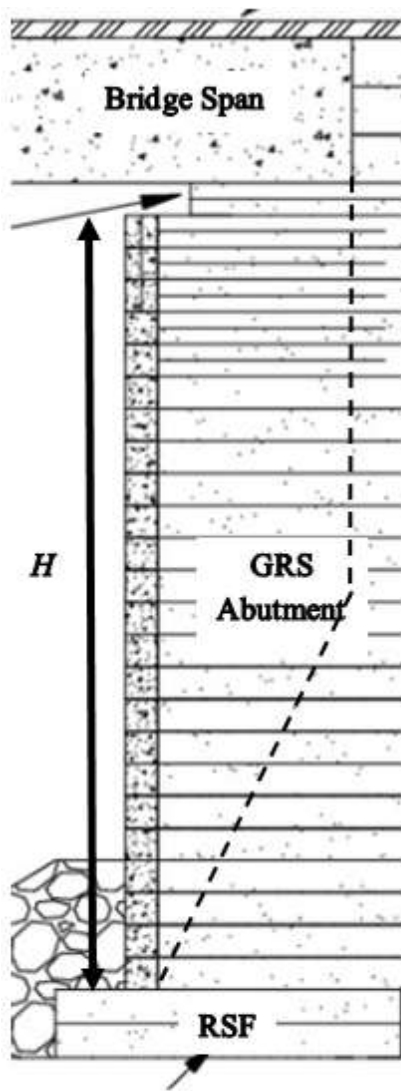


Figure 110
Effect of foundation type on the strain distribution along geosynthetics

Effect of Bearing Width (b)

Simulations were conducted for five different bearing widths ($b = 48, 55, 63, 71, \text{ and } 79 \text{ in.}$) to study the effect of bearing width on the GRS-IBS behavior in terms of maximum strain distribution along the reinforcement and lateral facing pressure. Figure 111 presents the effect of the bearing width on the strain distribution along the reinforcement at 20, 40, 60, and 80% of the abutment height as measured from the bottom of the abutment. It can be seen that the maximum strain along the reinforcement slightly decreases by increasing the bearing width; this is most probably due to increasing the area underneath the bridge span, which will reduce the pressure on top of the GRS abutment. It was noted that the location of the maximum strain is associated with the bearing width, in which the maximum strain envelope is located right under the inner edge of the bearing width for the reinforcement layer at $0.8 H$ of the abutment height as measured from the bottom of the abutment. This result is very similar to the punching shear failure envelope defined by a previous study conducted by Chen et al. on reinforced crushed limestone underneath spread footing [92]. Takemura et al. investigated the failure mechanism of reinforced sand by using centrifuge test [93]. Their results showed that the intensely shear bands were developed from the edges of the footing and is extending vertically downward. Figure 112c shows that the lateral facing deformation is increasing by decreasing the bearing width. The figures indicate that increasing the bearing width will improve the GRS-IBS performance in terms of lateral facing displacement and maximum strain distribution especially at the top of GRS abutment.

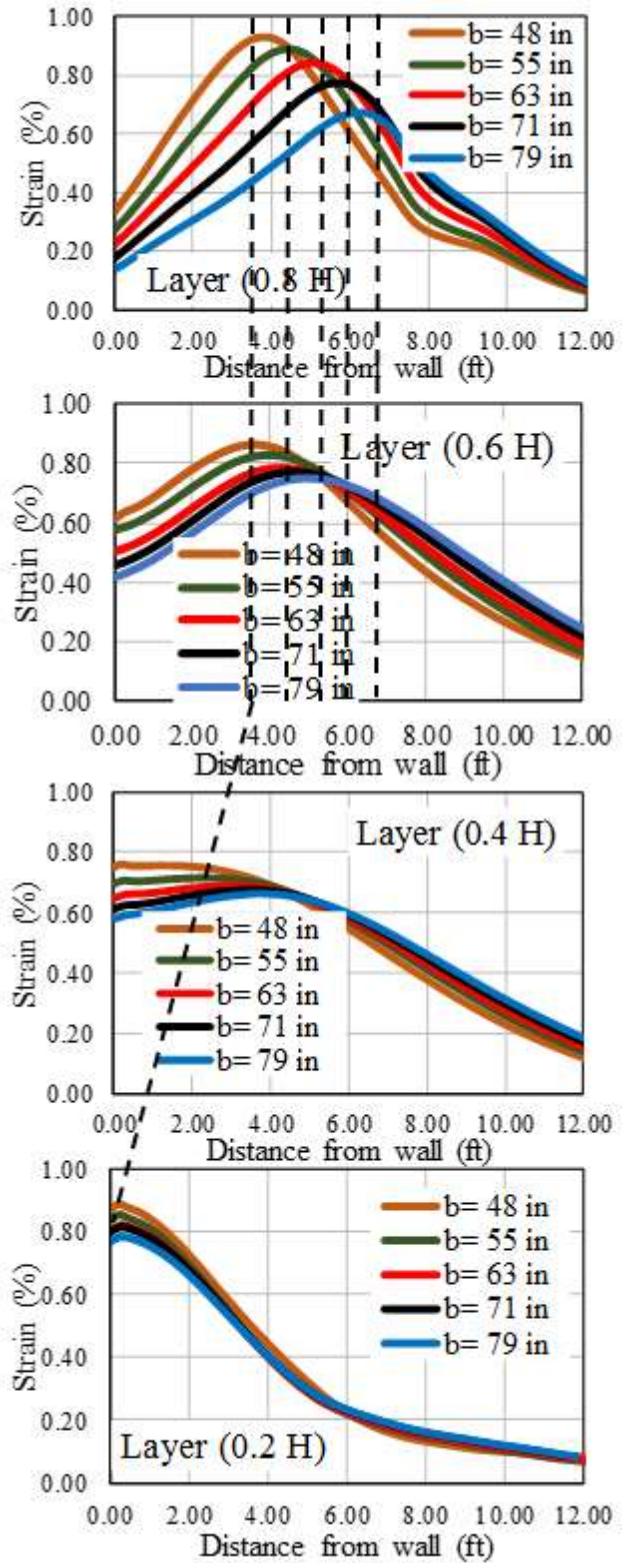
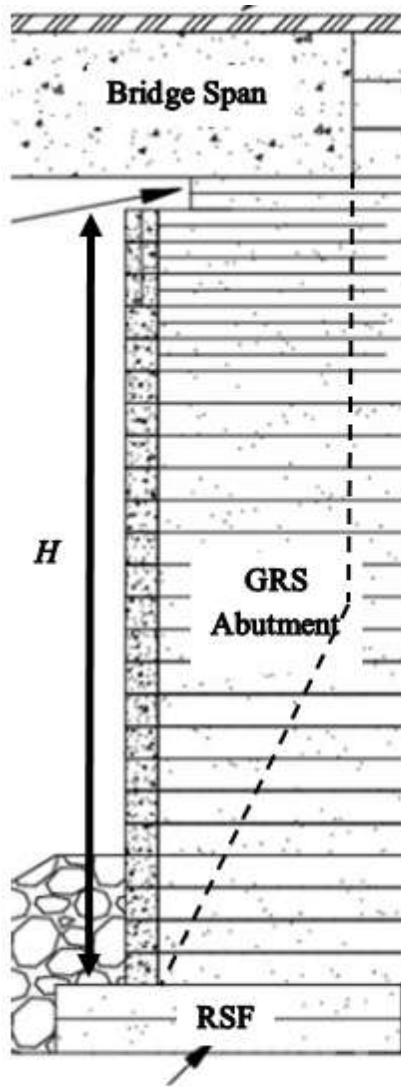
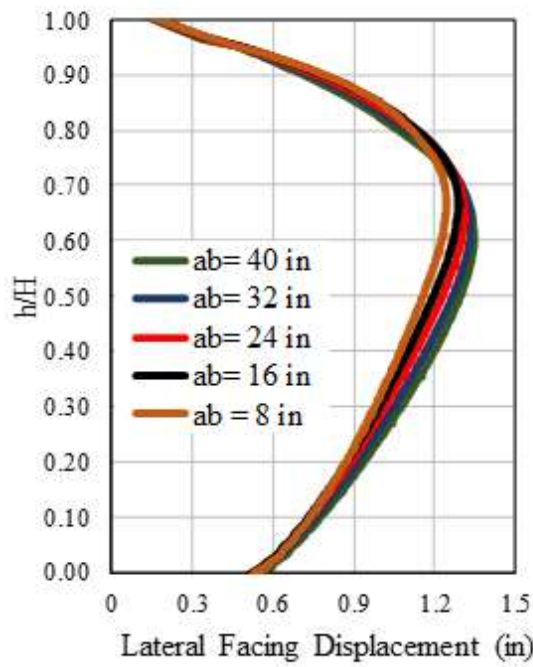
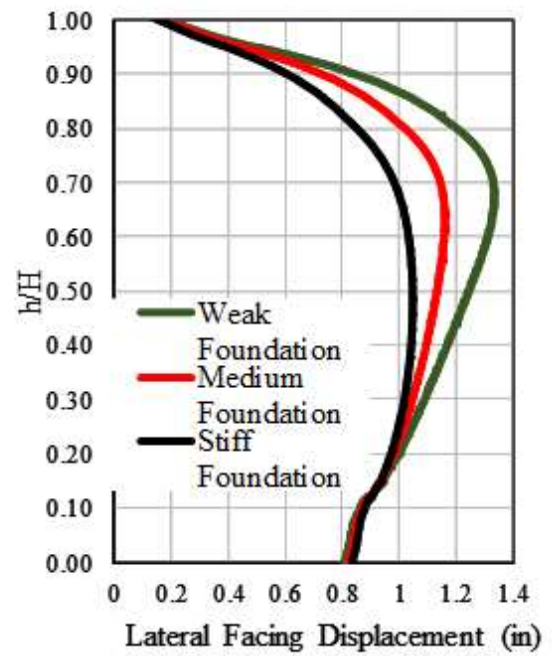


Figure 111

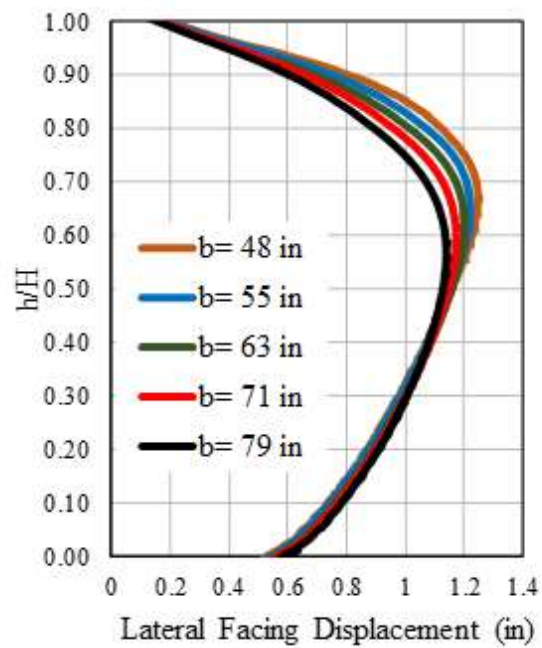
Effect of bearing width on the strain distribution along geosynthetics



(a)



(b)



(c)

Figure 112

Effect of (a) setback distance; (b) foundation type; (c) bearing width on the lateral facing displacement

Tables 15 and 16 present summary of the maximum strain distribution along the geosynthetic and lateral facing displacement for the parametric results.

Table 15
Summary of maximum strain results

Maximum strain (%)									
	0.2 H	0.4 H	0.6 H	0.8 H		0.2 H	0.4 H	0.6 H	0.8 H
Effect of Reinforcement Spacing (in.)					Effect of Internal Friction Angle (°)				
4	0.6	0.5	0.5	0.6	35°	1.5	1.2	1.3	1.3
8	0.9	0.7	0.8	0.9	40°	1.3	1	1.1	1.1
12	1.2	1	1.2	1.2	45°	1.1	0.9	1	1
16	1.4	1.2	1.4	1.7	50°	0.9	0.8	0.9	0.9
Effect of Reinforcement Stiffness (k/ft.)					Effect of Span Length (ft.)				
20.5	1.3	1.1	1.3	1.3	40	0.6	0.4	0.4	0.3
41	0.9	0.8	0.9	0.9	60	0.65	0.5	0.5	0.4
61.5	0.72	0.6	0.7	0.7	80	0.7	0.6	0.6	0.5
82	0.6	0.5	0.6	0.6	100	0.8	0.65	0.7	0.7
102.5	0.5	0.42	0.5	0.5	120	0.9	0.8	0.9	0.9
Effect of Reinforcement Length					Effect of Width of RSF				
0.3 H	0.86	0.75	0.85	1.0	1.00 B	0.9	0.8	0.8	0.9
0.5 H	0.86	0.75	0.85	1.0	1.25 B	0.9	0.8	0.8	0.9
0.7 H	0.86	0.75	0.85	1.0	1.50 B	0.9	0.8	0.8	0.9
1.0 H	0.86	0.75	0.85	1.0					
Effect of Abutment Height (ft.)					Effect of Foundation Type				
17	0.7	0.7	0.7	0.8	Weak	0.9	0.8	0.9	0.9
23	0.8	0.8	0.9	0.9	Medium	0.8	0.7	0.7	0.7
30	1.1	0.9	1.1	1.0	Stiff	0.6	0.6	0.5	0.5
Effect of Setback Distance (in.)					Effect of Bearing Width (in.)				
8	0.9	0.8	0.86	0.9	48	0.85	0.8	0.8	0.9
16	0.9	0.8	0.9	0.97	55	0.85	0.75	0.75	0.85
24	0.9	0.8	0.95	1.0	63	0.8	0.7	0.7	0.8
32	0.9	0.8	1.0	1.0	71	0.8	0.7	0.7	0.75
40	0.9	0.8	1.0	1.0	79	0.8	0.7	0.7	0.7

Table 16
Summary of maximum lateral facing deformation

Lateral Facing Deformation (in.)			
Effect of Reinforcement Spacing (in.)		Effect of Internal Friction Angle (°)	
4	1.1	35°	2.1
8	1.2	40°	1.7
12	1.4	45°	1.5
16	1.6	50°	1.3
Effect of Reinforcement Stiffness (k/ft.)		Effect of Span Length (ft.)	
20.5	1.5	40	1.0
41	1.2	60	1.0
61.5	1.1	80	1.0
82	1.0	100	1.1
102.5	0.9	120	1.3
Effect of Reinforcement Length		Effect of Width of RSF	
0.3 <i>H</i>	1.4	1.00 <i>B</i>	1.25
0.5 <i>H</i>	1.3	1.25 <i>B</i>	1.23
0.7 <i>H</i>	1.3	1.50 <i>B</i>	1.22
1.0 <i>H</i>	1.3		
Effect of Abutment Height (ft.)		Effect of Foundation Type	
17	1.0	Weak	1.3
23	1.2	Medium	1.2
30	1.4	Stiff	1.1
Effect of Setback Distance (in.)		Effect of Bearing Width (in.)	
8	1.3	48	1.22
16	1.3	55	1.2
24	1.3	63	1.2
32	1.3	71	1.2
40	1.3	79	1.15

Effect of Soil Compaction

This section presents the effect of soil compaction on the performance of the GRS-IBS in terms of lateral deformation of wall facing and strain distribution along geosynthetics. Four different cases were considered and compared with the control section that has an internal friction angle $\phi = 50^\circ$ and a geotextile stiffness of 41 kips/ft. (600 kN/m) spaced at 8 in. The first case (Case 1) simulates the reduced compaction (and hence strength/stiffness of backfill properties) within 3 ft. from the

wall block facing (for 75% degree of compaction), with an average angle of internal friction = $\phi = 45^\circ$. Case 2 simulates the condition of reduced compaction all over the entire backfill material of the abutment (for 75% degree of compaction), with an average angle of internal friction $\phi = 45^\circ$. Case 3 simulates the worst scenario condition with low value of internal friction angle $\phi = 35^\circ$, and low value of geotextile stiffness of 20.5 kips/ft. (300 kN/m). Case 4 simulates the best scenario condition using high value of internal friction angle $\phi = 50^\circ$, and high value of geotextile stiffness of 82 kips/ft. (1200 kN/m). In all cases, the vertical spacing was fixed to 8 in.

Figure 113 presents the effect of soil compaction on the strain distribution along the geosynthetic reinforcement at 20, 40, 60, and 80% of the abutment height as measured from the bottom of the abutment, and the comparison with the results of control section. It can be seen that the magnitude of maximum strains are highly affected by the soil compaction, such that values of maximum strains increase with decreasing the degree of soil compaction. For the reinforcement layer located at 80% of the abutment height from the bottom, the maximum strain increases from about 0.9% for the control section to about 1.4% for Case 2 (75% reduction of compaction for the entire abutment), and to about 2.0% for the worst scenario Case 3. The values of maximum strain for Case 2 (75% reduction of compaction for the entire abutment) are slightly higher than those for Case 1 (75% reduction of compaction within 3 ft. from wall face). The observed results indicates that failure to deliver a proper compaction might increase the geotextile strains higher than the range specified in the FHWA manual (less than 2%) [5].

Figure 114 presents the effect of the soil compaction on the lateral deformation of wall facing, and the comparison with results of the control section. As can be seen in the figure, the maximum lateral facing deformation increases from about 1.2 in. for the control section to about 2.1 in. for Case 2 (25% reduction of compaction for the entire abutment), and to around 2.5 in. for the worst scenario Case 3. This clearly indicates that decreasing the soil compaction will increase the lateral deformation of wall facing.

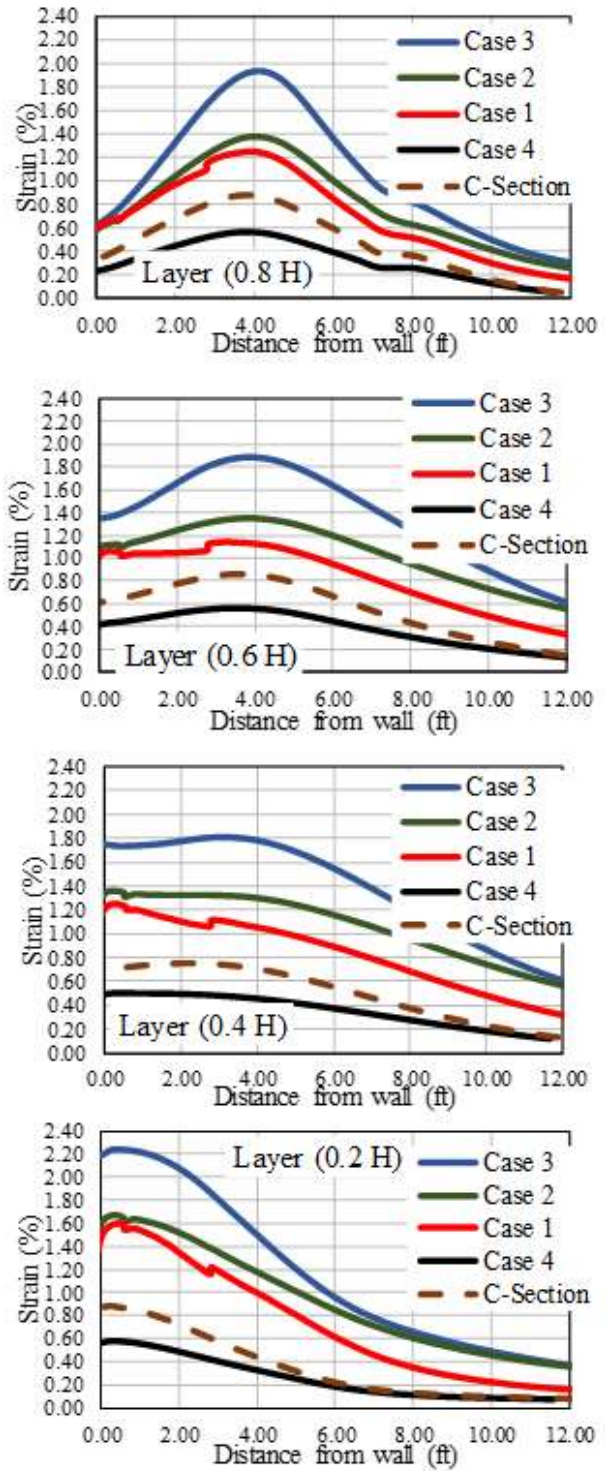
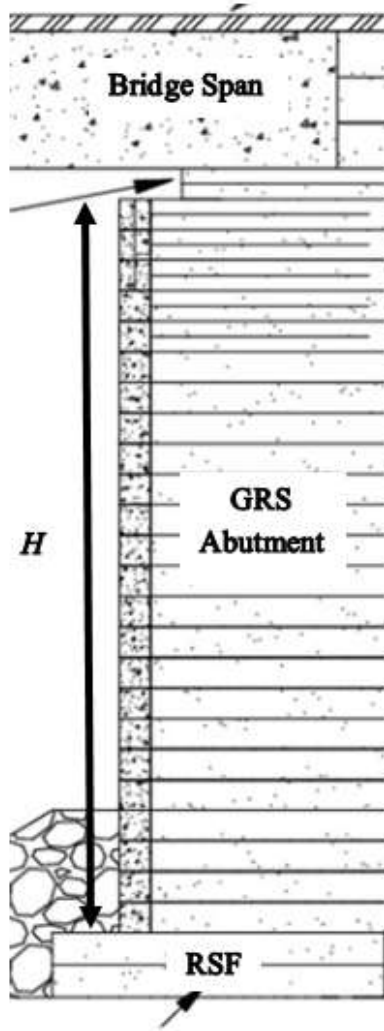


Figure 113
Effect of soil compaction on the strain distribution along geosynthetics

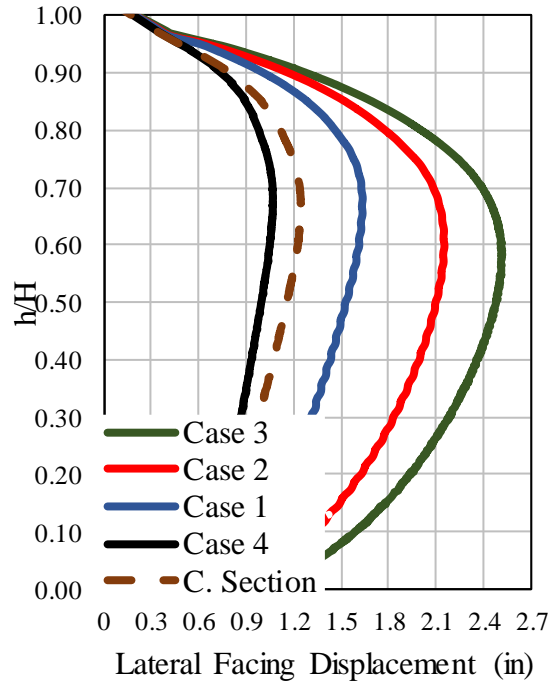


Figure 114

Effect of soil compaction on the lateral facing displacement

Location of Maximum Strain Envelope

Figure 115 presents the location of maximum strain envelope with depth for all cases. The figure depicts the potential failure envelope due to the effect of reinforcement spacing, reinforcement stiffness, and span length for the same height of 23 ft. It can be seen that the changing in reinforcement spacing, reinforcement stiffness, or span length does not affect the location of possible failure envelope. The location of maximum strain envelope indicates that the possible failure envelope developed from the inner edge of the footing extending vertically downward for the upper half of the bridge abutment and is followed by the general Rankine active failure envelope for the bottom half of the GRS-IBS abutment. This result is very similar to the punching shear failure envelope defined by a previous study conducted by Chen et al. on reinforced crushed limestone underneath spread footing [92]. Takemura et al. investigated the failure mechanism of reinforced sand by using centrifuge test [93]. Their results showed that the intensely shear bands were developed from the edges of the footing and extended vertically downward. For the purpose of comparison and verification, the results were compared with the active Rankine failure envelope as shown in Figure 115. It is interesting to notice that the results indicate that the failure envelope is a combination punching shear failure envelope (top) and Rankine failure envelope (bottom), in which the failure envelope is developed under the inner edge of the footing and extending vertically downward to intersect with the Rankine active failure envelope.

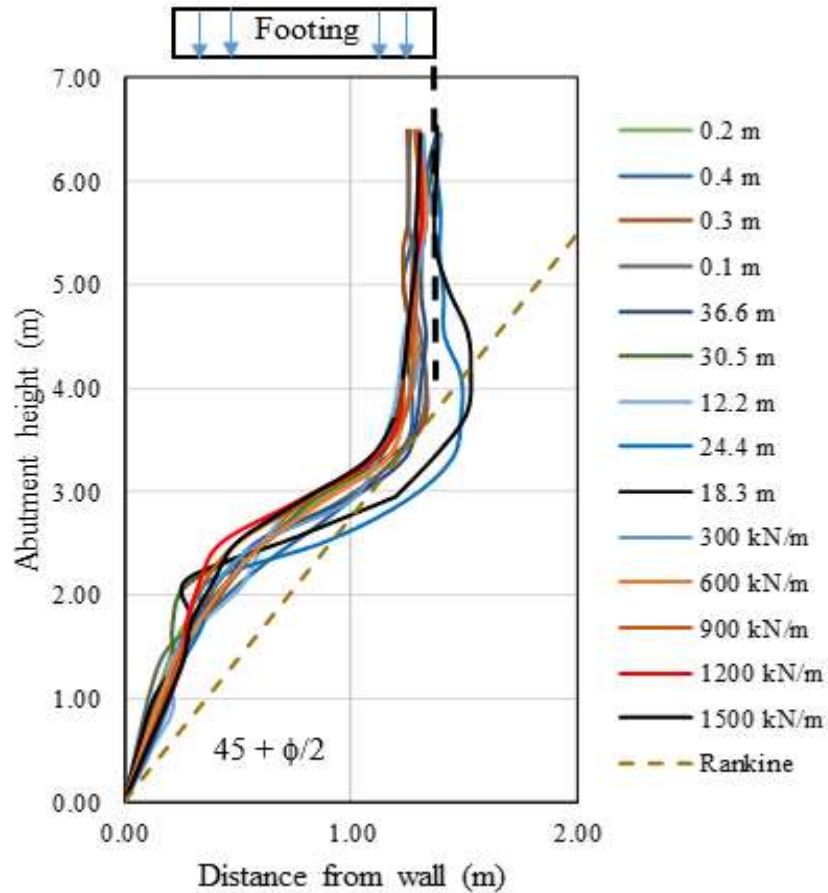


Figure 115

Effect of span length, reinforcement spacing, and reinforcement stiffness on the location of maximum strain envelope

Effect of Differential Settlement on Performance of GES-IBS

Control Sections

For comparison purposes, to evaluate the effect of differential settlement applied at certain locations, a control section was first developed and evaluated without imposing any differential settlement. Three numerical models having span length of 80, 100, and 120 ft. having a span depth of 3.63, 4.54, and 5.45 ft.; bridge abutment height of 17 ft., and 8 in. reinforcement spacing subjected to a uniformly distributed live load of 250 psf were considered as the control sections. The girder was modeled as a solid block ($L_b \times D \times 1$), assuming the bridge span to depth ratio = $L_{span}/D = 24$, composed of elastic elements with an equivalent unit of 75.5 lb./ft³. This procedure

was adopted from a previous work by Zheng and Fox [35]. The RSF dimensions are 1.5 by 7.55 ft. for all cases.

Effect of Differential Settlement on 120-ft. Span Length

Three different areas were assumed to be subjected to 2, 4, 6, and 8 in. differential settlement underneath the RSF, underneath the reinforced-zone including the RSF, and underneath the retained soil to evaluate the effect of the location on the performance of the GRS-IBS in terms of lateral facing displacement and strain distribution value.

Effect of Differential Settlement under the RSF (Case 1)

Four different values of differential settlements (2, 4, 6, and 8 in.) were considered underneath the RSF, in which only the RSF is subjected to a prescribed displacement while the rest of the model is unchanged. Figure 116 presents the effect of the differential settlement on the strain distribution along the geosynthetics at four different locations: 20, 40, 60, and 80% of bridge abutment height (H) from the top of the RSF. It can be seen that a differential settlement underneath the RSF has a high impact on the strain distribution. The maximum strain value obtained is 1.4% under 2 in. differential settlement at 40% of bridge abutment height from the top of the RSF and decreases to 0.75% under 6 in. differential settlement at the same location. The lateral facing displacement increases from about 1.1 in. under a differential settlement of 2 in. to about 1.65 in. under 8 in. as shown in Figure 117. It was noted that the lower reinforcement layers are highly effected by the differential settlement underneath the RSF. It can be seen that the at the right edge of the RSF, which is located 6 ft. away from the GRS abutment face, has a high impact on the strain distribution associated with those reinforcement layers located at the bottom of the GRS abutment. It was noted that the maximum strain value increases when the RSF subjected to a differential settlement of 2 in. and decreases when subjected to a differential settlement higher than 4 in. This can be explained by achieving better mobilization of the reinforcements with increasing the settlement Chen et al. [92].

Effect of Differential Settlement under the Reinforced-Zone including the RSF (Case 2)

The same procedure was followed in this case using the same numerical model under the same loading conditions (120 ft. span length) to evaluate the performance of the GRS-IBS subjected to a differential settlement under the reinforced-zone including the RSF. It was noted that the strain increases under a 2 in. of differential settlement and decreases when the abutment subjected to a differential settlement higher than 4 in. as shown in Figure 118. This is because the reinforcement zone including the RSF is subjected to the same displacement while in case 1 the reinforcement zone was subjected to a partial displacement under the RSF. The lateral facing displacement

increases from around 1.2 in. under a differential settlement of 2 in. to 1.5 in. under a differential settlement of 8 in. as shown in Figure 119.

Effect of Differential Settlement under the Retained-Soil (Case 3)

In this case, the retained soil was assumed to be subjected to the differential settlement, due to a special soil conditions underneath it, under the same loading conditions in cases 1 and 2. It can be seen in Figure 120 that the differential settlement has a low impact on the strain distribution value and shape as it does on the lateral facing displacement in Figure 121. It was noted that the differential settlement underneath the retained soil caused a rotational behavior for the lateral facing deformation. The lateral facing displacement at the bottom of the GRS abutment increases from around 0.2 in. under a differential settlement of 8 in. to around 0.75 in. under a differential settlement of 4 in. and to 1.2 in. under a differential settlement of 2 in.

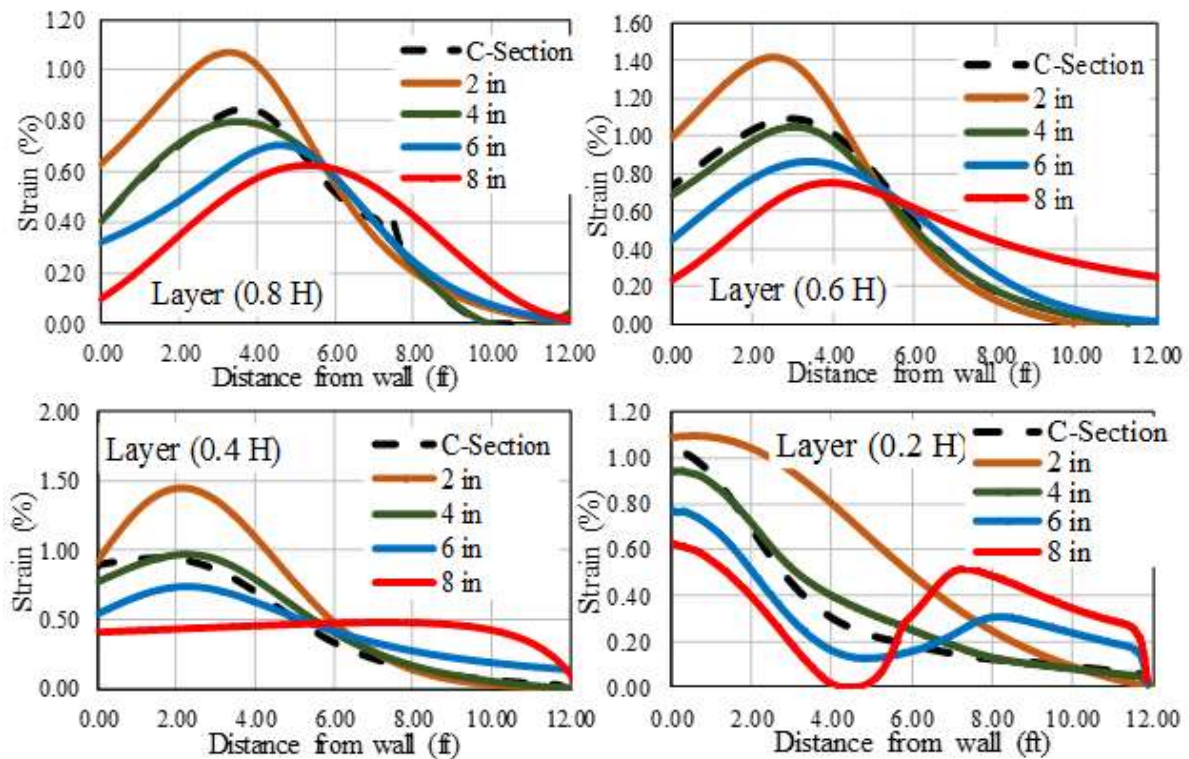


Figure 116

Effect of differential settlement under the RSF on the strain distribution along geosynthetics for a span length of 120 ft.

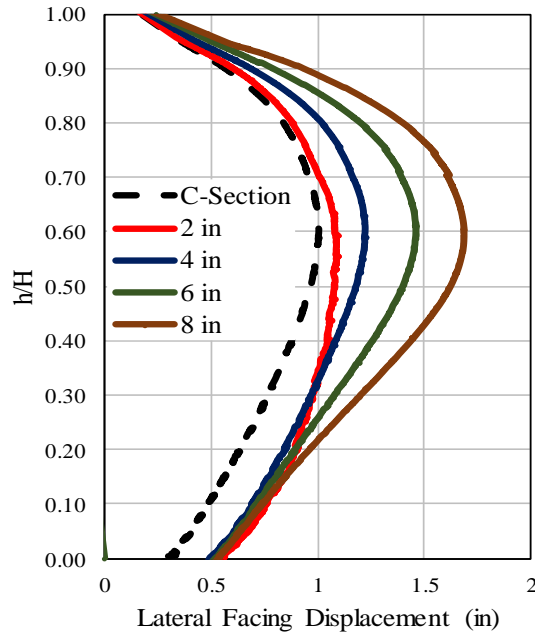


Figure 117

Effect of differential settlement under the RSF on the lateral facing displacement for a span length of 120 ft.

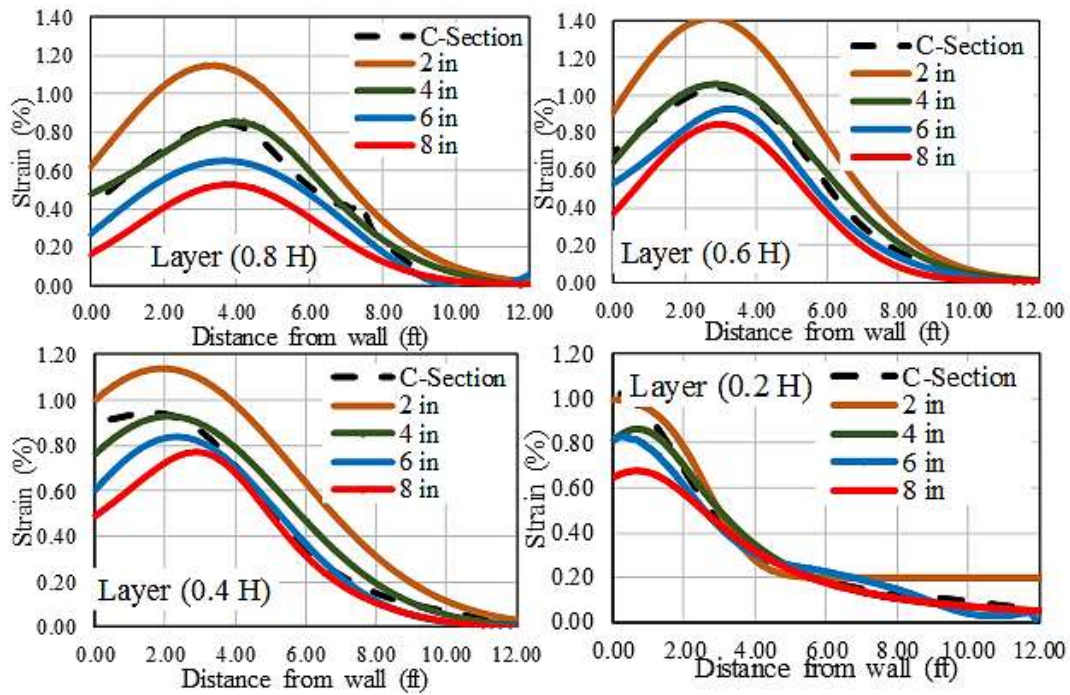


Figure 118

Effect of differential settlement of the reinforced-zone on the strain distribution along geosynthetics for a span length of 120 ft.

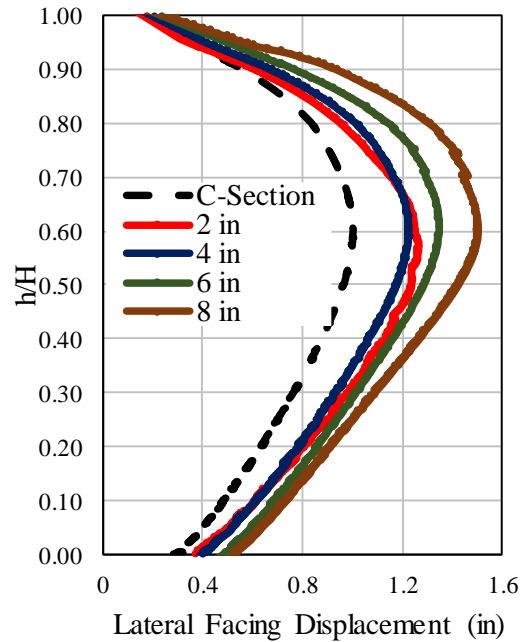


Figure 119

Effect of differential settlement of the reinforced-zone on the lateral facing displacement for a span length of 120 ft.

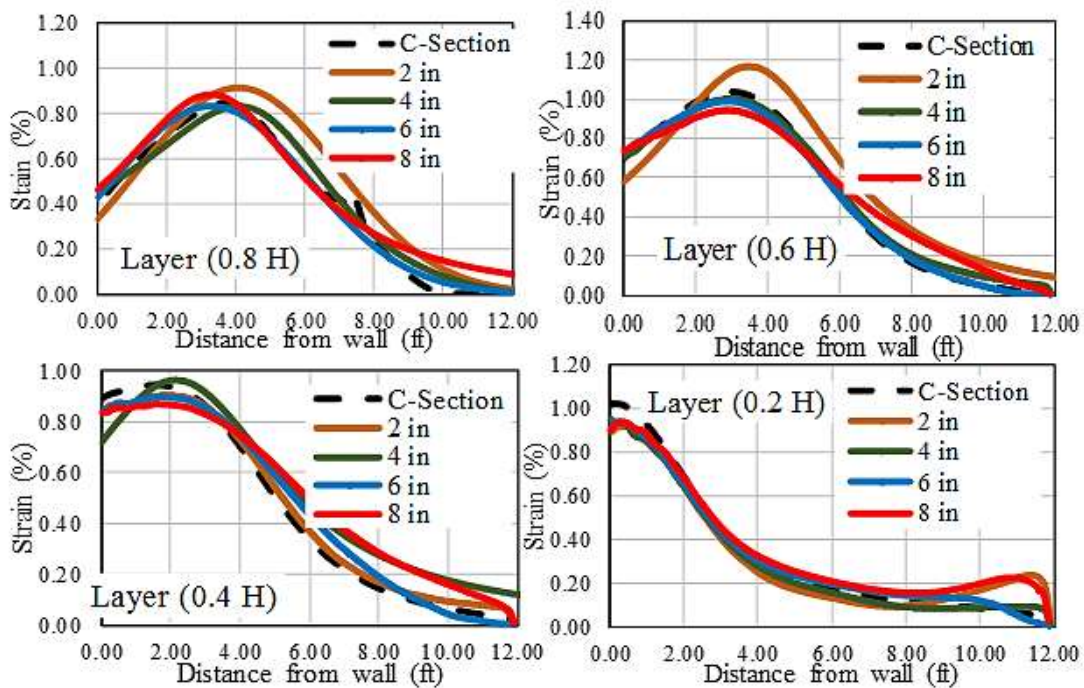


Figure 120

Effect of differential settlement of the retained soil on the strain distribution along geosynthetic for a span length of 120 ft.

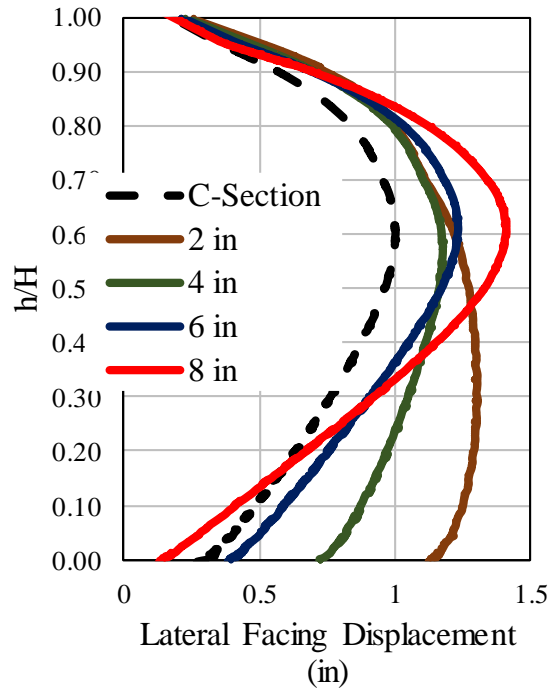


Figure 121

Effect of differential settlement of the retained soil on the lateral facing displacement for a span length of 120 ft.

Effect of Differential Settlement underneath the Reinforced-Zone on Different Span Lengths (Case 2)

In order to study the combination effects of differential settlement and span length on the strain distribution along the geosynthetic and the lateral facing displacement, case 2 differential settlement, where the reinforced-zone including the RSF is subjected to a differential settlement, was analyzed for span lengths of 100 and 80ft. to be compared with the same case situation for a span length of 120 ft. In this case, similar trend was observed due to a differential settlement of 2, 4, 6, 8 in. underneath the reinforced-zone but different values associated with the span lengths of 120, 100, and 80 ft. Figures 122 and 124 present the strain distribution along the geosynthetic at four different locations at 20, 40, 60, and 80% of the bridge abutment height from the top of the RSF. It can be seen in Figure 122 that the maximum strain value increases by applying a 2 in. differential settlement under the reinforced-zone and decreases when the differential settlement exceeds 4 in. The maximum strain value decreases from 1.12% under 2 in. differential settlement at 40% height of the bridge abutment from the top of the RSF for a span length of 120 ft. to 0.9% and 0.7% under the same conditions for the span length of 100 ft. and 80 ft., respectively.

Figures 123 and 125 present the effect of the differential settlement for different span lengths on the lateral facing deformation. It can be seen that the differential settlement accompanied with the span length has a high impact on the lateral facing deformation, in which the lateral facing deformation increases by increasing the differential settlement value and the span length, e.g., the lateral facing deformation decreases from 1.5 in. for a span length of 120 ft. to around 1.05 and 1.1 in. for span lengths of 100 and 80 ft., respectively, under 8 in. differential settlement.

It can be concluded that the differential settlement accompanied with the different span lengths have a high impact on the GRS-IBS performance in terms of strain distribution and lateral facing deformation.

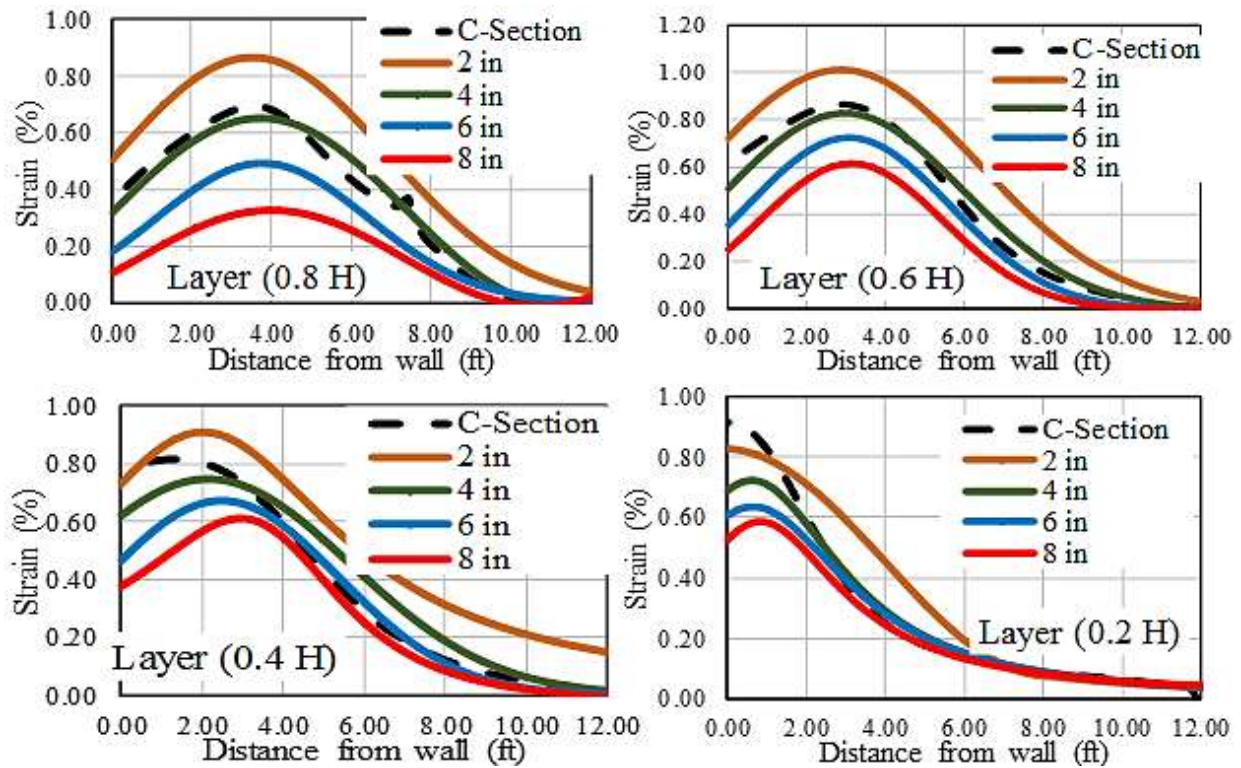


Figure 122

Effect of differential settlement of the reinforced-zone on the strain distribution along geosynthetics for a span length of 100 ft.

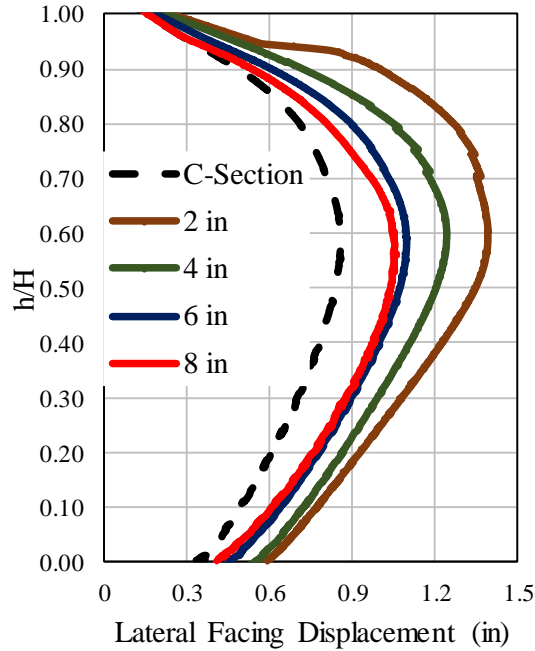


Figure 123

Effect of differential settlement of the reinforced-zone on the lateral facing displacement for a span length of 100 ft.

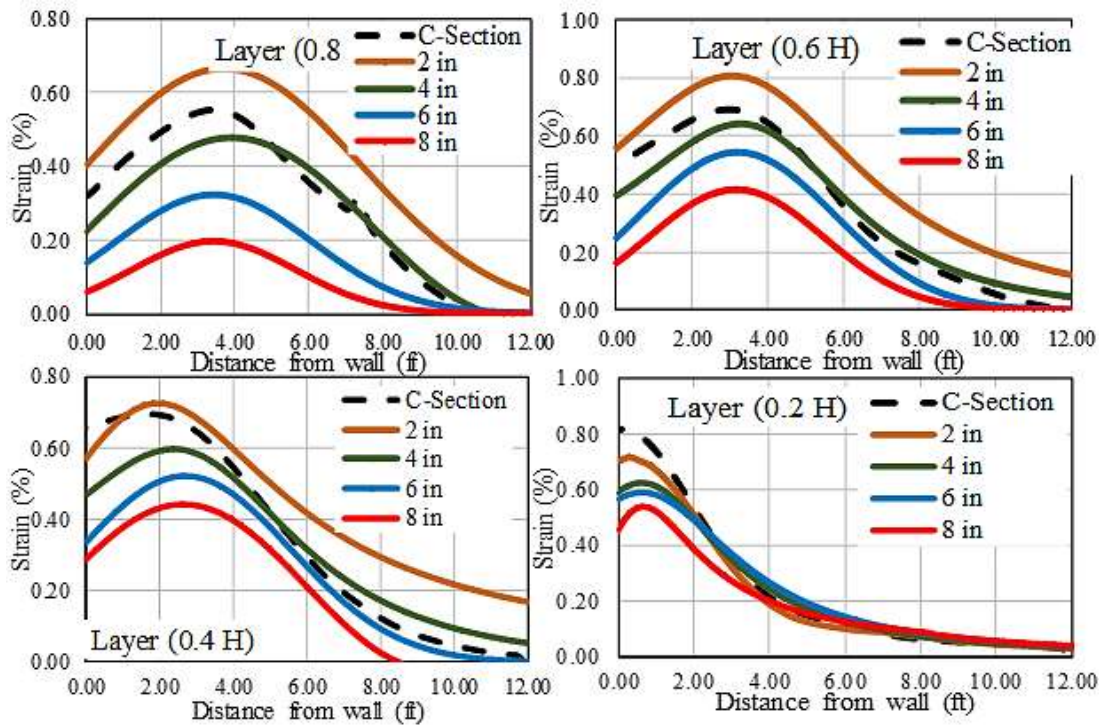


Figure 124

Effect of differential settlement of the reinforced-soil on the strain distribution along geosynthetics for a span length of 80 ft.

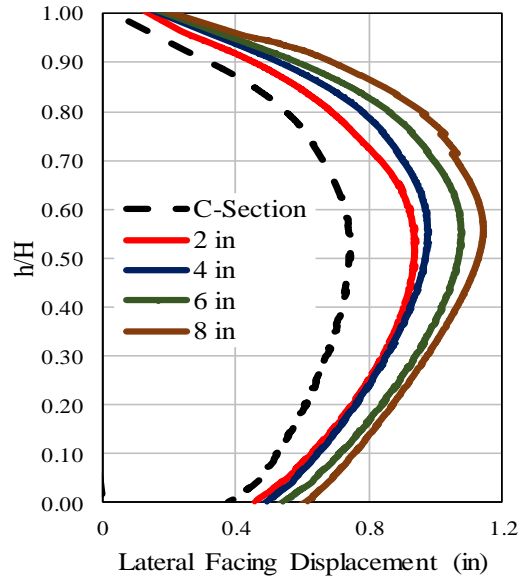


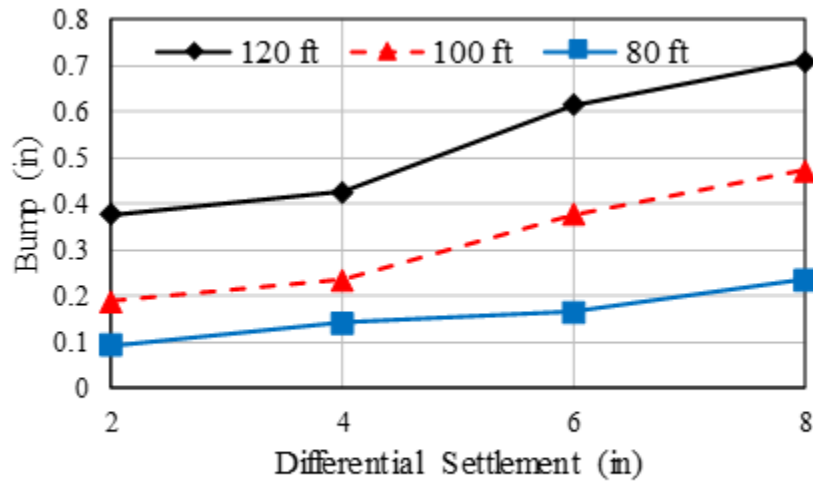
Figure 125

Effect of differential settlement of the reinforced-soil on the lateral facing displacement for a span length of 80 ft.

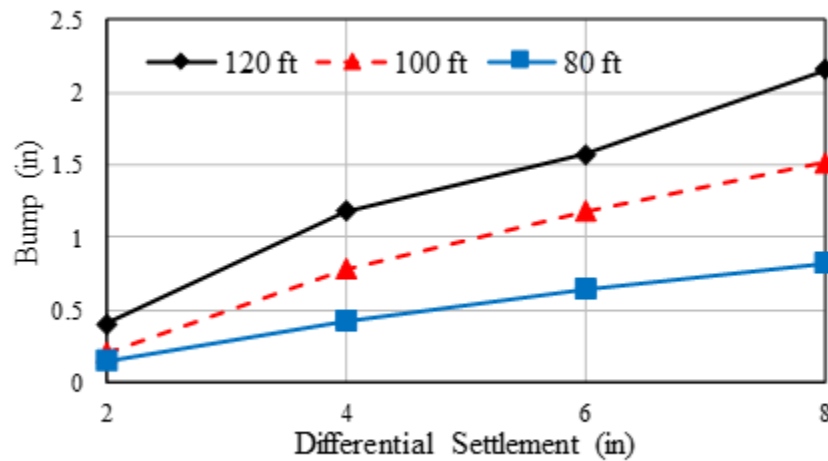
Effect of Differential Settlement on the Bump at the Bridge Slap and Approach Roadway Intersection

One of the main advantages of the GRS-IBS is alleviating the bump at the intersection between the bridge span and the approach roadway. Figures 126(a) and (b) present the effect of the differential settlement underneath the RSF and underneath the reinforced-zone including the RSF on the bump at the bridge slap-approach roadway intersection for three different spans length of 80, 100, and 120 ft. It can be seen that the bump at the bridge is proportional to the differential settlement value, in which the bump increases by increasing the differential settlement under both the RSF and the reinforced-zone. The maximum bump at the bridge for a span length of 120 ft. under a differential settlement of 8 in. underneath the RSF is 0.7 in., which is below the allowable differential settlement of 0.6-1.2 in. as was documented in previous literature [96 - 99]. However, the differential settlement underneath the reinforced-zone is highly effected the bump value. It can be seen that a differential value of 8 in. underneath the reinforced-zone for a bridge span of 120 ft. caused a 2.1 in. bump at the intersection of the bridge slab and the approach roadway which is higher than the allowable bump as documented in the literature. It can be concluded that a differential settlement up to 6 in. accompanied with a bridge span up to 100 ft. underneath the reinforced-zone subjected for surface loading will not create a serious riding comfort issue. However, care must be taken in case of a bridge span higher than 100 ft. built on weak or special

soils near water as recommended by Adams et al. that if the bridge is crossing water, the GRS-IBS should not be considered unless scour effect is properly addressed [5].



(a)



(b)

Figure 126

Effect of differential settlement on the bump at the intersection between the bridge slab and the approach roadway for different span lengths: a) underneath RSF, b) underneath reinforced-zone

Effect of Differential Settlement on Lateral Facing Pressure

Another serious issue that must be addressed here is the effect of the differential settlement underneath the reinforced including the RSF on the lateral facing pressure since the GRS-IBS facing is not considered as a structure element due to the composite behavior of the closely

reinforced soil that reduces the lateral facing pressure into very small value [5, 36, 94, 95]. In this case, four different values of differential settlement of 2, 4, 6, and 8 in. were considered underneath the reinforced-zone, the most critical case based on our analysis, for a bridge span length of 120 ft. subjected to surface loading. Figure 127 presents the effect of differential settlement underneath the reinforced-zone including the RSF on lateral facing pressure for a bridge span of 120 ft. under service loading condition. It can be seen that the differential settlement has a medium impact on the lateral facing pressure. It was noted that the top of the GRS-IBS abutment is the most effected location, in which the lateral facing pressure decrease by increasing the differential settlement except for 2 in. differential settlement. The lateral facing pressure decreases from 2 psi for the control section to 1 psi for 8 in. differential settlement and increase to 3 psi for 2 in. differential settlement. It can be concluded that that the recommendation about inserting pin in the top facing blocks by Adams et al. is necessary in designing the GRS-IBS bridge abutment [5].

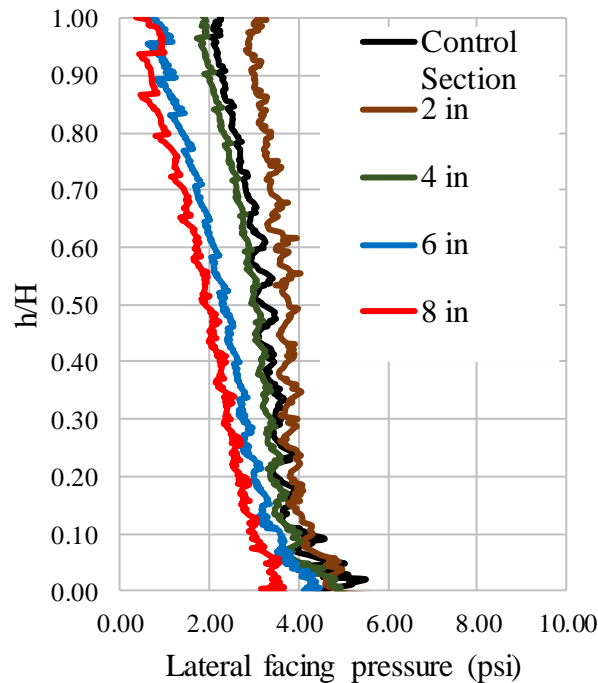


Figure 127

Effect of differential settlement on lateral facing pressure for a bridge span of 120 ft. under service loading condition

SUMMARY AND CONCLUSIONS

This report documents the findings of an extensive research study that was conducted to evaluate the performance of the Geosynthetic Reinforced Soil-Integrated Bridge System (GRS-IBS). The objectives of this study were achieved through conducting an experimental testing, monitoring program and a finite element numerical modeling program. The following sections summarize the findings and conclusions of each of these two programs.

Experimental Testing Program

The experimental testing program in this study included full instrumentation of in-service GRS-IBS abutment at Maree Michel Bridge in Louisiana to monitor and evaluate the performance of the abutment during construction and under service loading condition. Various types of instrumentations were installed in the south abutment of the GRS-IBS. The primary measurements were the vertical and horizontal deformations near the front wall, settlements due to the soil foundation and the GRS-IBS backfill; the stresses and distribution of stresses within the GRS-IBS abutment and below the reinforced soil foundation; and the distribution of strains along the geosynthetic reinforcements. Six different types of instrumentations were used to monitor the performance of the GRS-IBS abutment at Maree Michel Bridge: Shape Acceleration Array (SAA), earth pressure cells, strain gauges, piezometers, and thermocouples. Additionally, surveying was conducted at the bridge surface upon the completion of the construction. Based on the results of the experimental testing and monitoring program, the following conclusions can be drawn:

- In general, the satisfactory performance of the GRS-IBS abutment at Maree Michel Bridge and the expected economic benefits helps DOTD to gain more confidence in implementing the GRS-IBS technology. In fact, the performance results of the GRS-IBS abutment at Maree Michel Bridge demonstrate that the FHWA design of GRS-IBS is somehow conservative.
- The settlement and deformation measurements of the GRS-IBS exhibited logical and consistent trends. The soil foundation settlement was increased with lift placement, with more movements occurred near the center of the abutment than the corners. The measurements of abutment deformations indicate that the maximum total settlements across the GRS abutment were significantly less than the design value. The majority of this deformation (~70%) was due to settlement of foundation soil, while less than 30% of the total deformation occurred within the abutment and RSF. The maximum vertical strain in the abutment was less than 45% of maximum value specified by the FHWA.
- The maximum lateral movement was observed near the top of the wall. Following the construction of bridge abutment, the facing wall experienced some appreciable outward

(away from backfill) lateral deformation. After placing the steel girders, the lateral movement close to the wall significantly increased. However, the maximum lateral deformation of wall face was less than 1% of bearing width, as recommended by the FHWA.

- The measured vertical pressure values compared well with the predicted geostatic stresses.
- Measurements from horizontal pressure cells demonstrated that the lateral pressure on the wall face is negligible. In this study, the maximum lateral pressure of 0.087 psi was measured in the lower level of the abutment with no secondary reinforcement layer. The addition of secondary reinforcement within the top layers of abutment significantly reduced the lateral pressure. Moreover, no significant change in lateral pressure was observed during the construction stages.
- The observed geotextile strains were within the range specified in the FHWA manual (less than 2%). During the construction, the maximum strain observed along the reinforcement layers was half of the maximum strain specified by the FHWA.
- The magnitude and distribution of strain in geosynthetic layers varied in depth of the abutment. Strain measurements showed that the locus of the slip surface changed significantly after placement of the steel girders. Before the placement of the girders, the locus of maximum strains formed a bilinear surface with an angle close to theoretical Rankine failure surface up to certain height, followed by a vertical surface. However, after the placement of the steel girders, the distance of linear surface representing the locus of maximum strains increased with the abutment height at the lower levels and decreased sharply at the top layers of GRS abutment.
- A comparison between the GRS-IBS method and GSME approach shows that the GSME approach is more conservative in case of closely-spaced reinforced mass used as a bridge abutment. The calculated lateral pressure on the facing wall based on the GSME approach (Rankine theory) was significantly higher than measurements on the field. In addition, the measured lateral pressures did not change significantly by depth and surcharge load, which contradicts with the classical lateral pressure theory. Small lateral displacement of facing wall verifies the assumption that unlike regular GSME mass, block pull-out and connection force is not an issue in GRS-IBS.
- A maximum total deformation of 0.47 in. was observed during the truck load tests when two trucks were placed bridge at location 2. However, more than 60% (0.3 in) of the vertical deformation was due to the dead weight of bridge, less than 40% of total deformation occurred regarding to live load.
- A maximum lateral displacement of 0.02 in. was recorded during the truck load tests at the top of the abutment when two trucks were placed on the bridge at location 2. This measured

lateral movement behind the GRS mass is very small and within the range of resolution limit of SAA sensors.

- A maximum vertical pressure of 2.9 psi was measured at layer 19 of abutment when two trucks were placed bridge at location 2. It should be noted here that the maximum total vertical stress at layer 19 (2.7 ft. below the strip footing) due to both dead weight and static truck loads is about 7.5 psi (4.6 psi + 2.9 psi), or 1080 psf. Accordingly, it is expected that the maximum vertical stress below strip footing will be far less than 4000 psf, as recommended by FHWA.
- A maximum reinforcement strain of about 1.2% was measured for layer 19 during the truck load tests, which is much less than the FHWA criteria of 2%.

Finite Element Numerical Modeling Program

2D and 3D-Finite element analyses were conducted to numerically simulate the performance of the GRS-IBS under different loading conditions, which was verified using the results of the fully-instrumented GRS-IBS abutment at Maree Michel Bridge in Louisiana, and to conduct a comprehensive parametric study on the effect of different parameters on the performance of GRS-IBS. The FE parametric study included the effects of abutment height H , span length L_{span} , reinforcement spacing S_v , reinforcement stiffness, EA , backfill internal friction angle, ϕ , length of reinforcement, L_r , width of reinforcement soil footing, B_{RSF} , secondary reinforcement, setback distance, a_b , subgrade soil conditions, bearing width, b , and the effect of differential settlement. Different constitutive models were used to describe the behavior of materials used in the GRS-IBS abutment. The second order hyperbolic elastoplastic hardening soil model was selected to describe the behavior of the backfill material. The linear elastic model with Mohr–Coulomb failure criterion model was used to simulate the mechanical behavior of the interface between the backfill material and geotextile and the facing blocks. Both the geotextiles and facing blocks were modeled using linear elastic model. An elastic-perfectly plastic model was used to simulate the subgrade soils. Based on the results of the numerical modeling program, the following conclusions can be drawn:

- The maximum lateral deformations of the GRS-IBS wall face were 0.16 in. (0.11% of the GRS-IBS height) and 0.35 in. (0.24% of the GRS-IBS height) for the service loading condition and the abnormal loading condition (dead load + 3 times service load), respectively. These values are much less than the values recommended by the FHWA (< 1%).
- The maximum settlement of the GRS-IBS under the service loading condition as predicted by the FE analysis was 0.4 in., which is 0.3% of the GRS-IBS wall height and less than the FHWA recommendations (0.5% of the GRS-IBS wall height) and two times the field

measurements (0.2 in.). This is most probably due to the over consolidated soil caused by the old bridge.

- The maximum reinforcement strain in the GRS-IBS abutment under service loading was 1.2%, which is two times higher than the strain in the RSF and less than the typical design value of 2%, indicating that the reinforcing is sufficiently stiff to avoid excessive deformation.
- The results of this study clearly demonstrated that the plain strain 2D-FE analysis can be used to simulate the performance of GRS-IBS with good satisfactory, and the results are very close to those predicted by the 3D-FE analyses.
- The bridge span length has a significant effect on the GRS-IBS performance such that the magnitude of maximum strain and lateral facing displacement increase with increasing the span length. The maximum reinforcement strain increased from about 0.4% for span length of 40 ft. to about 0.9% for a span length of 120 ft. at 0.6 H above the bottom of the abutment, and the lateral facing displacement increased from around 1.0 in. for a 40 ft. span length to 1.2 in. for a 120 ft. span length. The results indicated that while the magnitude of reinforcement strain is affected by span length and abutment height, the shape of the strain distribution is not affected.
- The reinforcement spacing has significant influence on the strain distribution along the reinforcement and the lateral facing displacement, in which the maximum strain and lateral facing displacement increase with increasing reinforcement spacing. The maximum strain increases from 0.62% for a reinforcement spacing of 4 in. to 1.63% for a reinforcement spacing of 16 in. at 0.8 H from bottom of abutment. The maximum lateral facing displacement increases from 1.1 in. for a reinforcement spacing of 4 in. to about 1.6 in. for a reinforcement spacing of 16 in.
- The reinforcement stiffness has significant effect on the behavior of GRS-IBS in terms of reducing the lateral facing displacement and the magnitude of strain distribution along the reinforcement with increasing stiffness up to a certain point. After this point, the impact tends to decrease in contrary to the effect of reinforcement spacing, which shows a constant impact on the performance of GRS-IBS.
- It was noted that the reinforcement spacing has more significant role in the performance of the GRS-IBS than the reinforcement stiffness for reinforcement spacing equal or higher than 8 in. However, the reinforcement stiffness has close effect to reinforcement spacing for reinforcement spacing less than 8 in, which indicates that the 8 in. reinforcement spacing might be the optimum reinforcement spacing for GRS-IBS.
- The FE results indicated that the failure envelope is most likely a combination of punching shear failure envelope (at top) and Rankine failure envelope (at bottom), in which the

failure envelope is developed under the inner edge of the footing and extending vertically downward to intersect with the Rankine active failure envelope.

- It was found that the maximum strains along reinforcements are significantly affected by the degree of soil compaction, such that the magnitude of strains increases with decreasing the degree of compaction either for the entire abutment material or within 3 ft. from wall block facing. The reinforcement layers at the bottom have higher strains than those in the top layers. For the reinforcement layer located at 80% of the abutment height from the bottom, the maximum strain increases from about 0.9% for the control section ($\phi = 50^\circ$ and geotextile stiffness = 41 kips/ft.) to about 1.4% for the case with 75% reduction of compaction ($\phi = 45^\circ$) for the entire abutment, and to about 2.0% for the worst case scenario ($\phi = 35^\circ$ and geotextile stiffness = 20.5 kips/ft.). The values of maximum strain for the case with 75% reduction of compaction of the entire abutment are slightly higher than those for the 75% reduction of compaction within the 3 ft. from the wall block facing.
- The lateral facing deformation are also affected by the soil compaction, either for the entire abutment or within 3 ft. from the wall block facing. The maximum lateral deformation of wall facing increases from about 1.2 in. for the control section ($\phi = 50^\circ$ and geotextile stiffness = 41 kips/ft.) to about 1.7 in. for case with 75% reduction of compaction for the entire abutment ($\phi = 45^\circ$), and to about 2.5 in. for the worst scenario case ($\phi = 35^\circ$ and geotextile stiffness = 20.5 kips/ft.). This clearly indicates that decreasing the soil compaction will result in increasing the lateral deformation of wall facing.
- The reinforcement length had low effect on the performance of the GRS-IBS abutment, especially for $L_r \geq 0.5 H$. For example, the lateral facing displacement increases from around 1.2 in. for $L_r \geq 0.5 H$ to around 1.4 in. for $L_r = 0.3 H$, which indicates that increasing the reinforcement length will not significantly decrease the lateral facing displacement.
- The results of FE indicate that the secondary reinforcement has slightly effect on the performance of GRS-IBS in terms of lateral deformation of wall face. Meanwhile, the magnitudes of maximum strains along the reinforcement increased by about 20% for reinforcements located at 80% of the abutment height as measured from the bottom of the abutment (i.e., within bearing bed zone), which are still less than the recommended value by FHWA (2%). However, it is necessity to keep the secondary reinforcement within the top layers of abutment to help improve the compaction of backfill material, especially within 3 ft. zone from the wall face, and hence improve the performance of GRS-IBS.
- The differential settlement under the reinforced-zone and RSF has high effect on the performance of the GRS-IBS in terms of strain distribution along the geosynthetic and the lateral facing displacement. The maximum strain value obtained was 1.4% under 2 in. differential settlement at 40% of bridge abutment height from the top of the RSF and decreased to 0.75% under 6 in. differential settlement at the same location. The lateral

facing displacement increased from 1.1 in. under a differential settlement of 2 in. to 1.65 in. under 8 in. for abutment height of 120 ft. However, the maximum reinforcement strain associated with a differential settlement of 8 in. for a span length of 120 ft. under service loading condition was 1.4%, which is less than the typical design value of 2% as recommended by the FHWA [5]. It should be noted here that one advantage of using GRS is that it is flexible and can accommodate differential settlements.

- The differential settlement under the retained soil has little effect on the reinforcement strain along the geosynthetic but has a moderate effect on the lateral facing displacement at 50% of the bridge abutment height from the top of the RSF. It was observed that the differential settlement underneath the retained soil can cause a rotational behavior for the lateral facing deformation. The lateral facing displacement at the bottom of the GRS abutment increases from around 0.2 in. under a differential settlement of 8 in. to around 0.75 in. under a differential settlement of 4 in. and to 1.2 in. under a differential settlement of 2 in.
- The maximum predicted bump at the bridge span - approach roadway intersection was 0.7 in., which is associated with 8 in. differential settlement under the RSF for a span length of 120 ft. under service loading. This value is less than the allowable differential settlement values as documented in the literature.
- A differential settlement up to 6 in. accompanied with a bridge span up to 100 ft. underneath the reinforced-zone subjected to service loading will not create a serious riding comfort issue. However, care must be taken in case of a bridge span higher than 100 ft. built on weak or special soils near water as recommended by Adams et al., and that if the bridge is crossing water, the GRS-IBS should not be considered unless scour effect is properly addressed [5].
- The differential settlement has moderate effect on the magnitude of lateral facing pressure. The top of the GRS-IBS abutment was the most effected location, in which the lateral facing pressure decreased with increasing the differential settlement, except for the 2 in. differential settlement. The lateral facing pressure decreased from 2.0 psi for the control section to 1.0 psi for 8 in. differential settlement and increased to 3.0 psi for a 2 in. differential settlement. This demonstrates that that the recommendation about inserting reinforcement in the top facing blocks by Adams et al. is necessary in designing the GRS-IBS 1 abutment [5].

RECOMMENDATIONS

- Based on the satisfactory field performance of the GRS-IBS at Maree Michel Bridge, it is highly recommended that DOTD design engineers start implementing the GRS-IBS technology in the design of new bridge abutments in Louisiana.
- Consider verifying the findings of this finite element parametric study, such as the effects of length of reinforcement, reinforcement stiffness/spacing, and secondary reinforcement on the performance of GRS-IBS through field instrumenting, monitoring and testing of full-scale GRS-IBS bridge abutments.
- Consider an experimental study to evaluate the combined effects of reinforcement spacing and reinforcement stiffness to optimize the performance of GRS-IBS abutments and to develop and implement the composite concept in the design of GRS-IBS abutments.
- Consider a research study to investigate the benefits of geogrid-backfill interlocking on the performance of the GRS-IBS abutment, and the interaction between the aggregate size and geogrid aperture when using the geogrid as a reinforcement.

ACRONYMS, ABBREVIATIONS, AND SYMBOLS

a_b	setback distance
AASHTO	American Association of State Highway and Transportation Officials
ASTM	American Standard for Testing Materials
b	bearing width
B_{RSF}	width of reinforced soil footing
B_{total}	base width
c	cohesion
CDOT	Colorado Department of Transportation
D_L	lateral displacement
D_{max}	maximum particle size
DOTD	Louisiana Department of Transportation and Development
D_{rsf}	depth of the RSF
D_v	vertical settlement
E	Young's modulus
EA	axial stiffness
EDC	Every Day Counts
E_s	soil stiffness
E_r	reinforcement stiffness
FE	Finite element
FHWA	Federal Highway Administration
ft.	foot(feet)
F_{bin}	thrust force against the wall face
$F.S.$	factor of safety
GMSE	geosynthetic mechanically stabilized earth
GRS	geosynthetic reinforced soil
GSGC	Generic Soil-Geosynthetic Composite
IBS	Integrated bridge system
H	height of wall
in.	inch(es)
K_{ab}	active earth pressure coefficient
kip	kilo pounds
kN	kilonewton
K_p	coefficient of passive earth pressure
kPa	kilopascal
ksf	kilo pounds per square foot

lb.	pound(s)
L_r	length of reinforcement
L_{rb}	length of bearing bed
LRFD	load and resistance factor design
LTRC	Louisiana Transportation Research Center
L_{span}	span length
m	meter(s)
M-C	Mohr-Coulomb
MSE	mechanically stabilized earth
MPa	megapascal
OCR	over-consolidation ratio
psf	pounds per square feet
psi	pounds per square inch
R_i	reduction factor
RSF	reinforced soil foundation
RSS	reinforced soil slopes
SAA	Shape Acceleration Array
S_v	vertical reinforcement spacing
T_f	tensile strength of reinforcement
USFS	US Forest Service
2D	two-dimensional
3D	three-dimensional
δ	interface friction angle
γ	unit weight
γ_b	unit weight of the retained backfill
γ_d	dry unit weight
γ_r	unit weight of the reinforced fill
γ_t	wet unit weight
ν	Poisson's ratio
ϕ	internal friction angle
ϕ_{cv}	critical state friction angle
ϕ_p	peak friction angle
ψ	dilation angle

REFERENCES

1. Schanz, T., Vermeer P. A., and Bonnier, P. G. (1999). The Hardening Soil Model - Formulation and Verification. *Proceedings of Plaxis Symposium, Beyond 2000 in Computational Geotechnics*, Amsterdam, Balkema, pp. 281-296.
2. Phillips, E. K. (2014). *Investigation of Required Tensile Strength Predicted by Current Reinforced Soil Design Methodologies*. M.S. Thesis, Virginia Tech, Blacksburg, Blacksburg, VA.
3. Elias, V., Christopher, B., and Berg, R. (2001). *Mechanically Stabilized Earth Walls and Reinforced Soil Slopes Design and Construction Guidelines*. FHWA-NHI-00-043, Federal Highway Administration, McLean, VA.
4. Wu, J. T. H. (2007). Lateral Earth Pressure against the Facing of Segmental GRS Walls. *Geosynthetics in Reinforcement and Hydraulic Applications (GSP 165)*, Gabr and Bowders (Eds.). ASCE, Reston, VA, 165-175.
5. Adams, M. T., Nicks, J., Stabile, T., Wu, J. T. H., Schlatter, W., and Hartmann, J. (2011). *Geosynthetic Reinforced Soil Integrated Bridge System - Interim Implementation Guide*. FHWA-HRT-11-026, Federal Highway Administration, McLean, VA.
6. Keller, G. R., and Devin, S. C. (2003). Geosynthetic-Reinforced Soil Bridge Abutments. *Transportation Research Board*, Washington, D.C.
7. Lee, K. Z. Z., and Wu, J. T. H. (2004). A Synthesis of Case Histories on GRS Bridge-Supporting Structures with Flexible Facing. *Geotextiles and Geomembranes*, 22(4), 181-204.
8. Liu, H. (2012). Long-term Lateral Displacement of Geosynthetic-Reinforced Soil Segmental Retaining Walls. *Geotextiles and Geomembranes*, 32, 18-27.
9. Liu, H., Wang, X., and Song, E. (2011). Reinforcement Load and Deformation Mode of Geosynthetic-Reinforced Soil Walls Subject To Seismic Loading during Service Life. *Geotextiles and geomembranes*, 29(1), 1-16.
10. Rowe, R. K., and Ho, S. K. (1998). Horizontal Deformation in Reinforced Soil Walls. *Canadian Geotechnical Journal*, 35(2), 312-327.
11. Bathurst, R. J., Allen, T. M., and Walters, D. L. (2005). Reinforcement Loads in Geosynthetic Walls and the Case for a New Working Stress Design Method. *Geotextiles and geomembranes*, 23(4), 287-322.
12. Helwany, S. M. B., Reardon, G., and Wu, J. T. H. (1999). Effects of Backfill on the Performance of GRS Retaining Walls. *Geotextiles and Geomembranes*, 17(1), 1-16.

13. Ho, S. K., and Rowe, R. K. (1996). Effect of wall Geometry on the Behaviour of Reinforced Soil Walls. *Geotextiles and Geomembranes*, 14(10), pp.521-541.
14. Helwany, S. M., Wu, J. T., and Froessl, B. (2003). GRS Bridge Abutments - An Effective Means to Alleviate Bridge Approach Settlement. *Geotextiles and Geomembranes*, 21(3), 177-196.
15. Wu, J. T., Lee, (2006). *Design and Construction Guidelines for Geosynthetic-Reinforced Soil Bridge Abutments with a Flexible Facing*, Report No. 556. Transportation Research Board.
16. Wu, J. T. H., Lee, K. Z. Z., Helwany, S. M. B., and Ketchart, K. (2006). *Design and Construction Guidelines for GRS Bridge Abutment with a Flexible Facing*. Report No. 556, National Cooperative Highway Research Program, Washington, D.C.
17. Zheng, Y., Fox, P. J., and Shing, P. B. (2014). Numerical Simulations for Response of MSE Wall-Supported Bridge Abutments to Vertical Load. *Ground Improvement and Geosynthetics*, pp. 493-502.
18. Zheng, Y., Fox, P. J., and Benson Shing, P. (2015a). Numerical Study of Deformation Behavior for a Geosynthetic-Reinforced Soil Bridge Abutment under Static Loading. *IFCEE 2015*, pp. 1503-1512.
19. Zheng, Y., Fox, P. J., and Shing, P. B. (2015b). Verification of Numerical Model for Static Analysis of Geosynthetic-Reinforced Soil Bridge Abutments. *Geosynthetics 2015*, pp. 152-160.
20. Zheng, Y. and Fox, P. J. (2016). Numerical Investigation of Geosynthetic-Reinforced Soil Bridge Abutments under Static Loading. *Journal of Geotechnical and Geoenvironmental Engineering*, 142(5), p.04016004.
21. Christopher, B. R., Gill, S. A., Giroud, J. P., Juran, I., Mitchell, J. K., Schlosser, F., and Dunncliff, J. (1990). *Reinforced Soil Structures Volume I. Design and Construction Guidelines*, Report No. FHWA-RD-89-043.
22. Adib, M., Mitchell, J. K., and Christopher, B. (1990). Finite Element Modeling Of Reinforced Soil Walls and Embankments. *Design and Performance of Earth Retaining Structures*, pp. 409-423.
23. Ling, H. I., Tatsuoka, F., and Tateyama, M. (1995). Simulating Performance of GRS-RW by Finite-Element Procedure. *Journal of geotechnical engineering*, 121(4), pp.330-340.
24. Ling, P., and Leshchinsky, D. (1996). *Mesa Walls: Field Data Reduction, Finite Element Analysis, and Preliminary Design Recommendations*. Report to Tensar Earth Technologies, Inc., Atlanta, GA, February 1, 1996.
25. Leshchinsky, D. and Vulova, C. (2001). Numerical Investigation of the Effects of Geosynthetic Spacing on Failure Mechanisms in MSE Block Walls. *Geosynthetics International*, 8(4), pp.343-365.
26. Holtz, R. D., and Lee, W. F. (2002). *Internal Stability Analyses of Geosynthetic Reinforced Retaining Walls*. Report WA-RD 532.1, Washington State Department of Transportation, Washington.

27. Guler, E., Hamderi, M., and Demirkan, M. M. (2007). Numerical Analysis of Reinforced Soil-Retaining Wall Structures with Cohesive and Granular Backfills. *Geosynthetics International*, 14(6), pp.330-345.
28. Huang, J., Bin-Shafique, S., Han, J. and Rahman, M. S. (2014). Modelling of Laterally Loaded Drilled Shaft Group In Mechanically Stabilized Earth Wall. *Proceedings of the Institution of Civil Engineers-Geotechnical Engineering*, 167(4), pp.402-414.
29. Huang, J., Han, J., Parsons, R. L. and Pierson, M. C. (2013). Refined Numerical Modeling of A Laterally-Loaded Drilled Shaft in an MSE Wall. *Geotextiles and Geomembranes*, 37, pp.61-73.
30. Huang, J., Parsons, R. L., Han, J. and Pierson, M. (2011). Numerical Analysis of A Laterally Loaded Shaft Constructed within an MSE Wall. *Geotextiles and Geomembranes*, 29(3), pp.233-241.
31. Mirmoradi, S. H., and Ehrlich, M. (2014a). Modeling of the Compaction-Induced Stresses in Numerical Analyses of GRS Walls. *International Journal of Computational Methods*, 11(02): 1342002.
32. Mellas, M., Mabrouki, A., Benmeddour, D. and Rahmouni, O. (2015). Numerical Study of Geogrid-Reinforced Segmental Earth Retaining Wall. *Journal of Applied Engineering Science and Technology*, 1(2), pp.43-49.
33. Rahmouni, O., Mabrouki, A., Benmeddour, D., and Mellas, M. (2016). A Numerical Investigation into the Behavior of Geosynthetic-Reinforced Soil Segmental Retaining Walls. *International Journal of Geotechnical Engineering*, 10(5), pp.435-444.
34. Liu, H. (2015). Reinforcement Load and Compression of Reinforced Soil Mass under Surcharge Loading. *Journal of Geotechnical and Geoenvironmental Engineering*, 141(6), p.04015017.
35. Zheng, Y. and Fox, P. J. (2017). Numerical Investigation of the Geosynthetic Reinforced Soil-Integrated Bridge System under Static Loading. *Journal of Geotechnical and Geoenvironmental Engineering*, 143(6), p.04017008.
36. Ardah, A., Abu-Farsakh, M., and Voyiadjis, G. (2017). Numerical Evaluation of the Performance of a Geosynthetic Reinforced Soil-Integrated Bridge System (GRS-IBS) under Different Loading Conditions. *Geotextiles and Geomembranes*, 45(6): pp. 558-569.
37. Abu-Farsakh, M., Ardah, A., and Voyiadjis, G. (2018). 3D Finite Element Analysis of the Geosynthetic Reinforced Soil-Integrated Bridge System (GRS-IBS) under Different Loading Conditions. *Transportation Geotechnics*, 15, pp.70-83.
38. Abu-Farsakh, M., Ardah, A. and Voyiadjis, G. (2018). Numerical Investigation of the Performance of Geosynthetic Reinforced Soil-Integrated Bridge System (GRS-IBS) Subjected to Differential Settlement. *Geosynthetics International*, No. 18-01788.
39. Abu-Farsakh, M., Ardah, A., and Voyiadjis, G., (2018). Numerical Investigation of the Performance of a Geosynthetic Reinforced Soil-Integrated Bridge System (GRS-IBS) under Working Stress Conditions. *IFCEE 2018* (pp. 76-87).

40. Ardah, A., Abu-Farsakh, M. Y., and Voyiadjis, G. Z. (2018). Numerical Evaluation of the Effect of Differential Settlement on the Performance of GRS-IBS. *Geosynthetics International*, 25(4), pp.427-441.
41. Abu-Farsakh, M., Saghebfar, M., Ardah, A., and Chen, Q. (2017). A Case Study on Evaluating the Performance of a Geosynthetic Reinforced Soil Integrated Bridge System (GRS-IBS). *Geotechnical Frontiers*, pp. 12-22.
42. Wu, J. T., Yang, K. H., Mohamed, S., Pham, T., and Chen, R. H. (2014). Suppression of Soil Dilation - A Reinforcing Mechanism of Soil-Geosynthetic Composites. *Transportation Infrastructure Geotechnology*, 1(1), 68-82.
43. Adams, M. and Nicks, J. (2014). Secondary Settlement of Geosynthetic-Reinforced Soil Piers: Preliminary Results. *Geo-Congress 2014: Geo-characterization and Modeling for Sustainability* (pp. 4228-4237).
44. Nicks, J. E., Adams, M. T., and Ooi, P. S. K. (2013a). *Geosynthetic Reinforced Soil Performance Testing—Axial Load Deformation Relationships*. Federal Highway Administration. Report No. FHWA-HRT-13-066, McLean, VA.
45. Nicks, J.E., Adams, M.T., and Stabile, T. (2013b). Performance Testing for Geosynthetic Reinforced Soil Composites. *Proceedings of the 5th International Young Geotechnical Engineers' Conference*. 2013b.
46. Pham, T. (2009). *Investigating Composite Behavior of Geosynthetic-Reinforced Soil (GRS)* Mass. Ph.D. Thesis, University of Colorado at Denver, Denver, CO.
47. Wu, J. T., Yang, K. H., Mohamed, S., Pham, T., and Chen, R. H. (2014). Suppression of Soil Dilation - A Reinforcing Mechanism of Soil-Geosynthetic Composites. *Transportation Infrastructure Geotechnology*, 1(1): 68-82.
48. Schlosser, F. and Long, N. T. (1974). Recent Results in French Research on Reinforced Earth, *Journal of Construction*, Division 100(3), pp 223-237.
49. Yang, Z. (1972). *Strength and Deformation Characteristics of Reinforced Sand*. PhD. Thesis, University of California at Los Angeles, Los Angeles, CA.
50. Wu, J. T., and Pham, T. Q. (2013). Load-carrying Capacity and Required Reinforcement Strength of Closely Spaced Soil-Geosynthetic Composites. *Journal of Geotechnical and Geoenvironmental Engineering*, 139(9), 1468-1476.
51. VanBuskirk, C. (2010). Adoption and implementation of GRS design concepts A consultant's perspective. *19th Vancouver Geotechnical Society Symposium*, Geosynthetic Reinforced Walls, Slopes, and Earthworks, Vancouver, Canada.
52. Broms, B. (1977). Triaxial Tests with Fabric-Reinforced Soil. *Proc. of the International Conference on the use of Fabric in Geotechnics*, Paris, 3, 129-134.

53. Wu, J. T. H., and Helwany, S. M. B. (1996). A Performance Test for Assessment of Long-Term Creep Behavior of Soil-Geosynthetic Composites. *Geosynthetics International*, 3(1), 107-124.
54. Ketchart, K., and Wu, J. T. H. (1996). *Long-term Performance Tests of Soil-Geosynthetic Composites*. Rep. CDOT-CTI-96-1, Colorado Dept. of Transportation, Denver, CO.
55. Ketchart, K., and Wu, J. T. H. (2001). *Performance Test for Geosynthetic Reinforced Soil Including Effects of Preloading*, Report FHWA-RD-01-018, Federal Highway Administration, Washington, D.C.
56. Adams, M. T. (1997). Performance of a Prestrained Geosynthetic Reinforced Soil Bridge Pier, *Proceedings of the International Symposium on Mechanically Stabilized Backfill*, J.T.H. Wu (Ed) A.A. Balkema, Rotterdam, 35-53.
57. Elton, D. J., and Patawaran, M. A. B. (2005). *Mechanically Stabilized Earth (MSE) Reinforcement Tensile Strength from Tests of Geotextile Reinforced Soil*. Report submitted to the Alabama Highway Research Center, Auburn University, 77 pages.
58. Elton, D. J., and Patawaran, M. A. B. (2004). Mechanically Stabilized Earth Reinforcement Tensile Strength from Tests of Geotextile-Reinforced Soil. *Transportation Research Board*, Washington, D.C.
59. Adams, M. T., Kanop, K., and Wu, J. T. H. (2007). Mini Pier Experiments-Geosynthetic Reinforcement Spacing and Strength as Related to Performance. American Society of Civil Engineers. *Geosynthetics in Reinforcement and Hydraulic Applications (GSP 165)*, pp. 18-21.
60. Ziegler, M., Heerten, G., and Ruiken, G. (2008). Progress in the Understanding of Geosynthetic/Soil Composite Material Behaviour in Geosynthetic Reinforced Earth Structures. *The First Pan American Geosynthetics Conference and Exhibition*, 2-5 March 2008, Cancun, Mexico.
61. Kost, A., Filz, G., and Cousins, T. (2014). *Differential Settlement of a GRS Abutment: Full-Scale Investigation*. Virginia Center for Transportation Innovation and Research Charlottesville, VA.
62. Abu-Hejleh, N., Wang, T., and Zornberg, J. G. (2000). Performance of Geosynthetic-Reinforced Walls Supporting Bridge and Approaching Roadway Structures. *Advances in Transportation and Geoenvironmental Systems Using Geosynthetics*, ASCE, Reston, VA, 218-243
63. Warren, K. A., Schlatter, W., Adams, M., Stabile, T., and LeGrand, D. (2010). Preliminary Results for a GRS Integrated Bridge System Supporting a Large Single Span Bridge. *Proceedings of the Earth Retention Conference 3*, ASCE, Reston, VA, 612-619.
64. Warren, K. A., Whelan, M., Adams, M., and Nicks, J. (2013). Preliminary Evaluation of Thermally Induced Strains and Pressures Developed in GRS Integrated Bridge System. *Geosynthetics Conference*, Long Beach, CA.

65. Mohamed, K., Abouzakhm, M., and Elias, M. (2011). Applications and Performance of Geosynthetic-Reinforced Soil Abutments on Soft Subsurface Soil Conditions. *Transportation Research Board*.
66. Lee, W. F. (2000). *Internal Stability Analyses of Geosynthetic Reinforced Retaining Walls*. Ph.D. Thesis, Dept. of Civil and Environmental Engineering, University of Washington.
67. Chen, T.C, Chen, R.H, Lin, S.S. (2000). A Nonlinear Homogenized Model Applicable to Reinforced Soil Analysis. *Geotextile and Geomembranes*, 18, 349-366.
68. Zhang, M.X., Javadi, A.A., Lai, Y.M., and Sun, J. (2006). Analysis of Geosynthetic Reinforced Soil Structures with Orthogonal Anisotropy. *Geotechnical and Geological Engineering*, 24, 903-917.
69. Vulova, C., and Leshchinsky, D. (2003). *Effect of Geosynthetic Reinforcement Spacing on the Performance of Mechanically Stabilized Earth Walls*. Report No. FHWA-RD-03-048, Federal Highway Administration, McLean, VA.
70. Skinner, G. D., and Rowe, R. K. (2005). Design and Behavior of a Geosynthetic Reinforced Retaining Wall and Bridge Abutment on a Yielding Foundation. *Geotextiles and Geomembranes*, 23(3), pp.234-260.
71. Chou, N. N. S., and Wu, J. T. H. (1993). *Investigating Performance of Geosynthetic-reinforced Soil Walls*. Final Report No. CDOT-UCD-R-93-21.
72. Helwany, S. M., Wu, J. T., and Kitsabunnarat, A. (2007). Simulating the Behavior of GRS Bridge Abutments. *Journal of Geotechnical and Geoenvironmental Engineering*, 133(10), pp.1229-1240.
73. Berg, R. R., Allen, T. M., and Bell, J. R. (1998). Design Procedures for Reinforced Soil Walls - A Historical Perspective. *Sixth International Conference on Geosynthetics*. Atlanta, GA
74. Berg, R. R., Barry R. C., and Naresh, C. S. (2009). *Design of Mechanically Stabilized Earth Walls and Reinforced Soil Slopes - Volume II*. Report No. FHWA-NHI-10-025.
75. Zornberg, J. G., Christopher, B., Leshchinsky, D., Han, J., and Tanyu, B. F. (2014). *Defining the Boundary Conditions for Composite Behavior of Geosynthetic Reinforced Soil (GRS) Structures*. National Cooperative Highway Research Program (NCHRP) Phase I Interim Report.
76. Wu, J.T. (2001). *Revising the AASHTO Guidelines for Design and Construction of GRS Walls*. Report No. CDOT-DTD-R-2001-16.
77. Duncan, J. M., Byrne, P., Wong, K. S., and Mabry, P. (1980). *Strength, Stress-Strain and Bulk Modulus Parameters for Finite-Element Analysis of Stresses and Movements in Soil Masses*. Report No. UCB/GT/80-01, UC Berkeley, CA, USA.

78. Walters, D., Hatami, K., Bathurst, R. J., Vlachopoulos, N., Saunders, D., Burgess, G. P., and Allen, T. M. (2000). Full-scale Testing and Modeling of Geosynthetic Reinforced Soil Retaining Walls. *Proceedings of the 53rd Canadian Geotechnical Conference*, Montreal, Canada.
79. Hatami, K., and Bathurst, R. J. (2005). Development and Verification of a Numerical Model for the Analysis of Geosynthetic-Reinforced Soil Segmental Walls under Working Stress Conditions. *Canadian Geotechnical Journal*, 42(4): 1066-1085.
80. Brandon, T., Al-Qadi, I., Lacina, B. and Bhutta, S. (1996). Construction and Instrumentation of Geosynthetically Stabilized Secondary Road Test Sections. *Transportation Research Record: Journal of the Transportation Research Board*, (1534), pp.50-57.
81. Dantas, B. T. (2004). *Working Stress Analysis Method for Reinforced Cohesive Soil Slopes*, Doctoral dissertation, D. Sc. Thesis, COPPE/UFRJ, Rio de Janeiro (in Portuguese).
82. Morrison, K. F., Harrison, F. E., Collin, J. G., Dodds, A. M., and Arndt, B. (2006). *Shored mechanically stabilized earth (SMSE) wall systems design guidelines*, Report No. FHWA-CFL/TD-06-001.
83. Ehrlich, M., and Mirmoradi, S. H. (2013). Evaluation of the Effects of Facing Stiffness and Toe Resistance on the Behavior of GRS Walls. *Geotextiles and Geomembranes*, 40, pp.28-36.
84. Mirmoradi, S. H., and Ehrlich, M. (2014b). Numerical Evaluation of the Behavior of GRS Walls with Segmental Block Facing under Working Stress Conditions. *Journal of Geotechnical and Geoenvironmental Engineering*, 141(3): 04014109.
85. Riccio, M., Ehrlich, M., and Dias, D. (2014). Field Monitoring and Analyses of the Response of a Block-Faced Geogrid Wall Using Fine-Grained Tropical Soils. *Geotextiles and Geomembranes*, 42(2): 127-138.
86. Brinkgreve, R. B. J. (2002). *PLAXIS: Finite Element Code for Soil and Rock Analyses: 2D-Version 8: [user's Guide]*. Balkema.
87. Bolton, M. D. (1986). The Strength and Dilatancy of Sands. *Geotechnique*, 36(1): 65-78.
88. Adams, M., Nicks, J., and Lynch, C. (2015). Lateral Deformation of GRS Bridge Abutments. *International Geosynthetics* (Vol. 2015).
89. Lunne, T., Robertson, P. K., and Powell, J. J. M. (1997). *Cone Penetration Testing*. Geotechnical Practice.
90. Yu, Y., Damians, I. P., and Bathurst, R. J. (2015). Influence of Choice of FLAC and PLAXIS Interface Models on Reinforced Soil - Structure Interactions. *Computers and Geotechnics*, 65: 164-174.
91. Nazzal, M. D. (2007). *Laboratory Characterization and Numerical Modeling of Geogrid Reinforced Bases in Flexible Pavements*. Ph.D. Dissertation, Louisiana State University, Baton Rouge, LA.
92. Chen, Q., Abu-Farsakh, M., and Sharma, R. (2009). Experimental and Analytical Studies of Reinforced Crushed Limestone. *Geotextiles and Geomembranes*, 27(5), pp.357-367.

93. Takemura, J. (1992). Bearing Capacities and Deformations of Sand Reinforced with Geogrids. *Proc. of International Symposium on Earth Reinforcement Practice (IS Kyushu'92)*, Fukuoka, Japan (Vol. 1, pp. 695-700).
94. Saghebfar, M., Abu-Farsakh, M. Y., Ardah, A., Chen, Q., and Fernandez, B. A. (2017a). Full-Scale Testing of Geosynthetic-Reinforced, Soil-Integrated Bridge System. *Transportation Research Record: Journal of the Transportation Research Board*, (2656): 40-52.
95. Saghebfar, M., Abu-Farsakh, M., Ardah, A., Chen, Q., and Fernandez, B. A. (2017b). Performance Monitoring of Geosynthetic Reinforced Soil Integrated Bridge System (GRS-IBS) in Louisiana. *Geotextiles and Geomembranes*, 45(2): 34-47.
96. Zaman, M., Laguros, J.G., and Jha, R. (1995). *Statistical Models for Identification of Problematic Bridge Sites and Estimation of Approach Settlements*. Progress Report (DRAFT) (No. Study 2188), 110 p.
97. Stark, T. D., Olson, S. M., and Long, J. H. (1995). *Differential Movement at the Embankment/Structure Interface-Mitigation and Rehabilitation*, Final Report (No. Project IAB-H1, FY 93). See <https://trid.trb.org/view/447707> (accessed 28/05/2018). TRB, Washington, DC, USA.
98. Long, J., Olson, S., Stark, T., and Samara, E. (1998). Differential Movement at Embankment-Bridge Structure Interface in Illinois. *Transportation Research Record: Journal of the Transportation Research Board*, (1633): 53-60.
99. Ardah, A. (2018). *Field Instrumentations and Numerical Analysis of Geosynthetic Reinforced Soil - Integrated Bridge System (GRS-IBS)*, Ph.D. Dissertation, Louisiana State University, Baton Rouge, LA.

This public document is published at a total cost of \$250. 42 copies of this public document were published in this first printing at a cost of \$250. The total cost of all printings of this document including reprints is \$250. This document was published by Louisiana Transportation Research Center to report and publish research findings as required in R.S. 48:105. This material was duplicated in accordance with standards for printing by state agencies established pursuant to R.S. 43:31. Printing of this material was purchased in accordance with the provisions of Title 43 of the Louisiana Revised Statutes.